Investigation of highly efficient Bismuth-based electrocatalysts for CO_2 electroreduction to formate

by

Shaoqing Liu

A thesis submitted in partial fulfillment of the requirements for the degree of

Doctor of Philosophy

in

Materials Engineering

Department of Chemical and Materials Engineering
University of Alberta

Abstract

Renewable energy-powered electrochemical CO_2 reduction (ECR) is considered as a promising approach to producing high value-added chemicals to mitigate the ever-increasing accumulation of CO_2 in the atmosphere. It could offer a sustainable route to achieving both carbon neutrality in the energy cycle and the storage of renewable energy. Among all the possible products of CO_2 reduction, formate has attracted great attention because it is being widely explored as a hydrogen storage material and chemical fuel for fuel cells. It is therefore highly desirable to pursue efficient electrocatalysts for ECR toward formate production. However, the high reaction energy barrier and complicated multi proton-coupled electron transfer steps result in the slow kinetics and broad distributions of the products over most electrocatalysts. Meanwhile, the highly competitive side reaction, hydrogen evolution reaction (HER), always occurs accompanying with ECR. Therefore, the key issue for practical formate production *via* ECR lies in searching for efficient catalysts that can actively and selectively transform CO_2. In this thesis, I aim to develop efficient, cost-effective, and earth-abundant bismuth-based catalysts for simultaneously achieving high activity and selectivity towards ECR, and also to explore and reveal the reaction mechanisms that lead to the enhancement effects of the developed catalysts.

One of the key issues for most of the existing Bi-based catalysts toward ECR is that they do not simultaneously possess high activity (current density > 45 mA cm^{-2}) and high selectivity [faradaic efficiency (FE)] > 90 % in H-cell. Hence, I developed a catalyst of S-doped Bi_2O_3 nanosheets (NSs) coupled with carbon nanotubes (S-Bi_2O_3-CNT) and investigated its ECR performance. Compared with the undoped control catalyst (Bi_2O_3-CNT), the S-Bi_2O_3-CNT not only exhibits an outstanding catalytic activity for CO_2 to formate conversion through ECR, but also can maintain high faradaic efficiency (FE > 90 %) of formate at high current density (48.6 mA cm^{-2}), which outperforms most

of the previously reported catalysts. Theoretical calculations reveal that the S doping causes the electronic delocalization of Bi sites, which can benefit the CO_2 adsorption and stabilize *OCHO intermediates while suppressing HER through hindering *H adsorption. All these synergistically favor formate production over H_2 evolution.

The limited solubility and diffusion of CO_2 in an aqueous solution greatly limit the current catalysts to maintain the high formate selectivity and activity over a wide potential window. I developed a catalyst of Bi_2O_3 NSs grown on carbon nanofiber (Bi_2O_3@C/HB) with inherent hydrophobicity and applied it for ECR toward formate production. In H-cell system, Bi_2O_3@C/HB achieved high formate Faradaic efficiency ($FE_{formate}$) of >93 % over an extremely wide potential window of 1000 mV and a peak formate current density of 102.1 mA cm^{-2}. In addition, the developed Bi_2O_3@C/HB demonstrated a good antiflooding capability when operating in a flow-cell system and can deliver a current density of 300 mA cm^{-2}. Molecular dynamics simulations indicate that the hydrophobic can create a favorable solid-liquid-gas triple-phase boundary which boosts the ECR activity through forming a highly concentrated CO_2 layer and meanwhile inhibiting HER by reducing proton contacts.

Thermodynamic analysis suggests the counter anodic oxygen evolution reaction (OER) consumes ~ 90 % of the overall energy input in a full ECR electrolyzer because of its sluggish kinetics. Its product, O_2, is not of significant economic value. Herein, I present a pair-electrosynthesis tactic for low energy generation of formate *via* coupling selectively anodic electrochemical ethylene glycol oxidation (EGO) and cathodic ECR. I used Ni modified Co phosphide grown on nickel foam (NiCoP/NF) and single Cu atom doped Bi (BiCu) as efficient anodic and cathodic electrocatalysts, respectively. The prepared NiCoP/NF exhibited high performance for anodic EGO to formate conversion with >90 % selectivity and a current density of 500 mA cm^{-2}.

Meanwhile, the cathodic BiCu catalysts can simultaneously achieve high activity, selectivity, and long stability for formate production from ECR. Consequently, the new coupled ECR-EGO system can operate at a cell voltage of ~ 760 mV lower as compared to the conventional ECR-OER system.

Preface

This thesis is an original work conducted by Shaoqing Liu (S. Q. Liu) and under the supervision of Dr. Jing-Li Luo (J.-L. Luo).

Chapter 1 is the introduction that contains the background knowledge and principles of electrochemical CO_2 reduction.

Chapter 2 covers the literature survey of electrocatalysts for electrochemical CO_2 reduction toward formate production.

Chapter 3 briefly introduces the employed methodologies and characterizations.

Chapter 4 has been published as S. Q. Liu, M.-R. Gao, R.-F. Feng, L. Gong, Hongbo. Zeng, J.-L. Luo. Electronic Delocalization of Bismuth Oxide Induced by Sulfur Doping for Efficient CO_2 Electroreduction to formate. *ACS Catalysis*, 2021, 11, 7604-7612. M.-R. Gao conducted the DFT calculations, Dr. R.-F. Feng worked on the synchrotron measurements, Dr. Hongbo Zeng and Dr. L. Gong helped with the atomic force microscope measurements, and Dr. J.-L. Luo provided valuable discussion, comments, suggestions, and feedback for manuscript writing and revision.

Chapter 5 has been published as S. Q. Liu, Ehsan Shahini, M.-R. Gao, L. Gong, P.-F. Sui, Tian Tang, Hongbo Zeng, J.-L. Luo. Bi_2O_3 Nanosheets Grown on Carbon Nanofiber with Inherent Hydrophobicity for High Performance CO_2 Electroreduction in a Wide Potential Window. *ACS Nano*, 2021, 15, 17757-17768. Ehsan Shahini worked on the molecular dynamics, Dr. Hongbo Zeng and Dr. L. Gong helped with the CO_2 bubble adhesion test, P.-F. Sui provided guidance for the flow cell setup, Dr. Tian Tang provided valuable suggestions on the molecular dynamic simulations, and Dr. J.-L. Luo provided valuable discussion, comments, suggestions and feedback for manuscript writing and revision.

Chapter 6 has been submitted to Journal as S. Q. Liu, M.-R. Gao, R.-F. Feng, C.-Y. Xu, J.-L. Luo. Single Cu atom doped Bi enables low energy electroreduction CO_2 to formate *via* integrating with ethylene glycol electro-oxidation. M.-R. Gao conducted DFT calculations, R.-F. F and C.-Y. Xu helped with the synchrotron measurements, and Dr. J.-L. Luo provided valuable discussion, comments, suggestions and feedback for manuscript writing and revision.

Chapter 7 includes the summary and prospects.

Acknowledgments

This thesis is dedicated to all those who have supported me along the path of my academic journey here.

First and foremost, I would like to express my deepest and sincerest gratitude to my supervisor, Dr. Jing-Li Luo, who provided me with the great opportunity to start a wonderful research journey at UofA. Dr. Jing-Li Luo's enthusiasm, professionalism, and efficient work habit have guided me in the past four years and will continue to inspire me in the future. I have learned so much from Dr. Jing-Li Luo throughout my Ph.D. studies, not only about science and academia, but also about leadership and trust, the courage to face failure, and the strength to continue until reaching success. Most importantly, I learned the power of communication. Thank you, Dr. Jing-Li Luo, for letting me be a part of your group, for providing me with an excellent research platform, for supporting my scholarships, my publications, and my attendance at conferences, to name just a few.

I would like to thank all my supervisory committee members, Dr. Natalia Semagina and Dr. Jing Liu, for their valuable suggestions and guidance during my research progress. Special thanks to Dr. Subiao Liu for his valuable suggestions in editing my first paper. I would also like to acknowledge NSERC for its support *via* my graduate scholarships for the past four years.

Furthermore, I would like to express my appreciation to all my colleagues, Dr. Zhou Chen, Dr. Chenyu Xu, Mr. Minrui Gao, Mr. Pengfei Sui, Mr. Bowen Zhang, Ms. Mengnan Zhu, Ms. Yuanyuan Hong, and Ms. Jing Xiao, for all their help and collaborations during my research in the lab. Besides, many thanks go to Dr. Shihong Xu, Dr. Nancy Zhang, Dr. Haoyang Yu, and Dr. Peng Li, for their assistance in the materials characterizations.

I would like to express my deepest appreciation to my parents for all their love, care, trust, and support during the period of my Ph.D. studies. Finally, I want to acknowledge a beautiful lady Ms. Shuwen Wu: I cannot thank you enough for encouraging me to pursue my research career and for the collaborative mutual assistance between us for all these years. Your understanding, patience, and encouragement have kept me focused through this challenging yet memorable journey.

Table of Contents

List of Tables

List of Figures

List of Symbols

E^0	Equilibrium potential
F	Faraday's constant
η	Overpotential
R_{ct}	Charge transfer resistance
C_{dl}	Double layer capacitance
j	Current density
Φ	Work function
ΔG	Gibbs free energy
P_{limit}	Limiting potential

List of Abbreviations

ECR	Electrochemical CO_2 reduction
HER	Hydrogen evolution reaction
FE	Faradaic efficiency
CNT	Carbon nanotube
OER	Oxygen evolution reaction
EG	Ethylene glycol
EGO	Electrochemical ethylene glycol oxidation
NiCoP	Ni modified Co phosphide
NF	Nickel foam
BiCu	Single Cu atom doped Bi
CCS	Carbon capture & storage
PEM	Polymer electrolyte membrane
GDE	Gas diffusion electrode
GDL	Gas diffusion layer
MEA	Membrane electrode assembly
EE	Energy efficiency
2D	Two-dimensional
3D	Three-dimensional
LSV	Linear sweep voltammetry curves
MOF	Metal-organic framework
NT	Nanotube
NW	Nanowire

EIS	Electrochemical impedance spectroscopy
RHE	Reversible hydrogen electrode
SCE	Saturated calomel electrode
PVDF	Poly(vinylidene fluoride)
PTFE	Polytetrafluoroethylene
GBs	Grain boundaries
QDs	Quantum dots
rGO	Reduced graphene oxide
DFT	Density functional theory
SACs	Single-atom catalysts
ECSA	Electrochemical surface area
SEM	Scanning electron microscopy
TEM	Transmission electron microscopy
AFM	Atomic force microscopy
XRD	X-ray diffraction
XPS	X-ray photoelectron spectroscopy
UPS	Ultraviolet photoelectron spectroscopy
TGA	Thermogravimetric analysis
FTIR	Fourier transform infrared spectroscopy
XANES	X-ray absorption near-edge structure
EXAFS	Extended X-ray adsorption fine structure
GC	Gas chromatography
IC	Ionic chromatography

Chapter 1. Introduction

1.1 Research Motivation

The global demand for inexpensive sources of energy has grown rapidly and consistently since the industrial revolution. The extensive use of fossil fuels has not only caused global energy crisis, but also brought various environmental issues.[1-2] The excessive emission of CO_2 from burning fossil fuels and anthropogenic activities has broken the balance of carbon neutral cycle. In 2020, the concentration of CO_2 in atmosphere has reached 414 ppm, far higher than the "safe" level (350 ppm).[3] As a greenhouse gas, the excessive emission of CO_2 poses a critical challenge to humankind, including global warming, sea level rise and ocean acidification.[4-5] It is imperative and necessary to develop carbon capture & storage (CCS) and utilization technologies to mitigate climate changes.

1.2 CO_2 utilization

CO_2 molecule is linear and centrosymmetric with two carbon-oxygen double bonds (C=O). The bond length is 1.16 Å and an energy up to ~ 800 kJ mol^{-1} is required to dissociate this bond.[6-7] Thus, CO_2 is extremely stable, and a high energy (temperature and pressure) input is required for the conversion of CO_2. To date, CO_2 conversion technologies can be generally divided into the following four categories: photochemical, biochemical, thermochemical, and electrochemical (Figure 1.1).[8-11] Out of all these proposed routes for CO_2 conversion, the ECR powered by electricity generated from renewable energy sources (such as solar power and wind) holds the greatest promise due to its unique merits as follows: (1) The electrocatalytic process is under mild conditions (room temperature and pressure); (2) The products are adjustable by controlling the potential applied or different catalysts used; (3) The electrolytes are recyclable which can minimize

consumption of chemicals; (4) The system is simple, modular and compact for large scale applications.

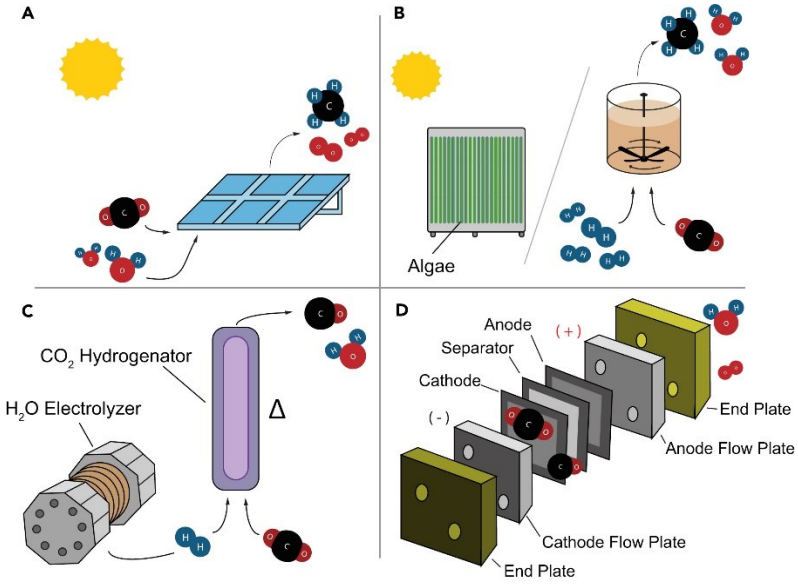

Figure 1.1 Schematic illustration of some popular CO_2 fixation strategies.[8] Reprinted with permission from Reference 8. Copyright 2018, Elsevier.

1.3 Overview of electrochemical CO_2 reduction (ECR)

As shown in Figure 1.2, using electricity generated from renewable energy to drive ECR and transform CO_2 into fuel and chemicals can promote the closure of carbon cycle, thus reducing the concentration of CO_2 in the atmosphere and mitigating the greenhouse effect. In addition, electric energy is stored in the form of chemical energy regardless of the geographical, seasonal, and intermittent nature of renewable energy. This section will give an overview of ECR, including thermodynamics, reaction mechanism, catalytic system, and performance merits.

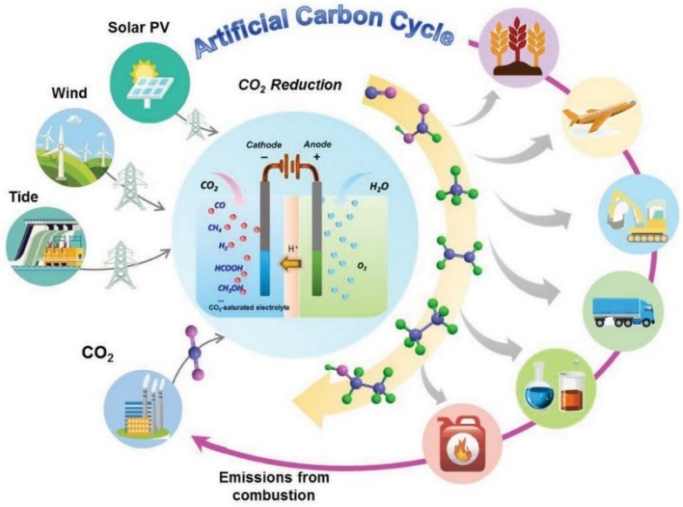

Figure 1.2 Schematic illustration of the artificial carbon cycle *via* electrochemical CO_2 reduction powered by renewable energy sources.[12] Reprinted with permission from Reference 12. Copyright 2019, Wiley.

1.3.1 Thermodynamics of ECR

A typical ECR catalytic process usually involves three steps.[13] The first step is the chemisorption of CO_2 molecules onto the surface of an electrocatalyst. The second step is the transfer of electrons and protons to dissociate the C=O bond and/or produce C–H and C–O bonds. The last step is the desorption of products from the catalyst surface.[14] For most heterogeneous catalysts, these steps occur at the interface of solid catalyst and CO_2-saturated electrolyte. Table 1.1 lists possible ECR pathways and general competitive side reaction (hydrogen evolution reaction, HER) and corresponding equilibrium potentials (E^0).

The activation of CO_2 (Equation 1.1) requires large energy since the original linear CO_2 molecule is rearranged to a bent radical anion (CO_2^{-}).[15] The following proton-coupled electron transfer steps take place more efficiently since these steps are much more thermodynamically favorable compared with the first activation step. However, the high activity of CO_2^{-} anion radical and small potential differences among various potential products (Equations 1.2-1.9) make selectivity

become the main issue once the reduction proceeds, which strongly depends on the specific activity of different catalyst surfaces and active sites.

Table 1.1 Electrochemical reductions with equilibrium potentials (pH 7 in aqueous solution *versus* standard hydrogen electrode, 25 °C, 1 atmosphere gas pressure, and 1 M for other solutes).[9] Reprinted with permission from Reference 9. Copyright 2018, Elsevier.

Reactions	E^0 (V)	Equation
$CO_2 + e^- \rightarrow CO_2^-$	–1.90	1.1
$CO_2 + 2H^+ + 2e^- \rightarrow CO + H_2O$	–0.52	1.2
$CO_2 + 2H^+ + 2e^- \rightarrow HCOOH$	–0.61	1.3
$CO_2 + 4H^+ + 4e^- \rightarrow HCHO + H_2O$	–0.51	1.4
$CO_2 + 8H^+ + 8e^- \rightarrow CH_4 + 2H_2O$	–0.24	1.5
$2CO_2 + 12H^+ + 12e^- \rightarrow C_2H_4 + 4H_2O$	–0.34	1.6
$CO_2 + 6H^+ + 6e^- \rightarrow CH_3OH + H_2O$	–0.38	1.7
$2CO_2 + 12H^+ + 12e^- \rightarrow C_2H_5OH + 3H_2O$	–0.33	1.8
$2H^+ + 2e^- \rightarrow H_2$	–0.42	1.9

1.3.2 Reaction mechanism of ECR

The ECR is a process with multiple pronto-electron transfer steps leading to different carbon-based products and water:

$$mCO_2 + n(H^+ + e^-) \rightarrow \text{products} + xH_2O$$

Over the past few decades, the reaction mechanisms for different products have been studied both experientially and theoretically.[16-18] A consensus has been reached that the rate-determining step of ECR is the first electron transfer to form $*CO_2^-$ intermediate (where * represents the adsorption site on catalysts).[18] The next step is determined by which atom of CO_2^- is combined to the

adsorption site. If the O atom binds to the adsorption site, the sequent protonation step will form *OCHO intermediate which eventually produces formate or formic acid. If the C atom binds to the adsorption site, the sequent protonation step will form *COOH intermediate which then produces CO. For some materials, such as Cu, the *CO will be further reduced instead of desorption from the surface.[19-20] This will lead to the formation of CH_4 or other multicarbon (C_{2+}) products such as C_2H_4 and C_2H_5OH.

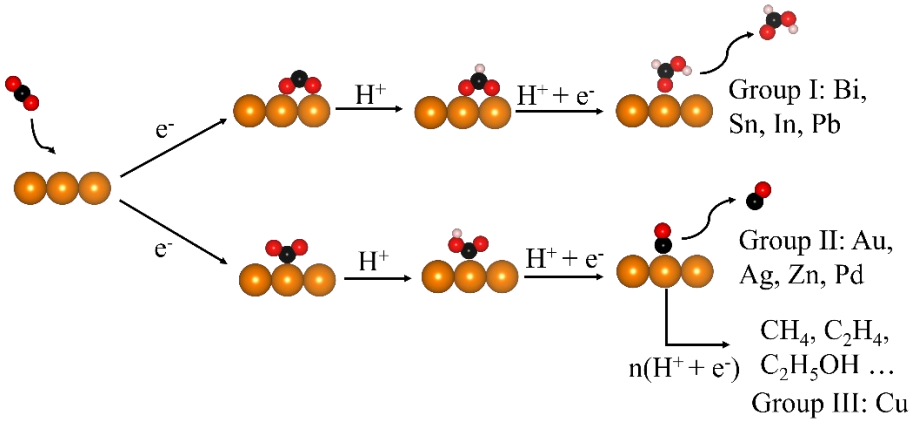

Figure 1.3 Possible reaction pathways for ECR.

The selectivity of ECR is closely related to the binding strength of the above key intermediates and *H (intermediate for HER).[21] Catalytic active sites with strong binding of *COOH would relatively favor the CO production while those active sites with strong binding of *OCHO would relatively favor the formate production (Figure 1.3). Based on this consideration, the metallic ECR catalysts can be generally divided into three groups.[22] Group I metals, including Bi, Sn, In, and Pb, thermodynamically favor the binding of *OCHO over *COOH and then generally produce formate as the main product. Group II metals, such as Au, Ag, Zn, and Pd, thermodynamically favor the binding of *COOH over *OCHO, thus producing CO as the main product. Cu in the Group III is the only pure metal that can reduce CO_2 beyond two electrons due to its ability to relatively stabilizing both *COOH and *CO.[23]

1.3.3 Catalytic system of ECR

The performance of ECR is usually evaluated in a three-electrode system, in which CO_2 reduction reaction takes place at the cathode and oxygen evolution reaction (OER) occurs at the anode. With the in-depth study of ECR, it is found that the ECR performance does not only depend on the development of highly efficient electrocatalyst, but also strongly relates to the reaction device.

H-type electrolytic cell is the most common electrocatalysis system for ECR in the laboratory. As shown in Figure 1.4, the cathode chamber and anode chamber are separated by an ion-exchange membrane (Nafion membrane) to prevent product crossover. Near-neutral electrolyte ($KHCO_3$ or KCl) is usually used in H-type cell. In the cathode chamber, the CO_2 molecules are first dissolved into the electrolyte and then diffuse to the catalyst surface for reaction. Since CO_2 is a nonpolar molecule, the poor solubility of CO_2 (~ 34 mM at 25 °C) in aqueous electrolytes is an intrinsic limitation for achieving high energy efficiency and conversion rate.[24] This results in limited current densities (< 100 mA cm^{-2}).[25] Although the application of ionic liquids can offer much higher CO_2 solubility than water, the improvement of current density is still limited.[26]

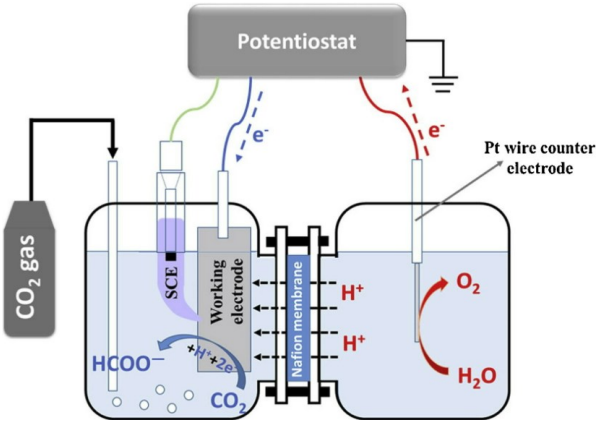

Figure 1.4 Schematic illustration of the conventional H-type cell for ECR.[27] Reprinted with permission from Reference 27. Copyright 2016, Elsevier.

To overcome the mass transport limitation of CO_2 in H-type cell, flow cell is thus widely used for ECR.[28] In a typical flow cell setup, the CO_2 is directly fed to the cathode in the gas phase and reduced at the solid-liquid-gas triple phase boundary (Figure 1.5). The OER is driven at anode and also affects the design of an efficient CO_2 reactor. Cathode and anode chambers are separated by a polymer electrolyte membrane (PEM) that facilitates the flow of ions while attenuating product crossover. Gas diffusion electrodes (GDE) are considered as the core of most flow cells, which are prepared using the fabrication techniques common to the fuel cell community. The nanoparticle catalysts and binders are deposited as porous catalyst layers on the hydrophobic gas diffusion layer (GDL) supports.[29] The most common GDL architecture for ECR is composed of a microporous layer and a carbon fiber layer. In addition, the use of alkaline electrolyte (potassium hydroxide) instead of buffer solution further improves the ECR efficiency by inhibiting HER.[30] Meanwhile, the catholyte is continuously flowing which effectively mitigates the problem of accumulation of the liquid products. Therefore, commercial level ECR performance (current density > 200 mA cm^{-2}) can be achieved when using flow cell reactor. For example, the state-of-the-art current density of the C_2 product (C_2H_4) on a Cu catalyst reaches ~ 1 A cm^{-2} in flow cell.[31] Although much higher performance can be achieved, the poor stability of flow cell is a key issue. This is caused by two possible failure modes for GDE: flooding and (bi)carbonate formation.[32-33] Flooding is a common phenomenon during ECR due to a dramatic decrease in GDE hydrophobicity known as electrowetting, which occurs when operating for a long period of time.[34] The CO_2 diffusion is then impeded when GDE pores become flooded (fully saturated with water), thus inhibiting the ECR by perturbing the gas-liquid phase equilibrium within GDE. In addition, a high pH in the catalyst layer can reduce CO_2 availability because hydroxides readily react with dissolved CO_2 to form (bi)carbonates through the following reactions:

$$CO_2\,(g) \leftrightarrow CO_2\,(aq)$$

$$CO_2\,(aq) + OH^-\,(aq) \leftrightarrow HCO_3^-\,(aq)$$

$$HCO_3^-\,(aq) + OH^-\,(aq) \leftrightarrow CO_3^{2-}\,(aq) + H_2O\,(l)$$

These chemical reactions often consume more CO_2 than ECR and deplete the CO_2 concentration at the catalyst.[35-36]

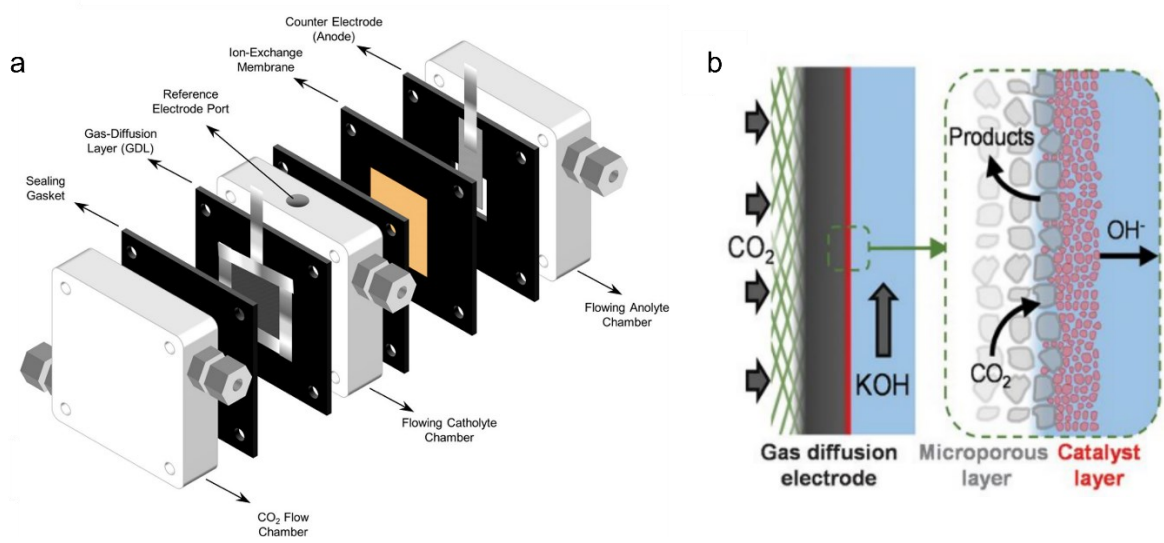

Figure 1.5 (a) Schematic illustration of the flow cell configuration.[37] (b) Schematic of the GDE cathode.[29] Reprinted with permission from Reference 37. Copyright 2019, American Chemical Society. Reprinted with permission from Reference 29. Copyright 2018, American Association for the Advancement of Science.

Based on abundant knowledge of fuel cells and water electrolyzers, an alternative approach is to use a membrane electrode assembly (MEA) reactor.[38-39] In a MEA reactor, gaseous CO_2 and water vapor are fed to the cathode using a compact fuel cell configuration. The catalyst on the cathode is directly pressed against the ion-exchange membrane in a zero-gap configuration. This kind of configuration not only avoids the flooding issue due to the absence of aqueous electrolyte, but also reduces the ohmic losses. More importantly, the side reactions, including HER and (bi)carbonate formation, between electrolytes can be eliminated under electrolyte-free MEA reactor. Based on

this design, the start-of-the-art Faradic efficiency of the C_2H_4 on Cu catalyst reaches ~ 60% with 190 hours of stability.[40] MEA is also suitable for large-scale applications. Zhang et al. achieved a CO current of 8 A on a single Ni atom catalyst in 10 × 10 cm^2 MEA reactor.[41]

1.3.4 Techno-economic analysis of products obtained from ECR

As discussed above, various products can be obtained from ECR at similar potentials. Then, a critical question arises: which CO_2 reduction product is the most profitable? To answer this question, we need to consider the value of the products, the supply and demand of certain ECR products, the electricity cost, the device cost, and the separation cost of the products.

From the market capacity and demand for each product perspective, electrochemically converting CO_2 into CH_4, CH_3OH, C_2H_5OH, and C_2H_4 is promising because each of these has a market size larger than 80 million tons (Mt) per year (Figure 1.6a).[42-43] From the point of view of market price (US \$ t^{-1}), C_2H_5OH and C_2H_4 with much higher market prices per ton are good target products compared to CH_3OH and CH_4. Since electricity cost is one of the major contributions to the operation cost of ECR, the price is normalized to the electrical energy input to better compare the economics of different products. This analysis makes formate and CO the most economically viable products, whereas those C_{2+} products other than propanol are not even profitable (Figure 1.6b).[8, 44] This is understandable because two-electron ECR to CO or formate possesses the highest electrocatalytic performance. The performance for C_{2+} products is relatively poor because the production of C_{2+} products through C-C coupling requires the adsorption of multiple CO_2 molecules on electrode surface and concerted transformation, and is statistically challenging.[45] For example, the selectivity for CO or formate of current state-of-the-art electrocatalysts can reach near 100% with current density > 1 A cm^{-2}, while the selectivity for C_{2+} products is usually lower than 60%.[46] Poor selectivity not only leads to low electricity utilization efficiency, but also brings

additional costs for separation. Therefore, it is not until the further decrease of electricity cost and improvement of electrocatalyst performance that the mass production of C_{2+} products would become economically profitable. To this end, formate production from ECR is so far our target product.

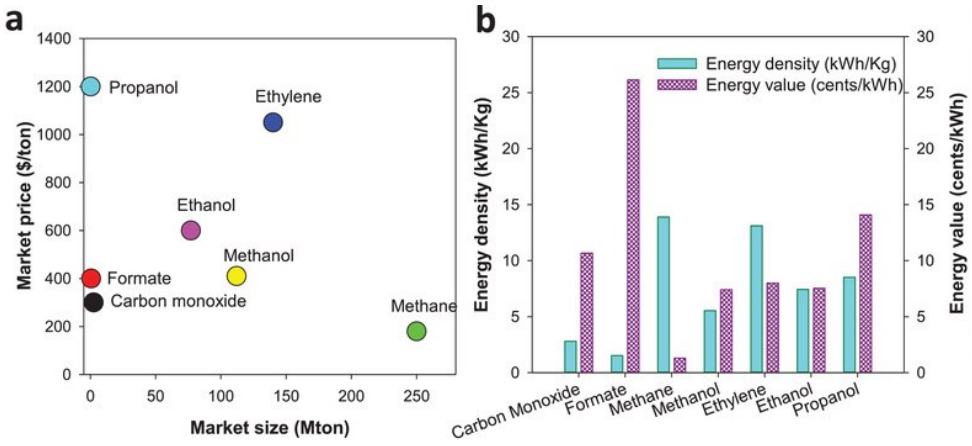

Figure 1.6 (a) Market size and market price of common ECR products. (b) Energy stored (kWh kg^{-1}) for ECR products and their energy values (current market price per energy unit).[42] Reprinted with permission from Reference 42. Copyright 2019, Wiley.

1.3.5 Performance figures of merit

The performances of ECR catalysts are usually evaluated for their activity, selectivity and stability in terms of the following key performance merits.

1. Faradaic efficiency

Faradaic efficiency (FE) is defined as the percentage of electrons consumed for the formation of a certain product.[47] The FE can be simply calculated by following equation:

$$FE = \frac{anF}{Q}$$

where a is the number of electrons transferred for a given product (e.g., $a = 2$ for formate production), n is the number of moles produced for a desired product, F is the Faraday's constant

(96485 C mol^{-1}), while Q is the total charge passed. The FE directly refers to the selectivity of the products during the reduction process.[48]

2. Current density

The overall current density in CO_2 reduction is typically calculated by dividing the current by the geometric surface area of the working electrode. As a measure of the reaction rate, this parameter is crucial for practical applications since it determines the electrolyzer size and the cost needed for the process. Moreover, the partial current density for a specific product can be acquired by multiplying the corresponding FE by the overall current density.

3. Energy efficiency

Energy efficiency (EE) defines the overall energy utilization toward the desired product. EE can be calculated as follows:

$$EE = \frac{E_{eq,cell}}{E_{eq,cell} + \eta_{cathode}} \times FE$$

where $E_{eq,cell}$ is the equilibrium potential between anode and cathode reactions, $E_{eq,cell} = 1.23 + (-E_{eq})$, 1.23V and E_{eq} are the equilibrium potentials for anode oxygen evolution reaction and cathode ECR-to-formate, respectively. $\eta_{cathode}$ is the cathode overpotential.

4. Tafel slope

The Tafel slope is a plot of overpotential versus the logarithm of the partial current density. The calculated number is an indicator of the reaction path and the rate-determining step. For example, a Tafel slope of approximately 59 mV dec^{-1} indicates a reduction mechanism encompassing a fast pre-equilibrium involving $1e^-$ transfer to form CO_2^- and a subsequent slower chemical reaction as the rate-determining step.[49] The slope of approximately 118 mV dec^{-1} is consistent with a rate-

determining initial electron transfer to CO_2 to form a surface adsorbed CO_2^- intermediate, which is commonly invoked for metal electrodes.[50]

5. Stability

The stability of ECR electrocatalysts measures their capability of retaining the activity and selectivity under prolonged galvanostatic or potentiostatic polarization. Many electrode materials are subjected to the gradual loss and poisoning of active sites or irreversible structural failure under the harsh ECR condition. At present, the stability studies of most ECR electrocatalysts in laboratory are carried out for only tens of hours at the most. Successful commercialization of this technology, however, would demand a catalyst lifetime of thousands of hours. This huge gap needs to be bridged in the near future. An electrocatalyst with satisfactory stability can reduce the maintenance and replacement costs as well as downtime during operation. On the other hand, studying and understanding the material degradation mechanism may inspire possible further improvements, and eventually lead to new generations of electrocatalysts.

1.4 References

1. Gao, D.; Arán-Ais, R. M.; Jeon, H. S.; Cuenya, B. R. J. N. C., Rational catalyst and electrolyte design for CO_2 electroreduction towards multicarbon products. *Nat. Catal.* 2019, *2* (3), 198-210.

2. Gao, W.; Liang, S.; Wang, R.; Jiang, Q.; Zhang, Y.; Zheng, Q.; Xie, B.; Toe, C. Y.; Zhu, X.; Wang, J.; Huang, L.; Gao, Y.; Wang, Z.; Jo, C.; Wang, Q.; Wang, L.; Liu, Y.; Louis, B.; Scott, J.; Roger, A. C.; Amal, R.; He, H.; Park, S. E., Industrial carbon dioxide capture and utilization: state of the art and future challenges. *Chem. Soc. Rev.* 2020, *49* (23), 8584-8686.

3. National Ocean and Atmospheric Administration (NOAA), Climate Change: Atmospheric Carbon Dioxide. https://www.climate.gov/news-features/understanding-climate/climate-change-atmospheric-carbon-dioxide.

4. Tzimas, E.; Peteves, S., *Controlling Carbon Emissions: The Option of Carbon Seqestration*. Office for Official Publications of the European Communities Luxembourg: 2003.

5. Davis, S. J.; Caldeira, K.; Matthews, H. D., Future CO_2 emissions and climate change from existing energy infrastructure. *Science* 2010, *329* (5997), 1330-1333.

6. Li, H.; Zhao, J.; Luo, L.; Du, J.; Zeng, J., Symmetry-Breaking Sites for Activating Linear Carbon Dioxide Molecules. *Acc. Chem. Res.* 2021, *54* (6), 1454-1464.

7. Chang, X.; Wang, T.; Gong, J., CO_2 photo-reduction: insights into CO_2 activation and reaction on surfaces of photocatalysts. *Energy Environ. Sci.* 2016, *9* (7), 2177-2196.

8. Chen, C.; Kotyk, J. F. K.; Sheehan, S. W., Progress toward commercial application of electrochemical carbon dioxide reduction. *Chem* 2018, *4* (11), 2571-2586.

9. Wang, Y.; Han, P.; Lv, X.; Zhang, L.; Zheng, G., Defect and interface engineering for aqueous electrocatalytic CO_2 reduction. *Joule* 2018, *2* (12), 2551-2582.

10. Liu, Q.; Wu, L.; Jackstell, R.; Beller, M., Using carbon dioxide as a building block in organic synthesis. *Nat. Commun.* 2015, *6* (1), 1-15.

11. Shi, J.; Jiang, Y.; Jiang, Z.; Wang, X.; Wang, X.; Zhang, S.; Han, P.; Yang, C., Enzymatic conversion of carbon dioxide. *Chem. Soc. Rev.* 2015, *44* (17), 5981-6000.

12. Han, N.; Ding, P.; He, L.; Li, Y.; Li, Y. J. A. E. M., Promises of main group metal–based nanostructured materials for electrochemical CO_2 reduction to formate. *Adv. Energy Mater.* 2020, *10* (11), 1902338.

13. Sun, Z.; Ma, T.; Tao, H.; Fan, Q.; Han, B., Fundamentals and challenges of electrochemical CO_2 reduction using two-dimensional materials. *Chem* 2017, *3* (4), 560-587.

14. Zhang, L.; Zhao, Z. J.; Gong, J., Nanostructured materials for heterogeneous electrocatalytic CO_2 reduction and their related reaction mechanisms. *Angew. Chem., Int. Ed.* 2017, *56* (38), 11326-11353.

15. Zhu, D. D.; Liu, J. L.; Qiao, S. Z., Recent advances in inorganic heterogeneous electrocatalysts for reduction of carbon dioxide. *Adv. Mater.* 2016, *28* (18), 3423-3452.

16. Peterson, A. A.; Abild-Pedersen, F.; Studt, F.; Rossmeisl, J.; Nørskov, J. K., How copper catalyzes the electroreduction of carbon dioxide into hydrocarbon fuels. *Energy Environ. Sci.* 2010, *3* (9), 1311-1315.

17. Feaster, J. T.; Shi, C.; Cave, E. R.; Hatsukade, T.; Abram, D. N.; Kuhl, K. P.; Hahn, C.; Nørskov, J. K.; Jaramillo, T. F., Understanding selectivity for the electrochemical reduction of

carbon dioxide to formic acid and carbon monoxide on metal electrodes. *ACS Catal.* 2017, *7* (7), 4822-4827.

18. Kortlever, R.; Shen, J.; Schouten, K. J. P.; Calle-Vallejo, F.; Koper, M. T., Catalysts and reaction pathways for the electrochemical reduction of carbon dioxide. *J. Phys. Chem. Lett.* 2015, *6* (20), 4073-4082.

19. Kuhl, K. P.; Cave, E. R.; Abram, D. N.; Jaramillo, T. F., New insights into the electrochemical reduction of carbon dioxide on metallic copper surfaces. *Energy Environ. Sci.* 2012, *5* (5), 7050-7059.

20. Gattrell, M.; Gupta, N.; Co, A., A review of the aqueous electrochemical reduction of CO_2 to hydrocarbons at copper. *J. Electroanal. Chem.* 2006, *594* (1), 1-19.

21. Yoo, J. S.; Christensen, R.; Vegge, T.; Nørskov, J. K.; Studt, F., Theoretical insight into the trends that guide the electrochemical reduction of carbon dioxide to formic acid. *ChemSusChem* 2016, *9* (4), 358-363.

22. Hori, Y.; Wakebe, H.; Tsukamoto, T.; Koga, O., Electrocatalytic process of CO selectivity in electrochemical reduction of CO_2 at metal electrodes in aqueous media. *Electrochim. Acta* 1994, *39* (11-12), 1833-1839.

23. Montoya, J. H.; Shi, C.; Chan, K.; Nørskov, J. K., Theoretical insights into a CO dimerization mechanism in CO_2 electroreduction. *J. Phys. Chem. Lett.* 2015, *6* (11), 2032-2037.

24. Li, J.; Chen, G.; Zhu, Y.; Liang, Z.; Pei, A.; Wu, C.-L.; Wang, H.; Lee, H. R.; Liu, K.; Chu, S., Efficient electrocatalytic CO_2 reduction on a three-phase interface. *Nat. Catal.* 2018, *1* (8), 592-600.

25. Ren, W.; Zhao, C., Paths towards enhanced electrochemical CO_2 reduction. *Natl. Sci. Rev.* 2020, *7* (1), 7-9.

26. Asadi, M.; Kim, K.; Liu, C.; Addepalli, A. V.; Abbasi, P.; Yasaei, P.; Phillips, P.; Behranginia, A.; ECRrato, J. M.; Haasch, R., Nanostructured transition metal dichalcogenide electrocatalysts for CO_2 reduction in ionic liquid. *Science* 2016, *353* (6298), 467-470.

27. Zhao, C.; Wang, J., Electrochemical reduction of CO_2 to formate in aqueous solution using electro-deposited Sn catalysts. *Chem. Eng. J.* 2016, *293*, 161-170.

28. Higgins, D.; Hahn, C.; Xiang, C.; Jaramillo, T. F.; Weber, A. Z., Gas-diffusion electrodes for carbon dioxide reduction: a new paradigm. *ACS Energy Lett.* 2018, *4* (1), 317-324.

29. Dinh, C.-T.; Burdyny, T.; Kibria, M. G.; Seifitokaldani, A.; Gabardo, C. M.; García de Arquer, F. P.; Kiani, A.; Edwards, J. P.; De Luna, P.; Bushuyev, O. S., CO_2 electroreduction to ethylene *via* hydroxide-mediated copper catalysis at an abrupt interface. *Science* 2018, *360* (6390), 783-787.

30. Gong, Q.; Ding, P.; Xu, M.; Zhu, X.; Wang, M.; Deng, J.; Ma, Q.; Han, N.; Zhu, Y.; Lu, J., Structural defects on converted bismuth oxide nanotubes enable highly active electrocatalysis of carbon dioxide reduction. *Nat. Commun.* 2019, *10* (1), 1-10.

31. García de Arquer, F. P.; Dinh, C.-T.; Ozden, A.; Wicks, J.; McCallum, C.; Kirmani, A. R.; Nam, D.-H.; Gabardo, C.; Seifitokaldani, A.; Wang, X., CO_2 electrolysis to multicarbon products at activities greater than 1 A cm^{-2}. *Science* 2020, *367* (6478), 661-666.

32. Endrodi, B.; Kecsenovity, E.; Samu, A.; Darvas, F.; Jones, R.; Török, V.; Danyi, A.; Janáky, C., Multilayer electrolyzer stack converts carbon dioxide to gas products at high pressure with high efficiency. *ACS Energy Lett.* 2019, *4* (7), 1770-1777.

33. Verma, S.; Hamasaki, Y.; Kim, C.; Huang, W.; Lu, S.; Jhong, H.-R. M.; Gewirth, A. A.; Fujigaya, T.; Nakashima, N.; Kenis, P. J., Insights into the low overpotential electroreduction of CO_2 to CO on a supported gold catalyst in an alkaline flow electrolyzer. *ACS Energy Lett.* 2017, *3* (1), 193-198.

34. Kutana, A.; Giapis, K., Atomistic simulations of electrowetting in carbon nanotubes. *Nano Lett.* 2006, *6* (4), 656-661.

35. Larrazábal, G. O.; Strøm-Hansen, P.; Heli, J. P.; Zeiter, K.; Therkildsen, K. T.; Chorkendorff, I.; Seger, B., Analysis of mass flows and membrane cross-over in CO_2 reduction at high current densities in an MEA-type electrolyzer. *ACS Appl. Mater. Interfaces* 2019, *11* (44), 41281-41288.

36. Yang, K.; Kas, R.; Smith, W. A., *In situ* infrared spectroscopy reveals persistent alkalinity near electrode surfaces during CO_2 electroreduction. *J. Am. Chem. Soc.* 2019, *141* (40), 15891-15900.

37. Liu, K.; Smith, W. A.; Burdyny, T., Introductory guide to assembling and operating gas diffusion electrodes for electrochemical CO_2 reduction. *ACS Energy Lett.* 2019, *4* (3), 639-643.

38. Ge, L.; Rabiee, H.; Li, M.; Subramanian, S.; Zheng, Y.; Lee, J. H.; Burdyny, T.; Wang, H., Electrochemical CO_2 reduction in membrane-electrode assemblies. *Chem* 2022, *8* (3), 663-692.

39. Kim, D.; Choi, W.; Lee, H. W.; Lee, S. Y.; Choi, Y.; Lee, D. K.; Kim, W.; Na, J.; Lee, U.; Hwang, Y. J., Electrocatalytic Reduction of Low Concentrations of CO_2 Gas in a Membrane Electrode Assembly Electrolyzer. *ACS Energy Lett.* 2021, *6* (10), 3488-3495.

40. Li, F.; Thevenon, A.; Rosas-Hernández, A.; Wang, Z.; Li, Y.; Gabardo, C. M.; Ozden, A.; Dinh, C. T.; Li, J.; Wang, Y., Molecular tuning of CO_2-to-ethylene conversion. *Nature* 2020, *577* (7791), 509-513.

41. Zheng, T.; Jiang, K.; Ta, N.; Hu, Y.; Zeng, J.; Liu, J.; Wang, H., Large-scale and highly selective CO_2 electrocatalytic reduction on nickel single-atom catalyst. *Joule* 2019, *3* (1), 265-278.

42. Kibria, M. G.; Edwards, J. P.; Gabardo, C. M.; Dinh, C. T.; Seifitokaldani, A.; Sinton, D.; Sargent, E. H., Electrochemical CO_2 reduction into chemical feedstocks: from mechanistic electrocatalysis models to system design. *Adv. Mater.* 2019, *31* (31), 1807166.

43. Jouny, M.; Luc, W.; Jiao, F., General techno-economic analysis of CO_2 electrolysis systems. *Ind. Eng. Chem. Res.* 2018, *57* (6), 2165-2177.

44. Bushuyev, O. S.; De Luna, P.; Dinh, C. T.; Tao, L.; Saur, G.; van de Lagemaat, J.; Kelley, S. O.; Sargent, E. H., What should we make with CO_2 and how can we make it? *Joule* 2018, *2* (5), 825-832.

45. Garza, A. J.; Bell, A. T.; Head-Gordon, M., Mechanism of CO_2 reduction at copper surfaces: pathways to C_2 products. *ACS Catal.* 2018, *8* (2), 1490-1499.

46. Reller, C.; Krause, R.; Volkova, E.; Schmid, B.; Neubauer, S.; Rucki, A.; Schuster, M.; Schmid, G., Selective electroreduction of CO_2 toward ethylene on nano dendritic copper catalysts at high current density. *Adv. Energy Mater.* 2017, *7* (12), 1602114.

47. Delacourt, C.; Ridgway, P. L.; Kerr, J. B.; Newman, J., Design of an electrochemical cell making syngas (CO+ H_2) from CO_2 and H_2O reduction at room temperature. *J. Electrochem. Soc.* 2007, *155* (1), B42.

48. Liu, S.; Tao, H.; Zeng, L.; Liu, Q.; Xu, Z.; Liu, Q.; Luo, J.-L., Shape-dependent electrocatalytic reduction of CO_2 to CO on triangular silver nanoplates. *J. Am. Chem. Soc.* 2017, *139* (6), 2160-2163.

49. Gileadi, E., *Electrode kinetics for chemists, chemical engineers, and materials scientists*. Capstone: 1993.

50. Lee, C. W.; Cho, N. H.; Im, S. W.; Jee, M. S.; Hwang, Y. J.; Min, B. K.; Nam, K. T., New challenges of electrokinetic studies in investigating the reaction mechanism of electrochemical CO_2 reduction. *J. Mater. Chem. A* 2018, *6* (29), 14043-14057.

Chapter 2. Literature review of catalysts for ECR towards formate

To date, various catalysts have been studied for ECR to formate. In this section, I will review the current development status of different main group metal-based catalysts in detail. I will mainly focus on Bi, Sn, and In-based materials due to their wide popularity in the literature.

2.1 Main design principles of Bi-based catalysts

Morphology control

The morphological architecture of catalysts has been identified to be an important factor in determining the catalytic performance. Different morphologies will lead to different physical/chemical properties including conductivity, surface area, adsorption/desorption of species, and exposure of different active sites. Therefore, tuning the morphology of Bi-based catalysts has been regarded as an effective strategy to improve the ECR to formate.

Bi possesses a layered structure by folding a six-membered ring of Bi atoms in a manner similar to that of black phosphorus.[1] It is then possible to make two-dimensional (2D) Bi nanosheets from bulk Bi by overcoming the weak interlayer van der Waals forces.[2] 2D materials, compared with bulk materials, are able to expose more active sites due to large surface area and large amount of undercoordinated atoms.[3-4] In addition, 2D structure could facilitate the mass transfer of reactants and electrolytes. Thus, 2D Bi-based materials have been widely reported as electrocatalysts for ECR towards formate production. Li et al. prepared 2D Bi nanosheets (NS) *via in situ* topological transformation of BiOI nanosheets (thickness: 8.7 nm).[5] FE of formate could be kept over 95% in a broad potential range (from −1.5 V to −1.7 V *vs*. RHE) on Bi NS. Density functional theory (DFT) calculation indicated that the high selectivity of Bi NS was attributed to the favorable adsorption of *OCHO on Bi (001) facet over *COOH and *H, thus inhibiting the CO and H_2

formation. Likewise, Yang et al. synthesized single layer Bi NS (bismuthene) with a thickness of 0.65 nm. The bismuthene exhibited a superior selectivity (99%) toward formate at low potential of −0.6 V.[2] By contrast, the thicker Bi NS (4.2 and 11.3 nm) required more negative (−0.8 V and −0.9 V) potential to reach an equivalent FE, indicating a higher energy barrier (Figure 2.1b). Theoretical calculations suggested that thicker Bi NS was preferable to expose (011) facet while bismuthene monolayer exposed (111) facet. The reaction intermediates were bound on (011) facet so strong that the active site was poisoned by those species (Figure 2.1c, d). This explains their lower activity and stability compared with bismuthene.

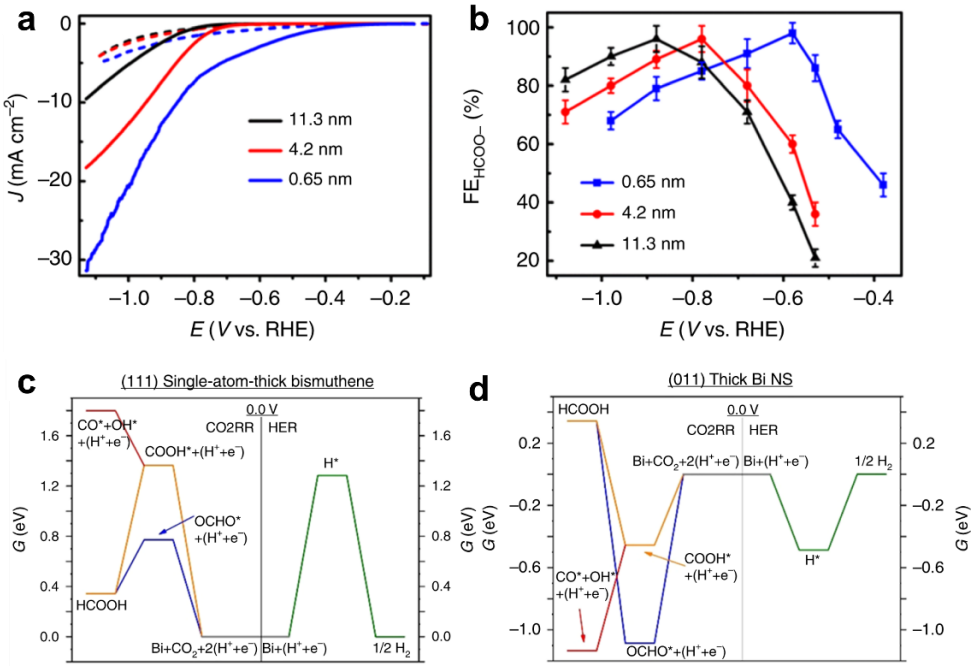

Figure 2.1 (a) Linear sweep voltammetry curves (LSV) in the CO_2 saturated and N_2 saturated 0.5 M $KHCO_3$ for Bi NSs with different thicknesses. (b) Comparison of FE for formate for Bi NSs with different thicknesses. Calculated free energy diagrams for ECR and HER on (111) single-atom-thick Bismuthene (c) and (011) thick Bi nanosheets (d).[2] Reprinted with permission from Reference 2. Copyright 2020, Springer Nature Group.

Recently, metal-organic framework (MOF)-based material has received great attention in catalysis and energy storage due to its high porosity, low density, large specific surface area and controllable pore size.[6-9] Bi-based MOF material has also been used as precursor to prepare Bi NS. The derived Bi NS inherits the excellent properties of MOF precursor. Xu et al. successfully prepared the ultrathin bismuthene (1.28 nm) with graphene like structure through *in situ* electrochemical reduction of ultrathin Bi MOF.[10] The unique structure of the bismuthene not only provided extremely large electrochemical activity area, but also greatly enhanced the intrinsic activity of metal atoms. When directly used as electrocatalyst for ECR, it showed excellent electrocatalytic performance: current density of 70 mA cm^{-2} with FE of formate near 100% was achieved. Similarly, Wu et al. prepared leafy Bi NS with Bi/BiO hybrid structure derived from claviform Bi-MOF (CAU-17).[11] It is found that the energy barrier for $*CO_2$ to *OCHO on Bi-O surface was largely decreased as compared to Bi surface, which accounts for the improved activity. In addition, 2D $Bi_2O_2CO_3$ has also been proved as a good candidate for ECR to formate. Zhang et al. obtained $Bi_2O_2CO_3$ nanosheets with 4 nm thickness using *in situ* oxidation-exfoliation in Na_2CO_3 aqueous solution.[12] It could deliver a FE of 85 % for formate at −0.7 V *vs*. RHE. Unlike the above works where *in situ* formed metallic Bi was the active site, the authors found that if $Bi_2O_2CO_3$ was pre-reduced to metallic Bi and then used to catalyze ECR, the FE of formate decreased to only 60%. The activity could recover to original state when the electrode was immersed into 0.5 M $NaHCO_3$ for long enough time to allow the restoration of $Bi_2O_2CO_3$, confirming the critical role of $Bi_2O_2CO_3$ for ECR.

Defect engineering

The incorporation of defects into Bi-based catalysts could tailor its local electronic states and create unsaturated sites with specific activities which facilitate an optimal adsorption/desorption of

intermediates. Li group fabricated defects-rich Bi_2O_3 nanotube (NT) by controlling the hydrolysis of bismuth acetate in ethylene glycol using poly(vinyl pyrrolidone) (PVP) as a surfactant.[13] The Bi_2O_3 NT was *in situ* transformed to defective metallic Bi NT. Benefiting from the abundant defects, the energy barrier of *OCHO formation greatly decreased, which enables the ECR to formate with near 100% FE and stable working for 50 hours. More importantly, the Bi NT achieved a commercial level current density of 288 mA cm^{-2} at −0.61 V in flow cell system, showing great potential for practical implementation.

Zhu group designed a self-supported three-dimensional (3D) porous conductive network of bismuthene using a versatile electrochemical template strategy.[14] The as-prepared bismuthene possessed abundant defects in the roughened plane edges and in-plane pore edges, which were interconnected and thus facilitate the high exposure of active sites. The unique bismuthene catalysts were able to show a remarkably boosted ECR to formate performance with ~ 100% selectivity in a broad potential window and exceptional current density up to 500 mA cm^{-2}. DFT simulations and operando attenuated total reflection-infrared (ATR-IR) spectroscopy uncovered that the abundant edge-site defects of the bismuthene could stabilize *OCHO intermediate and account for the enhanced performance.

Hetero-atom doping is another effective strategy to improve Bi-based catalysts by regulating the electronic structure. The modulated electronic structure could adjust the adsorption of intermediates and smooth reaction pathways. Previous theoretical studies reveal that incorporating p-block atoms could break the linear scaling relations for the Gibbs free energy of *COOH and *OCHO.[15-16] Liu et al. prepared boron doped Bi catalyst and studied for ECR.[17] They found that incorporation of boron pushed the p-band center of Bi upward and thus increased the electron density around Bi. The tuned electronic state adjusted the free energy of *OCHO intermediates

while hindering the formation of *COOH and *H intermediates. This consequently leads to favorable production of formate over CO and H_2. Except for non-metal element doping, metal element also has been incorporated into Bi catalyst. For instance, Tan et al. reported Sn doped BiO_x nanowire (NW) through an electrochemical dealloying method.[18] The doping of Sn allows the CO_2 molecules to experience fast adsorption and proton-coupled electron transfer toward *OCHO, thus accelerating the production of formate.

Alloying

The alloying strategy is another important route to enhancing the activity, selectivity, and stability of Bi-based catalysts for ECR. The synergistic effect between two different metals can regulate the surface electronic states and binding energies of intermediates, thus adjusting the selectivity of products from ECR. Chen group designed Bi-Sn bimetallic catalyst deposited on carbon fabric substrate for ECR.[19] A much higher FE of formate and a very high formate production rate (0.74mmol h^{-1} cm^{-2}) were observed as compared to pure Sn catalyst. The superior performance can be attributed to the orbital modulation of Sn by interfacing with Bi nanoparticles. Recently, the group of Zhong investigated ECR on alloyed $Bi_{0.1}Sn$ catalyst.[20] They found that an active and stable Sn-Bi/SnO_2 surface would be *in situ* formed on $Bi_{0.1}Sn$ during ECR, and these catalysts exhibited unprecedented long stability (100 days) accompanied by high FE of formate (95%) at an overpotential of −0.65 V. Their DFT calculations revealed that the binding of *OCHO on pure Bi surface was too weak while that on pure Sn surface was too strong, and that on BiSn surface was near-optimal, resulting in a low reaction energy for formate formation.

Coupling with substrates

Integrating Bi-based catalysts with carbon substrates or directly growing Bi-based catalysts on conductive substrate (carbon cloth, carbon fiber paper, copper foam) is an attractive strategy to

promote electrocatalytic CO_2 reduction by modifying the electronic structure of Bi and improving interfacial electron transfer. In addition, 3D framework substrate (such as copper foam) with open structure can accelerate electron transfer and mass transportation. Liu group reported the synthesis of 2D/0D composite catalyst consisted of bismuth oxide NS and nitrogen-doped graphene quantum dots (Bi_2O_3-NGQDs) for ECR to formate.[21] The Bi_2O_3-NGQDs showed a nearly 100% FE of formate at −0.9 V *vs*. RHE, and maintained FE > 90% in a wide potential range from −0.9 V to −1.2 V *vs*. RHE. In addition, electrochemical impedance spectroscopy (EIS) showed that the charge transfer resistance (R_{ct}) of Bi_2O_3 decreased after integrating with NGQDs, suggesting an improved electron transfer at the catalyst/electrolyte interface. Furthermore, the amino groups of NGQDs enhanced the CO_2 adsorption capacity, which benefits the activation of CO_2. Same enhancement effect was also observed on a SnS/Aminated-C catalyst.[22]

Besides the intrinsic reactivity of the catalyst, the availability of electroactive sites and electron transfer ability are also crucial to the performance of ECR to formate. Lou group reported Bi_2O_3 NS growing on a conductive multiple channel carbon matrix (Bi_2O_3 NS@MCCM) for ECR and found that the obtained electrocatalyst showed a partial current density of 17.7 mA cm^{-2} at moderate overpotential and FE was maintained at around 90% in a wide potential range (Figure 2.2).[23] The improved activity was attributed to the synergistic effects of Bi_2O_3 NS and MCCM, where the interwoven MCCM facilitated electron transfer, CO_2 adsorption as well as fast transfer of electrolyte to the active sites, while Bi_2O_3 NS offered abundant active sites and lowered contact resistance. In addition, high ratio of pyrrolic-N and pyridinic-N in MCCM was able to stabilize $CO_2{\cdot}^-$ intermediate, thus lowering the thermodynamic energy barrier for ECR to formate. In addition, Jin group designed pipet-like bismuth nanorods semi-filled in nitrogen-doped carbon nanotubes (Bi-NRs@NCNTs) and found it exhibited a high selectivity (90.9%) and stability for

ECR to formate at −0.9 V *vs*. RHE.[24] The nano-capillary and nanoconfinement effects of the unique structure synergistically facilitated the mass transfer, adsorption, and concentration of reactant CO_2 molecules onto the active sites, which promotes the ECR to formate. Coupling Bi-based catalysts with other carbon materials, including reduced graphene oxide (rGO),[25] black phosphorus (BP),[26] carbon cloth,[27] carbon paper,[28-29] carbon black,[30] and 3D carbon foam,[31] has also been reported and shown the improved electrocatalytic performance for ECR.

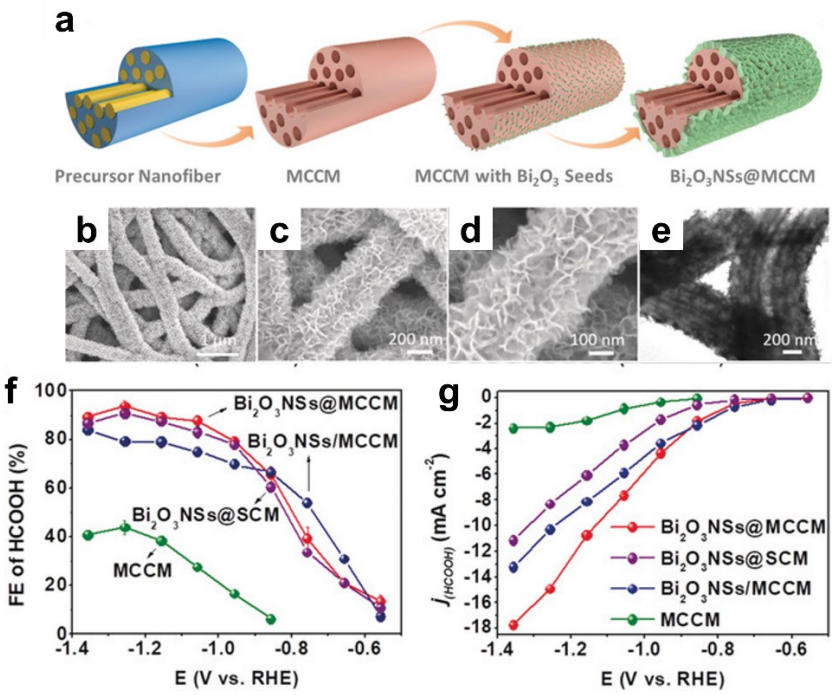

Figure 2.2 (a) Illustration of the formation of the Bi_2O_3 NS@MCCM. (b-e) SEM and TEM images of Bi_2O_3 NS@MCCM. (f) FE of formate and (g) formate partial current density for Bi_2O_3 NS@MCCM and other control catalysts.[23] Reprinted with permission from Reference 23. Copyright 2019, Wiley.

Metal foam has been widely used as substrate to support electrocatalyst due to its large number of connected holes evenly distributed in the metal matrix, as well as excellent conductivity and ductility. Zhang group developed a lattice-dislocated Bi nanowires on copper foam (Cu foam@Bi NW) through ligand-assisted electrochemical replacement method.[32] The Cu foam@ BiNW was

found to be highly selective (FE of 95%) toward formate production and reached a peak partial current density of ~ 48 mA cm^{-2}. The high ECR activity is attributed to the high intrinsic activity arising from the presence of crystal lattice dislocations on the Bi NW and the large catalytic surface area associated with the porous structure. Likewise, the group of Li reported the growth of large-area vertically aligned bismuthene NS arrays on copper foam *via* galvanic replacement process and it was able to catalyze the formate production with high selectivity > 90% and high partial current density of 45 mA cm^{-2} at −0.9 V.[33]

Constructing favorable triple-phase boundary

Besides the aforementioned strategies to adjust catalysts inherent reactivity, recent findings demonstrated that the ECR is also very sensitive to the local CO_2 concentration and mass transportation of gas-involved species.[34-38] It is well known that the gaseous CO_2/solid electrode/liquid electrolyte triple-phase boundary is the cornerstone of ECR, where CO_2 encounters electrons and protons and is reduced.[39] Therefore, the properties of electrochemical interfaces play an important role in the ECR behaviors. Rational design of electrode to get an optimal contact with CO_2 and H_2O could provide opportunities to achieve high accessibility of concentrated CO_2 molecules to the surface of catalyst while hindering HER. Recently, Qiu et al. have reported Bi nanospheres loading on superhydrophobic porous carbon nanosheets (Bi-C) for ECR to formate.[40] A much higher FE of formate and current density were observed on Bi loaded on hydrophobic carbon supports as compared that on hydrophilic carbon supports. The hydrophobic carbon constructed a three-phase interface of CO_2 (gas), electrolyte (liquid) and catalyst (solid), facilitating the accessibility of high concentrated CO_2 to the Bi surface. DFT simulations indicated that the rate-determining step ($CO_2 + * + e^- \rightarrow *CO_2^{\cdot -}$) could proceed thermodynamically favorably due to the three-phase catalytic interfaces. A similar enhanced

phenomenon was also observed by the Yang group. They designed hydrophobic carbon coated on copper oxide catalyst (H-CuO_x@C) for ECR to CH_4 generation.[41] The H-CuO_x@C delivered a high partial current density of CH_4 (–39 mA cm^{-2}) with a peak CH_4 FE of 81%, while the wettable CuO_x controls produced CH_4 with only FE of 31%. The hydrophobic carbon shell pushed away aqueous electrolyte and led to a low local H_2O concentration at the catalyst surface, thus promoting *CO protonation to form CH_4. Except for this hydrophobic carbon engineering to tune the wettability of catalyst surface, modifying catalyst with hydrophobic organics, including 1-octadecanethiol,[42] dodecanethiol,[43] poly(vinylidene fluoride) (PVDF),[44] Nafion,[45] amino acid,[46] and poly(acrylamide)[47] is another effective way to construct a favorable hydrophobic surface for ECR (these organic modification strategies are so far mainly focused on Cu-based catalysts for C_{2+} products).

Although the surface hydrophobic strategy can improve the ECR by increasing the local CO_2 concentration, an optimal balance between gas and liquid in the catalyst layer is required for efficient ECR.[48] An excessive hydrophobic will suppress the availability of electrolyte and protons for ECR. Feng group reported that the addition of hydrophobic polytetrafluoroethylene (PTFE) nanoparticles could substantially enhance the ECR to formate over Bi-based catalyst.[49] The electrochemical tests showed that the Bi catalyst with the addition of 30% PTFE could achieve a ECR current density of 686 mA cm^{-2} and formate FE of 91%, which were about 1.72 and 1.82-fold higher than that of Bi catalyst without adding PTFE (Figure 2.3). However, the excessive loading of PTFE would lower the selectivity and activity due to the over-suppressed availability of electrolyte. This is because HER is more robust in competing for protons than the ECR at low electrolyte availability. This work revealed that a moderate hydrophobicity of the catalyst layer is

important since it can establish a microenvironment with an optimal balanced gaseous CO_2-liquid electrolyte availability.

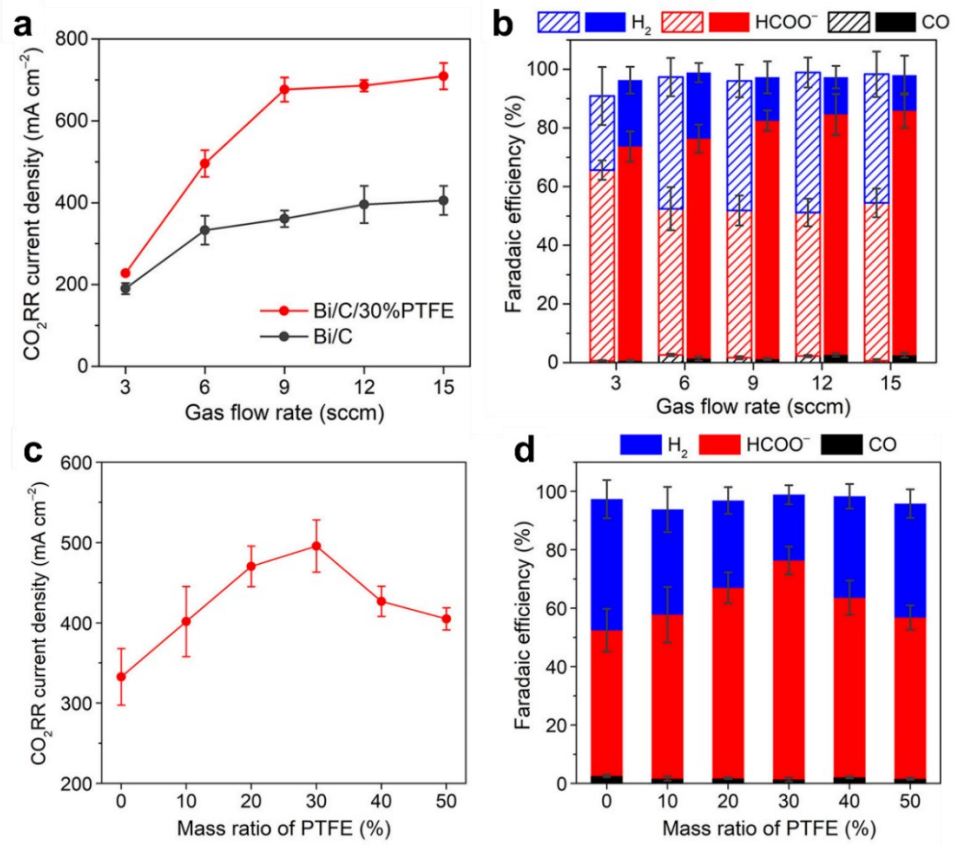

Figure 2.3 Partial current densities for ECR on two electrodes (one with 30% PTFE loading and another without PTFE addition). (b) FEs for two electrodes under various CO_2 gas flow rates. (c) Partial current densities and (d) FEs of Bi catalyst with various PTFE loading.[49] Reprinted with permission from Reference 49. Copyright 2021, American Chemical Society.

2.2 Sn-based catalysts

Sn is one of the most widely investigated materials for ECR to formate. Hori is the pioneer in investigating bulk Sn electrode as ECR catalyst but with relatively high overpotential and low current density.[50] Sn, like other main group metals, is prone to be oxidized in air and covered by oxide layers on its surface. These surface oxide layers would be reduced to metallic Sn (Sn^0) before

ECR can take place according to the standard redox potential. Nevertheless, a recent study suggests that the oxidation state of Sn ($Sn^{\delta+}$) can stably exist during ECR and play a critical role in catalytic performance. Bocarsly et al. used *in situ* attenuated total reflectance infrared spectroscopy (ATR-IR) to investigate the Sn electrode in ECR process and found that a layer of Sn oxyhydroxide (Sn^{2+}) will be *in situ* formed on $Sn_6O_4(OH)_4$ and SnO_2 nanoparticles surface during ECR.[51] These Sn^{2+} were believed to be the real catalytic species for ECR to formate and it would not further be reduced to Sn^0 because this redox event was suppressed by the excellent activity of Sn^{2+} during ECR process. The Gong group reported amorphous $SnO_x(OH)_y$ (Sn^{2+}) for ECR to formate.[52] The surface hydroxyls were beneficial to CO_2 adsorption in the form of H_2CO_3 *via* hydrogen bonds and facilitated the formate production. This study further confirms the important role of Sn^{2+} in the observed catalytic formation of formate. Guan et al. experimentally and theoretically investigated the different roles of Sn^{2+} and Sn^{4+} in ECR.[53] The Sn^{2+} can improve the formate selectivity by enlarging the energy barrier difference between HER and ECR, while the Sn^{4+} can lower the formation energy of *OCHO intermediate and reduce the overpotential. Therefore, Sn-based catalysts composed of mixed valence states (Sn^{2+} and Sn^{4+}) might be the optimal choice for formate yield. This was further confirmed by later works where Sn catalyst with mixed valence states showed superior activity to single valence catalyst.[54-55]

It is generally recognized that the bottleneck of ECR is the competing adsorption of various intermediates (*$CO_2^{\cdot-}$, *COOH, *OCHO, *H and so on) and the desorption barrier of the products. This requires that the catalyst not only possesses rapid transfer of charge carriers (electron and proton), but also has enough active sites.[57] Therefore, developing catalysts with abundant active sites is the key to realizing high performance. Constructing nanoporous structure is an easy and effective strategy to improve Sn-based catalysts activity by increasing the number of catalytic sites.

Liu group synthesized mesoporous SnO_2 nanosheet ($mSnO_2$ NS) by a soft-template co-assembly approach.[58] Benefiting from the large surface area (96.8 m^2 g^{-1}) and fast mass transfer ability, the $mSnO_2$ NS showed a boosted activity for formate formation. The group of Zhang reported a 3D hierarchical electrode consisting of porous SnO_2 NS on flexible carbon cloth through calcination of SnS_2 NS precursor (Figure 2.4).[56] The resultant catalyst exhibited a high partial current density of ~ 45 mA cm^{-2} at moderate overpotential. The superior performance was attributed to the highly porous hierarchical structure having a large specific surface area, enlarging the contact surface between electrode and electrolyte, thus facilitating the charge and mass transfer during ECR.

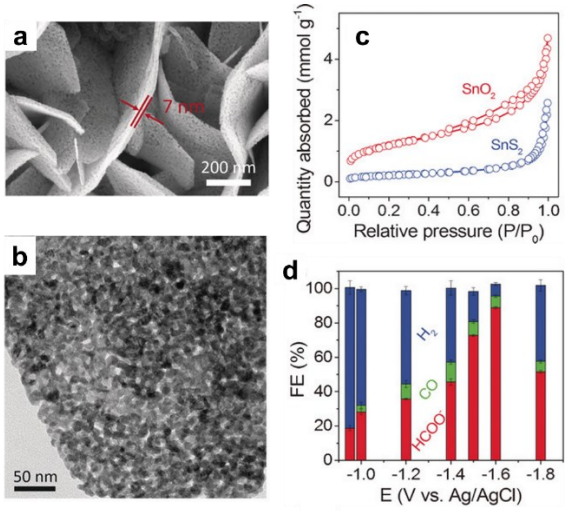

Figure 2.4 (a) SEM and (b) TEM images for porous SnO_2 NSs. (c) Nitrogen adsorption-desorption isotherms for SnS_2 and SnO_2 NSs. (d) FEs for SnO_2 NSs.[56] Reprinted with permission from Reference 56. Copyright 2017, Wiley.

Theoretical study indicates that breaking the local spatial symmetry near grain boundaries (GBs) can tune the binding strength of key intermediate and facilitate ECR.[59] Spurfeon et al. prepared SnO_2 porous nanowire (Sn-pNW) with a high density of GBs by solvo-plasma technique and found that the GBs-rich Sn-pNW exhibited a significantly improved formate production as compared GBs-free Sn nanowires.[60] The introduction of GBs not just increased the density of active sites,

but more importantly, reformed the absorbate-to-metal σ-bonding and metal-to-adsorbate π-backbonding strengths. In a parallel study, Lou and co-workers prepared ultrathin sun-2 nm SnO_2 quantum wires (QWs) composed of individual quantum dots (QDs) with GBs exposed on the surface.[61] These authors suggested that the high density of GBs increased the intrinsic activity by bringing more active sites and enhanced the absorption of CO_2. Electrochemical measurements showed that SnO_2 QWs delivered a much higher current density and FE of formate than SnO_2 nanoparticles.

Integrating Sn-based catalysts with conductive and high-surface-area carbon supports is an effective strategy to further improve their electrocatalytic performance. The carbon supports can accelerate the electron transfer to and from the catalyst, can also improve the catalyst dispersion and mitigate possible particle agglomeration during long-term operation. More importantly, the synergistic effect between catalyst and carbon support could optimize the adsorption of key intermediates and thus, attain an unexpected performance. As a representative of the early works, Meyer et al. deposited ~ 5nm SnO_2 nanoparticles on different carbon supports (graphene and carbon black) and found that the graphene supports delivered a higher FE for formate (93.6%) and the nearly twice high current density as for carbon black supports.[62] The difference in catalytic activity might be attributed to the stronger electron donating ability of graphene compared to carbon black, this ability promoted the adsorption of CO_2 and $CO_2^{\cdot -}$. In a very recent study, Ito and co-workers developed the reduced graphene oxide (rGO) supported Sn NPs to investigate the role of rGO supports in ECR.[63] Compared to the Sn NPs supported on graphite, Sn NPs supported on rGO presented an enhanced formate FE of 98% and higher current density of 9.9 mA cm^{-2}. DFT calculations revealed that oxidized functional groups on rGO significantly enhanced the CO_2 adsorption, which then transferred to the adjacent Sn surface and facilitated rate determining

*OCHO formation. To further investigate the strong metal-support interaction (SMSI) in carbon supported Sn-based catalysts and their influences on the electrocatalytic performance, Hu et al. loaded SnO_2 on undoped, N-doped, S-doped, and N, S-codoped nanoporous carbon supports, respectively.[64] Among all the investigated carbon supports, the N, S-codoped one exhibited the best activity due to its strongest interaction with SnO_2.

Single-atom catalysts (SACs) featuring isolated metal atoms dispersed on a conductive support have recently become a research frontier in catalysis and displayed exceptional catalytic performance in various processes.[65-68] Downsizing the metal sizes to atomic scale endows the catalysts with multiple advantages: 1) the full exposure of metal atoms enables metal atom utilization in SACs to reach ~ 100% compared with nanoparticle catalysts where only surface metal atoms can involve in catalytic reaction; 2) the catalytic sites in SACs are identical in terms of morphology and electronic structure, providing a good platform to investigate the reaction mechanism; 3) the strong interaction between metal atoms and the supports offers a potential to manipulate the catalytic activity by adjusting the supports. Xie et al. prepared single-atom Sn on N-doped graphene through a quick freeze-vacuum drying-calcination method and achieved a record of turnover frequency (TOF) up to 11930 h^{-1} for formate formation.[69] The DFT simulations revealed that the dispersed Sn atoms have positive charges, which favored the stabilization of $*CO_2^{\cdot -}$ and *OCHO and thus enabled CO_2 activation and protonation to proceed spontaneously. The coordination environment of the isolated atoms is of vital importance to the final catalytic performance. Zhang and co-workers developed two different single atom Sn catalysts (four N atoms coordinated Sn-N_4 and one F atom axially coordinated Sn-C_2O_2F).[70] Electrochemical measurements suggested that CO was the exclusive product on Sn-C_2O_2F catalyst while formate was predominantly formed on Sn-N_4 catalyst. Based on the DFT calculation results, the C and O

coordination modulated the binding strength of intermediates, while the Sn-bonded F atom significantly suppressed the HER, thereby promoting CO production. At the same time, the ECR to formate *via* O-bond intermediates was prohibited. Besides the SACs, constructing dual-atom catalysts (two different metal atoms are loaded on support) has emerged as another effective route to boosting ECR.[71-72] For example, Wei and co-workers explored NiSn atomic pair catalysts (NiSn-APC) consisting of adjacent Ni and Sn, each coordinating with four N atoms (N_4-Ni-Sn-N_4) for ECR.[73] The authors found that the Sn sites in NiSn-APC served as the intrinsic active site for ECR to formate, while the adjacent Ni regulated the electronic structure of Sn, which reduced the energy barrier of *OCHO formation.

Recent studies showed that the introduction of oxygen vacancies (OVs) would result in the appearance of a new defect level and electrons accumulation around the valence band maximum of catalyst.[74] These localized electrons around the valence band facilitate the CO_2 activation through the exchange and transfer of electrons between the OVs and CO_2. When SnO_2 is used as ECR catalyst, OVs will be formed on its surface or subsurface due to self-reduction at negative potential. The content of OVs will gradually increase with the increase of reduction time. However, this does not mean the more OVs, the better ECR performance. Gong group found that during ECR, SnO_2 electrode would undergo the following transformation: $SnO_2 \rightarrow SnO_x/SnO_2 \rightarrow SnO/SnO_2 \rightarrow Sn/SnO_2$.[75] DFT calculations indicated that SnO/SnO_2 with optimal in-plane oxygen vacancies (O_{v_ip}) could offer the best ECR to formate activity. A further increase of O_{v_ip} would rather weaken the adsorption of *OCHO. The experimental results showed that the selectivity of formate on SnO_2 first increased to a peak value and then started to decrease in the long-term ECR, agreeing well with the DFT calculation. Since an appropriate amount of OVs can simultaneously improve the adsorption of *OCHO intermediates and inhibit hydrogen evolution, the introduction

of moderate amount of OVs should be an effective way to regulate the ECR properties of SnO_2 catalysts. The generation of OVs can be realized by the reduction of catalyst in reducing atmosphere (such as hydrogen and ammonia) or plasma etching. Hu et al. reported OVs dominated porous SnO_2 (V_O-SnO_2) catalyst, and it achieved a maximum FE value of 92.4% at –0.7 V *vs*. RHE, while the OVs-free SnO_2 only delivered a maximum FE of 82.8% at a more negative potential of –1.0 V *vs*. RHE.[76] The OVs confined in V_O-SnO_2 lowered the free energy barrier of *OCHO. Qiu group prepared SnO_x with different amounts of OVs supported on carbon foam (V_O-SnO_x/CF) by plasma etching.[74] The V_O-SnO_x/CF-40 with the highest OVs concentration (56%) showed the highest formate FE (86%) compared with V_O-SnO_x/CF-22 (13%) and V_O-SnO_x/CF-60 (11%). The enhanced ECR performance could be attributed to the higher OVs that increased electrochemical surface area and boosted CO_2 adsorption and activation.

Besides SnO_2, the sulfide counterparts (SnS_x) have also been frequently investigated as the catalysts for ECR to formate. Luo and co-workers developed SnS_2 monolayers *via* a Li-intercalation/exfoliation method and found that monolayer SnS_2 achieved a formate FE of 94% at –0.8 V *vs*. RHE while that of bulk SnS_2 was only 29%.[77] The authors, through DFT calculation, uncovered that the *OCHO tended to form favorably on monolayer SnS_2, which explained its high selectivity. Zhang group prepared SnS_2 NS with different doping amounts of Ni and studied its effect on formate production.[78] The SnS_2 with Ni doping amount of 5wt% showed the highest formate selectivity (80%) and the mechanistic analysis found that the doping of Ni brought a defect level at conduction band edge and lower the work function. Very recently, Liu group developed Cu doped SnS_2 nanoflowers (Cu-SnS_2) and found that it underwent *in situ* dynamic restructuring during ECR to form catalytically highly active S-doped Cu/Sn alloy.[79] The resultant S-doped Cu/Sn alloy exhibited a very high partial current density and formate FE since both S-doping and

Cu-alloying optimized the adsorption of the *OCHO intermediate on Sn active site. Sargent group deposited SnS_x on Au nanoneedles *via* atomic layered deposition, then electrochemically reduced it to form S modified Sn (Sn(S)/Au) catalyst (Figure 2.5).[80] The DFT calculation indicated that the S doping could favor the formation of *OCHO and promote undercoordinated Sn sites. Electrochemical measurements showed that the (Sn(S)/Au) exhibited an excellent performance for formate production with current density of 55 mA cm^{-2} and formate FE of 93% at low potential of –0.75 V *vs*. RHE.

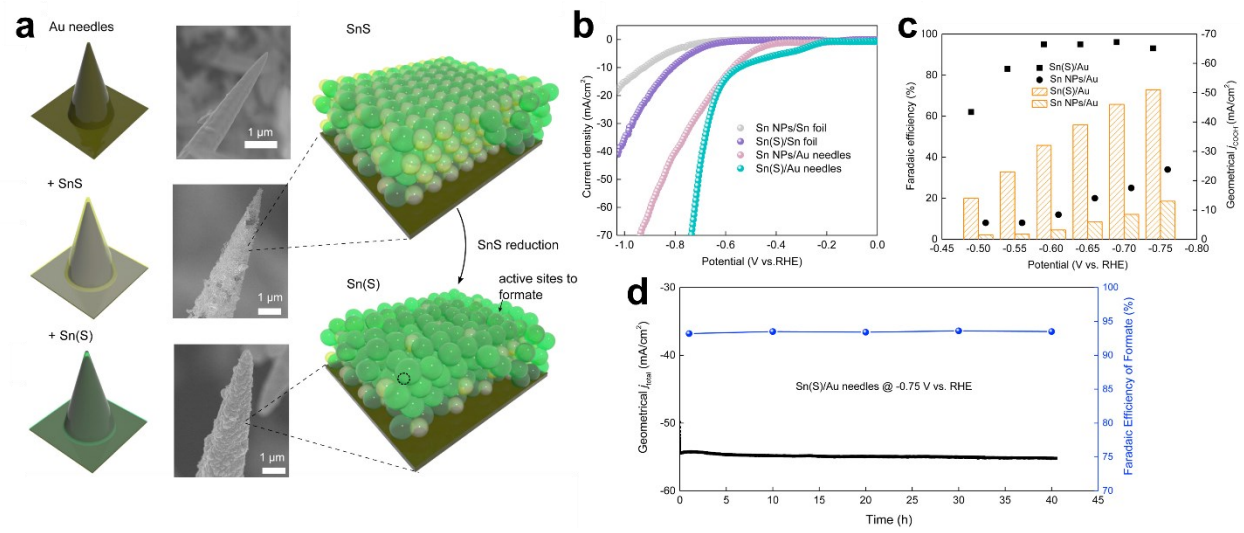

Figure 2.5 (a) SEM images and schematics showing the preparation procedure of Sn(S) nanostructured electrode. (b) The LSV curves for Sn(S)/Au and other control electrodes. (c) formate FE for Sn(S)/Au. (d) Stability test for Sn(S)/Au electrode.[80] Reprinted with permission from Reference 80. Copyright 2017, Elsevier.

2.3 In-based catalysts

Similar to Bi and Sn, In is another metal that can drive ECR to formate. The aforementioned strategies to improve catalytic performance of Bi and Sn-based catalysts are also applicable to In-based catalysts. In-based catalysts with various morphologies such as nanoparticles,[81] nanowires,[82] nanosheets,[83] dendrites[84] have all been synthesized. Besides, In-based catalysts with porous

structure which could facilitate CO_2 diffusion were also reported. Luo and coworkers electrodeposited dendritic In on Cu mesh using hydrogen bubble dynamic template technique.[85] In an aqueous electrolyte, the dendritic In catalyst achieved a high formate FE of 90% within the potential range of –1.0 to –1.2 V *vs*. RHE. The authors suggested that the porous structure not only offered an enlarged surface area but also led to an increase in local pH to suppress HER.

Coupling carbonaceous support with In-based catalysts has been frequently used to improve the dispersion of catalysts and accelerate charge transfer. For example, Zhang group integrated In_2O_3 nanobelts with rGO (In_2O_3-rGO).[86] The chemical coupling interaction between In_2O_3 and rGO increased the electron density on In_2O_3 surface, lowered the formation energy of *OCHO intermediate. Compared to physically mixed catalysts (In_2O_3/rGO), In_2O_3-rGO showed a higher formate FE and partial current density. Developing isolated In atoms on carbon support to form In single-atoms (In SACs) can further improve the utilization of the metal atoms. Recently, *in situ* pyrolysis of organic ligands of MOF into atomically dispersed metal sites (M-N_x) for ECR is widely reported. Li group designed In-SACs catalyst derived from In doped zeolitic imidazolate frameworks (ZIF-8).[87] The In-SACs exhibited an extremely large TOF up to 12500 h^{-1} at –0.95 V *vs*. RHE and a high FE for formate of 96% at a low potential of –0.65 V. By conducting theoretical simulations, the authors found that the $In^{\delta+}$-N_4 sites favorably benefited the formation of *OCHO over *COOH *via* the first proton-electron pair addition.

Creating defect sites (oxygen vacancy or elements doping) in In-based catalysts can modify their electronic structure and tune the adsorption configuration of reactive intermediates. Huang group proved that the introduction of OVs could effectively boost In-based catalysts catalytic performance.[88] They prepared both low vacancy InO_x (O-InO_x) and high-vacancy (H-InO_x) by calcination of pristine InO_x (P-InO_x) in air and H_2 atmosphere, respectively. The electrochemical

tests indicated that the formate FE increased with the increase of OVs amount within the catalysts. The H-InO_x achieved a formate FE of 91.7%, much higher than that of 60% and 48% observed on P-InO_x and O-InO_x, respectively. DFT calculation revealed that the OVs helped the CO_2 adsorption and activation. Wang group found that doping In catalyst with 4.9 mol% of S resulted in the best ECR to formate performance (Figure 2.6).[89] The resultant catalyst yielded formate at a production rate of 1449 μmol h^{-1} cm^{-2} with FE of 93% and current density of 84 mA cm^{-2}. The authors proposed, according to experimental and theoretical analyses, that a proper amount of S doping could benefit the protonation step for ECR by activating water molecules, which substantially increased the productivity of formate.

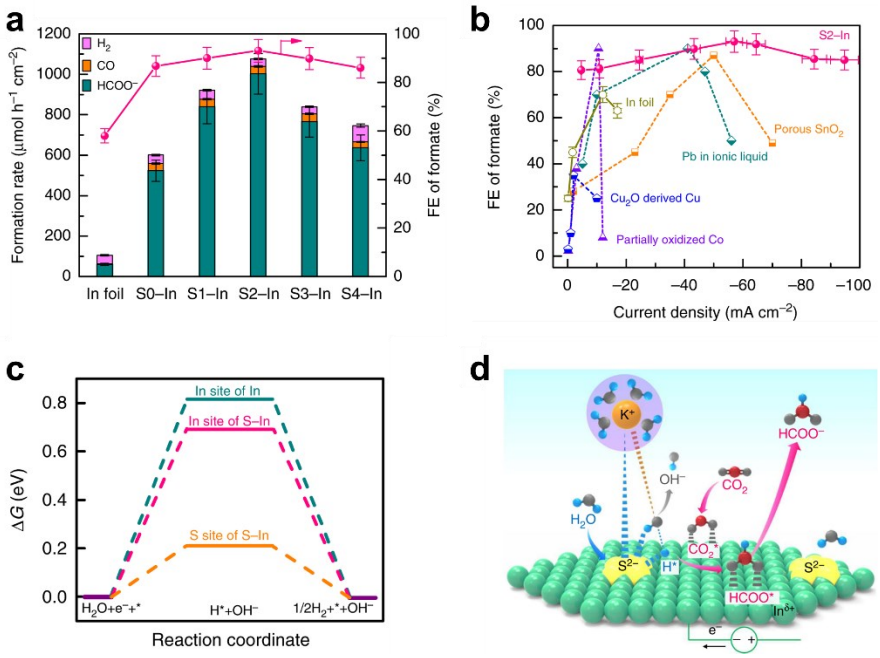

Figure 2.6 Formation rates of H_2, CO and formate and FE of formate for In foil and S−In catalysts at −0.98 V vs RHE for 1 h. (b) Plot of FE of formate versus current density for S2−In catalyst. (c) Gibbs free energies for the formation of *H on pure In (101), In and S sites of S−In (101) surfaces. (d) Schematic illustration for the role of S^{2-} in promoting water dissociation and *H formation for the reduction of CO_2 to formate.[89] Reprinted with permission from Reference 89. Copyright 2019, Springer Nature Group.

Besides the metallic and metal oxide form of In-based catalysts, its sulfide (In_2S_3) and nitride (InN) have also been reported highly active for formate yield. Zeng group prepared InN NS for ECR and found that it would reconstruct to form the In-rich surface.[90] The electronic interaction between surface In and subsurface InN resulted in the redistribution of surface charge that significantly decreased the formation energy of *OCHO, promoting ECR to formate at high rate (formate partial current density of 40.7 mA cm^{-2}). Harmonizing the electronic structures of the adsorbate and catalysts can also modulate the adsorption of intermediates. Zhang et al. incorporated Mn in In_2S_3 catalyst.[83] The Mn doping enabled the harmonic overlaps between the p orbitals of O atoms and d orbitals of Mn atoms near the conduction band edge of the Mn-In_2S_3 slab upon the bidendate adsorption of *OCHO species. Benefiting from the unique electronic structure, Mn-In_2S_3 exhibited a lower energy barrier for CO_2 activation into *OCHO as compared to the undoped pure In_2S_3. In addition to the activity aspect, the stability of catalyst has always been a very challenging aspect but rarely investigated. The catalytic activity of ECR catalysts deteriorates rapidly during high-rate electrolysis due to the likely occurrence of catalysis agglomeration, active-phase change and element dissolution. Take In_2S_3 as an example, the S in In_2S_3 will be dissolved continuously into the electrolyte and lose its original activity. Gao and co-workers incorporated Zn into In_2S_3 ($ZnIn_2S_4$) to solve this S leaching issue.[91] They found that the amount of S in In_2S_3 dropped to 2.13 wt% from its original state (23.6 wt%) within the first 1h of ECR, followed by a slow drop to almost zero over the next 2h as confirmed by inductively coupled plasma atomic emission spectroscopy (ICP-AES). By contrast, the $ZnIn_2S_4$ catalyst showed negligible loss of S after 60 h electrolysis. Benefiting from the excellent structure stability, the $ZnIn_2S_4$ could catalyze ECR to formate with an average FE of 99% for 60h without any decay (Figure 2.7). However, the formate FE decreased to only 30% from initial 90% within 8h operation on In_2S_3 catalyst. Further

theoretical analysis indicated that the Zn doping modified the electronic structure and made the bond breaking between In(Zn) and S in $ZnIn_2S_4$ kinetically cumbersome.

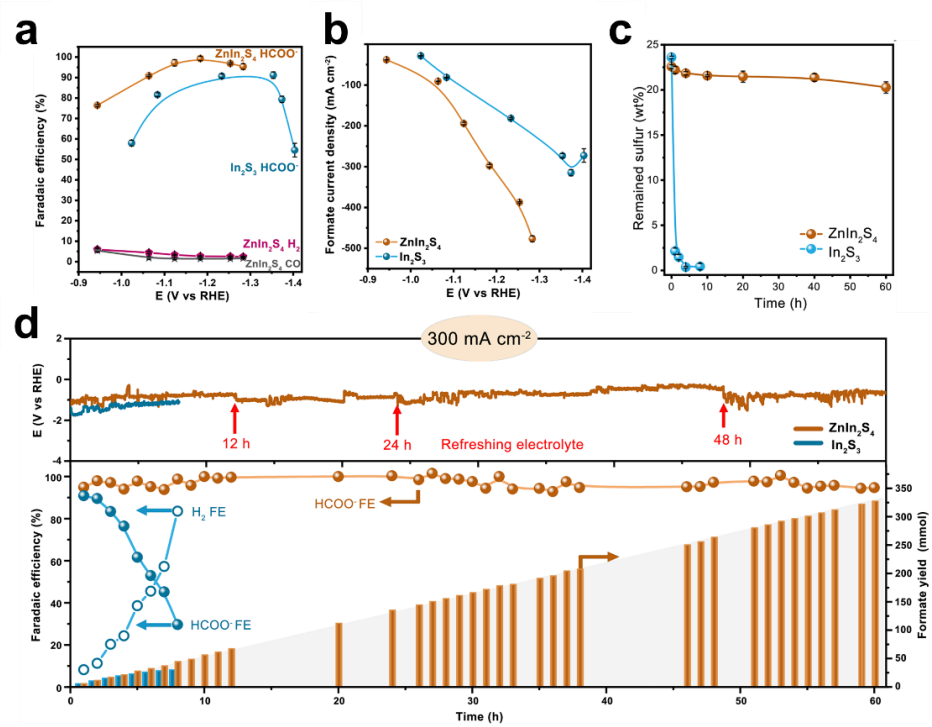

Figure 2.7 (a) FEs and (b) formate partial current densities for $ZnIn_2S_4$ and In_2S_3. (c) The remained sulfur in the $ZnIn_2S_4$ and In_2S_3 after running for various times at 300 mA cm^{-2}. (d) Stability test of $ZnIn_2S_4$ and In_2S_3 at 300 mA cm^{-2}.[91] Reprinted with permission from Reference 91. Copyright 2021, Springer Nature Group.

2.4 Other main group metal-based catalysts

In addition to the widely reported P group metals (Bi, Sn, and In) as discussed above, Pb and Sb-based catalysts are also reported to produce formate as the main product. Although Pb can catalyze ECR to formate with good activity and selectivity, its high intrinsic toxicity and adverse environmental impact limit its practical applications. However, it is of fundamental importance to study the ECR behavior over Pd-based catalysts. Kanan and co-workers prepared an oxide-derived nanocrystalline Pb film (OD-Pb) by reducing Pd oxide films.[92] The OD-Pb exhibited near 100%

formate FE between –0.75 and –1.0 V *vs*. RHE with 730-fold suppression of HER compared to polycrystalline Pd foil. The significant improvement of selectivity was attributed to metastable Pd oxide in the OD-Pd surface, which inhibited HER but was active for ECR. Recently, Zhang et al. reported a highly stable and active hydrocerussite ($Pb_3(CO_3)_2(OH)_2$) catalyst through *in situ* electroreduction of tanni-lead (TA-Pb) complex.[93] The hydrocerussite could stably exist during ECR process instead of self-reduction to metallic Pb, because its self-reduction was hindered by the dominant ECR.

Sb, as another main group metal, locates next to Bi and Sn in the periodic table but received much less attention. Bulk Sb has been reported to catalyze ECR with limited formate FE.[94] Nano-structural engineering represents an effective approach to solving this problem and promoting the selectivity. Zhang et al. obtained few-layer Sb nanosheets *via* cathodic exfoliation process.[4] After integration with graphene, it achieved a formate FE up to 88.5% with good stability outperforming the bulk Sb catalyst. The improved performance was attributed to high exposure of active sites and strong electronic interaction between Sb nanosheets and graphene. In addition, Sb single-atoms (Sb SACs) catalyst was also reported to be highly active for ECR to formate.[95]

2.5 Current status and remaining challenges

The above sections intensively summarized the recent considerable progress in main group metal-based catalyst for ECR to formate. Main group metals including Bi, Sn, In, Pb, Sb, and so on represent promising candidates for formate production. This is because they favorably adsorb and stabilize *OCHO (intermediate for formate pathway) over *COOH (intermediate for CO pathway) and *H (intermediate for H_2 pathway). From the practical implementation perspective, Pb is not an ideal catalyst material due to its high toxicity and environmental hazard. Despite low toxicity, In has a relatively high cost (about 10 times that of Sn or Bi). This essentially leaves us with Sn or

Bi as the only choices. Based on extensive literature survey, Bi-based materials hold a greater promise since many of them catalyzed ECR to formate with high selectivity (> 90%) and activity (current density> 30 mA cm^{-2}). Despite the fruitful progress that has been made in Bi-based catalysts, there are still inevitable challenges that need to be resolved to put forward the CO_2 electrolysis technology into practical implementation. First, the competing HER during ECR greatly restricts the activity of Bi-based catalysts at high current densities with the consequence that most of the reported Bi-based catalysts fail to work under high activity (current density > 45 mA cm^{-2}) and selectivity (FE > 90%).

Secondly, the CO_2 mass transport in aqueous medium is an intrinsic limitation for achieving high formation rate of formate. To our knowledge, most existing catalysts typically work with low formate formation rate (< 1500 μmol h^{-1} cm^{-2} in H-type cell). Meanwhile, the leveling of ECR causes most catalysts only to work effectively (FE > 90%) in a narrow range of potential window (< 750 mV).

Thirdly, the kinetically sluggish and energy-intensive oxygen evolution reaction (OER) in anode requires large overpotential to obtain appreciable current densities and thus could drag down the whole electrochemical efficiency of ECR. On the other hand, the anode catalysts for OER are noble metals (Pt, IrO_2, or RuO_2) which inevitably increases the cost of the system.

Last but not least, the ECR mechanisms remain ambiguous and under debate. For example, is CO_2 directly reduced or do bicarbonate anions serve as the dominant source? What are the real catalytic sites in heteroatom doped carbon catalysts (dopants or defects)? Most mechanism studies of ECR are based on *ex situ* characterization of catalyst before and after CO_2 reduction. These *ex situ* characterizations can not catch important information in the real ECR process, since the catalyst usually undergoes surface reconstruction, morphological transformation, and active site evolution.

Based on the above remaining challenges, the objectives of this research are as follows:

1. Develop a S doping strategy that enables catalyst to work under high activity and selectivity.
2. Develop a surface hydrophobic engineering method that can significantly enhance performance of ECR over a broad potential window by resolving the CO_2 mass transport limitation issue in aqueous medium.
3. Develop a coupling system that can greatly reduce the energy input in the overall ECR system.

2.6 References

1. Pumera, M.; Sofer, Z., 2D monoelemental arsenene, antimonene, and bismuthene: beyond black phosphorus. *Adv. Mater.* 2017, *29* (21), 1605299.
2. Yang, F.; Elnabawy, A. O.; Schimmenti, R.; Song, P.; Wang, J.; Peng, Z.; Yao, S.; Deng, R.; Song, S.; Lin, Y., Bismuthene for highly efficient carbon dioxide electroreduction reaction. *Nat. Commun.* 2020, *11* (1), 1-8.
3. Wang, Y.; Li, Y.; Liu, J.; Dong, C.; Xiao, C.; Cheng, L.; Jiang, H.; Jiang, H.; Li, C., $BiPO_4$-Derived 2D Nanosheets for Efficient Electrocatalytic Reduction of CO_2 to Liquid Fuel. *Angew. Chem., Int. Ed.* 2021, *60* (14), 7687-7685.
4. Li, F.; Xue, M.; Li, J.; Ma, X.; Chen, L.; Zhang, X.; MacFarlane, D. R.; Zhang, J., Unlocking the electrocatalytic activity of antimony for CO_2 reduction by two-dimensional engineering of the bulk material. *Angew. Chem., Int. Ed.* 2017, *56* (46), 14718-14722.
5. Han, N.; Wang, Y.; Yang, H.; Deng, J.; Wu, J.; Li, Y.; Li, Y., Ultrathin bismuth nanosheets from *in situ* topotactic transformation for selective electrocatalytic CO_2 reduction to formate. *Nat. Commun.* 2018, *9* (1), 1-8.
6. Lamagni, P.; Miola, M.; Catalano, J.; Hvid, M. S.; Mamakhel, M. A. H.; Christensen, M.; Madsen, M. R.; Jeppesen, H. S.; Hu, X. M.; Daasbjerg, K., Restructuring metal–organic frameworks to nanoscale bismuth electrocatalysts for highly active and selective CO_2 reduction to formate. *Adv. Funct. Mater.* 2020, *30* (16), 1910408.

7. Deng, P.; Yang, F.; Wang, Z.; Chen, S.; Zhou, Y.; Zaman, S.; Xia, B. Y., Metal–Organic Framework-Derived Carbon Nanorods Encapsulating Bismuth Oxides for Rapid and Selective CO_2 Electroreduction to Formate. *Angew. Chem., Int. Ed.* 2020, *59* (27), 10807-10813.

8. Yao, D.; Tang, C.; Vasileff, A.; Zhi, X.; Jiao, Y.; Qiao, S. Z., The Controllable Reconstruction of Bi-MOFs for Electrochemical CO_2 Reduction through Electrolyte and Potential Mediation. *Angew. Chem., Int. Ed.* 2021, *60* (33), 18178-18184.

9. Zhang, E.; Wang, T.; Yu, K.; Liu, J.; Chen, W.; Li, A.; Rong, H.; Lin, R.; Ji, S.; Zheng, X., Bismuth single atoms resulting from transformation of metal–organic frameworks and their use as electrocatalysts for CO_2 reduction. *J. Am. Chem. Soc.* 2019, *141* (42), 16569-16573.

10. Cao, C.; Ma, D. D.; Gu, J. F.; Xie, X.; Zeng, G.; Li, X.; Han, S. G.; Zhu, Q. L.; Wu, X. T.; Xu, Q., Metal–organic layers leading to atomically thin bismuthene for efficient carbon dioxide electroreduction to liquid fuel. *Angew. Chem., Int. Ed.* 2020, *59* (35), 15014-15020.

11. Yang, J.; Wang, X.; Qu, Y.; Wang, X.; Huo, H.; Fan, Q.; Wang, J.; Yang, L. M.; Wu, Y., Bi-based metal-organic framework derived leafy bismuth nanosheets for carbon dioxide electroreduction. *Adv. Energy Mater.* 2020, *10* (36), 2001709.

12. Zhang, Y.; Zhang, X.; Ling, Y.; Li, F.; Bond, A. M.; Zhang, J., Controllable synthesis of few-layer bismuth subcarbonate by electrochemical exfoliation for enhanced CO_2 reduction performance. *Angew. Chem.* 2018, *130* (40), 13467-13471.

13. Gong, Q.; Ding, P.; Xu, M.; Zhu, X.; Wang, M.; Deng, J.; Ma, Q.; Han, N.; Zhu, Y.; Lu, J., Structural defects on converted bismuth oxide nanotubes enable highly active electrocatalysis of carbon dioxide reduction. *Nat. Commun.* 2019, *10* (1), 1-10.

14. Zhang, M.; Wei, W.; Zhou, S.; Ma, D.-D.; Cao, A.; Wu, X.-T.; Zhu, Q.-L., Engineering a conductive network of atomically thin bismuthene with rich defects enables CO_2 reduction to formate with industry-compatible current densities and stability. *Energy Environ. Sci.* 2021, *14* (9), 4998-5008.

15. Lim, H.-K.; Shin, H.; Goddard III, W. A.; Hwang, Y. J.; Min, B. K.; Kim, H., Embedding covalency into metal catalysts for efficient electrochemical conversion of CO_2. *J. Am. Chem. Soc.* 2014, *136* (32), 11355-11361.

16. Wu, Y.; Cao, S.; Hou, J.; Li, Z.; Zhang, B.; Zhai, P.; Zhang, Y.; Sun, L., Rational design of nanocatalysts with nonmetal species modification for electrochemical CO_2 reduction. *Adv. Energy Mater.* 2020, *10* (29), 2000588.

17. Chen, X.; Chen, H.; Zhou, W.; Zhang, Q.; Yang, Z.; Li, Z.; Yang, F.; Wang, D.; Ye, J.; Liu, L., Boron Dopant Induced Electron-Rich Bismuth for Electrochemical CO_2 Reduction with High Solar Energy Conversion Efficiency. *Small* 2021, *17* (29), 2101128.

18. Zhao, Y.; Liu, X.; Liu, Z.; Lin, X.; Lan, J.; Zhang, Y.; Lu, Y.-R.; Peng, M.; Chan, T.-S.; Tan, Y., Spontaneously Sn-Doped Bi/BiO_x Core–Shell Nanowires Toward High-Performance CO_2 Electroreduction to Liquid Fuel. *Nano Lett.* 2021, *21* (16), 6907-6913.

19. Wen, G.; Lee, D. U.; Ren, B.; Hassan, F. M.; Jiang, G.; Cano, Z. P.; Gostick, J.; Croiset, E.; Bai, Z.; Yang, L., Orbital interactions in Bi-Sn bimetallic electrocatalysts for highly selective electrochemical CO_2 reduction toward formate production. *Adv. Energy Mater.* 2018, *8* (31), 1802427.

20. Li, L.; Ozden, A.; Guo, S.; García de Arquer, F. P.; Wang, C.; Zhang, M.; Zhang, J.; Jiang, H.; Wang, W.; Dong, H., Stable, active CO_2 reduction to formate *via* redox-modulated stabilization of active sites. *Nat. Commun.* 2021, *12* (1), 1-9.

21. Chen, Z.; Mou, K.; Wang, X.; Liu, L., Nitrogen-doped graphene quantum dots enhance the activity of Bi_2O_3 nanosheets for electrochemical reduction of CO_2 in a wide negative potential region. *Angew. Chem.* 2018, *130* (39), 12972-12976.

22. Chen, Z.; Zhang, X.; Jiao, M.; Mou, K.; Zhang, X.; Liu, L., Engineering Electronic Structure of Stannous Sulfide by Amino-Functionalized Carbon: Toward Efficient Electrocatalytic Reduction of CO_2 to Formate. *Adv. Energy Mater.* 2020, *10* (8), 1903664.

23. Liu, S.; Lu, X. F.; Xiao, J.; Wang, X.; Lou, X. W., Bi_2O_3 nanosheets grown on multi-channel carbon matrix to catalyze efficient CO_2 electroreduction to HCOOH. *Angew. Chem.* 2019, *131* (39), 13966-13971.

24. Zhang, W.; Yang, S.; Jiang, M.; Hu, Y.; Hu, C.; Zhang, X.; Jin, Z., Nanocapillarity and nanoconfinement effects of pipet-like bismuth@carbon nanotubes for highly efficient electrocatalytic CO_2 reduction. *Nano Lett.* 2021, *21* (6), 2650-2657.

25. Duan, Y. X.; Liu, K. H.; Zhang, Q.; Yan, J. M.; Jiang, Q., Efficient CO_2 reduction to HCOOH with high selectivity and energy efficiency over Bi/rGO catalyst. *Small Methods* 2020, *4* (5), 1900846.

26. Huang, J.; Guo, X.; Yang, J.; Wang, L., Electrodeposited Bi dendrites/2D black phosphorus nanosheets composite used for boosting formic acid production from CO_2 electroreduction. *J. CO_2 Util.* 2020, *38*, 32-38.

27. Wu, D.; Wang, X.; Fu, X.-Z.; Luo, J.-L., Ultrasmall Bi nanoparticles confined in carbon nanosheets as highly active and durable catalysts for CO_2 electroreduction. *Appl. Catal. B* 2021, *284*, 119723.

28. Su, P.; Xu, W.; Qiu, Y.; Zhang, T.; Li, X.; Zhang, H., Ultrathin bismuth nanosheets as a highly efficient CO_2 reduction electrocatalyst. *ChemSusChem* 2018, *11* (5), 848-853.

29. Tran-Phu, T.; Daiyan, R.; Fusco, Z.; Ma, Z.; Amal, R.; Tricoli, A., Nanostructured β-Bi_2O_3 fractals on carbon fibers for highly selective CO_2 electroreduction to formate. *Adv. Funct. Mater.* 2020, *30* (3), 1906478.

30. Lee, C. W.; Hong, J. S.; Yang, K. D.; Jin, K.; Lee, J. H.; Ahn, H.-Y.; Seo, H.; Sung, N.-E.; Nam, K. T., Selective electrochemical production of formate from carbon dioxide with bismuth-based catalysts in an aqueous electrolyte. *ACS Catal.* 2018, *8* (2), 931-937.

31. Meng, F. L.; Zhang, Q.; Liu, K. H.; Zhang, X. B., Integrated Bismuth Oxide Ultrathin Nanosheets/Carbon Foam Electrode for Highly Selective and Energy-Efficient Electrocatalytic Conversion of CO_2 to HCOOH. *Chem. Eur. J.* 2020, *26* (18), 4013-4018.

32. Zhang, X.; Sun, X.; Guo, S.-X.; Bond, A. M.; Zhang, J., Formation of lattice-dislocated bismuth nanowires on copper foam for enhanced electrocatalytic CO_2 reduction at low overpotential. *Energy Environ. Sci.* 2019, *12* (4), 1334-1340.

33. Fan, J.; Zhao, X.; Mao, X.; Xu, J.; Han, N.; Yang, H.; Pan, B.; Li, Y.; Wang, L.; Li, Y., Large-Area Vertically Aligned Bismuthene Nanosheet Arrays from Galvanic Replacement Reaction for Efficient Electrochemical CO_2 Conversion. *Adv. Mater.* 2021, *33* (35), 2100910.

34. Park, G.; Hong, S.; Choi, M.; Lee, S.; Lee, J., Au on highly hydrophobic carbon substrate for improved selective CO production from CO_2 in gas-phase electrolytic cell. *Catal. Today* 2020, *355*, 340-346.

35. Hall, A. S.; Yoon, Y.; Wuttig, A.; Surendranath, Y., Mesostructure-induced selectivity in CO_2 reduction catalysis. *J. Am. Chem. Soc.* 2015, *137* (47), 14834-14837.

36. Weekes, D. M.; Salvatore, D. A.; Reyes, A.; Huang, A.; Berlinguette, C. P., Electrolytic CO_2 reduction in a flow cell. *Acc. Chem. Res.* 2018, *51* (4), 910-918.

37. Wakerley, D.; Lamaison, S.; Ozanam, F.; Menguy, N.; Mercier, D.; Marcus, P.; Fontecave, M.; Mougel, V., Bio-inspired hydrophobicity promotes CO_2 reduction on a Cu surface. *Nat. Mater.* 2019, *18* (11), 1222-1227.

38. Niu, Z.-Z.; Gao, F.-Y.; Zhang, X.-L.; Yang, P.-P.; Liu, R.; Chi, L.-P.; Wu, Z.-Z.; Qin, S.; Yu, X.; Gao, M.-R., Hierarchical copper with inherent hydrophobicity mitigates electrode flooding for high-rate CO_2 electroreduction to multicarbon products. *J. Am. Chem. Soc.* 2021, *143* (21), 8011-8021.

39. Pan, F.; Yang, Y., Designing CO_2 reduction electrode materials by morphology and interface engineering. *Energy Environ. Sci.* 2020, *13* (8), 2275-2309.

40. Jiang, Y.; Zhang, X.; Xu, D.; Li, W.; Liu, M.; Qiu, X., Efficient three-phase electrocatalytic CO_2 reduction to formate on superhydrophobic Bi–C interfaces. *Chem. Commun.* 2021, *57* (49), 6011-6014.

41. Zhang, X. Y.; Li, W. J.; Wu, X. F.; Liu, Y. W.; Chen, J.; Zhu, M.; Yuan, H. Y.; Dai, S.; Wang, H. F.; Jiang, Z., Selective methane electrosynthesis enabled by a hydrophobic carbon coated copper core–shell architecture. *Energy Environ. Sci.* 2022, *15* (1) 234-243.

42. Xue, L.; Wu, X.; Liu, Y.; Xu, B.; Wang, X.; Dai, S.; Liu, P.; Yang, H., Hydrophobic 1-octadecanethiol functionalized copper catalyst promotes robust high-current CO_2 gas-diffusion electrolysis. *Nano Res.* 2022, *15* (2), 1393-1398.

43. Wang, J.; Yang, H.; Liu, Q.; Liu, Q.; Li, X.; Lv, X.; Cheng, T.; Wu, H. B., Fastening Br– Ions at Copper–Molecule Interface Enables Highly Efficient Electroreduction of CO_2 to Ethanol. *ACS Energy Lett.* 2021, *6* (2), 437-444.

44. Liang, H.-Q.; Zhao, S.; Hu, X.-M.; Ceccato, M.; Skrydstrup, T.; Daasbjerg, K., Hydrophobic copper interfaces boost electroreduction of carbon dioxide to ethylene in water. *ACS Catal.* 2021, *11* (2), 958-966.

45. Chang, S.; Xuan, Y.; Duan, J.; Zhang, K., High-Performance Electroreduction CO_2 to Formate at Bi/Nafion Interface. *Appl. Catal. B* 2022, 306, 121135.

46. Machan, C. W.; Yin, J.; Chabolla, S. A.; Gilson, M. K.; Kubiak, C. P., Improving the efficiency and activity of electrocatalysts for the reduction of CO_2 through supramolecular assembly with amino acid-modified ligands. *J. Am. Chem. Soc.* 2016, *138* (26), 8184-8193.

47. Ahn, S.; Klyukin, K.; Wakeham, R. J.; Rudd, J. A.; Lewis, A. R.; Alexander, S.; Carla, F.; Alexandrov, V.; Andreoli, E., Poly-amide modified copper foam electrodes for enhanced electrochemical reduction of carbon dioxide. *ACS Catal.* 2018, *8* (5), 4132-4142.

48. Xing, Z.; Hu, L.; Ripatti, D. S.; Hu, X.; Feng, X., Enhancing carbon dioxide gas-diffusion electrolysis by creating a hydrophobic catalyst microenvironment. *Nat. Commun.* 2021, *12* (1), 1-11.

49. Xing, Z.; Hu, X.; Feng, X., Tuning the microenvironment in gas-diffusion electrodes enables high-rate CO_2 electrolysis to formate. *ACS Energy Lett.* 2021, *6* (5), 1694-1702.

50. Hori, Y.; Wakebe, H.; Tsukamoto, T.; Koga, O., Electrocatalytic process of CO selectivity in electrochemical reduction of CO_2 at metal electrodes in aqueous media. *Electrochim. Acta* 1994, *39* (11-12), 1833-1839.

51. Baruch, M. F.; Pander III, J. E.; White, J. L.; Bocarsly, A. B., Mechanistic insights into the reduction of CO_2 on tin electrodes using *in situ* ATR-IR spectroscopy. *ACS Catal.* 2015, *5* (5), 3148-3156.

52. Deng, W.; Zhang, L.; Li, L.; Chen, S.; Hu, C.; Zhao, Z.-J.; Wang, T.; Gong, J., Crucial role of surface hydroxyls on the activity and stability in electrochemical CO_2 reduction. *J. Am. Chem. Soc.* 2019, *141* (7), 2911-2915.

53. An, X.; Li, S.; Yoshida, A.; Wang, Z.; Hao, X.; Abudula, A.; Guan, G., Electrodeposition of tin-based electrocatalysts with different surface tin species distributions for electrochemical reduction of CO_2 to HCOOH. *ACS Sustain. Chem. Eng.* 2019, *7* (10), 9360-9368.

54. Wu, J.; Bai, X.; Ren, Z.; Du, S.; Song, Z.; Zhao, L.; Liu, B.; Wang, G.; Fu, H., Multivalent Sn species synergistically favours the CO_2-into-HCOOH conversion. *Nano Res.* 2021, *14* (4), 1053-1060.

55. Chen, Z.; Gao, M.-R.; Duan, N.; Zhang, J.; Zhang, Y.-Q.; Fan, T.; Zhang, J.; Dong, Y.; Li, J.; Liu, Q., Tuning adsorption strength of CO_2 and its intermediates on tin oxide-based electrocatalyst for efficient CO_2 reduction towards carbonaceous products. *Appl. Catal. B* 2020, *277*, 119252.

56. Li, F.; Chen, L.; Knowles, G. P.; MacFarlane, D. R.; Zhang, J., Hierarchical mesoporous SnO_2 nanosheets on carbon cloth: a robust and flexible electrocatalyst for CO_2 reduction with high efficiency and selectivity. *Angew. Chem.* 2017, *129* (2), 520-524.

57. Zhang, L.; Zhao, Z. J.; Gong, J., Nanostructured materials for heterogeneous electrocatalytic CO_2 reduction and their related reaction mechanisms. *Angew. Chem., Int. Ed.* 2017, *56* (38), 11326-11353.

58. Wei, F.; Wang, T.; Jiang, X.; Ai, Y.; Cui, A.; Cui, J.; Fu, J.; Cheng, J.; Lei, L.; Hou, Y., Controllably engineering mesoporous surface and dimensionality of SnO_2 toward high-performance CO_2 electroreduction. *Adv. Funct. Mater.* 2020, *30* (39), 2002092.

59. Kim, K.-S.; Kim, W. J.; Lim, H.-K.; Lee, E. K.; Kim, H., Tuned chemical bonding ability of Au at grain boundaries for enhanced electrochemical CO_2 reduction. *ACS Catal.* 2016, *6* (7), 4443-4448.

60. Kumar, B.; Atla, V.; Brian, J. P.; Kumari, S.; Nguyen, T. Q.; Sunkara, M.; Spurgeon, J. M., Reduced SnO_2 porous nanowires with a high density of grain boundaries as catalysts for efficient electrochemical CO_2-into-HCOOH conversion. *Angew. Chem., Int. Ed.* 2017, *56* (13), 3645-3649.

61. Liu, S.; Xiao, J.; Lu, X. F.; Wang, J.; Wang, X.; Lou, X. W., Efficient electrochemical reduction of CO_2 to HCOOH over sub-2 nm SnO_2 quantum wires with exposed grain boundaries. *Angew. Chem., Int. Ed.* 2019, *58* (25), 8499-8503.

62. Zhang, S.; Kang, P.; Meyer, T. J., Nanostructured tin catalysts for selective electrochemical reduction of carbon dioxide to formate. *J. Am. Chem. Soc.* 2014, *136* (5), 1734-1737.

63. Tsujiguchi, T.; Kawabe, Y.; Jeong, S.; Ohto, T.; Kukunuri, S.; Kuramochi, H.; Takahashi, Y.; Nishiuchi, T.; Masuda, H.; Wakisaka, M., Acceleration of electrochemical CO_2 reduction to formate at the Sn/reduced graphene oxide interface. *ACS Catal.* 2021, *11* (6), 3310-3318.

64. Yuan, L.-P.; Jiang, W.-J.; Liu, X.-L.; He, Y.-H.; He, C.; Tang, T.; Zhang, J.; Hu, J.-S., Molecularly engineered strong metal oxide–support interaction enables highly efficient and stable CO_2 electroreduction. *ACS Catal.* 2020, *10* (22), 13227-13235.

65. Pan, Y.; Lin, R.; Chen, Y.; Liu, S.; Zhu, W.; Cao, X.; Chen, W.; Wu, K.; Cheong, W.-C.; Wang, Y., Design of single-atom Co–N_5 catalytic site: a robust electrocatalyst for CO_2 reduction with nearly 100% CO selectivity and remarkable stability. *J. Am. Chem. Soc.* 2018, *140* (12), 4218-4221.

66. Zhang, H.; Li, J.; Xi, S.; Du, Y.; Hai, X.; Wang, J.; Xu, H.; Wu, G.; Zhang, J.; Lu, J., A graphene-supported single-atom FeN_5 catalytic site for efficient electrochemical CO_2 reduction. *Angew. Chem.* 2019, *131* (42), 15013-15018.

67. Su, X.; Yang, X.-F.; Huang, Y.; Liu, B.; Zhang, T., Single-atom catalysis toward efficient CO_2 conversion to CO and formate products. *Acc. Chem. Res.* 2018, *52* (3), 656-664.

68. Zheng, T.; Liu, C.; Guo, C.; Zhang, M.; Li, X.; Jiang, Q.; Xue, W.; Li, H.; Li, A.; Pao, C.-W., Copper-catalysed exclusive CO_2 to pure formic acid conversion *via* single-atom alloying. *Nat. Nanotechnol.* 2021, *16* (12), 1386-1393.

69. Zu, X.; Li, X.; Liu, W.; Sun, Y.; Xu, J.; Yao, T.; Yan, W.; Gao, S.; Wang, C.; Wei, S., Efficient and robust carbon dioxide electroreduction enabled by atomically dispersed $Sn^{\delta+}$ sites. *Adv. Mater.* 2019, *31* (15), 1808135.

70. Ni, W.; Gao, Y.; Lin, Y.; Ma, C.; Guo, X.; Wang, S.; Zhang, S., Nonnitrogen coordination environment steering electrochemical CO_2-to-CO conversion over single-atom tin catalysts in a wide potential window. *ACS Catal.* 2021, *11* (9), 5212-5221.

71. Zeng, Z.; Gan, L. Y.; Bin Yang, H.; Su, X.; Gao, J.; Liu, W.; Matsumoto, H.; Gong, J.; Zhang, J.; Cai, W., Orbital coupling of hetero-diatomic nickel-iron site for bifunctional electrocatalysis of CO_2 reduction and oxygen evolution. *Nat. Commun.* 2021, *12* (1), 1-11.

72. Ren, W.; Tan, X.; Yang, W.; Jia, C.; Xu, S.; Wang, K.; Smith, S. C.; Zhao, C., Isolated diatomic Ni-Fe metal–nitrogen sites for synergistic electroreduction of CO_2. *Angew. Chem., Int. Ed.* 2019, *58* (21), 6972-6976.

73. Xie, W.; Li, H.; Cui, G.; Li, J.; Song, Y.; Li, S.; Zhang, X.; Lee, J. Y.; Shao, M.; Wei, M., NiSn atomic pair on an integrated electrode for synergistic electrocatalytic CO_2 reduction. *Angew. Chem.* 2021, *133* (13), 7458-7464.

74. Li, H.; Xiao, N.; Wang, Y.; Liu, C.; Zhang, S.; Zhang, H.; Bai, J.; Xiao, J.; Li, C.; Guo, Z., Promoting the electroreduction of CO_2 with oxygen vacancies on a plasma-activated SnO_x/carbon foam monolithic electrode. *J. Mater. Chem. A* 2020, *8* (4), 1779-1786.

75. Li, L.; Zhao, Z.-J.; Hu, C.; Yang, P.; Yuan, X.; Wang, Y.; Zhang, L.; Moskaleva, L.; Gong, J., Tuning oxygen vacancies of oxides to promote electrocatalytic reduction of carbon dioxide. *ACS Energy Lett.* 2020, *5* (2), 552-558.

76. Liu, G.; Li, Z.; Shi, J.; Sun, K.; Ji, Y.; Wang, Z.; Qiu, Y.; Liu, Y.; Wang, Z.; Hu, P., Black reduced porous SnO_2 nanosheets for CO_2 electroreduction with high formate selectivity and low overpotential. *Appl. Catal. B* 2020, *260*, 118134.

77. He, J.; Liu, X.; Liu, H.; Zhao, Z.; Ding, Y.; Luo, J., Highly selective electrocatalytic reduction of CO_2 to formate over Tin (IV) sulfide monolayers. *J. Catal.* 2018, *364*, 125-130.

78. Zhang, A.; He, R.; Li, H.; Chen, Y.; Kong, T.; Li, K.; Ju, H.; Zhu, J.; Zhu, W.; Zeng, J., Nickel doping in atomically thin tin disulfide nanosheets enables highly efficient CO_2 reduction. *Angew. Chem.* 2018, *130* (34), 11120-11124.

79. Chen, M.; Wan, S.; Zhong, L.; Liu, D.; Yang, H.; Li, C.; Huang, Z.; Liu, C.; Chen, J.; Pan, H., Dynamic Restructuring of Cu-Doped SnS_2 Nanoflowers for Highly Selective Electrochemical CO_2 Reduction to Formate. *Angew. Chem., Int. Ed.* 2021, *60* (50), 26233-26237.

80. Zheng, X.; De Luna, P.; de Arquer, F. P. G.; Zhang, B.; Becknell, N.; Ross, M. B.; Li, Y.; Banis, M. N.; Li, Y.; Liu, M., Sulfur-modulated tin sites enable highly selective electrochemical reduction of CO_2 to formate. *Joule* 2017, *1* (4), 794-805.

81. Pan, B.; Yuan, G.; Zhao, X.; Han, N.; Huang, Y.; Feng, K.; Cheng, C.; Zhong, J.; Zhang, L.; Wang, Y., Highly Dispersed Indium Oxide Nanoparticles Supported on Carbon Nanorods Enabling Efficient Electrochemical CO_2 Reduction. *Small Science* 2021, *1* (10), 2100029.

82. Jang, Y. J.; Lee, J.; Kim, J. H.; Lee, B. J.; Lee, J. S., One-dimensional CuIn alloy nanowires as a robust and efficient electrocatalyst for selective CO_2-to-CO conversion. *J. Power Sources* 2018, *378*, 412-417.

83. Zhang, A.; Liang, Y.; Li, H.; Zhao, X.; Chen, Y.; Zhang, B.; Zhu, W.; Zeng, J., Harmonizing the electronic structures of the adsorbate and catalysts for efficient CO_2 reduction. *Nano Lett.* 2019, *19* (9), 6547-6553.

84. Hoffman, Z. B.; Gray, T. S.; Moraveck, K. B.; Gunnoe, T. B.; Zangari, G., Electrochemical reduction of carbon dioxide to syngas and formate at dendritic copper–indium electrocatalysts. *ACS Catal.* 2017, *7* (8), 5381-5390.

85. Luo, W.; Xie, W.; Li, M.; Zhang, J.; Züttel, A., 3D hierarchical porous indium catalyst for highly efficient electroreduction of CO_2. *J. Mater. Chem. A* 2019, *7* (9), 4505-4515.

86. Zhang, Z.; Ahmad, F.; Zhao, W.; Yan, W.; Zhang, W.; Huang, H.; Ma, C.; Zeng, J., Enhanced electrocatalytic reduction of CO_2 *via* chemical coupling between indium oxide and reduced graphene oxide. *Nano Lett.* 2019, *19* (6), 4029-4034.

87. Shang, H.; Wang, T.; Pei, J.; Jiang, Z.; Zhou, D.; Wang, Y.; Li, H.; Dong, J.; Zhuang, Z.; Chen, W., Design of a Single-Atom Indium$^{\delta+}$–N_4 Interface for Efficient Electroreduction of CO_2 to Formate. *Angew. Chem., Int. Ed.* 2020, *59* (50), 22465-22469.

88. Zhang, J.; Yin, R.; Shao, Q.; Zhu, T.; Huang, X., Oxygen vacancies in amorphous InO_x nanoribbons enhance CO_2 adsorption and activation for CO_2 electroreduction. *Angew. Chem., Int. Ed.* 2019, *58* (17), 5609-5613.

89. Ma, W.; Xie, S.; Zhang, X.-G.; Sun, F.; Kang, J.; Jiang, Z.; Zhang, Q.; Wu, D.-Y.; Wang, Y., Promoting electrocatalytic CO_2 reduction to formate *via* sulfur-boosting water activation on indium surfaces. *Nat. Commun.* 2019, *10* (1), 1-10.

90. Zhang, A.; Liang, Y.; Li, H.; Zhang, B.; Liu, Z.; Chang, Q.; Zhang, H.; Zhu, C.-F.; Geng, Z.; Zhu, W., In-situ surface reconstruction of InN nanosheets for efficient CO_2 electroreduction into formate. *Nano Lett.* 2020, *20* (11), 8229-8235.

91. Chi, L.-P.; Niu, Z.-Z.; Zhang, X.-L.; Yang, P.-P.; Liao, J.; Gao, F.-Y.; Wu, Z.-Z.; Tang, K.-B.; Gao, M.-R., Stabilizing indium sulfide for CO_2 electroreduction to formate at high rate by zinc incorporation. *Nat. Commun.* 2021, *12* (1), 1-9.

92. Lee, C. H.; Kanan, M. W., Controlling H^+ vs CO_2 reduction selectivity on Pb electrodes. *ACS Catal.* 2015, *5* (1), 465-469.

93. Shi, Y.; Ji, Y.; Long, J.; Liang, Y.; Liu, Y.; Yu, Y.; Xiao, J.; Zhang, B., Unveiling hydrocerussite as an electrochemically stable active phase for efficient carbon dioxide electroreduction to formate. *Nat. Commun.* 2020, *11* (1), 1-10.

94. Medina-Ramos, J.; Pupillo, R. C.; Keane, T. P.; DiMeglio, J. L.; Rosenthal, J., Efficient conversion of CO_2 to CO using tin and other inexpensive and easily prepared post-transition metal catalysts. *J. Am. Chem. Soc.* 2015, *137* (15), 5021-5027.

95. Jiang, Z.; Wang, T.; Pei, J.; Shang, H.; Zhou, D.; Li, H.; Dong, J.; Wang, Y.; Cao, R.; Zhuang, Z., Discovery of main group single $Sb–N_4$ active sites for CO_2 electroreduction to formate with high efficiency. *Energy Environ. Sci.* 2020, *13* (9), 2856-2863.

Chapter 3. Methodology and experimental section

3.1 Electrochemical analysis

3.1.1 Electrochemical measurements in H-type cell

The experiments were performed on a Solartron 1286 Potentiostat in a Nafion 117 membrane separated H-type cell using the as-prepared carbon paper electrode as working electrode, carbon rod as counter electrode and saturated calomel electrode (SCE) as reference electrode in CO_2-saturated 0.5 M $KHCO_3$ solution. Prior to the electrochemical measurements, CO_2 was bubbled (with a flow rate of 20 ml min^{-1}) into the electrolyte for at least 30 min. Liner sweep voltammetry (LSV) test with a scan rate of 20 mV s^{-1} was repeated for 6 times and the last one was plotted. During the electrolysis, the cathode electrolyte was stirred at a rate of 500 rpm with a magnetic stirrer. The gas products directly went into gas chromatograph (GC, Agilent 6890N) and were quantified. Liquid products were analyzed using ionic chromatography (IC) and quantified according to the calibration curve. The charge transfer resistance was determined by conducting electrochemical impedance spectroscopy (EIS) from 100 kHz to 0.1 Hz at −0.9 V *vs*. RHE. Double layer capacitance (C_{dl}) was measured by conducting cyclic voltammetry between 0 and 0.1 V *vs*. SCE to evaluate the electrochemical surface area (ECSA) of an electrode. The double charge current density was plotted against the scan rates, and the linear fitting gave the C_{dl} value. All the potentials were converted to RHE using E (V *vs*. RHE) = E (V *vs*. SCE) + 0.241 + 0.0592 × pH. All the electrochemical data were obtained without *iR*-compensation if not mentioned.

3.1.2 Electrochemical measurements in flow cell

The electrochemical measurements were carried out in a custom-built flow cell configuration with catalysts coated gas diffusion layer (GDL, Sigracet 22 BB) as working electrode, Pt foil as counter

electrode, and SCE as reference electrode. The working electrode area was controlled at 1 cm^2. 1.0 M KOH was used as electrolyte and circulated through catholyte and anolyte chambers respectively with flow rate of 10 mL min^{-1} by a precision peristaltic pump (BINACA PUMPS). During the measurements, CO_2 gas was directly fed to the cathode GDL at a rate of 20 sccm.

3.1.3 Preparation of Working Electrodes

For the preparation of working electrodes for H-cell measurements, 10 mg catalyst powders and 5 mg carbon black (Vulcan XC-72) were dispersed in a solution containing 750 µl of isopropanol (IPA), 230 µl of deionized (DI) water and 20 µl of Nafion resin solution (5 wt %) with the help of ultrasonication to form catalyst ink. Then, dropping 50 µl the catalyst ink onto the one side of carbon paper (Toray TGP-H-060) to achieve a mass loading of 0.5 mg cm^{-2}. The electrode was then air-dried for 3 h before the test. For the preparation of working electrodes for flow-cell measurements, 10 mg catalyst powders and 10 mg carbon black were ultrasonically dissolved in a mixture solution of 1550 µl of IPA, 400 µl of DI water, and 50 µl of Nafion. Then, 200 µl of catalyst ink was drop cast on GDL to reach a mass loading of 1mg cm^{-2} and air-dried overnight.

3.1.4 Calculation

The FE of gas products was calculated using following equation:

$$FE_g\ (\%) = \frac{Q_g}{Q_{total}} \times 100\ \% = \frac{N_g \times F \times v \times \mathrm{V}_g/V_m}{I_{total}} \times 100\ \%$$

where, N_g and V_g represent the number of electrons transferred and the volume concentration of gas species generated, respectively. F is Faraday constant (96485 C mol^{-1}), v is CO_2 flow rate (20 ml min^{-1}), V_m is the molar volume of gas (24 L mol^{-1}), I_{total} is the steady-state current.

The FE of formate was calculated as follows:

$$FE_{formate}\ (\%) = \frac{Q_{formate}}{Q_{total}} \times 100\ \% = \frac{N_{formate} \times V_{formate} \times F}{I_{total} \times t} \times 100\ \%$$

where $N_{formate}$ and $V_{formate}$ is the number of electrons transferred to produce formate and the amount of formate generated, respectively. t (s) is the electrolysis time.

The formation rate of formate is calculated as below:

$$formate\ formation\ rate = \frac{Q_{total} \times FE_{formate}}{F \times N_{formate} \times t \times S}$$

where Q_{total} is the total passed charge to produce formate, t (h) is the electrolysis time and S (cm^2) is the geometric area of the working electrode.

The partial current density is calculated as follows:

$$j_{formate} = j \times FE_{formate}$$

where *j* is the total current density obtained from the chronoamperometry tests.

The energy efficiency is calculated as follows:

$$EE_{formate} = \frac{\Delta E^0_{formate} \times FE_{formate}}{\Delta E_{formate}} \times 100\%$$

where $\Delta E^0_{formate}$ is the difference between the standard half reaction potential for water oxidation and the ECR towards formate production, $\Delta E_{formate}$ is the difference between the standard water oxidation potential and the applied potential at cathode, respectively.

3.2 Materials characterizations

Scanning electron microscopy (SEM): SEM measurements were carried out on a high-resolution Zeiss Sigma field emission scanning electron microscope (FESEM) configured with an EBSD detector.

Transmission electron microscopy (TEM): The low and high-resolution TEM and energy-dispersive X-ray spectroscopy (EDX) measurements were taken using a JEOL JEM-ARM200CF transmission electron microscope at an accelerating voltage of 200/300 kV.

Atomic force microscopy (AFM): AFM measurements were conducted on a Keysight 5500 atomic force microscope.

X-ray diffraction (XRD): Powder XRD patterns were collected by a Rigaku Ultima IV diffractometer with Cu-Kα radiation (40 kV, 44 mA).

X-ray photoelectron spectroscopy (XPS): XPS measurements were recorded on Kratos AXIS Ultra spectrometer. All biding energy corresponds to the adventitious carbon (C 1s) at binding energy of 284.6 eV.

Ultraviolet photoelectron spectroscopy (UPS): UPS measurements were acquired on a physical Electronic PHI 5000 photoelectron spectrometer using He I (21.22 eV) ultraviolet radiation.

CO_2 adsorption: CO_2 adsorption isotherms were determined by an Autosorb Quantachrome 1MP apparatus.

Thermogravimetric analysis (TGA): TGA was performed from 20 to 800 ℃ at a heating rate of 10 ℃/min in air on TA SDT Q600.

Fourier transform infrared spectroscopy (FTIR): FTIR measurements were conducted on Nicolet 8700.

Water contact angle: Water contact angle measurements were performed on FTA-200.

CO_2 bubble adhesion: Contact angle goniometer (KRUSS DSA 10, Germany) equipped with high-speed camera was used to investigate the CO_2 bubble adhesion at room temperature. The sample was pinned onto a transparent quartz container using double-sided adhesive tape, and the container

was immersed into 0.5 M $KHCO_3$ solution upside down. An individual CO_2 bubble was pumped out from the syringe needle under solution to the electrode surface. At the same time, the software was started to record the image.

In situ Raman spectroscopy: *In situ* Raman measurements were performed using a Renishaw InVIa Raman system calibrated by standard silicon wafer (520 cm^{-1}). A 532 nm laser was used as the excitation source. During the test, CO_2 continued to flow into the electrolyte.

In situ X-ray absorption spectroscopy: A custom-built cell was used for measurement on Bi L-edge. The cell had the working, counter (carbon rod), and references electrodes (Ag/AgCl) as well as gas (CO_2, 99.999%) inlets and outlets. The catalysts were drop-cast on a 0.2 mm thick carbon paper electrode and dried overnight. A small window was cut out on the cathode side and sealed with Kapton film to allow fluorescence signals to pass through from the electrode to the detector. To record the *in situ* X-ray absorption near-edge structure (XANES) spectra, the cell was subsequently filled with electrolyte. The 0.5 M $KHCO_3$ aqueous solution was bubbled with CO_2 for 30 min before testing. The XANES spectra were collected under *in situ* conditions (applied potential from open circuit potential to −0.8 V *vs*. RHE) after 30 min electrolysis. The data were recorded on the VESPERS beamline of the Canadian Light Source in fluorescence mode.

Phenolphthalein color transition experiment: 20 µl phenolphthalein (0.05 M) in ethanol was added into the catholyte close to the electrode. After electrolysis at −1.2 V for 10 s, the color change near the electrode was recorded by camera.

Chapter 4. Electronic delocalization effects in CO_2 electrolysis

In the previous chapters, I introduced the ECR, summarized strategies to increase activity of main group metals, outlined the metrics by which ECR catalysts are evaluated, and described the challenges in ECR. In this chapter, I describe how S doping strategy can be used to induce electronic delocalization that enhances ECR.

S doping can regulate the electronic structure of catalysts and thus can boost electrocatalytic performance, e.g., it has been shown that S doping can increase the activities of HER, OER, and oxygen reduction reaction. In this chapter, I prepared a S doped Bi_2O_3 *in situ* grown on carbon nanotube catalyst, wherein the S incorporation resulted in an electron-rich Bi site. The delocalized electrons benefit the CO_2 adsorption and stabilize the *OCHO. I then show how the S doping promotes the formate production on Bi_2O_3 catalysts by conducting comprehensive electrochemical measurements. The resultant catalyst provides ECR with a maximum formate current density of 48.6 mA cm^{-2} and can maintain FE > 90% between −0.7 and −1.2 V *vs*. RHE.

The work in this chapter has been published as a full research paper titled "Electronic Delocalization of Bismuth Oxide Induced by Sulfur Doping for Efficient CO_2 Electroreduction to Formate" in *ACS Catalysis*, 2021, 11, 7604-7612. Text and figures have been reproduced here with permission from ACS. As the first author, I designed and synthesized the catalysts, performed materials characterizations and electrocatalysis experiments, and wrote the manuscript. Min-Rui Gao performed the DFT calculations and analysis.

Abstract: Developing efficient electrocatalysts for electrochemical CO_2 reduction (ECR) to fuels and chemicals with high product faradaic efficiency (FE) and current density is desirable but remains challenging. Herein, S doped Bi_2O_3 electrocatalysts coupled with carbon nanotube (S-

Bi_2O_3-CNT) are synthesized for efficient ECR to formate. The obtained S2-Bi_2O_3-CNT (with S doping amount of 0.7 at%) is highly active for formate production (FE> 90%) over a wide current density range (2.77 mA cm^{-2} – 48.6 mA cm^{-2}) and a maximum formate FE of 97.06 % can be achieved at –0.9 V. The significantly enhanced selectivity and activity originated from the fast electron transfer, enhanced CO_2 adsorption and more undercoordinated Bi sites induced by the S doping. More importantly, DFT calculations revealed that S doping can lead to an electronic delocalization of Bi, which benefits the binding of *CO_2 and *OCHO for ECR while significantly inhibiting the hydrogen evolution reaction (HER) *via* weakening the adsorption of *H and thus, help achieve the high current density and FE. This work paves a promising way to tuning ECR activities at atomic level.

4.1 Introduction

Electrochemical CO_2 reduction (ECR) to value-added fuels and chemical feedstocks driven by renewable energy sources (such as solar power and wind) is one promising approach to alleviating the ever-increasing atmospheric CO_2 concentration and the rapid fossil fuels consumption.[1-6] Among various products formed, formate is a very attractive product due to its wide applications in textile and pharmaceutical industries, and in fuel cells as the hydrogen carrier.[7-9] Various materials have been employed as electrocatalysts to produce formate *via* ECR.[10-16] Among them, Bi-based electrocatalysts have been widely investigated because of their cost-effectiveness, low toxicity, and high activity.[17-22] However, most reported Bi-based electrocatalysts do not simultaneously possess high activity (current density > 45 mA cm^{-2}) and high selectivity (faradaic efficiency (FE) > 90%) due to the significant enhancement of hydrogen evolution reaction (HER) at high current densities. Therefore, developing the Bi-based electrocatalysts with high formate selectivity at high current density is imperative yet challenging.

So far, great efforts have been devoted to improving the catalytic performance of Bi-based electrocatalysts, such as tuning the size,[23] regulating the morphology,[24] and engineering with other materials.[25-26] Among these strategies, electronic regulation of electrocatalysts *via* element doping has been regarded as a powerful strategy to enhance the electrochemical activity of ECR. The introduction of heteroatoms can regulate the electron density and thus, precisely modify the electronic structures of the active sites, resulting in optimal adsorption energy of the reaction intermediates. For example, N modified Sn achieved a high formate production through ECR because of the enhanced activity credited to the valence regulation of Sn by N modification.[27] Bi within the Bi-Sn bimetallic electrocatalysts could upshift the electron states of Sn away from the Fermi level, thus decreasing the energy barrier of *OCHO formation and facilitating formate production.[28]

Previous studies have demonstrated that S modification of electrocatalysts can modulate the electronic structure of electrocatalysts, thus boosting the electrocatalytic activity for HER,[29] oxygen evolution reaction,[30] and oxygen reduction reaction.[31] Moreover, S doping can increase the adsorption capacity of CO_2 and decrease the energy barrier for the formation of *OCHO intermediate.[32-33] To that end, S doping is expected to be an effective strategy to improve the catalytic performance of ECR by tuning the electronic structure. On the other hand, engineering electrocatalysts with conductive carbon materials (e.g. graphene, graphene quantum dots, carbon, carbon cloth and carbon paper) can greatly enhance the charge and mass transfers, and consequently boost the catalytic activity.[19-20, 34-35] However, the studies on fine-tuning the electronic structure of Bi-based electrocatalysts for ECR by S doping have rarely been reported so far; a comprehensive understanding of the S doping effect on the ECR activity is also lacking.

In this study, S doped Bi_2O_3 nanosheets (NSs) strongly coupled with carbon nanotube (S-Bi_2O_3-CNT) were prepared to improve the activity for ECR to produce formate. Benefiting from the optimized electronic structure of Bi_2O_3, the prepared S2-Bi_2O_3-CNT with the S doping amount of 0.7 at% not only shows a high catalytic activity for CO_2 to formate conversion through ECR, but also can simultaneously maintain high FE of formate ($FE_{formate}$) at high current density. With a long-term stability, the $FE_{formate}$ can be stably kept at over 90% in a current density range from 2.77 mA cm^{-2} to 48.6 mA cm^{-2}, which outperforms most of previously reported electrocatalysts. Experimental characterizations and computational analysis suggest that this high catalytic activity can be attributed to the electronic delocalization of Bi induced by S doping, which can enhance the adsorption of CO_2, stabilize *CO_2 and *OCHO intermediates while hindering the adsorption of *H, thus suppressing HER and promoting the formate production.

4.2 Results and discussion

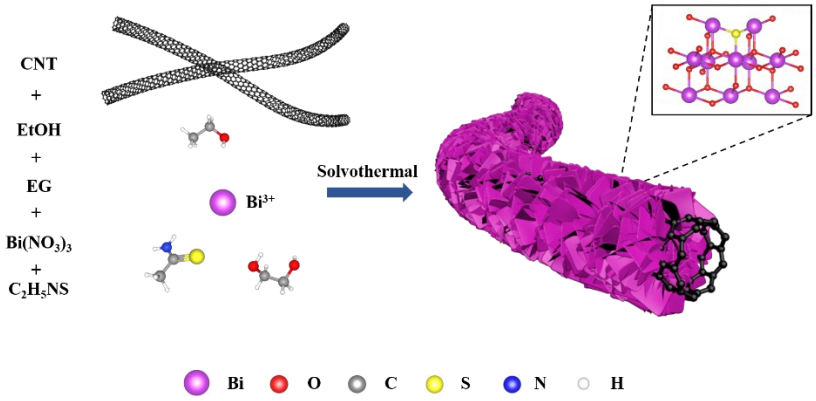

Figure 4.1 Illustration of the S-Bi_2O_3-CNT preparation process.

4.2.1 Synthesis and characterization of S-Bi_2O_3-CNT catalyst

The S-Bi_2O_3-CNT was prepared by a one-step solvothermal method as illustrated in Figure 4.1 Typically, different amounts of thioacetamide and a certain amount of bismuth nitrate pentahydrate were mixed in a solution containing ethanol and ethylene glycol, followed by heating at 160 ^oC for 5 hours. Pristine Bi_2O_3 NSs were also synthesized for comparison through the similar method except for the addition of CNT and thioacetamide. The as-prepared electrocatalysts with different amounts of S (0, 0.3, 0.7, 1.2 and 1.7 at%, determined by energy dispersive X-ray (EDX) mapping spectroscopy), were denoted as Bi_2O_3-CNT, S1-Bi_2O_3-CNT, S2-Bi_2O_3-CNT, S3-Bi_2O_3-CNT, and S4-Bi_2O_3-CNT, respectively. To reveal the morphological and structural information, scanning electron microscopy (SEM), transmission electron microscopy (TEM) and X-ray diffraction (XRD) were performed on the prepared electrocatalysts.

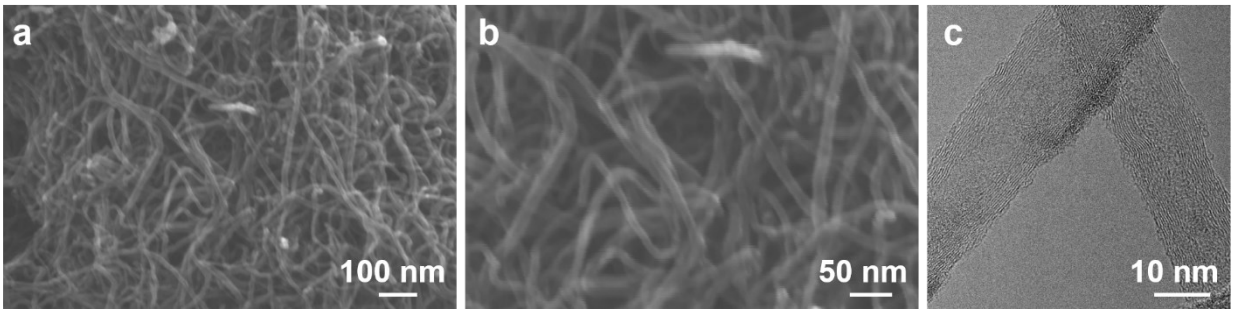

Figure 4.2 (a, b) SEM images of CNT. (c) TEM image of CNT.

Clearly, compared to the smooth CNT (Figure 4.2), Bi_2O_3 NSs are uniformly grown on the CNT surface after solvothermal process (Figure 4.3a-d; Figure S4.1). It is found that the samples with S amount from 0 to 1.2 at% possess a similar NSs morphology, whereas excessive S amount (1.7 at%) can result in adhesion of the NSs (Figure S4.1i-l). A higher resolution TEM image of an individual S2-Bi_2O_3-CNT (Figure 4.3e) shows that the NSs are densely grafted on CNT surface with ≈ 50 nm in width and only a few nanometers in thickness. The crystal lattice analyses of the

selected square regions in high resolution transmission electron microscopy images (HRTEM; Figure 4.3f, g and Figure S4.2) show that the same interplanar spacing of 0.38 nm was observed on both Bi_2O_3-CNT and S-Bi_2O_3-CNT, which can be assigned to the (110) plane of cubic Bi_2O_3. This indicates that the (110) facet of Bi_2O_3 NSs is preferentially exposed, and the corresponding ordered selected-area electron-diffraction pattern (SAED) suggests that the Bi_2O_3 NSs are highly crystalline (insert in Figure 4.3f). Moreover, the uniform distribution of Bi, O, and S on the surface of S2-Bi_2O_3-CNT can be verified by scanning TEM-energy-dispersive X-ray spectroscopy (STEM-EDX) mapping (Figure 4.3h-l). The diffraction peaks of S-Bi_2O_3-CNT XRD patterns (Figure 4.4a) can be indexed to the cubic phase of Bi_2O_3 (JCPDS No. 27-0052), indicating the successful preparation of Bi_2O_3 NSs. The thermal gravimetric analysis (TGA) in air (Figure 4.4b) shows that the loading of CNTs in the hybrid is estimated to be 30 wt%.

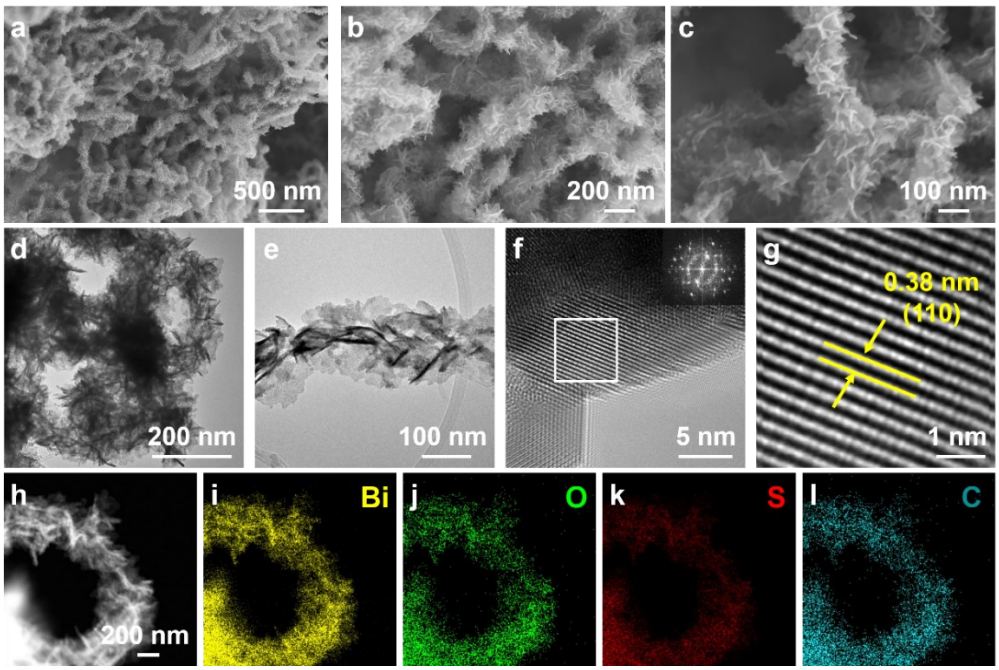

Figure 4.3 (a-c) FESEM images of S2-Bi_2O_3-CNT with different magnifications. (d-g) TEM images of S2-Bi_2O_3-CNT with different magnifications. (h-l) The HAADF-STEM images of S2-Bi_2O_3-CNT and corresponding elemental maps of Bi, O, S, and C.

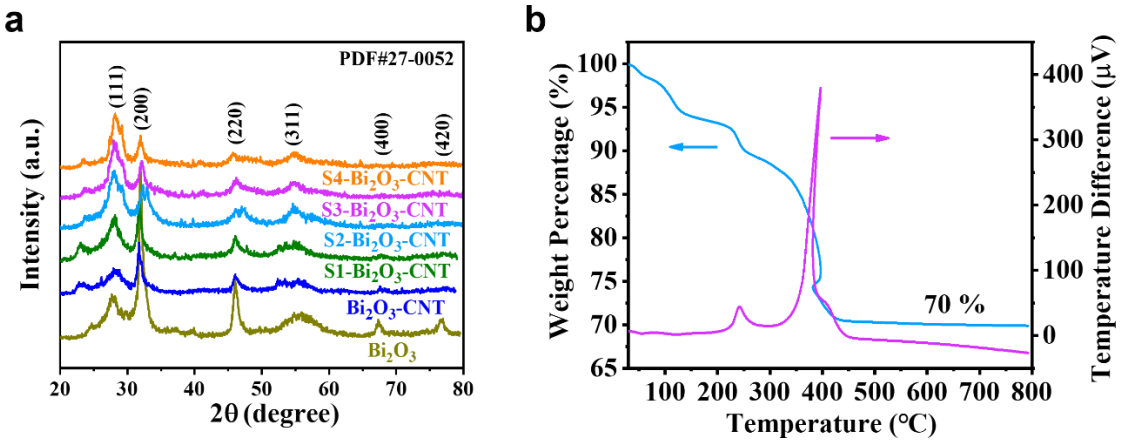

Figure 4.4 (a) XRD patterns of Bi_2O_3, Bi_2O_3-CNT, S1-Bi_2O_3-CNT, S2-Bi_2O_3-CNT, S3-Bi_2O_3-CNT, and S4-Bi_2O_3-CNT. (b) Weight loss and differential thermal analysis for S2-Bi_2O_3-CNT determined by the thermogravimetric analysis (TGA) in air.

To further investigate the composition and chemical state of S-Bi_2O_3-CNT electrocatalysts, the X-ray photoelectron spectroscopy (XPS) and X-ray absorption near-edge structure spectroscopy (XANES) were conducted. As shown in the high-resolution Bi 4f spectra (Figure 4.5a), two main peaks located at 164.9 and 159.6 eV are attributed to Bi $4f_{5/2}$ and Bi $4f_{7/2}$, respectively. For S doped samples, a small peak at 160.4 eV can be observed and could be assigned to S^{2-} in sulfides,[36] suggesting that S was most likely to take the O sites of Bi_2O_3. The decrease of lattice O intensity in S doped samples (Figure 4.6a and Table S4.1) further confirmed the partial replacement of lattice O by S atom in Bi_2O_3.[37] Moreover, the incorporation of S brings about a negative shift of approximately 0.3 eV for the peak of Bi $4f_{7/2}$, indicating a higher electron density around Bi atoms after S doping. It is well-known that the electronegativity of S is lower than that of O, implying that the withdrawing-electron capacity of S from the bonded Bi is weaker than that of O. This leads to fewer electrons of Bi to participate in Bi-S boning and consequently results in a lower oxidation state of Bi in S doped Bi_2O_3. The XANES measurements for S2-Bi_2O_3-CNT before the ECR display a negative shift compared to the Bi_2O_3-CNT in Bi L-edge (Figure 4.5b). This signifies a

lower valence state of Bi in the S2-Bi_2O_3-CNT than that in the Bi_2O_3-CNT, which is in a good agreement with the XPS results (Figure 4.5a). The L-edge of Bi_2O_3-CNT is similar to that of pure Bi_2O_3, suggesting the negative shift of S2-Bi_2O_3-CNT is induced by S doping rather than CNT introduction. In comparison to the S2-Bi_2O_3-CNT prior to ECR, the absorption onset of the Bi L-edge shifts toward lower energy for S2-Bi_2O_3-CNT after ECR and the absorption edge energies are lower than that in Bi_2O_3, but higher than that in metallic Bi, which indicates that chemical states of Bi in S2-Bi_2O_3-CNT after ECR are between Bi^0 and Bi^{3+}. The Fourier transformed K^2-weighted extended X-ray adsorption fine structure (EXAFS) spectra of S2-Bi_2O_3-CNT are similar to that Bi_2O_3-CNT (Figure 4.5c), where the strongest peaks correspond to the Bi-O peak.[38] Notably, the Bi-O peak for S2-Bi_2O_3-CNT (1.61 Å) displays a minor shift compared with Bi_2O_3-CNT (1.57 Å) along with a decrease in the peak density, which is possibly ascribed to the longer Bi-S length and the reduced O coordination number of Bi due to the existence of Bi-S bonds. The EXAFS curve-fitting results were exhibited in Figure 4.6b, c and Table S4.2. It is noted that the Bi coordination number (CN) from Bi−O shell of S2-Bi_2O_3-CNT is calculated to be 4.79, which is smaller compared with the value for Bi_2O_3-CNT (CN=5). This indicates the existence of undercoordinated Bi atoms in S2-Bi_2O_3-CNT. Moreover, the absorption edge of Bi L-edge of S2-Bi_2O_3-CNT after ECR (Figure 4.5d) shifts to higher energy compared to Bi_2O_3 after ECR (edge shift indicated by the red arrow), indicating a higher oxidation state of Bi in S2-Bi_2O_3-CNT than that in Bi_2O_3 after ECR. This implies that Bi in S2-Bi_2O_3-CNT after ECR was much easier to be oxidized to higher valence after exposure to air than the Bi in Bi_2O_3 after ECR. This is probably because the S2-Bi_2O_3-CNT possesses more undercoordinated Bi atoms than the Bi_2O_3 control sample, and previous studies have revealed that the undercoordinated atoms are the active ones for

ECR.[39-41] The XPS results together with XANES analysis reveal that S doping indeed modulates the electronic structure of Bi_2O_3.

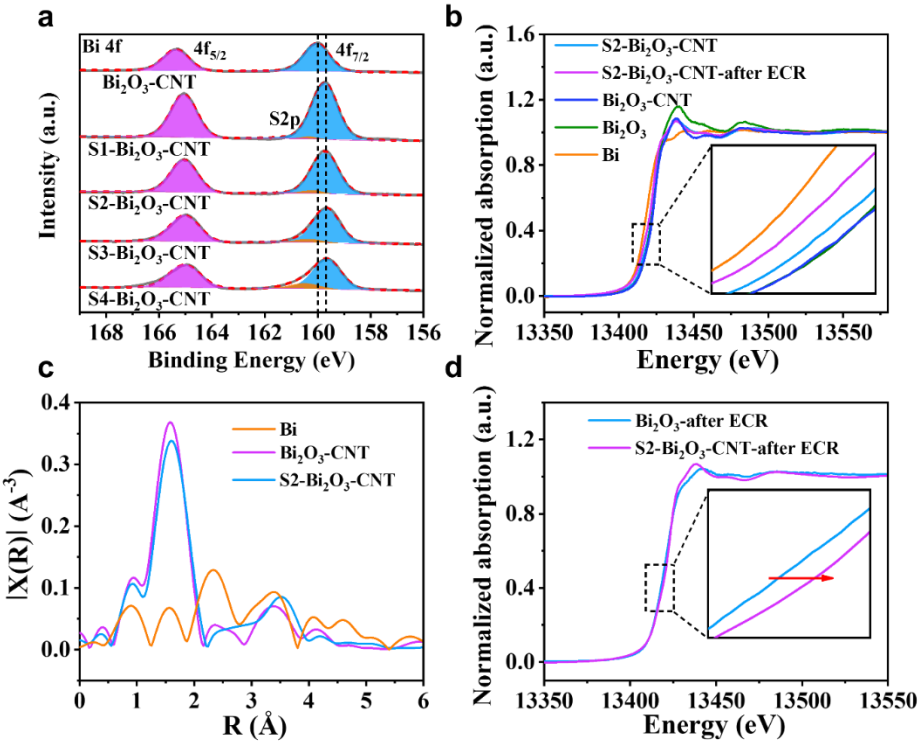

Figure 4.5 (a) Bi 4f XPS spectra of Bi_2O_3-CNT, S1-Bi_2O_3-CNT, S2-Bi_2O_3-CNT, S3-Bi_2O_3-CNT, and S4-Bi_2O_3-CNT. (b) Bi L-edge XANES spectra of S2-Bi_2O_3-CNT, Bi_2O_3-CNT, Bi_2O_3, and Bi. (c) Fourier transforms of K^2-weighted EXAFS data for the Bi L-edge of S2-Bi_2O_3-CNT, Bi_2O_3, and Bi. (d) Bi L-edge XANES spectra for S2-Bi_2O_3-CNT and Bi_2O_3 after ECR.

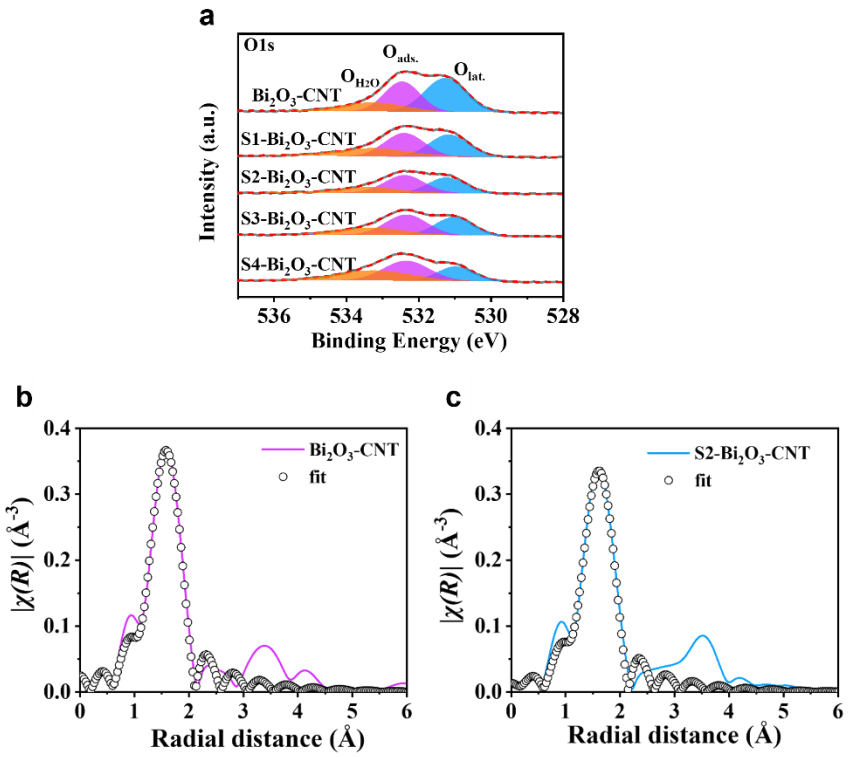

Figure 4.6 (a) O 1s XPS spectra of Bi_2O_3-CNT, S1-Bi_2O_3-CNT, S2-Bi_2O_3-CNT, S3-Bi_2O_3-CNT, and S4-Bi_2O_3-CNT. Fourier transforms of K^2-weighted EXAFS and the corresponding fitting data for Bi L-edge of (b) Bi_2O_3-CNT and (c) S2-Bi_2O_3-CNT.

4.2.2 ECR measurements on S-Bi_2O_3-CNT

The ECR catalytic performance of Bi_2O_3-CNT and S doped samples was first investigated by linear sweep voltammetry (LSV) in CO_2-saturated 0.5 M $KHCO_3$ within an H-type cell. All potentials mentioned in this work are referred to the reversible hydrogen electrode (RHE). For comparison, the electrocatalytic performance of pristine Bi_2O_3 and CNT was also measured. The LSV curves (Figure 4.7a) show that Bi_2O_3 and other Bi_2O_3 containing electrocatalysts exhibit much higher current densities and more positive onset potential than CNT, excluding the possibility that the superior electrochemical ECR catalytic activities are from the CNT support. Notably, the S2-Bi_2O_3-CNT demonstrates the highest current densities across the entire tested potential range among all the investigated materials. To further evaluate the ECR catalytic activity

of S2-Bi_2O_3-CNT, a controlled potential electrolysis at each given potential was conducted. The gas-phase and liquid-phase products were quantitatively determined by gas chromatography (GC) and ionic chromatography (IC), respectively. The results show that formate is detected to be the predominant product with minor amounts of CO and H_2 (Figure S4.3). As shown in Figure 4.7b, compared to other Bi_2O_3 containing electrocatalysts, the S2-Bi_2O_3-CNT exhibits the highest formate selectivity across the entire tested potential range, and maintains its $FE_{formate}$ > 90% in a wide potential range from −0.7 V to −1.2 V. Specifically, the S2-Bi_2O_3-CNT delivered the highest $FE_{formate}$ of 97.06% at −0.9 V (Figure 4.7c) among all the investigated materials (90.72% for S3-Bi_2O_3-CNT, 89.51% for S4-Bi_2O_3-CNT, 86.94% for S1-Bi_2O_3-CNT, 82.37% for Bi_2O_3-CNT, and 81.59% for Bi_2O_3). Furthermore, the partial current densities for formate ($j_{formate}$) and the formate formation rate are derived. The S2-Bi_2O_3-CNT achieves a $j_{formate}$ of −48.64 mA cm^{-2} at −1.2 V, four times higher than that of pristine Bi_2O_3 (−11 mA cm^{-2}). Naturally, S2-Bi_2O_3-CNT shows the highest formate formation rate among all the control samples, reaching up to 906 μmol h^{-1} cm^{-2} at −1.2 V (Figure 4.8a). More interestingly, this S doping strategy can be extended to other formate producing oxides (such as SnO_2 and In_2O_3). The S doped catalysts (S-SnO_2 and S-In_2O_3) exhibit the enhanced $FE_{formate}$ and $j_{formate}$ over un-doped catalysts (Figure S4.4). This suggests the generality of this S doping strategy for improving formate production. For better comparison, the relationship between the $j_{formate}$ and the $FE_{formate}$ is also derived. Remarkably, the high $FE_{formate}$ (> 90 %) of S2-Bi_2O_3-CNT can be maintained in a wide range of current densities from −2.77 mA cm^{-2} to −48.64 mA cm^{-2} (Figure 4.8b). By contrast, the maximum $FE_{formate}$ of Bi_2O_3 is 81.59 % at −9.33 mA cm^{-2} and then drops significantly to only 36.67 % at −11.33 mA cm^{-2}. The energy efficiency (EE) for formate production was determined to evaluate the energy conversion efficiency (Figure S4.5). The S2-Bi_2O_3-CNT achieved the highest EE (63 %) at −0.7 V among all

investigated materials. Consequently, the catalytic performance of S2-Bi_2O_3-CNT makes it stand out among the recently reported electrocatalysts for ECR toward formate (Table S4.3).

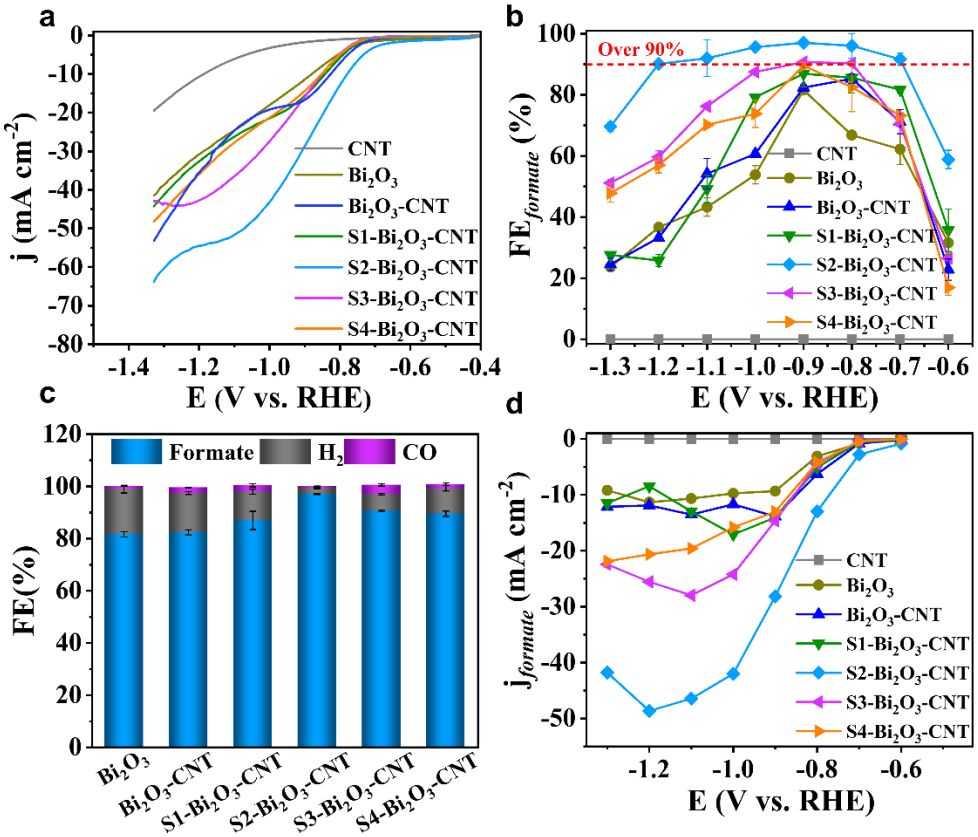

Figure 4.7 (a) LSVs of different electrocatalysts (CNT, Bi_2O_3, Bi_2O_3-CNT, S1-Bi_2O_3-CNT, S2-Bi_2O_3-CNT, S3-Bi_2O_3-CNT, and S4-Bi_2O_3-CNT) in CO_2-saturated 0.5 M $KHCO_3$. (b) FE of formate of different electrocatalysts at different potentials. (c) FE of all products for different catalysts at −0.9 V. (d) $j_{formate}$ for different electrocatalysts.

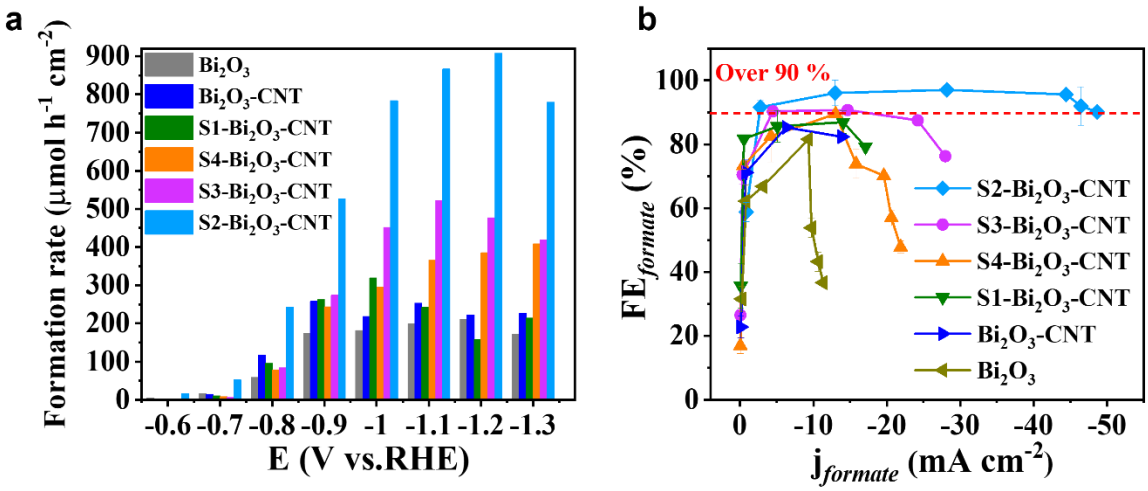

Figure 4.8 (a) Formate formation rate for Bi_2O_3, Bi_2O_3-CNT, S1-Bi_2O_3-CNT, S2-Bi_2O_3-CNT, S3-Bi_2O_3-CNT, and S4-Bi_2O_3-CNT at different potentials. (b) Plot of FE of formate versus current density for Bi_2O_3, Bi_2O_3-CNT, S1-Bi_2O_3-CNT, S2-Bi_2O_3-CNT, S3-Bi_2O_3-CNT, and S4-Bi_2O_3-CNT.

To investigate the effect of S on the improved ECR catalytic activity, the reaction kinetics of Bi_2O_3 and S doped samples was examined *via* Tafel plot. A Tafel slope of 117 mV dec^{-1} was observed on S2-Bi_2O_3-CNT (Figure 4.9a and Figure S4.6), which is close to the theoretical value of 118 mV dec^{-1}, suggesting that the first electron transfer should be the rate-determining step (RDS).[42] Moreover, the Tafel slope for S2-Bi_2O_3-CNT is much smaller than the values for Bi_2O_3 (187 mV dec^{-1}), Bi_2O_3-CNT (183 mV dec^{-1}) and other S doped samples, indicating a faster electron transfer rate on S2-Bi_2O_3-CNT. The electrochemical impedance spectroscopy measurements were carried out to evaluate the charge transfer process (Figure 4.9b). Apparently, the charge transfer resistance (R_{ct}) of Bi_2O_3-CNT (11.2 Ω) is lower than that of Bi_2O_3 (16.6 Ω), which underlines the advantage of CNT. The introduction of S further accelerates the charge transfer process, evidenced by the smaller R_{ct} (8.6 Ω) for S2-Bi_2O_3-CNT. However, the R_{ct} showed an increasing trend when the S amount was further increased. It has been reported that the thinner nanosheets are more beneficial to the rapid migration of charge carriers to the surface of the electrocatalyst.[43] Therefore, the

performance degradation observed over S3-Bi_2O_3-CNT and S4-Bi_2O_3-CNT can be attributed to the excessive S which will result in agglomeration (Figure S4.1).

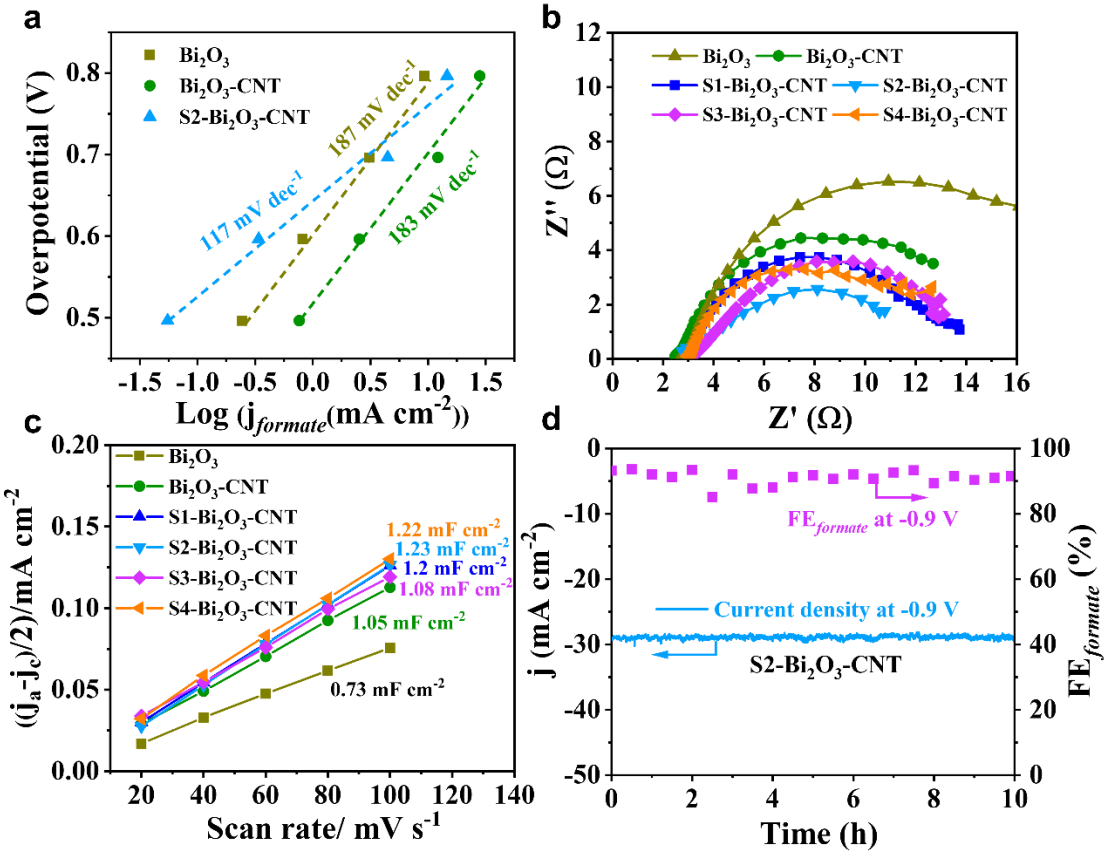

Figure 4.9 (a) Tafel plots of Bi_2O_3, Bi_2O_3-CNT, and S2-Bi_2O_3-CNT. (b) Electrochemical impedance spectra (EIS) of different electrocatalysts (Bi_2O_3, Bi_2O_3-CNT, S1-Bi_2O_3-CNT, S2-Bi_2O_3-CNT, S3-Bi_2O_3-CNT, and S4-Bi_2O_3-CNT). (c) Double-layer capacitance (C_{dl}) of different electrocatalysts. (d) Long-term stability for S2-Bi_2O_3-CNT.

The double-layer capacitance (C_{dl}) of the samples (Figure 4.9c; Figure S4.7; Table S4.4) was measured to estimate the electrochemical surface area (ECSA). The ECSA of Bi_2O_3 (36.5 cm^2) increases significantly to 52.5 cm^2 for Bi_2O_3-CNT because the one-dimensional CNT could avoid the agglomeration of Bi_2O_3 NSs. The S doped samples show a delicately increased ECSA compared to Bi_2O_3-CTN. However, the electrocatalytic ECR activity for S2-Bi_2O_3-CNT is

enhanced more than 4 times vs Bi_2O_3-CNT, implying that the enhanced activity is not due to the delicately increased ECSA. The durability of the S2-Bi_2O_3-CNT was evaluated by the long-term electrolysis experiments at −0.9 V for 10 hours (Figure 4.9d). Obviously, a very stable current density of −28 mA cm^{-2} together with an average $FE_{formate}$ of 90% was maintained over 10h of continuous electrolysis, indicating a remarkable durability of S2-Bi_2O_3-CNT for ECR. The remarkable durability of S2-Bi_2O_3-CNT was further confirmed by the minor variation of its SEM images post the 10h electrolysis (Figure S4.8). Post-electrolysis XRD measurement was also conducted, where a mixture of dominant $Bi_2O_2CO_3$ and minor metallic Bi can be observed (Figure S4.9). Similar phenomenon for Bi_2O_3 was also observed by previous studies.[19, 44]

The CO_2 adsorption isotherms were carried out to explore the reason for the enhanced electrocatalytic ECR performance of S2-Bi_2O_3-CNT (Figure 4.10a). The Bi_2O_3-CNT exhibits a higher CO_2 adsorption capacity than pristine Bi_2O_3 and CNT, indicating that the integration of Bi_2O_3 with CNT benefits the CO_2 adsorption. This can be attributed to 1) the enhanced accessibility of CO_2 molecules to the Bi_2O_3 NSs by improving the distribution of Bi_2O_3 NSs and avoiding agglomeration; 2) the hollow and disordered structure of CNT provides a large amount of sites for CO_2 capture; 3) the surface oxygen-containing groups on CNT can provide electron-trapping sites, further facilitating CO_2 adsorption.[45] Furthermore, S2-Bi_2O_3-CNT achieves a CO_2 adsorption capacity of 1062 μmol g^{-1} at 25 ℃ under 1 atm (1.43 and 3.54 times higher than the values for Bi_2O_3-CNT and Bi_2O_3, respectively), suggesting that S doping enhances the CO_2 adsorption. This increased CO_2 adsorption amount could provide sufficient reactants to further the CO_2 reduction process, which optimizes the activity and selectivity. To understand the effect of S doping on the electronic state, the ultraviolet photoemission spectroscopy (UPS) study was performed. The normalized secondary electron cutoff energy (E_{cutoff}) and onset energy (E_{onset}) are determined by

UPS data (Figure 4.10b, c). The work functions (Φ) of Bi_2O_3-CNT and S-Bi_2O_3-CNT can be calculated as $\Phi = hv - (E_{cutoff} - E_{onset})$,[46] where hv is the photon energy of the excitation light (21.22 eV). Clearly, the S2-Bi_2O_3-CNT possesses a smaller work function than Bi_2O_3-CNT (Figure 4.10d). The decreased work function accounted for the faster electron transfer from the surface of S2-Bi_2O_3-CNT to the adsorbed CO_2 and reaction intermediates (coinciding well with the EIS results), thereby enhancing the catalytic activity for ECR. Therefore, doping S into Bi_2O_3 strengthens the adsorption of CO_2 and accelerates the electron transfer between electrocatalysts and the reaction intermediates, thus boosting the electrochemical ECR to formate.

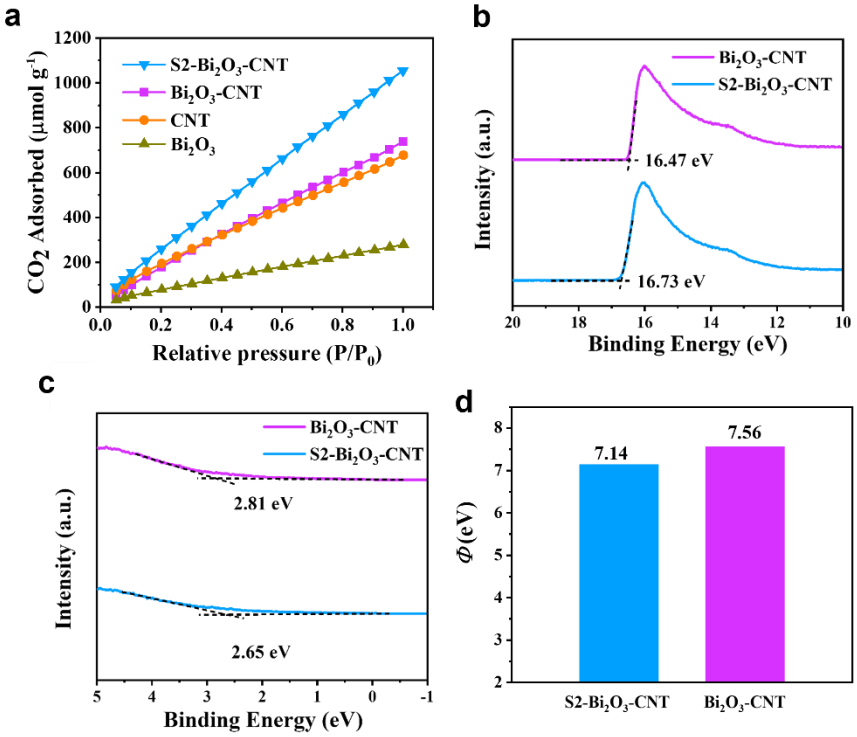

Figure 4.10 (a) CO_2 adsorption isotherms of S2-Bi_2O_3-CNT, Bi_2O_3-CNT, CNT, and Bi_2O_3. UPS spectra (b) in the normalized secondary electron cutoff energy (E_{cutoff}) regions and (c) in the onset (E_{onset}) energy regions of Bi_2O_3-CNT and S2-Bi_2O_3-CNT. (d) Calculated work function (Φ) stemming from UPS analysis.

4.2.3 Mechanics analysis

To further shed light on the promoting effect of S on Bi_2O_3 surfaces, the density functional theory (DFT) calculations were performed, and the results are summarized in Table S4.5. According to the TEM analysis (Figure 4.3g and Figure S4.2e-h), the Bi_2O_3 and S-Bi_2O_3 preferentially expose the (110) facet. Thus, we calculated the optimized adsorption structures and energetics of *CO_2, *COOH, *OCHO, *CO, and *HCOOH for ECR, as well as *H for HER, on (110) facet of Bi_2O_3 and S-Bi_2O_3. Apparently, the Gibbs free energy (ΔG) for the formation of *COOH (intermediate for CO pathway) is higher than that of *OCHO (intermediate for formate pathway) on both pure Bi_2O_3 and S-Bi_2O_3 surface (Figure 4.11a, b), suggesting that the formate pathway is more energy-favorable than CO pathway, which explains why the FE of formate is higher than that of CO on both Bi_2O_3 and S-Bi_2O_3. The formation of *CO_2 intermediate is an endothermic process on Bi_2O_3 surface while such process on S-Bi_2O_3 surface is exothermic instead, indicating that the *CO_2 intermediate is energetically favorable to be adducted on the S doped Bi_2O_3 surface than on Bi_2O_3 surface. Moreover, the *OCHO is more stable on S doped Bi_2O_3 than on Bi_2O_3, as confirmed by the more negative ΔG. To further investigate this, charge density distribution and Bader charge analysis were performed. According to the partial charge density (Figure 4.11c), the substitution of O for lower electronegative S causes distortion of neighboring Bi, and the charge density of Bi in S doped Bi_2O_3 increases compared with Bi_2O_3, which is consistent with the XPS and XANES results. For S doped Bi_2O_3, fewer electrons of Bi were transferred to adjacent S and O (ΔQ = 0.1512, Table S4.6), resulting in an electronic delocalization. The delocalized electrons around Bi are beneficial for CO_2 adsorption *via* donation of electrons to form *CO_2 intermediate. Furthermore, the adsorbed *OCHO on single Bi would shift to the electron delocalization region

of the neighboring Bi and hence automatically reached a more stable configuration (Figure 4.11d), thus enabling the favorable formation of *OCHO.

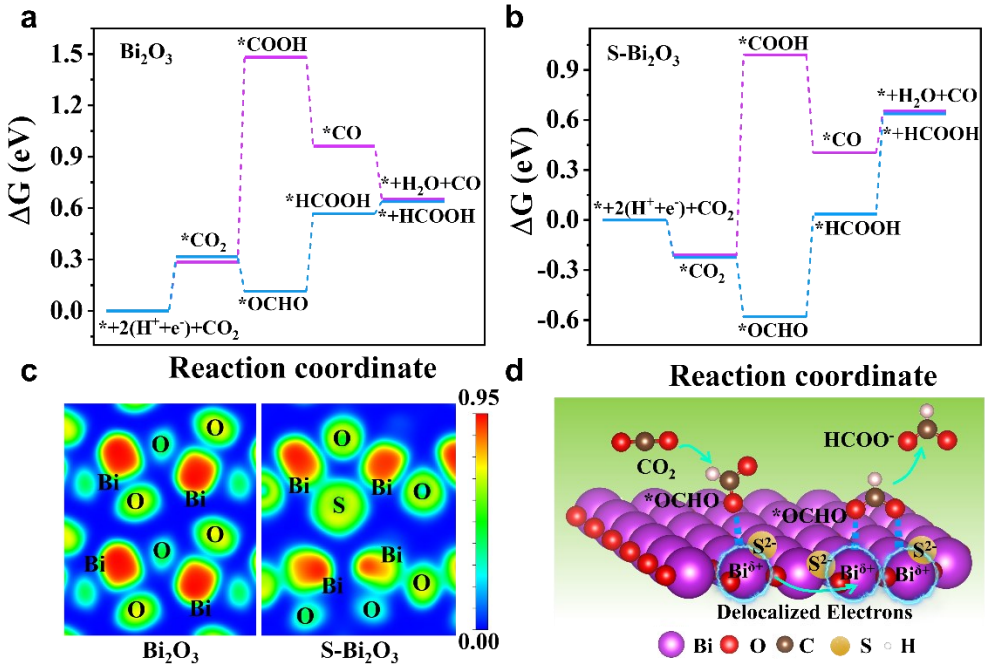

Figure 4.11 Gibbs free energy diagrams for ECR to CO and formate on (a) Bi_2O_3 (110) and (b) S-Bi_2O_3 (110) surface. (c) Charge density distribution of Bi_2O_3 and S-Bi_2O_3. (d) Schematic illustration for the role of S in promoting the reduction of CO_2 to formate.

In addition, the Gibbs free energy diagram for HER on Bi_2O_3 and S-Bi_2O_3 surface was also presented (Figure 4.12a), the energy barriers for HER over both O and S sites of S-Bi_2O_3 are higher than that over O site of Bi_2O_3, suggesting that HER is indeed inhibited after S doping. This is in good agreement with the experimental observed much lower H_2 selectivity over S2-Bi_2O_3-CNT. It is well known that the limiting potential (P_{limit}) difference between ECR and HER (ΔP_{limit}) is strongly correlated with the formate selectivity, and a more positive ΔP_{limit} indicates a higher formate selectivity. The P_{limit} is defined as the lowest potential that makes all reaction steps downhill in free energy, which is calculated as $P_{limit} = -\Delta G_0/e$; ΔG_0 is the energy barrier for the

limiting step.[47-48] The S-Bi_2O_3 exhibits a more positive ΔP_{limit} (−0.3 V) than that of Bi_2O_3 (−0.6 V) (Figure 4.12b), which is consistent with the experimental results. The density of state results (Figure 4.12c) reveal that the *d*-band center of S-Bi_2O_3 shifts upward from −2.96 eV (Bi_2O_3) to −2.62 eV, suggesting the modulated electronic states after S doping. As suggested by *d*-band theory,[49-50] this favorable upward shift of *d*-band center observed on S doped Bi_2O_3 benefits the ECR reaction, because the upward shift of *d*-band center pushes more anti-banding states above the Fermi level. This strengthens the adsorption of CO_2 and improves the binding strength of $*CO_2$ intermediate and thus, achieves a high ECR performance, which is in accordance with the Gibbs free energy analysis. On the basis of the experimental and computational results, such impressive ECR performance of S2-Bi_2O_3-CNT electrocatalyst can be attributed to several factors induced by the S doping: (i) the generated undercoordinated Bi sites provide more active sites for ECR; (ii) the enhanced CO_2 adsorption capacity facilitates the CO_2 activation process; (iii) the decreased work function enables faster electron transfer; (iv) the electronic delocalization of Bi stabilizes the *OCHO while hindering the adsorption of *H, thus simultaneously contributing to the high activity and high selectivity for ECR to formate. In this situation, the S doping strategy reported here effectively overcomes the problem that the formate FE loses to H_2 production at high current density, and this approach could inspire more creative ideas for the design of metal-based electrocatalysts for ECR processes which usually suffer from the same issue.

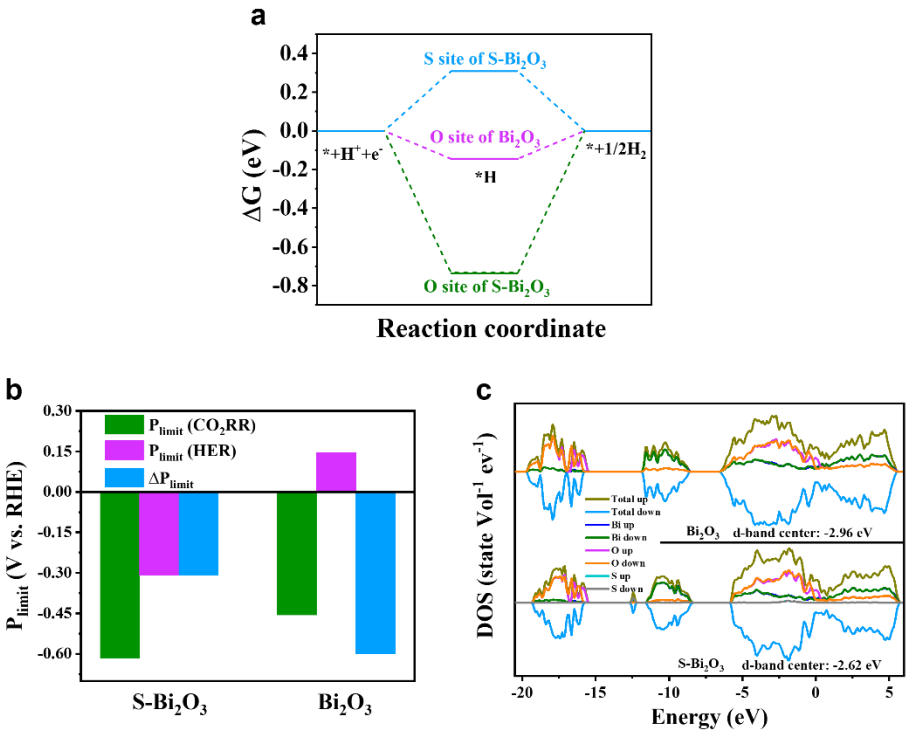

Figure 4.12 (a) Gibbs free energy diagram for HER on O site of Bi_2O_3, S and O sites of S-Bi_2O_3. (b) Calculated limiting potentials for ECR, HER, and their difference on Bi_2O_3 and S-Bi_2O_3. (c) Calculated densities of states (DOS) of Bi_2O_3 and S-Bi_2O_3 with the Fermi level aligned at 0 eV.

4. 3 Conclusions

In conclusion, S doped Bi_2O_3 coupled with CNT electrocatalysts have been successfully synthesized through a simple one-step hydrothermal method. The introduction of S dopants into Bi_2O_3 nanosheets considerably enhanced the catalytic activity for ECR to formate with high FE over a wide potential range, and also achieved high partial current density and good long-term stability. Experimental results and a series of characterizations highlighted the advantages of S doping which facilitates electron transfer, increases the adsorption of CO_2 and offers more undercoordinated Bi sites. Moreover, DFT results reveal that S doping induced the electronic delocalization of Bi sites, which optimized the adsorption of *CO_2 and *OCHO intermediates while hindering the adsorption of *H. Therefore, S doped Bi_2O_3 promotes the ECR to formate by

suppressing the competitive HER simultaneously. This work opens up an attractive avenue for developing highly efficient electrocatalyst for ECR at atomic level.

4.4 References

1. Nielsen, D. U.; Hu, X.-M.; Daasbjerg, K.; Skrydstrup, T., Chemically and electrochemically catalysed conversion of CO_2 to CO with follow-up utilization to value-added chemicals. *Nat. Catal.* 2018, *1* (4), 244-254.
2. Ross, M. B.; De Luna, P.; Li, Y.; Dinh, C.-T.; Kim, D.; Yang, P.; Sargent, E. H., Designing materials for electrochemical carbon dioxide recycling. *Nat. Catal.* 2019, *2* (8), 648-658.
3. Scofield, M. E.; Koenigsmann, C.; Wang, L.; Liu, H.; Wong, S. S., Tailoring the composition of ultrathin, ternary alloy PtRuFe nanowires for the methanol oxidation reaction and formic acid oxidation reaction. *Energy Environ. Sci.* 2015, *8* (1), 350-363.
4. Qiao, J.; Liu, Y.; Hong, F.; Zhang, J., A review of catalysts for the electroreduction of carbon dioxide to produce low-carbon fuels. *Chem. Soc. Rev.* 2014, *43* (2), 631-675.
5. Chen, Y.; Kanan, M. W., Tin oxide dependence of the CO_2 reduction efficiency on tin electrodes and enhanced activity for tin/tin oxide thin-film catalysts. *J. Am. Chem. Soc.* 2012, *134* (4), 1986-1989.
6. Centi, G.; Quadrelli, E. A.; Perathoner, S., Catalysis for CO_2 conversion: a key technology for rapid introduction of renewable energy in the value chain of chemical industries. *Energy Environ. Sci.* 2013, *6* (6), 1711-1731.
7. Ji, X.; Lee, K. T.; Holden, R.; Zhang, L.; Zhang, J.; Botton, G. A.; Couillard, M.; Nazar, L. F., Nanocrystalline intermetallics on mesoporous carbon for direct formic acid fuel cell anodes. *Nat. Chem.* 2010, *2* (4), 286-293.
8. Ding, J.; Liu, Z.; Liu, X.; Liu, J.; Deng, Y.; Han, X.; Zhong, C.; Hu, W., Mesoporous decoration of freestanding palladium nanotube arrays boosts the electrocatalysis capabilities toward formic acid and formate oxidation. *Adv. Energy Mater.* 2019, *9* (25), 1900955.
9. Fan, L.; Xia, C.; Zhu, P.; Lu, Y.; Wang, H., Electrochemical CO_2 reduction to high-concentration pure formic acid solutions in an all-solid-state reactor. *Nat. Commun.* 2020, *11* (1), 1-9.

10. Zhou, Y.; Zhou, R.; Zhu, X.; Han, N.; Song, B.; Liu, T.; Hu, G.; Li, Y.; Lu, J.; Li, Y., Mesoporous PdAg nanospheres for stable electrochemical CO_2 reduction to formate. *Adv. Mater.* 2020, *32* (30), 2000992.

11. Jiang, B.; Zhang, X.-G.; Jiang, K.; Wu, D.-Y.; Cai, W.-B., Boosting formate production in electrocatalytic CO_2 reduction over wide potential window on Pd surfaces. *J. Am. Chem. Soc.* 2018, *140* (8), 2880-2889.

12. Zhang, X.; Sun, X.; Guo, S.-X.; Bond, A. M.; Zhang, J., Formation of lattice-dislocated bismuth nanowires on copper foam for enhanced electrocatalytic CO_2 reduction at low overpotential. *Energy Environ. Sci.* 2019, *12* (4), 1334-1340.

13. Liu, S.; Xiao, J.; Lu, X. F.; Wang, J.; Wang, X.; Lou, X. W., Efficient electrochemical reduction of CO_2 to HCOOH over sub-2 nm SnO_2 quantum wires with exposed grain boundaries. *Angew. Chem., Int. Ed.* 2019, *58* (25), 8499-8503.

14. Jiang, Z.; Wang, T.; Pei, J.; Shang, H.; Zhou, D.; Li, H.; Dong, J.; Wang, Y.; Cao, R.; Zhuang, Z., Discovery of main group single $Sb–N_4$ active sites for CO_2 electroreduction to formate with high efficiency. *Energy Environ. Sci.* 2020, *13* (9), 2856-2863.

15. Zhang, A.; Liang, Y.; Li, H.; Zhang, B.; Liu, Z.; Chang, Q.; Zhang, H.; Zhu, C.-F.; Geng, Z.; Zhu, W., In-Situ Surface Reconstruction of InN Nanosheets for Efficient CO_2 Electroreduction into Formate. *Nano Lett.* 2020, *20* (11), 8229-8235.

16. Chen, Z.; Zhang, X.; Jiao, M.; Mou, K.; Zhang, X.; Liu, L., Engineering Electronic Structure of Stannous Sulfide by Amino-Functionalized Carbon: Toward Efficient Electrocatalytic Reduction of CO_2 to Formate. *Adv. Energy Mater.* 2020, *10* (8), 1903664.

17. Gong, Q.; Ding, P.; Xu, M.; Zhu, X.; Wang, M.; Deng, J.; Ma, Q.; Han, N.; Zhu, Y.; Lu, J., Structural defects on converted bismuth oxide nanotubes enable highly active electrocatalysis of carbon dioxide reduction. *Nat. Commun.* 2019, *10* (1), 1-10.

18. Zhang, W.; Hu, Y.; Ma, L.; Zhu, G.; Zhao, P.; Xue, X.; Chen, R.; Yang, S.; Ma, J.; Liu, J., Liquid-phase exfoliated ultrathin Bi nanosheets: uncovering the origins of enhanced electrocatalytic CO_2 reduction on two-dimensional metal nanostructure. *Nano Eenergy* 2018, *53*, 808-816.

19. Liu, S.; Lu, X. F.; Xiao, J.; Wang, X.; Lou, X. W., Bi_2O_3 Nanosheets Grown on Multi-Channel Carbon Matrix to Catalyze Efficient CO_2 Electroreduction to HCOOH. *Angew. Chem., Int. Ed.* 2019, *58* (39), 13828-13833.

20. Chen, Z.; Mou, K.; Wang, X.; Liu, L., Nitrogen-doped graphene quantum dots enhance the activity of Bi_2O_3 nanosheets for electrochemical reduction of CO_2 in a wide negative potential region. *Angew. Chem.* 2018, *130* (39), 12972-12976.

21. Zhang, Y.; Zhang, X.; Ling, Y.; Li, F.; Bond, A. M.; Zhang, J., Controllable synthesis of few-layer bismuth subcarbonate by electrochemical exfoliation for enhanced CO_2 reduction performance. *Angew. Chem.* 2018, *130* (40), 13467-13471.

22. Koh, J. H.; Won, D. H.; Eom, T.; Kim, N.-K.; Jung, K. D.; Kim, H.; Hwang, Y. J.; Min, B. K., Facile CO_2 electro-reduction to formate *via* oxygen bidentate intermediate stabilized by high-index planes of Bi dendrite catalyst. *ACS Catal.* 2017, *7* (8), 5071-5077.

23. Zhang, Z.; Chi, M.; Veith, G. M.; Zhang, P.; Lutterman, D. A.; Rosenthal, J.; Overbury, S. H.; Dai, S.; Zhu, H., Rational design of Bi nanoparticles for efficient electrochemical CO_2 reduction: the elucidation of size and surface condition effects. *ACS Catal.* 2016, *6* (9), 6255-6264.

24. Fan, K.; Jia, Y.; Ji, Y.; Kuang, P.; Zhu, B.; Liu, X.; Yu, J., Curved Surface Boosts Electrochemical CO_2 Reduction to Formate *via* Bismuth Nanotubes in a Wide Potential Window. *ACS Catal.* 2019, *10* (1), 358-364.

25. Li, Q.; Zhang, X.; Zhou, X.; Li, Q.; Wang, H.; Yi, J.; Liu, Y.; Zhang, J., Simply and effectively electrodepositing Bi-MWCNT-COOH composite on Cu electrode for efficient electrocatalytic CO_2 reduction to produce HCOOH. *J. CO_2 Util.* 2020, *37*, 106-112.

26. Pang, R.; Tian, P.; Jiang, H.; Zhu, M.; Su, X.; Wang, Y.; Yang, X.; Zhu, Y.; Song, L.; Li, C., Tracking structural evolution: operando regenerative CeO_x/Bi interface structure for high-performance CO_2 electroreduction. *Natl. Sci. Rev.* 2020, *8* (7) nwaa187.

27. Cheng, H.; Liu, S.; Zhang, J.; Zhou, T.; Zhang, N.; Zheng, X.-s.; Chu, W.; Hu, Z.; Wu, C.; Xie, Y., Surface Nitrogen-Injection Engineering for High Formation Rate of CO_2 Reduction to Formate. *Nano Lett.* 2020, *20* (8), 6097-6103.

28. Wen, G.; Lee, D. U.; Ren, B.; Hassan, F. M.; Jiang, G.; Cano, Z. P.; Gostick, J.; Croiset, E.; Bai, Z.; Yang, L., Orbital interactions in Bi-Sn bimetallic electrocatalysts for highly selective electrochemical CO_2 reduction toward formate production. *Adv. Energy Mater.* 2018, *8* (31), 1802427.

29. Yu, J.; Guo, Y.; Miao, S.; Ni, M.; Zhou, W.; Shao, Z., Spherical ruthenium disulfide-sulfur-doped graphene composite as an efficient hydrogen evolution electrocatalyst. *ACS Appl. Mater. Interfaces* 2018, *10* (40), 34098-34107.

30. Yu, L.; Wu, L.; McElhenny, B.; Song, S.; Luo, D.; Zhang, F.; Yu, Y.; Chen, S.; Ren, Z., Ultrafast room-temperature synthesis of porous S-doped Ni/Fe (oxy)hydroxide electrodes for oxygen evolution catalysis in seawater splitting. *Energy Environ. Sci.* 2020 *13* (10) 3439-3446.

31. Wang, Y. C.; Lai, Y. J.; Song, L.; Zhou, Z. Y.; Liu, J. G.; Wang, Q.; Yang, X. D.; Chen, C.; Shi, W.; Zheng, Y. P., S-doping of an Fe/N/C ORR catalyst for polymer electrolyte membrane fuel cells with high power density. *Angew. Chem.* 2015, *127* (34), 10045-10048.

32. Tian, W.; Zhang, H.; Sun, H.; Suvorova, A.; Saunders, M.; Tade, M.; Wang, S., Heteroatom (N or N-S)-Doping Induced Layered and Honeycomb Microstructures of Porous Carbons for CO_2 Capture and Energy Applications. *Adv. Funct. Mater.* 2016, *26* (47), 8651-8661.

33. Yang, H.; Wu, Y.; Lin, Q.; Fan, L.; Chai, X.; Zhang, Q.; Liu, J.; He, C.; Lin, Z., Composition Tailoring *via* N and S Co-doping and Structure Tuning by Constructing Hierarchical Pores: Metal-Free Catalysts for High-Performance Electrochemical Reduction of CO_2. *Angew. Chem.* 2018, *130* (47), 15702-15706.

34. Zhang, X.; Fu, J.; Liu, Y.; Zhou, X.-D.; Qiao, J., Bismuth Anchored on MWCNTs with Controlled Ultrafine Nanosize Enables High-Efficient Electrochemical Reduction of Carbon Dioxide to Formate Fuel. *ACS Sustain. Chem. Eng.* 2020, *8* (12), 4871-4876.

35. Wu, D.; Huo, G.; Chen, W.; Fu, X.-Z.; Luo, J.-L., Boosting formate production at high current density from CO_2 electroreduction on defect-rich hierarchical mesoporous Bi/Bi_2O_3 junction nanosheets. *Appl. Catal. B* 2020, 271, 118957.

36. Chen, W.; Li, X.; Duan, L.; Xie, X.; Cui, Y., Photoluminescence enhancement of $(NH_4)_2S_x$ passivated InP surface by rapid thermal annealing. *Appl. Surf. Sci.* 1996, *100*, 592-595.

37. Xu, L.; Jiang, Q.; Xiao, Z.; Li, X.; Huo, J.; Wang, S.; Dai, L., Plasma-engraved Co_3O_4 nanosheets with oxygen vacancies and high surface area for the oxygen evolution reaction. *Angew. Chem.* 2016, *128* (17), 5363-5367.

38. García de Arquer, F. P.; Bushuyev, O. S.; De Luna, P.; Dinh, C. T.; Seifitokaldani, A.; Saidaminov, M. I.; Tan, C. S.; Quan, L. N.; Proppe, A.; Kibria, M. G., 2D metal oxyhalide-derived catalysts for efficient CO_2 electroreduction. *Adv. Mater.* 2018, *30* (38), 1802858.

39. Reske, R.; Mistry, H.; Behafarid, F.; Roldan Cuenya, B.; Strasser, P., Particle size effects in the catalytic electroreduction of CO_2 on Cu nanoparticles. *J. Am. Chem. Soc.* 2014, *136* (19), 6978-6986.

40. Zheng, W.; Yang, J.; Chen, H.; Hou, Y.; Wang, Q.; Gu, M.; He, F.; Xia, Y.; Xia, Z.; Li, Z., Atomically defined undercoordinated active sites for highly efficient CO_2 electroreduction. *Adv. Funct. Mater.* 2020, *30* (4), 1907658.

41. Clark, E. L.; Ringe, S.; Tang, M.; Walton, A.; Hahn, C.; Jaramillo, T. F.; Chan, K.; Bell, A. T., Influence of Atomic Surface Structure on the Activity of Ag for the Electrochemical Reduction of CO_2 to CO. *ACS Catal.* 2019, *9* (5), 4006-4014.

42. Zhang, S.; Kang, P.; Ubnoske, S.; Brennaman, M. K.; Song, N.; House, R. L.; Glass, J. T.; Meyer, T. J., Polyethylenimine-enhanced electrocatalytic reduction of CO_2 to formate at nitrogen-doped carbon nanomaterials. *J. Am. Chem. Soc.* 2014, *136* (22), 7845-7848.

43. Yang, F.; Elnabawy, A. O.; Schimmenti, R.; Song, P.; Wang, J.; Peng, Z.; Yao, S.; Deng, R.; Song, S.; Lin, Y., Bismuthene for highly efficient carbon dioxide electroreduction reaction. *Nat. Commun.* 2020, *11* (1), 1-8.

44. Lee, C. W.; Hong, J. S.; Yang, K. D.; Jin, K.; Lee, J. H.; Ahn, H.-Y.; Seo, H.; Sung, N.-E.; Nam, K. T., Selective electrochemical production of formate from carbon dioxide with bismuth-based catalysts in an aqueous electrolyte. *ACS Catal.* 2018, *8* (2), 931-937.

45. Zhao, K.; Quan, X., Carbon-Based Materials for Electrochemical Reduction of CO_2 to C2+ Oxygenates: Recent Progress and Remaining Challenges. *ACS Catal.* 2021, *11* (4), 2076-2097.

46. Qi, H.; Yu, P.; Wang, Y.; Han, G.; Liu, H.; Yi, Y.; Li, Y.; Mao, L., Graphdiyne oxides as excellent substrate for electroless deposition of Pd clusters with high catalytic activity. *J. Am. Chem. Soc.* 2015, *137* (16), 5260-5263.

47. Ren, W.; Tan, X.; Yang, W.; Jia, C.; Xu, S.; Wang, K.; Smith, S. C.; Zhao, C., Isolated diatomic Ni-Fe metal–nitrogen sites for synergistic electroreduction of CO_2. *Angew. Chem., Int. Ed.* 2019, *58* (21), 6972-6976.

48. Shang, H.; Wang, T.; Pei, J.; Jiang, Z.; Zhou, D.; Wang, Y.; Li, H.; Dong, J.; Zhuang, Z.; Chen, W., Design of a Single-Atom Indium$^{\delta+}$–N_4 Interface for Efficient Electroreduction of CO_2 to Formate. *Angew. Chem., Int. Ed.* 2020, *59* (50), 22465-22469.

49. Nørskov, J. K.; Abild-Pedersen, F.; Studt, F.; Bligaard, T., Density functional theory in surface chemistry and catalysis. *Proc. Natl. Acad. Sci. U.S.A.* 2011, *108* (3), 937-943.

50. Hammer, B.; Nørskov, J. K., Theoretical surface science and catalysis—calculations and concepts. *Adv. Catal.* 2000, 45, 71-129.

4.5 Supporting information

4.5.1 Experimental section

Chemicals and Materials: Bismuth nitrate pentahydrate ($Bi(NO_3)_3{\cdot}5H_2O$), thioacetamide (C_2H_5NS), nitric acid (HNO_3) and Nafion perfluorinated ion-exchange resin solution (5 wt% in mixture of lower aliphatic alcohol & H_2O) were purchased from Sigma-Aldrich. Sulfuric acid (H_2SO_4) was purchased from ACROS Organics. Ethanol (EtOH), ethylene glycol (EG), potassium bicarbonate ($KHCO_3$) and isopropanol (IPA) were purchased from Fisher Scientific. Toray carbon paper 060 and Nafion 117 membrane with a thickness of 0.18 mm were purchased from Fuel Cell Store. NC7000 carbon nanotubes (CNT) were purchased from Nanocyl.

Acid treatment of CNT: 300 mg CNT was added into a solution containing 30 mL H_2SO_4 and 10 mL HNO_3. The solution was refluxed at 80 ℃ for 24 h. After the reflux, the products were washed with distilled water up to neutralization and freeze-dried in vacuum for 24 h.

Preparation of Bi_2O_3-CNT and S doped Bi_2O_3-CNT catalysts: In a typical synthesis, 0.97g $Bi(NO_3)_3{\cdot}5H_2O$ and a certain amount of thioacetamide were first dissolved into a solution consisting of 26mL EtOH and 13mL EG. For 0 at%, 0.3 at%, 0.7 at%, 1.2 at% and 1.7 at% S doped Bi_2O_3-CNT, the amounts of thioacetamide were 0, 4.5, 9, 18 and 27mg, respectively. Then, 100mg of acid-treated CNT was added and stirred for 30 min, followed by sonication for another 30 min. After that, the mixture was transferred into a 50-mL Teflon-lined stainless-steel autoclave, followed by heating at 160 ℃ for 5 h. After the hydrothermal process, the products were collected by centrifugation and washed with water and ethanol several times. The obtained powders were freeze-dried in vacuum for 24 h. Pristine Bi_2O_3 nanosheets were prepared through a similar process except for the addition of thioacetamide and CNT.

Preparation of S-SnO_2 catalyst: 0.9g $SnCl_2{\cdot}2H_2O$, 2.6g sodium citrate and 30mg thioacetamide were added into a solution containing 15 mL DI water and 15 mL EtOH. After vigorous stirring for 30 min, the mixture was transferred into a 50-mL Teflon-lined stainless-steel autoclave, followed by heating at 180 ℃ for 12 h. After the hydrothermal process, the products were collected by centrifugation and washed with water and ethanol several times. The obtained powders were dried in vacuum for 24 h. The procedures for preparation of SnO_2 were the same as those for the preparation of S-SnO_2, except for adding thioacetamide.

Preparation of S-In_2O_3 catalyst: 0.13g $In(NO_3)_3{\cdot}5H_2O$ and 3mg thioacetamide were added into 15 mL DMF. After vigorous stirring for 30 min, the mixture was transferred into a 50-mL Teflon-lined stainless-steel autoclave, followed by heating at 150 ℃ for 12 h. After the hydrothermal process, the products were collected by centrifugation and washed with water and ethanol several times. The obtained powders were dried in vacuum for 24 h. The procedures for preparation of In_2O_3 were the same as those for the preparation of S-In_2O_3, except for adding thioacetamide.

4.5.2 Computational Details

Density functional theory (DFT) calculations were performed using Perdew-Burke-Ernzerhof (PBE) generalized gradient approximation (GGA)[S1] function in Vienna Ab initio Simulation Package (VASP).[S2-3] The projector-augmented plane-wave (PAW)[S4] method was used to describe the electron-ion interactions and exchange-interaction effect. The cut-off energy was set at 520 eV and spin polarization was switched on for all the elements. Based on an optimized unit cell (a=5.58893 Angstrom), an undoped and a S-doped (110) surfaces of Bi_2O_3 model were built for further calculation. A vacuum layer of at least 15 Angstroms was added to avoid the interaction between neighbouring slabs. Monkhorst-Pack (4×3×1)[S5] was used for Brillouin zone k points sampling. A Gaussian smearing of 0.1eV was set for surface geometry optimization while it was

set at 0.01eV for gas-phase species. Relaxation of degree of ions was not terminated until achieving a maximum force component of 0.05 eV/Angstrom. Different geometries of surface with and without the adsorption of intermediates were considered and the one with the lowest electronic energy was chosen. During surface optimization, adsorbed species and the top three atomic layers of catalyst surface were fully relaxed while the remaining layers were fixed. Brillouin zone k points were then increased to (12×9×1) for non-self-consistent calculations for the determination of partial density of states (PDOS). A charge density difference analysis was also carried out to evaluate the charge transfer between S and Bi_2O_3. The Gibbs free energy was calculated as:

$$G = E_{DFT}+ZPE+\int C_p dT-TS \quad (1)$$

where E_{DFT} is the calculated electronic energy, ZPE is the zero-point energy, $\int C_p dT$ is the enthalpy correction, S is the calculated entropy, and T is the standard temperature of 298.15 K. Contributions from PV were neglected. 3N freedom degrees were treated as frustrated harmonic vibrations to calculate ZPE and enthalpy correction while a proposed standard method was used to calculate entropy contribution and transfer it to thermodynamic data at room temperature.[S6-7] The computational hydrogen electrode (CHE) model[S8] was employed to specify the Gibbs free energy of the proton-electron pair as the function of electrical potential. Reaction mechanisms for generating formate (S4.1-S4.4), CO (S4.5-S4.8), and H_2 (S4.9-S4.10) were assumed to be

$$*+CO_2+2(H^++e^-) \leftrightarrow *CO_2+2(H^++e^-) \quad (S4.1)$$

$$*CO_2+2(H^++e^-) \leftrightarrow *OCHO+(H^++e^-) \quad (S4.2)$$

$$*OCHO+(H^++e^-) \leftrightarrow *HCOOH \quad (S4.3)$$

$$*HCOOH \leftrightarrow *+HCOOH \quad (S4.4)$$

$$*+CO_2+2(H^++e^-) \leftrightarrow *CO_2+2(H^++e^-) \quad (S4.5)$$

$$*CO_2+2(H^++e^-) \leftrightarrow *COOH+(H^++e^-) \quad (S4.6)$$

$$*COOH+(H^+ + e^-) \leftrightarrow *CO+H_2O \quad \text{(S4.7)}$$

$$*CO+H_2O \leftrightarrow *+CO+H_2O \quad \text{(S4.8)}$$

$$*+H^+ + e^- \leftrightarrow *H \quad \text{(S4.9)}$$

$$*H \leftrightarrow *+1/2H_2 \quad \text{(S4.10)}$$

where * represents either a vacant surface catalytic active site, or intermediate species adsorbed on the active site. The initial state where CO_2 molecular is freely above clean surface is taken as the reference. Therefore, the Gibbs free energy change of each step is calculated as follows:

$$\Delta G[*CO_2] = G[*CO_2] - G[*] - G[CO_2] \quad \text{(S4.11)}$$

$$\Delta G[*OCHO] = G[*OCHO] - G[*] - G[CO_2] - G[H^+ + e^-] \quad \text{(S4.12)}$$

$$\Delta G[*HCOOH] = G[*HCOOH] - G[*] - G[CO_2] - 2G[H^+ + e^-] \quad \text{(S4.13)}$$

$$\Delta G[HCOOH] = G[HCOOH] - G[CO_2] - 2G[H^+ + e^-] \quad \text{(S4.14)}$$

$$\Delta G[*COOH] = G[*COOH] - G[*] - G[CO_2] - G[H^+ + e^-] \quad \text{(S4.15)}$$

$$\Delta G[*CO] = G[*CO] + G[H_2O] - G[*] - G[CO_2] - 2G[H^+ + e^-] \quad \text{(S4.16)}$$

$$\Delta G[CO] = G[CO] + G[H_2O] - G[CO_2] - 2G[H^+ + e^-] \quad \text{(S4.17)}$$

$$\Delta G[*H] = G[*H] - G[*] - G[H^+ + e^-] \quad \text{(S4.18)}$$

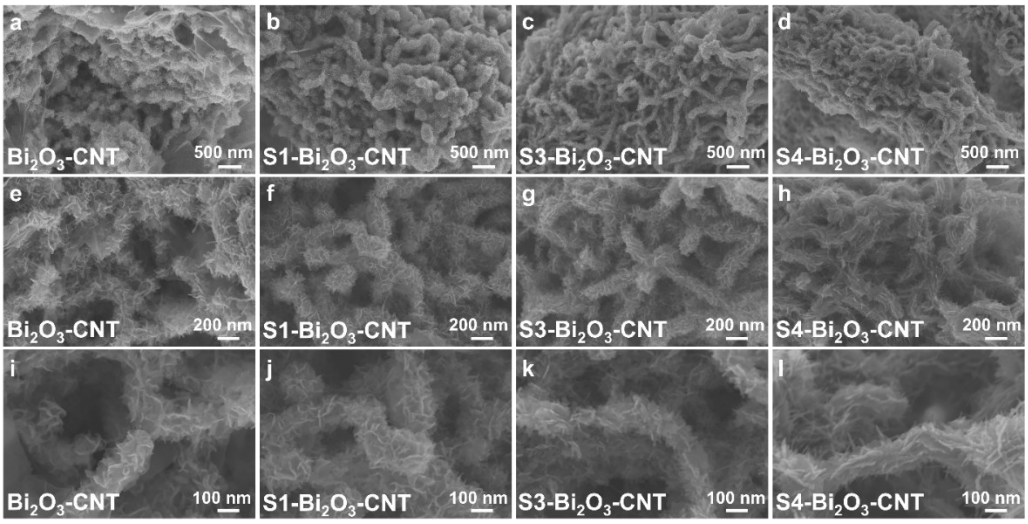

Figure S4.1 FESEM images of Bi_2O_3-CNT, S1-Bi_2O_3-CNT, S3-Bi_2O_3-CNT, and S4-Bi_2O_3-CNT with different magnifications.

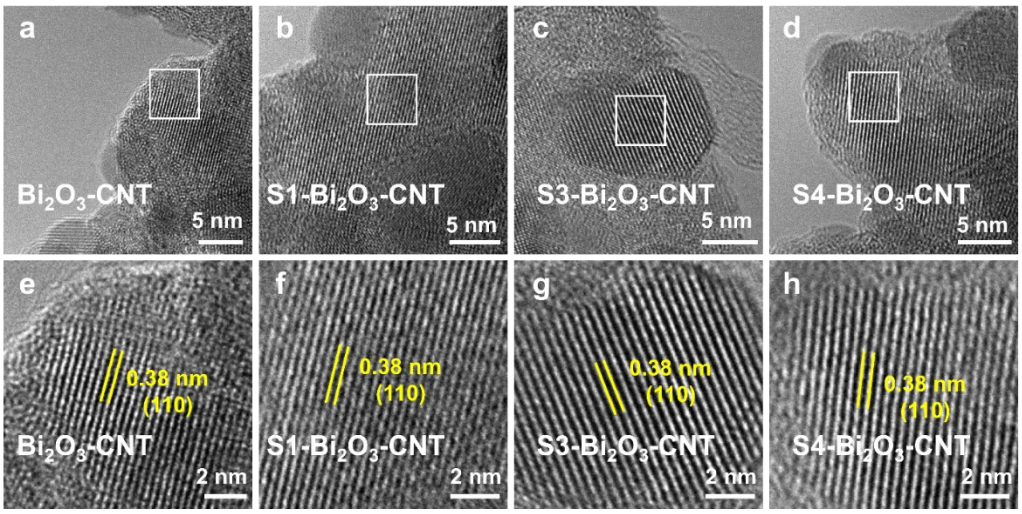

Figure S4.2 HRTEM images of Bi_2O_3-CNT, S1-Bi_2O_3-CNT, S3-Bi_2O_3-CNT, and S4-Bi_2O_3-CNT.

Table S4.1 The content of $O_{lat.}$, $O_{ads.}$ and O_{H_2O} species in Bi_2O_3-CNT and S doped samples determined from the O 1s XPS spectra.

Samples	$O_{lat.}$	$O_{ads.}$	O_{H_2O}
Bi_2O_3-CNT	46.1 %	35.3 %	18.6 %
S1-Bi_2O_3-CNT	36.2 %	39.5 %	24.3 %
S2-Bi_2O_3-CNT	35.4 %	43.1 %	21.5 %
S3-Bi_2O_3-CNT	33.8 %	42.1 %	24.1 %
S4-Bi_2O_3-CNT	24.1 %	41.8 %	34.1 %

Table S4.2 Fit parameters of Bi EXAFS spectra for Bi_2O_3-CNT and S2-Bi_2O_3-CNT.

Sample	Path	N[a]	R[b]	σ^2 (10^{-3} Å^2)[c]	ΔE_0 (eV)[d]
Bi_2O_3-CNT	Bi-O	5.0	2.17	4.9	−4.6
S-Bi_2O_3-CNT	Bi-O	3.0	2.28	11.4	−3.0
	Bi-S	1.79	2.76	11.4	−3.0

[a] Coordination number; [b] Distance between absorber and backscattered atoms; [c] Debye-Waller factor; [d] Inner potential correction.

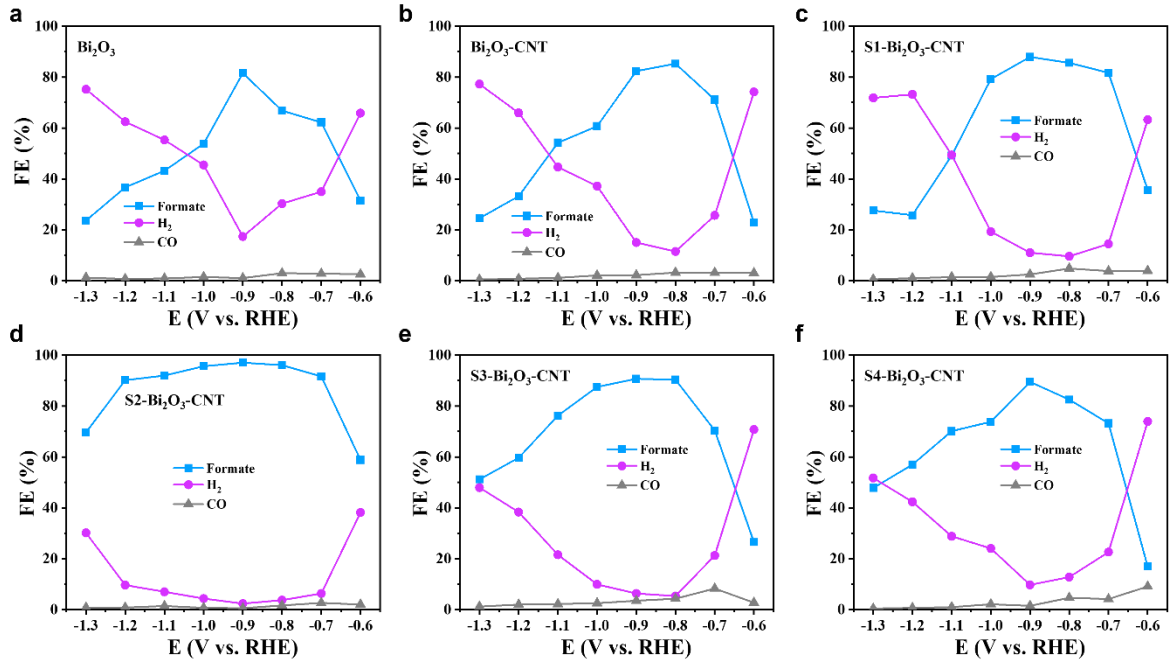

Figure S4.3 FE of all products for (a) Bi_2O_3, (b) Bi_2O_3-CNT, (c) S1-Bi_2O_3-CNT, (d) S2-Bi_2O_3-CNT, (e) S3-Bi_2O_3-CNT, and (f) S4-Bi_2O_3-CNT at different potentials.

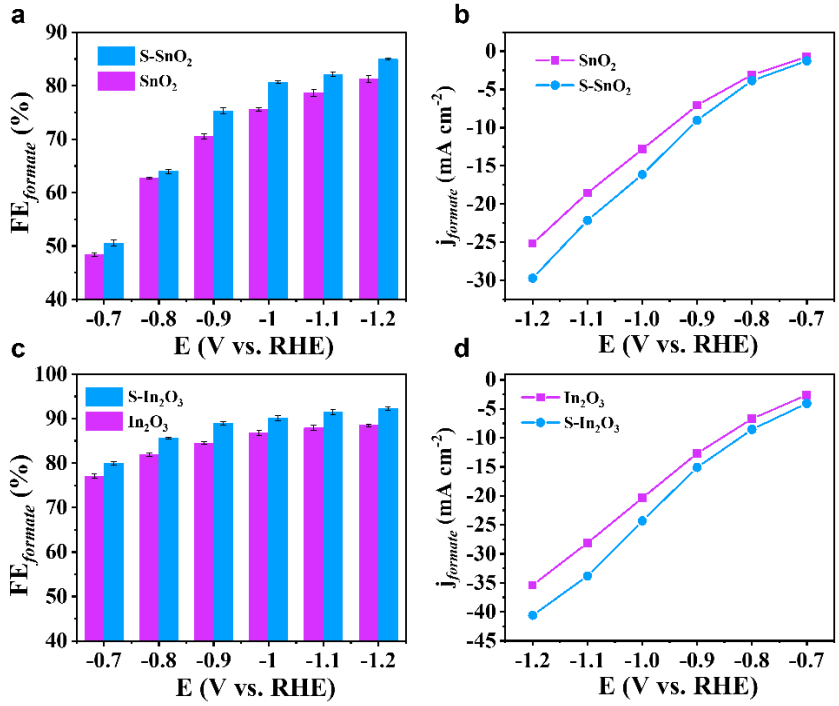

Figure S4.4 (a) $FE_{formate}$ and (b) $j_{formate}$ for S-SnO_2 and SnO_2. (c) $FE_{formate}$ and (d) $j_{formate}$ for S-In_2O_3 and In_2O_3.

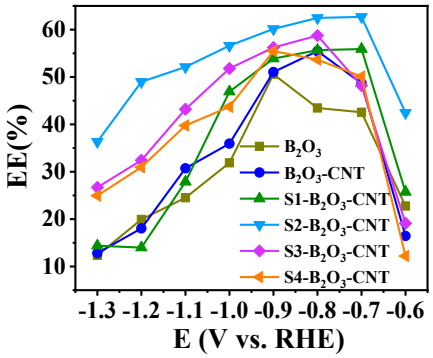

Figure S4.5 EE for Bi_2O_3, Bi_2O_3-CNT, S1-Bi_2O_3-CNT, S2-Bi_2O_3-CNT, S3-Bi_2O_3-CNT, and S4-Bi_2O_3-CNT.

Table S4.3 Electrocatalytic performances for CO_2 to formate in H-type cell over state-of-the-art catalysts reported recently.

Element	Catalyst	Electrolyte	Potential (V vs. RHE)	$j_{formate}$ (mA cm^{-2})	$FE_{formate}$ (%)	Ref.
In-based	S-In_2O_3 derived In	0.5 M $KHCO_3$	-0.98	57	93	S9
	hp-In	0.1 M $KHCO_3$	-1.2	67.5	90	S10
	Dendritic In	0.5 M $KHCO_3$	-0.86	5.8	86	S11
Cu-based	Cu_2S	0.1 M $NaHCO_3$	-0.9	18	87.3	S12
	S modified Cu	0.1 M $KHCO_3$	-0.8	10	80	S13
Sn-based	Porous SnO_2	0.5 M $NaHCO_3$	-0.99	45	87	S14
	S Modified Sn	0.1 M $KHCO_3$	-0.75	55	93	S15
	Bi doped SnO_x	0.5 M $KHCO_3$	-0.88	20.9	95.8	S16
	2D SnO_x	0.5 M $KHCO_3$	-1.37	45	90.2	S17
	Sn-pNW	0.1 M $KHCO_3$	-0.9	7	83	S18

Bi-based	Wire-in-Tube SnO_2	0.1 M $KHCO_3$	-1.29	9	62	S19
	Sub-2nm SnO_2	0.1 M $KHCO_3$	-1.26	18.1	89.8	S20
	SnO_2/carbon black	0.1 M $NaHCO_3$	-1.26	5.3	86.2	S21
	Ultra-small SnO	0.5 M $KHCO_3$	-0.86	20	75	S22
	Bi NWs/copper foam	0.5 M $NaHCO_3$	-0.69	15	95	S23
	Bi_2O_3@C	0.5 M $KHCO_3$	-0.9	7.5	92	S24
	Bi(btb)	0.5 M $KHCO_3$	-0.97	5	95	S25
	Bi_2O_3NSs@MCCM	0.1 M $KHCO_3$	-1.256	15	93.8	S26
	Bi_2O_3-NGQDs	0.5 M $KHCO_3$	-0.9	18	100	S27
	Bismuthene	0.5 M $KHCO_3$	-0.58	2.9	98	S28
	Bi dendrite	0.5 M $KHCO_3$	-0.74	2.7	89	S29
	Bi nanosheets	0.1 M $KHCO_3$	-1.1	16.5	86	S30
	BiOBr	0.1 M $KHCO_3$	-0.9	60	95	S31
	$Bi_2O_2CO_3$	0.5 M $NaHCO_3$	-0.7	11	95	S32
	Bi nanotubes	0.5 M $KHCO_3$	-1.0	22	95	S33
	Bi-Sn/CF	0.5 M $KHCO_3$	-1.14	43.2	96	S34
	B-Bi_2O_3 fractals	0.1 M $KHCO_3$	-1.2	22	87	S35
	POD-Bi	0.5 M $KHCO_3$	-1.16	57	95	S36
	Mesoporous Bi nanosheets	0.5 M $NaHCO_3$	-0.9	15	99	S37
	Bi_{45}/GDE	0.5 M $KHCO_3$	-0.782	6.5	90	S38
	Bi_2S_3-Bi_2O_3@rGO	0.5 M $KHCO_3$	-0.9	3.5	90	S39
	S-Bi_2O_3-CNT	0.5 M $KHCO_3$	-1.2 -1.1 -1.0 -0.9 -0.8 -0.7	48.64 46.44 42.39 28.17 12.97 2.77	90.14 91.98 95.63 97.06 96.07 91.65	This study

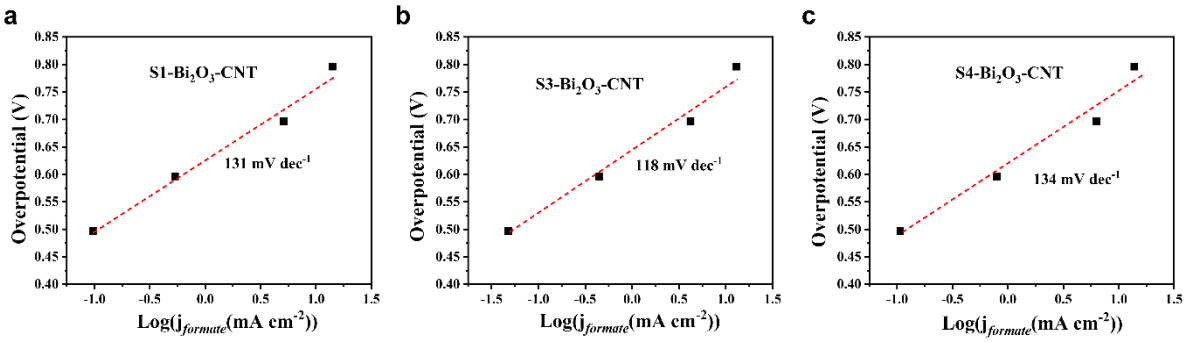

Figure S4.6 Tafel plots for a) S1-Bi_2O_3-CNT, b) S3-Bi_2O_3-CNT, and c) S4-Bi_2O_3-CNT.

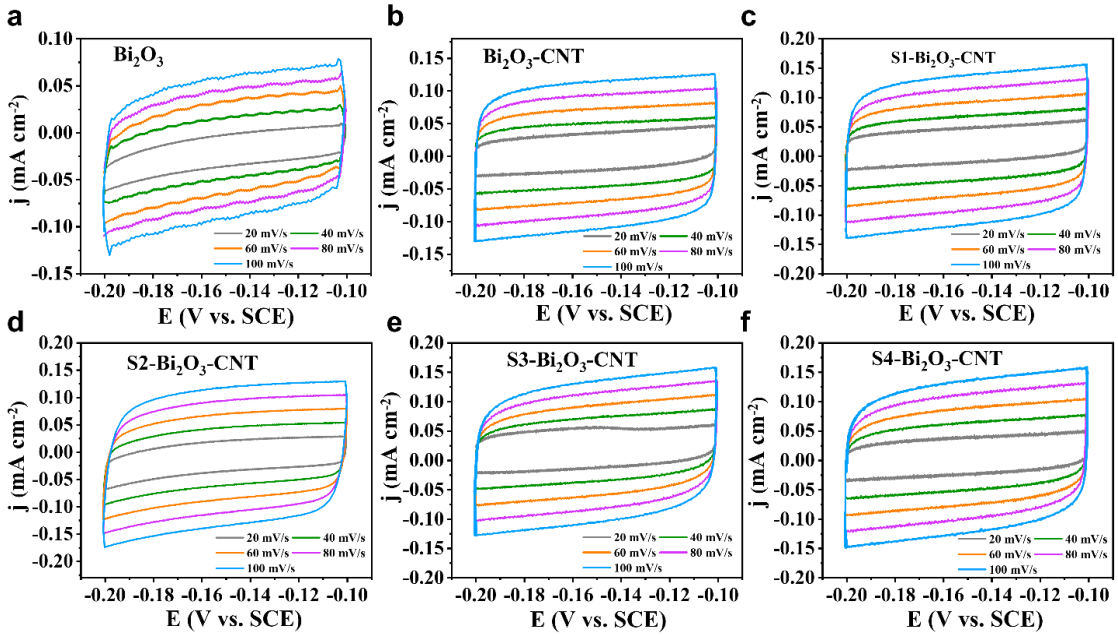

Figure S4.7 CV curves of a) Bi_2O_3, b) Bi_2O_3-CNT, c) S1-Bi_2O_3-CNT, d) S2-Bi_2O_3-CNT, e) S3-Bi_2O_3-CNT, and f) S4-Bi_2O_3-CNTwith various scan rates.

Table S4.4 Electrochemical surface area (ECSA) for different catalysts.

Samples	C_{dl}	ECSA
Bi_2O_3	0.73 mF cm^{-2}	36.5 cm^2
Bi_2O_3-CNT	1.05 mF cm^{-2}	52.5 cm^2
S1-Bi_2O_3-CNT	1.2 mF cm^{-2}	60 cm^2
S2-Bi_2O_3-CNT	1.23 mF cm^{-2}	61.5 cm^2
S3-Bi_2O_3-CNT	1.08 mF cm^{-2}	54 cm^2
S4-Bi_2O_3-CNT	1.22 mF cm^{-2}	61 cm^2

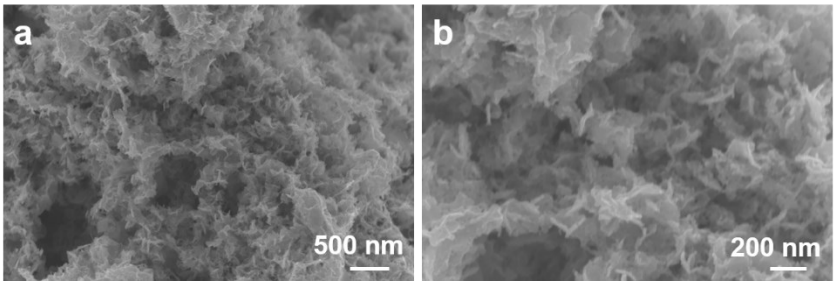

Figure S4.8 FESEM images of S2-Bi_2O_3-CNT after ECR test.

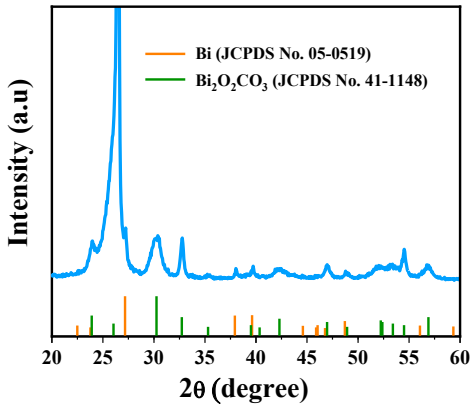

Figure S4.9 XRD pattern of S2-Bi_2O_3-CNT after ECR test.

Table S4.5 Summary of simulation parameters obtained from DFT calculation.

Calculated energy for gas-phase species (eV)					
Species	E_{DFT}	E_{ZPE}	−TS	$\int C_p dT$	G
CO_2	−22.960	0.309	−0.663	0.098	−23.216
H_2O	−14.219	0.589	−0.673	0.104	−14.204
H_2	−6.767	0.290	−0.403	0.090	−6.789
CO	−14.779	0.136	−0.596	0.090	−15.149
HCOOH	−29.874	0.895	0.11	−0.500	−29.368
Calculated energy for surfaces and intermediates on pure Bi_2O_3 (eV)					
Species	E_{DFT}	E_{ZPE}	−TS	$\int C_p dT$	G
*	−311.625				
*CO_2 (CO pathway)	−334.595	0.319	−0.399	0.151	−334.525
*CO_2 (HCOOH pathway)	−334.649	0.319	−0.378	0.149	−334.557
*COOH	−337.148	0.590	−0.345	0.147	−336.756
*CO	−326.441	0.152	−0.311	0.135	−326.466
*OCHO	−338.581	0.599	−0.282	0.140	−338.123
*HCOOH	−341.702	0.906	−0.441	0.174	−341.062
*H	−315.448	0.288	−0.042	0.038	−315.165
Calculated energy for surfaces and intermediates on pure S-Bi_2O_3 (eV)					
Species	E_{DFT}	E_{ZPE}	−TS	$\int C_p dT$	G
*	−309.455				
*CO_2 (CO pathway)	−332.985	0.319	−0.378	0.149	−332.895
*CO_2 (HCOOH pathway)	−332.965	0.319	−0.383	0.150	−332.880
*COOH	−335.577	0.637	−0.260	0.126	−335.074
*CO	−324.800	0.148	−0.338	0.139	−324.852
*OCHO	−337.125	0.599	−0.257	0.137	−336.645
*HCOOH	−340.087	0.920	−0.428	0.171	−339.424
*H	−312.731	0.201	−0.057	0.046	−312.541

Table S4.6 Bader charge analysis and their difference to purely ionic models (ΔQ) of Bi_2O_3 and S-Bi_2O_3.

Samples	Bader electrons			ΔQ		
	Bi	O	S	Bi	O	S
Bi_2O_3	3.479	7.074	---	−1.521	1.074	---
S-Bi_2O_3	3.488	7.073	6.887	−1.512	1.073	0.887

4.5.3 References

S1. Perdew, J. P.; Burke, K.; Ernzerhof, M., Generalized gradient approximation made simple. *Phys. Rev. Lett.* 1996, *77* (18), 3865.

S2. Kresse, G.; Hafner, J., Ab initio molecular dynamics for liquid metals. *Phys. Rev. B* 1993, *47* (1), 558.

S3. Kresse, G.; Furthmüller, J., Efficient iterative schemes for ab initio total-energy calculations using a plane-wave basis set. *Phys. Rev. B* 1996, *54* (16), 11169.

S4. Blöchl, P. E., Projector augmented-wave method. *Phys. Rev. B* 1994, *50* (24), 17953.

S5. Monkhorst, H. J.; Pack, J. D., Special points for Brillouin-zone integrations. *Phys. Rev. B* 1976, *13* (12), 5188.

S6. Cramer, C. J., *Essentials of computational chemistry: theories and models*. John Wiley & Sons: 2013.

S7. Tripković, V.; Skúlason, E.; Siahrostami, S.; Nørskov, J. K.; Rossmeisl, J., The oxygen reduction reaction mechanism on Pt (111) from density functional theory calculations. *Electrochim. Acta* 2010, *55* (27), 7975-7981.

S8. Peterson, A. A.; Abild-Pedersen, F., F. studt, J. Rossmeisl and JK Nørskov. *Energy Environ. Sci* 2010, *3*, 1311-1315.

S9. Ma, W.; Xie, S.; Zhang, X.-G.; Sun, F.; Kang, J.; Jiang, Z.; Zhang, Q.; Wu, D.-Y.; Wang, Y., Promoting electrocatalytic CO_2 reduction to formate *via* sulfur-boosting water activation on indium surfaces. *Nat. Commun.* 2019, *10* (1), 1-10.

S10. Luo, W.; Xie, W.; Li, M.; Zhang, J.; Züttel, A., 3D hierarchical porous indium catalyst for highly efficient electroreduction of CO_2. *J. Mater. Chem. A* 2019, *7* (9), 4505-4515.

S11. Xia, Z.; Freeman, M.; Zhang, D.; Yang, B.; Lei, L.; Li, Z.; Hou, Y., Highly selective electrochemical conversion of CO_2 to HCOOH on dendritic indium foams. *ChemElectroChem* 2018, *5* (2), 253-259.

S12. He, W.; Liberman, I.; Rozenberg, I.; Ifraemov, R.; Hod, I., Electrochemically Driven Cation Exchange Enables the Rational Design of Active CO_2 Reduction Electrocatalysts. *Angew. Chem.* 2020, *132* (21), 8339-8346.

S13. Shinagawa, T.; Larrazábal, G. n. O.; Martín, A. J.; Krumeich, F.; Pérez-Ramírez, J., Sulfur-modified copper catalysts for the electrochemical reduction of carbon dioxide to formate. *ACS Catal.* 2018, *8* (2), 837-844.

S14. Li, F.; Chen, L.; Knowles, G. P.; MacFarlane, D. R.; Zhang, J., Hierarchical mesoporous SnO_2 nanosheets on carbon cloth: a robust and flexible electrocatalyst for CO_2 reduction with high efficiency and selectivity. *Angew. Chem.* 2017, *129* (2), 520-524.

S15. Zheng, X.; De Luna, P.; de Arquer, F. P. G.; Zhang, B.; Becknell, N.; Ross, M. B.; Li, Y.; Banis, M. N.; Li, Y.; Liu, M., Sulfur-modulated tin sites enable highly selective electrochemical reduction of CO_2 to formate. *Joule* 2017, *1* (4), 794-805.

S16. Yang, Q.; Wu, Q.; Liu, Y.; Luo, S.; Wu, X.; Zhao, X.; Zou, H.; Long, B.; Chen, W.; Liao, Y., Novel Bi-Doped Amorphous SnO_x Nanoshells for Efficient Electrochemical CO_2 Reduction into Formate at Low Overpotentials. *Adv. Mater.* 2020, 2002822.

S17. Yuan, T.; Hu, Z.; Zhao, Y.; Fang, J.; Lv, J.; Zhang, Q.; Zhuang, Z.; Gu, L.; Hu, S., Two-Dimensional Amorphous SnO_x from Liquid Metal: Mass Production, Phase Transfer, and Electrocatalytic CO_2 Reduction toward Formic Acid. *Nano Lett.* 2020, *20* (4), 2916-2922.

S18. Kumar, B.; Atla, V.; Brian, J. P.; Kumari, S.; Nguyen, T. Q.; Sunkara, M.; Spurgeon, J. M., Reduced SnO_2 porous nanowires with a high density of grain boundaries as catalysts for efficient electrochemical CO_2-into-HCOOH conversion. *Angew. Chem., Int. Ed.* 2017, *56* (13), 3645-3649.

S19. Fan, L.; Xia, Z.; Xu, M.; Lu, Y.; Li, Z., 1D SnO_2 with Wire-in-Tube Architectures for Highly Selective Electrochemical Reduction of CO_2 to C_1 Products. *Adv. Funct. Mater.* 2018, *28* (17), 1706289.

S20. Liu, S.; Xiao, J.; Lu, X. F.; Wang, J.; Wang, X.; Lou, X. W., Efficient electrochemical reduction of CO_2 to HCOOH over sub-2 nm SnO_2 quantum wires with exposed grain boundaries. *Angew. Chem., Int. Ed.* 2019, *58* (25), 8499-8503.

S21. Zhang, S.; Kang, P.; Meyer, T. J., Nanostructured tin catalysts for selective electrochemical reduction of carbon dioxide to formate. *J. Am. Chem. Soc.* 2014, *136* (5), 1734-1737.

S22. Gu, J.; Héroguel, F.; Luterbacher, J.; Hu, X., Densely packed, ultra small SnO nanoparticles for enhanced activity and selectivity in electrochemical CO_2 reduction. *Angew. Chem.* 2018, *130* (11), 2993-2997.

S23. Zhang, X.; Sun, X.; Guo, S.-X.; Bond, A. M.; Zhang, J., Formation of lattice-dislocated bismuth nanowires on copper foam for enhanced electrocatalytic CO_2 reduction at low overpotential. *Energy Environ. Sci.* 2019, *12* (4), 1334-1340.

S24. Deng, P.; Yang, F.; Wang, Z.; Chen, S.; Zhou, Y.; Zaman, S.; Xia, B. Y., Metal–Organic Framework-Derived Carbon Nanorods Encapsulating Bismuth Oxides for Rapid and Selective CO_2 Electroreduction to Formate. *Angew. Chem., Int. Ed.* 2020, *59* (27) 10807-10813

S25. Lamagni, P.; Miola, M.; Catalano, J.; Hvid, M. S.; Mamakhel, M. A. H.; Christensen, M.; Madsen, M. R.; Jeppesen, H. S.; Hu, X. M.; Daasbjerg, K., Restructuring metal–organic frameworks to nanoscale bismuth electrocatalysts for highly active and selective CO_2 reduction to formate. *Adv. Funct. Mater.* 2020, *30* (16), 1910408.

S26. Liu, S.; Lu, X. F.; Xiao, J.; Wang, X.; Lou, X. W., Bi_2O_3 Nanosheets Grown on Multi-Channel Carbon Matrix to Catalyze Efficient CO_2 Electroreduction to HCOOH. *Angew. Chem., Int. Ed.* 2019, *58* (39), 13828-13833.

S27. Chen, Z.; Mou, K.; Wang, X.; Liu, L., Nitrogen-doped graphene quantum dots enhance the activity of Bi_2O_3 nanosheets for electrochemical reduction of CO_2 in a wide negative potential region. *Angew. Chem.* 2018, *130* (39), 12972-12976.

S28. Yang, F.; Elnabawy, A. O.; Schimmenti, R.; Song, P.; Wang, J.; Peng, Z.; Yao, S.; Deng, R.; Song, S.; Lin, Y., Bismuthene for highly efficient carbon dioxide electroreduction reaction. *Nat. Commun.* 2020, *11* (1), 1-8.

S29. Koh, J. H.; Won, D. H.; Eom, T.; Kim, N.-K.; Jung, K. D.; Kim, H.; Hwang, Y. J.; Min, B. K., Facile CO_2 electro-reduction to formate *via* oxygen bidentate intermediate stabilized by high-index planes of Bi dendrite catalyst. *ACS Catal.* 2017, *7* (8), 5071-5077.

S30. Zhang, W.; Hu, Y.; Ma, L.; Zhu, G.; Zhao, P.; Xue, X.; Chen, R.; Yang, S.; Ma, J.; Liu, J., Liquid-phase exfoliated ultrathin Bi nanosheets: uncovering the origins of enhanced electrocatalytic CO_2 reduction on two-dimensional metal nanostructure. *Nano Energy* 2018, *53*, 808-816.

S31. García de Arquer, F. P.; Bushuyev, O. S.; De Luna, P.; Dinh, C. T.; Seifitokaldani, A.; Saidaminov, M. I.; Tan, C. S.; Quan, L. N.; Proppe, A.; Kibria, M. G., 2D metal oxyhalide-derived catalysts for efficient CO_2 electroreduction. *Adv. Mater.* 2018, *30* (38), 1802858.

S32. Zhang, Y.; Zhang, X.; Ling, Y.; Li, F.; Bond, A. M.; Zhang, J., Controllable synthesis of few-layer bismuth subcarbonate by electrochemical exfoliation for enhanced CO_2 reduction performance. *Angew. Chem.* 2018, *130* (40), 13467-13471.

S33. Fan, K.; Jia, Y.; Ji, Y.; Kuang, P.; Zhu, B.; Liu, X.; Yu, J., Curved Surface Boosts Electrochemical CO_2 Reduction to Formate *via* Bismuth Nanotubes in a Wide Potential Window. *ACS Catal.* 2019, *10* (1), 358-364.

S34. Wen, G.; Lee, D. U.; Ren, B.; Hassan, F. M.; Jiang, G.; Cano, Z. P.; Gostick, J.; Croiset, E.; Bai, Z.; Yang, L., Carbon Dioxide Electroreduction: Orbital Interactions in Bi-Sn Bimetallic Electrocatalysts for Highly Selective Electrochemical CO_2 Reduction toward Formate Production. *Adv. Energy Mater.* 2018, *8* (31), 1870138.

S35. Tran-Phu, T.; Daiyan, R.; Fusco, Z.; Ma, Z.; Amal, R.; Tricoli, A., Nanostructured β-Bi_2O_3 fractals on carbon fibers for highly selective CO_2 electroreduction to formate. *Adv. Funct. Mater.* 2020, *30* (3), 1906478.

S36. He, S.; Ni, F.; Ji, Y.; Wang, L.; Wen, Y.; Bai, H.; Liu, G.; Zhang, Y.; Li, Y.; Zhang, B., The p-orbital delocalization of main-group metals to boost CO_2 electroreduction. *Angew. Chem.* 2018, *130* (49), 16346-16351.

S37. Yang, H.; Han, N.; Deng, J.; Wu, J.; Wang, Y.; Hu, Y.; Ding, P.; Li, Y.; Li, Y.; Lu, J., Selective CO_2 reduction on 2D mesoporous Bi nanosheets. *Adv. Energy Mater.* 2018, *8* (35), 1801536.

S38. Zhang, X.; Lei, T.; Liu, Y.; Qiao, J., Enhancing CO_2 electrolysis to formate on facilely synthesized Bi catalysts at low overpotential. *Appl. Catal. B* 2017, *218*, 46-50.

Chapter 5 Hydrophobic engineering for CO_2 electrolysis

In Chapter 4, I developed the S doping strategy that induced the electronic delocalization of catalyst to resolve the issue of formate FE dropping at high current density. Although this strategy is proven to be highly effective, the current density for the catalyst is still below 100 mA cm^{-2} in H-type cell due to the CO_2 mass transport limitation. The focus of this chapter will be on creating favorable triple-phase boundary by tuning the wettability of carbon support for formate production at high rate (> 100 mA cm^{-2}). I will demonstrate that the hydrophobic engineering can be used as an effective approach to increasing the reaction rate of other catalyst materials.

In this chapter, I describe how the surface chemistry of carbon support can tune surface hydrophobicity/hydrophilicity and how the hydrophobic catalyst surface can enhance local CO_2 concentration, thereby promoting the ECR to formate. With the knowledge of molecular dynamics, the relationship between wettability and oxygen contents on carbon surface, I explored and synthesized Bi_2O_3 nanosheet on hydrophobic carbon nanofiber by a one-step hydrothermal method. The hydrophobic surface accelerates ECR to formate at a current density of 102.1 mA cm^{-2} with a formate FE of 93%. Furthermore, the catalyst delivered a commercial level current density of 300 mA cm^{-2} when moved to the flow cell reactor.

The work in this chapter has been published as a full research paper titled "Bi_2O_3 Nanosheets Grown on Carbon Nanofiber with Inherent Hydrophobicity for High Performance CO_2 Electroreduction in a Wide Potential Window" in *ACS Nano*, 2021, 15, 17757-17768. Text and figures have been reproduced here with permission from ACS. As the first author, I designed and characterized the catalysts, performed electrolysis experiments, and wrote the manuscript. Ehsan Shahini conducted the molecular dynamics simulation with the suggestions of Dr. Tian Tang.

Abstract: The ever-increasing concern for the adverse climate changes has propelled the worldwide research on the reduction of CO_2 emission. In this regard, ECR to formate is one of the promising approaches to converting CO_2 to useful product. However, to achieve a high production rate of formate, the existing catalysts for ECR fall short of expectation in maintaining the high formate selectivity and activity over a wide potential window. Through this study, we report that Bi_2O_3 nanosheets (NSs) grown on carbon nanofiber (CNF) with inherent hydrophobicity achieve a peak formate current density of 102.1 mA cm^{-2} and high formate Faradaic efficiency of >93 % over a very wide potential window of 1000 mV. To the best of our knowledge, this outperforms all the relevant achievements reported so far. In addition, the Bi_2O_3 NSs on CNF demonstrate a good anti-flooding capability when operating in flow cell system, and can deliver a current density of 300 mA cm^{-2}. Molecular dynamics (MD) simulations indicate that hydrophobic carbon surface can repel the water molecules to form a robust solid-liquid-gas triple-phase boundary and a concentrated CO_2 layer; both can boost ECR activity with the local high concentration of CO_2 and through inhibiting hydrogen evolution reaction (HER) by reducing protons contacts. This water repelling effect also increases the local pH at the catalyst surface, thus inhibiting HER further. More significantly, the concept and methodology of this hydrophobic engineering could be broadly applicable to other formate-producing materials from ECR.

5.1 Introduction

Modern industrialization is accompanied with the extensive usage of fossil fuels for energy demands and consequently, an excessive emission of CO_2 into the atmosphere. To combat the injurious greenhouse effects, ECR to feedstocks and fuels becomes an appealing approach to reducing CO_2 emission and simultaneously producing useful products.[1-2] Since formate is one of the most attractive ECR products and has now become an ideal hydrogen carrier for fuel cells,[3-4]

various strategies have been developed including size,[5] morphology,[6] defect,[7] grain boundary,[8] element doping[9] and heterostructure engineering,[10] all aiming to enhance the electrocatalytic performance. Despite some encouraging achievements, the performances of these catalysts still fall quite short in meeting the requirements for commercial production and based on our knowledge, most existing catalysts suffer from the low formate formation rate (<1500 μmol h^{-1} cm^{-2} in H-type cell) due to the limited current density (j < 90 mA cm^{-2}).[11-13] Concurrently, a desirable formate Faradaic efficiency ($FE_{formate}$) of > 90% is limited to only a narrow range of potential window (< 750 mV) due to the decrease of $FE_{formate}$ at high overpotentials. This decrease can be attributed to the enhancement of HER and leveling of ECR. The direct reduction of HCO_3^- at high overpotential is believed to account for the HER enhancement.[14] Meanwhile, the CO_2 mass transport limitation and its hydration reaction with OH^- ($CO_2+OH^- \rightarrow HCO_3^-$) will further inhibit ECR performance.[15,16] Therefore, it is a high priority task and a great challenge to develop effective catalysts that can be easily synthesized for ECR to formate production with high formation rate and j over a much wider potential window.

It is generally recognized that the solid-catalyst/liquid-electrolyte/gaseous-CO_2 triple-phase boundary is the key microstructure feature of ECR, where CO_2 molecules react with protons (H^+) and e^- and are reduced.[17] Besides the intrinsic activity of catalyst itself and the accessibility of active sites, ECR performance also strongly depends on the transport of H^+ and CO_2 molecules through electrolyte to catalyst surface. Apparently, the availability of H^+ in aqueous solution can be readily achieved *via* H_2O ionization, while the low solubility of CO_2 limits the supply of CO_2 to the catalyst surface.[16] Moreover, previous study has demonstrated that complete depletion of CO_2 on the catalyst surface can even occur when high overpotential is applied.[18] In this regard, rationally designing the structure of catalyst to increase the concentration of CO_2 at the triple-

phase boundary is immensely significant for ECR since this could overcome the limited diffusion of CO_2 in aqueous medium.

Recently, surface hydrophobicity engineering has been proved to be a wise tactic to increase the local CO_2 concentration by trapping CO_2 near the catalyst surface, thus improving CO_2 electrolysis.[19-21] For example, modification of the hydrophobic organics on catalyst surface could create triple-phase boundary and increase CO_2 concentration on catalyst surface, these improved ECR performance and simultaneously inhibited HER.[22] Unfortunately, the insulative organics coated on the catalyst surface will sacrifice its activity, while some small pieces of organics may desorb from the surface or in the case of flow cell, these pieces can be flushed away by the fluid.[23] Alternatively, the hydrophobicity can be realized by depositing catalysts on hydrophobic substrates,[24] typically gas diffusion layer (GDL), with hydrophobicity imposed within a carbon matrix *via* polytetrafluoroethylene (PTFE) treatment. However, flooding of the GDL will often happen due to the excessive electrolyte contact, especially in a flow cell system, which hinders the mass transport of CO_2 and consequently renders the selectivity in favor of HER.[25] Since most catalysts are *in situ* grown on carbon support with the advantages of rapid electron transfer and seamless contact,[10, 26] it is possible to tailor the microenvironment around the catalyst through chemical modification of carbon support. For example, platinum-based catalysts supported on hydrophobic carbon with a desirable microenvironment display a state-of-the-art catalytic activity for oxygen reduction reaction.[27] However, few studies have been conducted to investigate how the carbon support can be modified to create a favorable triple-phase boundary for ECR.

Bi-based materials (metallic Bi and Bi_2O_3) are well known for their unusually low toxicity, low cost and desirable environmental benignity, therefore, have stood out as the candidate materials for effective fromate-production *via* ECR. More importantly, Bi-based materials are not only inert

for HER, but also are beneficial for the stabilization of $CO_2^{\bullet-}$, a key intermediate for formate production.[28] To that end, we have *in situ* grown Bi_2O_3 nanosheets (NSs) on two types of carbon materials, hydrophobic carbon nanofiber (Bi_2O_3@C/HB) and hydrophilic carbon nanofiber (Bi_2O_3@C/HL), respectively, and used them as the cathode catalysts for ECR. Compared to Bi_2O_3@C/HL, the as-obtained Bi_2O_3@C/HB exhibits significantly boosted ECR performances for formate formation with the high $FE_{formate}$ of > 93% over an extremely wide potential window of 1000 mV, high formate partial current density ($j_{formate}$) of 102.1 mA cm^{-2} and high formate formation rate of 1905 μmol h^{-1} cm^{-2}. Molecular dynamics (MD) simulations together with electrochemical measurements reveal that the hydrophobic carbon support can create a hydrophobic microenvironment by avoiding the formation of hydrogen bond. This increases the local CO_2 concentration and pH, both contributing to the enhancement of the overall ECR. We believe that the findings from this work can provide significant guidelines for designing highly active ECR catalysts and showcase a promising approach to improving other types of electrolysis involving gas phase.

5.2 Results and discussion

5.2.1 Synthesis and characterizations of Bi_2O_3@C/HB and Bi_2O_3@C/HL

To prepare Bi_2O_3@C/HB and Bi_2O_3@C/HL, hydrophobic (C/HB) and hydrophilic carbon nanofibers (C/HL) were used, respectively. C/HB was the original PR-25-XT-HHT while C/HL was obtained by acid-treatment of C/HB. C/HB and C/HL show similar nanofiber morphology with an average diameter of 100 nm as revealed by scanning electron microscopy (SEM) and transmission electron microscopy (TEM) images (Figure 5.1a-d). The C/HL shows a rough surface compared to C/HB, probably due to the corrosion effect of acid-treatment. X-ray diffraction (XRD) patterns indicate that C/HB and C/HL possess the identical features, suggesting that both C/HB

and C/HL are of the same graphitized carbon structure (Figure 5.1e). The surface environment was examined by Fourier transform infrared spectroscopy (FTIR). The C/HL exhibits much higher intensity than C/HB at the bands of ~ 1260 and 1730 cm^{-1} corresponding to C–O and C=O (Figure 5.2a), respectively. The bond at around 1600 cm^{-1} in C/HL can be assigned to the stretching bond of C=C, which is infrared silent in C/HB owing to the very high π-electron transmittance in symmetric carbons.[29] After acid-treatment, this bond is activated in C/HL by the formation of oxygen-containing groups. This suggests that the acid-treatment brings various oxygen-containing groups onto the carbon surface. The surface oxygen ratios ware quantitatively estimated from X-ray photoelectron spectroscopy (XPS) analysis which indicates that the C/HL possesses a higher surface oxygen-to-carbon ratio (10.57%) than C/HB (0.27%) (Figure 5.2b, c). The contact angle measurements illustrate that the C/HL is hydrophilic while C/HB shows hydrophobic feature (Figure 5.1f). The Bi_2O_3@C/HB and Bi_2O_3@C/HL were prepared using the previously reported solvothermal method,[10] which produced similar nanosheets morphology and identical cubic structure (Figure 5.2d-f, Figure S5.1a-c and Figure S5.2). As confirmed by the high-angle annular dark-field scanning TEM (HAADF-STEM) image and the energy-dispersive X-ray (EDX) element mappings, Bi and O elements were uniformly distributed across the carbon nanofiber surface (Figure 5.2g, h). In addition, the Bi_2O_3 NSs grown on the hydrophilic and hydrophobic carbon surfaces share the same electronic state, as illustrated by XPS (Figure S5.3). It is noteworthy that the growth of Bi_2O_3 on C/HL and C/HB surfaces has little impact on the wettability (Figure 5.2i, j), with only slightly weakened hydrophobicity resulting from the hydrophilic feature of Bi_2O_3. The thermogravimetric analysis demonstrates that the mass loadings of Bi_2O_3 on Bi_2O_3@C/HL (73.2%) and Bi_2O_3@C/HB (74.1%) are almost the same (Figure S5.4).

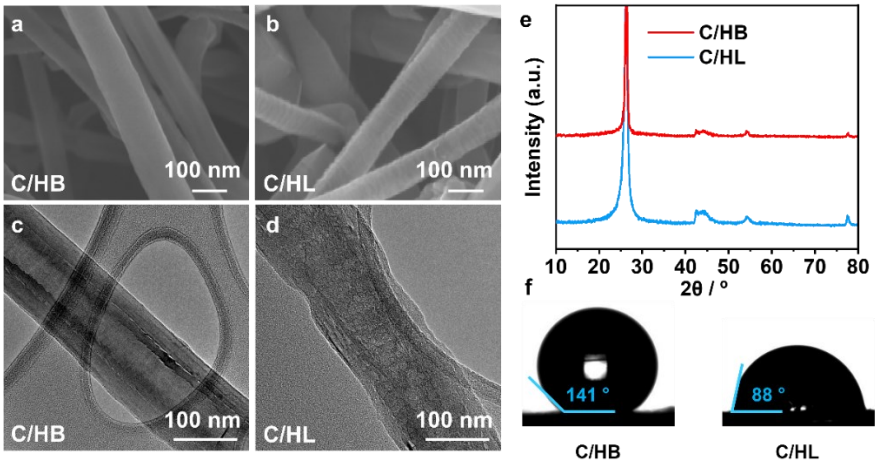

Figure 5.1 SEM and TEM images for (a, c) C/HB and (b, d) C/HL. (e) XRD patterns for C/HB and C/HL. (f) Contact angles of water on C/HB and C/HL.

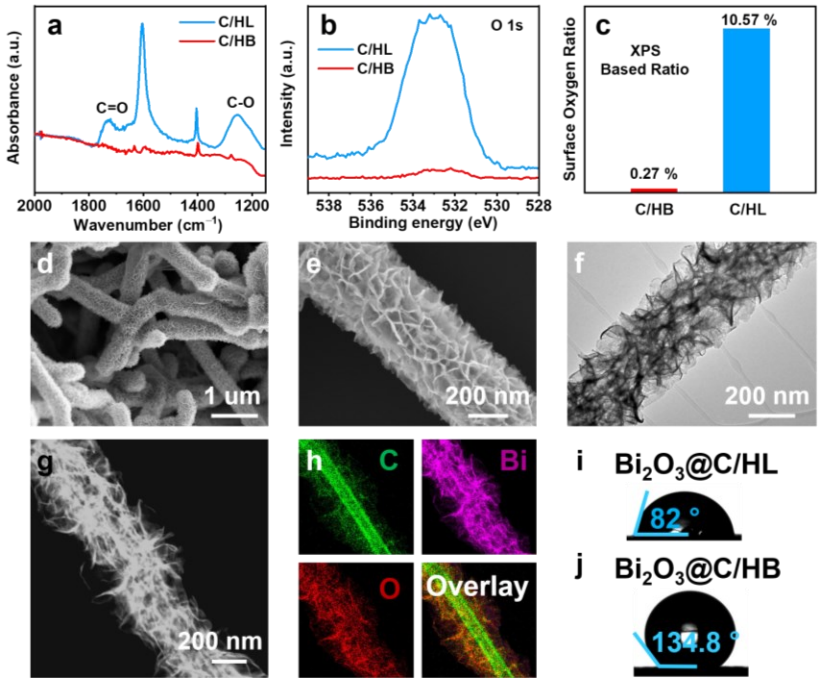

Figure 5.2 (a) FTIR and (b) O 1s XPS spectra for C/HB and C/HL. (c) The ratios of surface oxygen to carbon for C/HB and C/HL. (d-f) SEM and TEM images of Bi_2O_3@C/HB. (g, h) The HAADF-STEM image of Bi_2O_3@C/HB and the corresponding elemental maps of C, Bi, and O. Contact angles of water on (i) Bi_2O_3@C/HL and (j) Bi_2O_3@C/HB.

The CO_2 transport at the catalyst surface is of vital importance in the ECR. We speculate that the Bi_2O_3@C/HB could exhibit an aerophilic feature in water because of its hydrophobic surfaces in air.[30] The CO_2 bubble adhesion experiments in 0.5 M CO_2-saturated $KHCO_3$ solution were performed on Bi_2O_3@C/HB and Bi_2O_3@C/HL. The results show that the CO_2 bubble can immediately penetrate into the surface of Bi_2O_3@C/HB (Figure 5.3a), confirming its aerophilic feature. By contrast, the CO_2 bubble is readily pinned on the surface of Bi_2O_3@C/HL and can maintain on the electrode for 40 s (Figure 5.3b). This indicates that the hydrophobicity of the carbon support plays a key role in realizing CO_2 transport and accumulation across the catalyst surface.

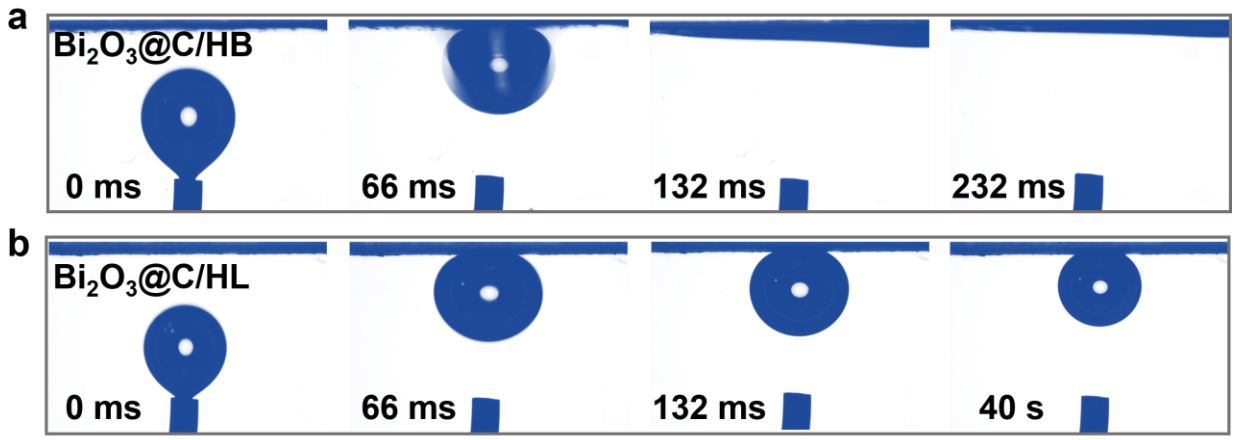

Figure 5.3 CO_2 bubble adhesion experiments and the corresponding optical pictures of (a) Bi_2O_3@C/HB and (b) Bi_2O_3@C/HL electrodes in 0.5 M CO_2-saturated $KHCO_3$ solution.

5.2.2 Electrocatalytic activities of Bi_2O_3@C/HB and Bi_2O_3@C/HL for ECR

The ECR catalytic performances of Bi_2O_3@C/HB and Bi_2O_3@C/HL were investigated in a typical three-electrode H-type cell in CO_2-saturated 0.5 M $KHCO_3$ solution; all the potentials in this work are *versus* to the reversible hydrogen electrode (RHE). As observed in Figure 5.4a, linear sweep voltammetry (LSV) curves show that Bi_2O_3@C/HB and Bi_2O_3@C/HL delivered much higher

current density, *j*, than C/HB and C/HL, the sign of higher activities of Bi_2O_3 NSs. Notably, Bi_2O_3@C/HB and Bi_2O_3@C/HL performed rather similarly at the less negative potentials. At more negative potentials where mass transport became dominant, the *j* differences between Bi_2O_3@C/HB and Bi_2O_3@C/HL began to appear: a much obvious increase of *j* was observed for Bi_2O_3@C/HB in comparison with Bi_2O_3@C/HL. This suggests that mass transport is more efficient on Bi_2O_3@C/HB than on Bi_2O_3@C/HL. To persuasively clarify that the increased *j* is attributed to ECR activity rather than HER, a controlled ECR was conducted between −0.6 and −1.7 V. The FE distributions of formate and gas products are shown in Figure 5.4b and Figure S5.5. An initial $FE_{formate}$ of 83.9% can be achieved at −0.6 V for Bi_2O_3@C/HB, then it increased to 93.8% at −0.7 V and maintained at greater than 96% over a wide potential range from −0.8 to −1.6 V. By contrast, Bi_2O_3@C/HL required more negative potential (−0.7 V) to reach an equivalent $FE_{formate}$ (85.7%); the $FE_{formate}$ reached maximum of 94.2% at −0.8 V but quickly dropped to 37.5% at −1.7 V. It is noteworthy that even the C/HB achieved a maximum $FE_{formate}$ of 41% at −1.2 V, while no formate was detected on C/HL. To explore the reason for this, the Tafel plot of C/HB was analyzed. The Tafel slope for C/HB (144.4 mV dec^{-1}) is close to theoretical value of 118 mV dec^{-1} (Figure S5.6), indicating that the formation of $CO_2^{\bullet-}$ serves as rate-limiting step. Generally, the formation of $CO_2^{\bullet-}$ involves the first adsorption of CO_2 and subsequent reduction process. Therefore, CO_2 adsorption isotherms of C/HB and C/HL were compared to evaluate the CO_2 adsorption capacity; the results indicate that C/HB absorbs CO_2 of two times higher than C/HL (Figure S5.7). Therefore, the enhanced formate production activity of C/HB over C/HL can be attributed to the enhanced CO_2 adsorption which promotes the formation of $CO_2^{\bullet-}$.[31] The enhanced CO_2 adsorption capacity of C/HB can be attributed to the CO_2 trapping feature of C/HB.[32] The $j_{formate}$ for Bi_2O_3@C/HB increased gradually from −0.6 to −1.7 V and achieved 102.1

mA cm^{-2} at −1.7 V (Figure 5.4c). The $j_{formate}$ for Bi_2O_3@C/HL shows a similar trend as Bi_2O_3@C/HB between −0.6 and −1.3 V. However, $j_{formate}$ starts to decrease significantly from −1.4 V and the difference of $j_{formate}$ between Bi_2O_3@C/HL and Bi_2O_3@C/HB is enlarged to 2.3-fold at −1.6 V where ECR begins to be hindered by CO_2 mass transport. Hence, the ECR activity of Bi_2O_3@C/HL is limited by the CO_2 mass transport especially at higher overpotentials, while this mass transport limitation of CO_2 can be overcome over Bi_2O_3@C/HB. Therefore, the competitive HER is drastically restrained over Bi_2O_3@C/HB. This can be further verified by the partial current density of H_2 (j_{H2}): As illustrated in Figure S5.8, the Bi_2O_3@C/HB displays a j_{H2} below 4 mA cm^{-2}, while Bi_2O_3@C/HL displays a dramatic increase of j_{H2} after −1.4 V and reaches up to 42 mA cm^{-2} at −1.7 V. Since the use of different carbon supports (C/HB and C/HL) has no major influence on the morphology, valence state and conductivity (see the electrochemical impedance spectra (EIS) in Figure S5.9), the performance differences observed for Bi_2O_3@C/HB and Bi_2O_3@C/HL can be originated from the induced changes in hydrophobicity/hydrophilicity, most likely because the hydrophobic microenvironment can increase the local CO_2 concentration at the catalyst surface due to the water repulsion effect. The high local concentration of CO_2 molecules facilitates their access to the catalyst, thus promoting ECR performance. Consequently, such a combination of high $FE_{formate}$ (> 90%) over an extremely wide potential window (1000 mV) and the outstanding $j_{formate}$ is superior to most of the reported formate-producing catalysts in H-type cell (Figure 5.4d and Table S5.1). Promisingly, besides Bi, this surface hydrophobicity engineering is generally applicable to formate-producing catalysts such as Sn and In. The engineered Sn or In-based catalysts on C/HB can significantly promote the production of formate (Figure 5.5). The achieved $j_{formate}$ values were −40 and −30 mA cm^{-2} over SnO_2@C/HB and In_2O_3@C/HB at −1.6 V, about 3 and 2 times higher than those of SnO_2 and In_2O_3 grown on C/HL, respectively. The above examples

are in support of the generality that surface hydrophobicity can accelerate ECR to formate *via* increasing surface CO_2 concentration through creating hydrophobic microenvironment around the catalyst.

The formate formation rate is another important criterion judging the feasibility of the catalyst for practical applications of ECR. As shown in Figure 5.4e, the formate formation rate for Bi_2O_3@C/HB can achieve 1905 μmol h^{-1} cm^{-2} at −1.7 V, exceeding those of Bi_2O_3@C/HL (490 μmol h^{-1} cm^{-2}) and many other reported catalysts (Table S5.1). Energy efficiency (EE), determined by η and FE, is a good indicator to evaluate the utilization efficiency of electrical energy. An EE of 60.5% can be delivered by Bi_2O_3@C/HB at −0.6 V due to the contributions of high $FE_{formate}$ and low η (Figure S5.10). Subsequently, the EE of Bi_2O_3@C/HB increased to a maximum value of 64.2% at −0.7 V and maintained at over 50% from −0.9 to −1.3 V, which outperforms that of Bi_2O_3@C/HL.

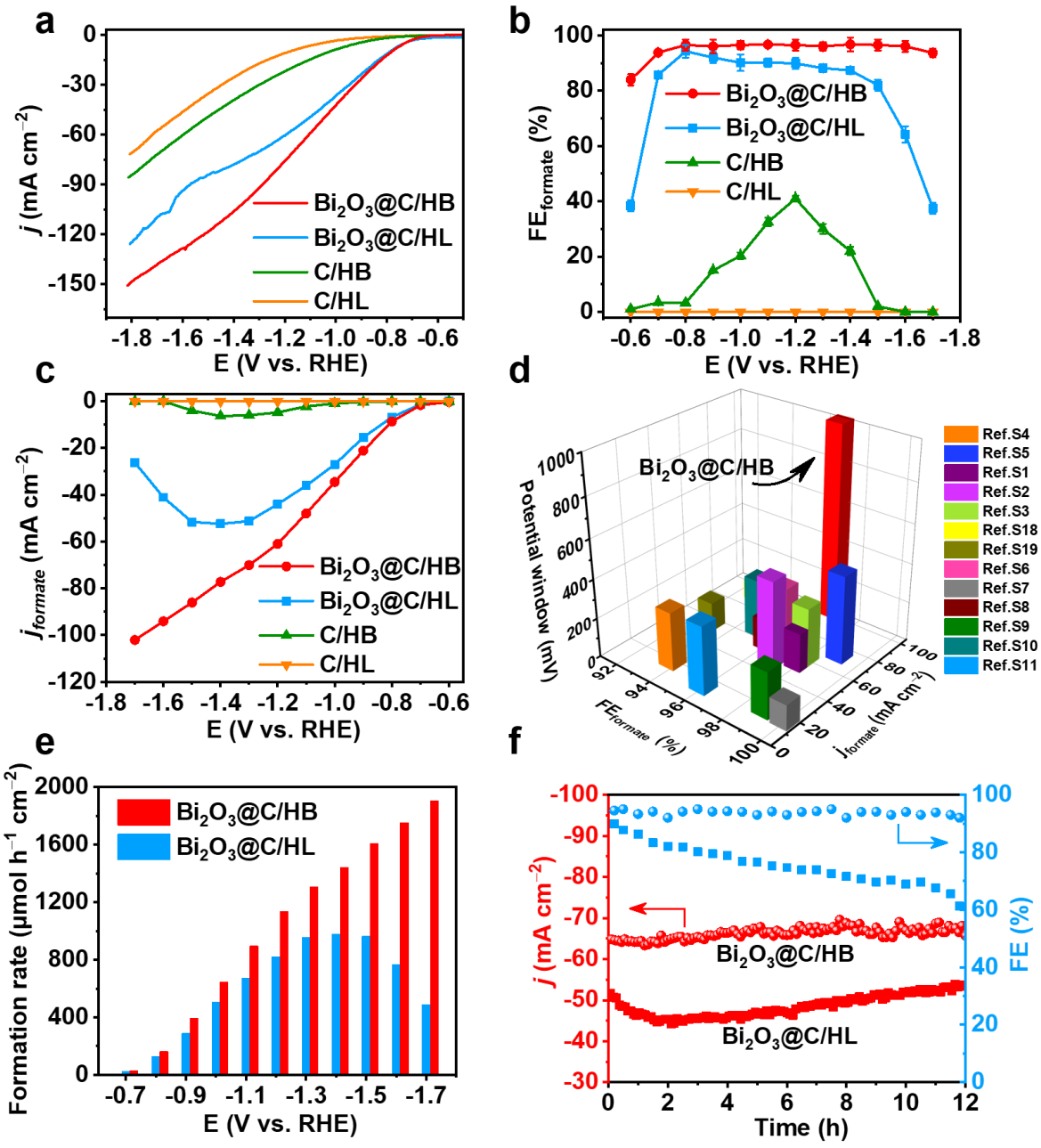

Figure 5.4 (a) LSVs, (b) $FE_{formate}$ and (c) $j_{formate}$ of Bi_2O_3@C/HB, Bi_2O_3@C/HL, C/HB and C/HL) in 0.5 M $KHCO_3$ saturated with CO_2. (d) Comparison of $FE_{formate}$, $j_{formate}$ and potential window ($FE_{formate}$ > 90%) for Bi_2O_3@C/HB and some typical Bi-based catalysts reported recently. (e) Formate formation rate of Bi_2O_3@C/HB and Bi_2O_3@C/HL. (f) Long-term stability tests of Bi_2O_3@C/HB and Bi_2O_3@C/HL at −1.2 V for 12 h.

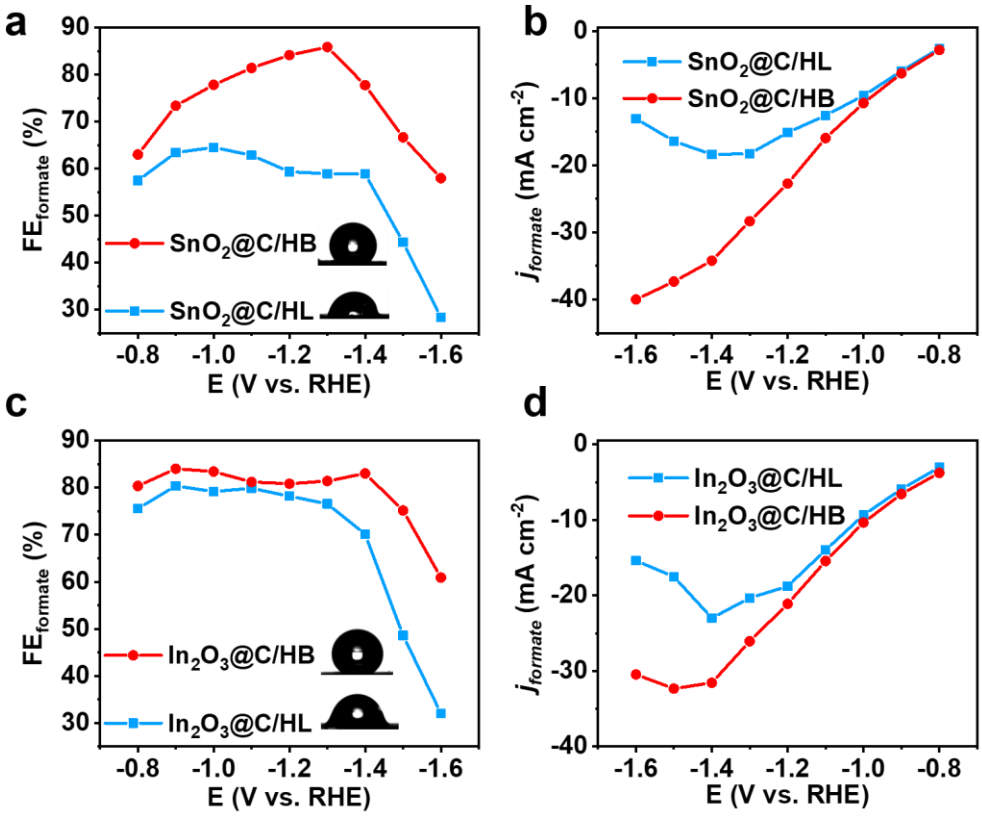

Figure 5.5 (a) FEs of formate and (b) partial current densities of formate for SnO_2@C/HB and SnO_2@C/HL. (c) FEs of formate and (d) partial current densities of formate for In_2O_3@C/HB and In_2O_3@C/HL.

To evaluate the stability of Bi_2O_3@C/HB, chronoamperometry at a fixed potential of −1.2 V was performed (Figure 5.4f). Apparently, the *j* and $FE_{formate}$ have no obvious degradation during the 12 h electrolysis, suggesting the favorable stability of Bi_2O_3@C/HB. By contrast, the $FE_{formate}$ of Bi_2O_3@C/HL decreased to only 60% after 12 h electrolysis. It has been reported that metallic Bi is prone to oxidation when exposed to air prior to post-mortem ECR characterizations. To examine the chemical state change of Bi_2O_3 during the ECR, *in situ* Raman spectroscopy was performed (Figure S5.11). A typical Raman signal at 313 cm^{-1} attributed to the Bi-O stretching mode can be observed at the open-circuit potential on Bi_2O_3@C/HB. This peak experienced a continuous decrease as the applied potential decreased, and completely disappeared at −0.8 V. This indicates

that the Bi^{3+} is *in situ* reduced to metallic Bi^0 during ECR. According to the recent experimental and theoretical studies,[33-34] the metallic Bi^0 can benefit the formation of *OCHO over *COOH, which leads to the formate production. This can explain that the $FE_{formate}$ can be largely maintained despite the occurrence of reduction of Bi_2O_3 to Bi. Furthermore, the nanosheets morphology underwent a significant transformation where a fractal nanostructure was observed (Figure 5.6a-d). As confirmed by a previous study,[35] the fractal structure would possess roughened edges and improved electron density,[35] which facilities the formation of $CO_2^{\bullet-}$. A recent study has also shown that the valance and morphology changes occur in the first hour of the ECR.[36] After this process, the catalyst could exist in a relatively stable state, therefore, the observation of the stable values of $FE_{formate}$ and j is logical and reasonable despite the valance and morphology change in the present case. More importantly, the hydrophobic and aerophilic features of Bi_2O_3@C/HB are preserved after the long-term ECR test (Figure 5.6e-h). This confirms the surface robustness of the C/HB even under high j_s through maintaining the triple-phase boundary during the ECR process.

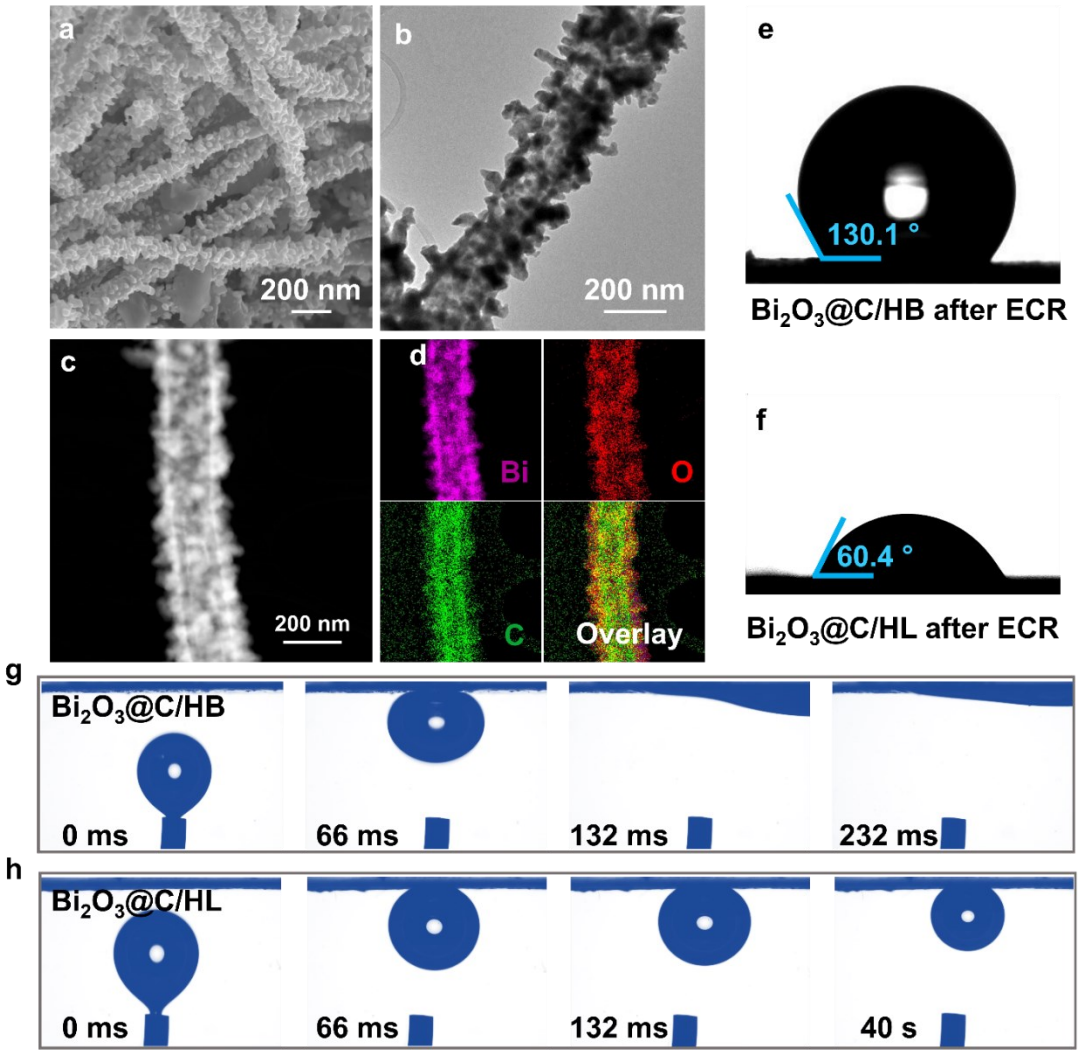

Figure 5.6 (a) SEM, (b) TEM images of Bi_2O_3@C/HB after stability test. (c) HAADF-STEM image of Bi_2O_3@C/HB and (d) corresponding elemental maps after stability test. Water contact angles of (e) Bi_2O_3@C/HB and (f) Bi_2O_3@C/HL after the stability test. CO_2 bubble adhesion experiments and the corresponding optical pictures of (g) Bi_2O_3@C/HB and (h) Bi_2O_3@C/HL electrodes in CO_2-saturated 0.5 M $KHCO_3$ solution after ECR.

A desirable ECR catalyst for formate-production should also be able to provide a satisfactory performance at the scale of commercial applications (> 200 mA cm^{-2}). Nonetheless, this is not an easy task to accomplish in a typical H-type cell due to the CO_2 mass transport limitation. To overcome this obstacle, the ECR performance of Bi_2O_3@C/HB was further evaluated in a flow

cell (Figure 5.8a). Previous studies have demonstrated that the use of alkaline electrolytes not only can benefit the activation of CO_2 molecules, but also can hinder the competitive HER, thus significantly accelerating the overall reaction rate.[37-39] In comparison with 1.0 M $KHCO_3$, the onset potential in 1.0 M KOH is obviously reduced (Figure 5.7a). Also, the use of alkaline electrolyte brings about high $FE_{formate}$ and j (Figure 5.7b).

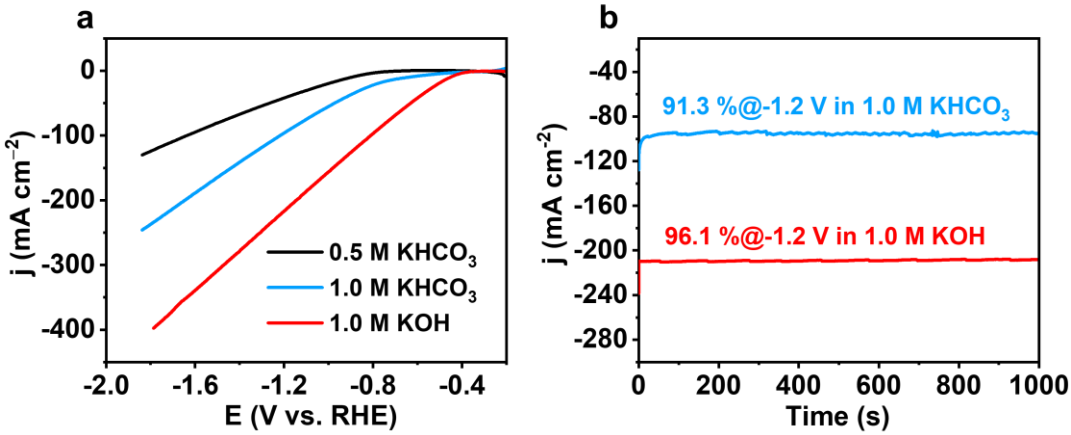

Figure 5.7 (a) LSV curves of Bi_2O_3@C/HB in different electrolytes in flow cell. (b) Chronopotentiometry curves at −1.2 V in 1.0 M $KHCO_3$ and 1.0 M KOH.

To this end, 1.0 M KOH was selected as the electrolyte in the flow cell. The onset potentials for Bi_2O_3@C/HB and Bi_2O_3@C/HL sharply decreased to about −0.41 V (Figure 5.8b), demonstrating the advantage of using flow cell reactor and alkaline electrolyte. As expected, Bi_2O_3@C/HB exhibits the higher current densities than Bi_2O_3@C/HL despite that they are both subjected to the same onset potential. Moreover, the use of highly concentrated electrolyte did not compromise the $FE_{formate}$ of Bi_2O_3@C/HB (Figure 5.8c). By contrast, the $FE_{formate}$ for Bi_2O_3@C/HL decreased significantly to 60% at −1.5 V, which may be attributed to the flooding issue of Bi_2O_3@C/HL electrode. Furthermore, Bi_2O_3@C/HB can deliver a $j_{formate}$ of −285 mA cm^{-2} at −1.5 V (Figure 5.8d), indicating its commercial viability. However, Bi_2O_3@C/HL only showed a $j_{formate}$ of −123 mA cm^{-2} due to the occurrence of flooding at −1.5 V. The anti-flooding capability of electrode

can be evaluated by capillary pressure difference ($\Delta P = P_{liquid} - P_{gas}$) across the liquid-gas interface,[16] which can be calculated according to Young-Laplace equation: $\Delta P = 2\sigma \sin(\Theta_a - 90°)/r$. In this equation, r and σ represent the pore radius and the surface tension of 1.0 M KOH (74.4 mN m^{-1}),[40] respectively. Θ_a is the advancing contact angle (134.8° for Bi_2O_3@C/HB and 82° for Bi_2O_3@C/HL). According to the above equation, a greater critical burst-through pressure is required for the hydrophobic electrode to allow the liquid to enter the pore (Figure 5.8e). Therefore, the anti-flooding capability of Bi_2O_3@C/HB is more effective than that of Bi_2O_3@C/HL. Moreover, liquid droplet can be clearly observed on the backside of Bi_2O_3@C/HL electrode after ECR test when compared with Bi_2O_3@C/HB electrode (Figure S5.12) This further suggests that the hydrophobicity of Bi_2O_3@C/HB can effectively prevent the catalyst from flooding, thus maintaining a stable hydrophobic microenvironment for ECR.

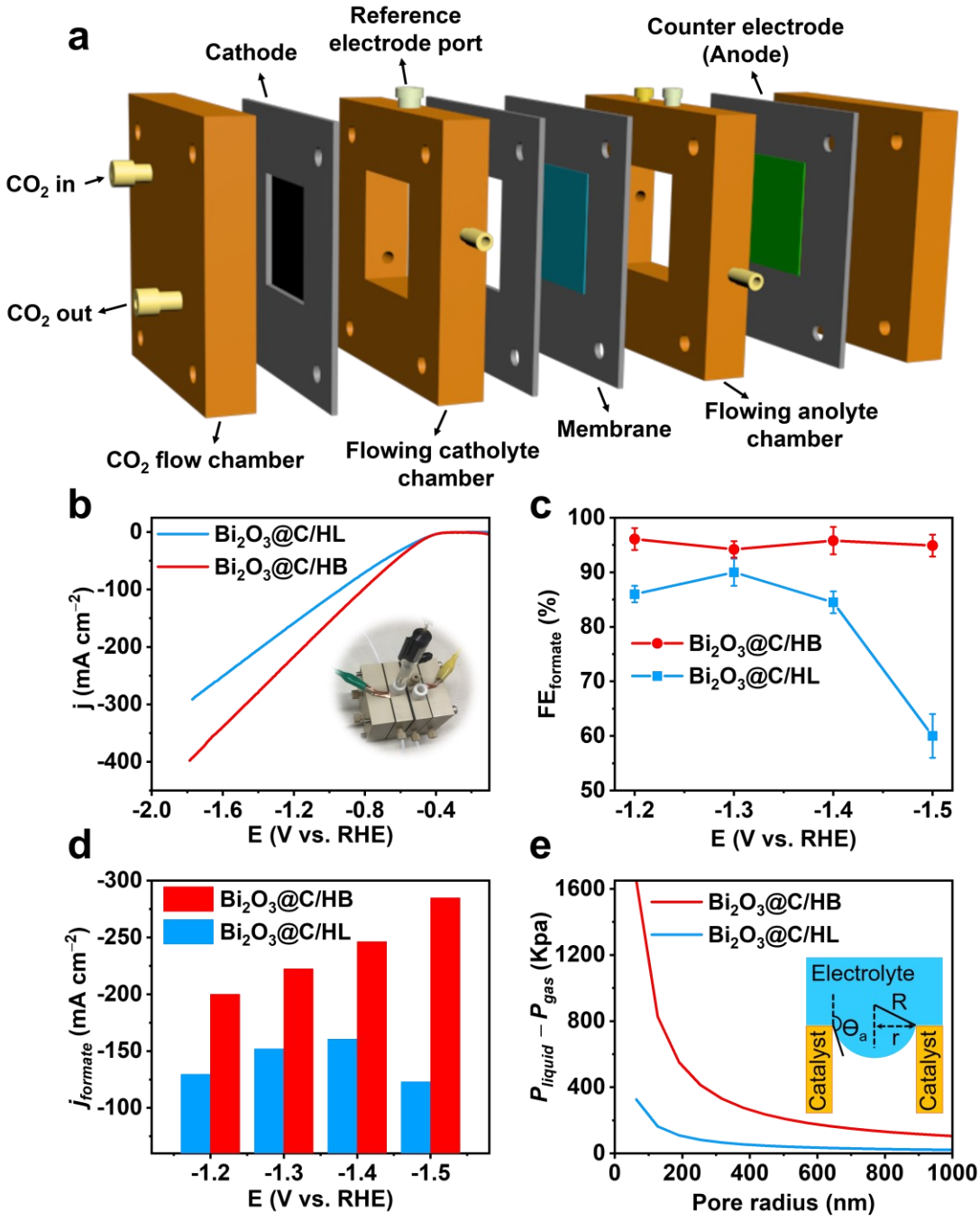

Figure 5.8 (a) Expanded diagram of flow cell reactor. (b) LSV curves, (c) $FE_{formate}$, and (d) $j_{formate}$ of Bi_2O_3@C/HL and Bi_2O_3@C/HB in flow cell reactor. (e) Critical burst-through pressure for Bi_2O_3@C/HL and Bi_2O_3@C/HB *versus* pore radius (inset: schematic diagram of advancing contact angle).

5.2.3 Mechanism of ECR promoted by the surface hydrophobic engineering

To uncover the origin of hydrophobic microenvironment-improved ECR performance, GROMACS (version 2020.4) was used to perform MD simulations.[41] Two carbon surface models with different surface oxygen-to-carbon ratios of 0.27 and 10.57% were built to represent C/HB and C/HL, respectively. Figure 5.9a and b show the snapshots of MD simulations for water/C/HB and water/C/HL, respectively. The radial distribution functions (RDFs) of water molecules around these two carbon surfaces (averaged from the last 3 ns of the simulation) are shown in Figure 5.9c. The RDFs for C/HL are higher than those of C/HB between 0.25 and 1.5 nm, indicating more water molecules in the proximity of C/HL because of the higher surface oxygen ratio. Moreover, for C/HL, water density reaches 90% of the bulk value (RDF = 0.9) at ~ 0.70 nm from the carbon surface, and the bulk density (RDF = 1) is reached at ~ 1.20 nm from the surface. For the C/HB, on the other hand, water density reaches 90% of the bulk value at a much greater distance of ~ 1.37 nm (almost doubling the distance in the case of C/HL), and the bulk density is attained at ~1.45 nm (a 20% increase from the case of C/HL). The numbers of hydrogen bonds formed between water and the carbon surface were also calculated and the results are plotted as the function of time in Figure 5.9d. Apparently, the average number of hydrogen bonds is 18 for C/HL while it is only 1 for the C/HB. Therefore, C/HB has facilitated the repulsion of water molecules away from the surface by avoiding the formation of hydrogen bonds, which explains why a much lower FE_{H2} was observed over Bi_2O_3@C/HB compared with that over Bi_2O_3@C/HL. These results collectively indicate that the C/HB can "push" water molecules away from the surface. Thus, the carbon support with lower surface oxygen ratio may be much less subjected to the flooding problem, which is the reason for the higher ECR performance over Bi_2O_3@C/HB than that over Bi_2O_3@C/HL in the flow cell system since flooding would favor HER over ECR.

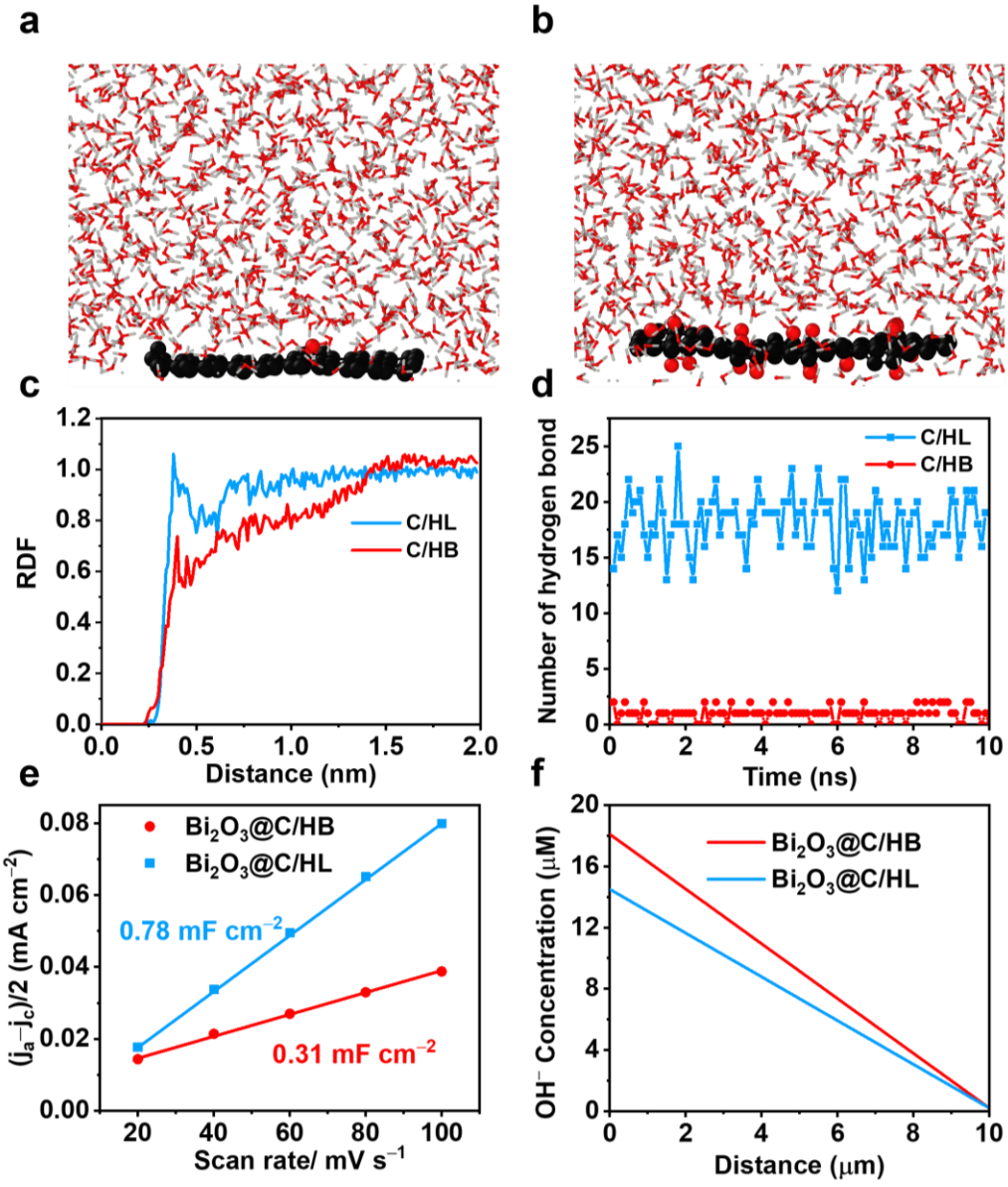

Figure 5.9 Interface structures after 3ns molecular dynamics simulations of (a) water/C/HB and (b) water/C/HL. Colors code: carbon, black; oxygen, red; grey, hydrogen. C/HB and C/HL are highlighted for viewing convenience. (c) The RDF of water molecules around C/HL and C/HB. (d) Number of hydrogen bonds formed between C/HL and C/HB. (e) Plots used for the double-layer capacitance (C_{dl}) calculation and to estimate the relative ECSA of Bi_2O_3@C/HB and Bi_2O_3@C/HL. (f) Calculated OH^- concentration profile in the boundary layer (10 μm) for Bi_2O_3@C/HB and Bi_2O_3@C/HL.

Since the MD simulations indicate that the C/HB can "push" water molecules away from its surface, we can surmise that a CO_2 gas layer is formed between solid catalysts and liquid electrolyte in the CO_2-saturated electrolyte due to the water repulsion effect of C/HB. To verify this hypothesis, the electrochemical active surface areas (ECSA) of Bi_2O_3@C/HL and Bi_2O_3@C/HB were compared. Previous study has demonstrated that a hydrophobic microenvironment around the catalyst could trap gases and then reduce ECSA because the gaseous layer would reduce the contact between electrode and electrolyte.[22] As shown in Figure 5.9e and Figure S5.13, the ECSA of Bi_2O_3@C/HB (0.31 mF cm^{-2}) decreased as compared to 0.78 mF cm^{-2} on Bi_2O_3@C/HL. This confirmed the presence of CO_2 gas layer and the formation of triple-phase boundary. The CO_2 adsorption capacity of Bi_2O_3@C/HB is 786.6 μmol g^{-1} (Figure S5.7), which is 1.96-fold higher than that of Bi_2O_3@C/HL (399.6 μmol g^{-1}), further suggesting the increased local CO_2 concentration. Additionally, surface hydrophobicity may change the concentration profile of OH^-, thus influencing the local pH on the catalyst surface.[42] The concentration profile of OH^- was constructed by a previous model.[43] Figure 5.9f shows that the concentration of OH^- over Bi_2O_3@C/HB increases more rapidly than that of Bi_2O_3@C/HL from the bulk electrolyte to the surface. This results in an increase of surface pH on Bi_2O_3@C/HB, as confirmed by the phenolphthalein test (Figure 5.10). The higher local pH on Bi_2O_3@C/HB surface not only can benefit the activation of CO_2 in the solution, but also greatly hinder HER because of the limited proton availability,[44] which benefits ECR.

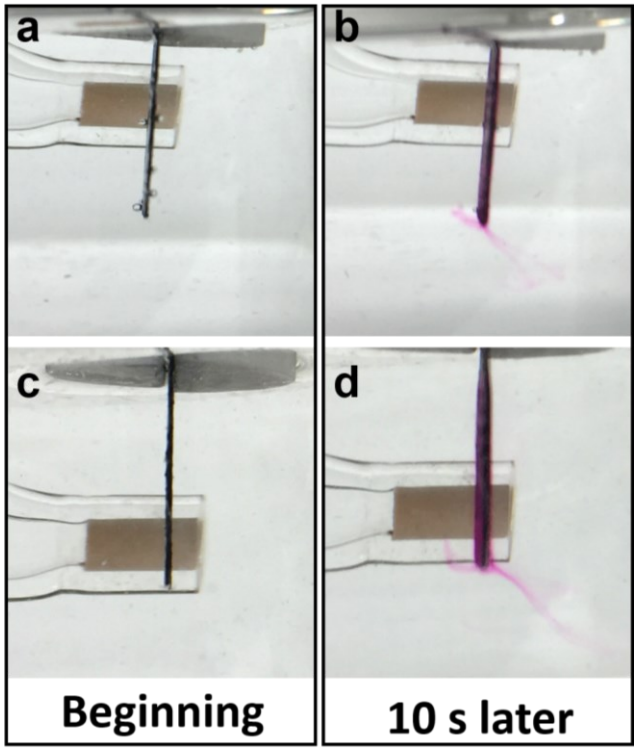

Figure 5.10 Phenolphthalein color transition experiment. Photographs of the phenolphthalein color transition experiment for (a, b) Bi_2O_3@C/HL and (c, d) Bi_2O_3@C/HB conducted at −1.2 V.

From the experimental and computational results, the hydrophobic carbon support can repel the water and form a concentrated CO_2 gas layer. This will bring about a large amount of triple-phase boundaries where active sites are accessible to both gaseous CO_2 and liquid electrolyte. Therefore, the CO_2 molecules from the gas layer, the H^+ from the liquid electrolyte, and the e^- transferred from the carbon support can greatly promote the ECR performance at the triple-phase boundary, as schematically shown in Figure 5.11a. The hydrophilic carbon support, however, cannot form such a desirable hydrophobic microenvironment because the active sites are fully in contact with the electrolyte, leading to H_2 formation due to an increased surface coverage of *H and the limited availability of CO_2 (Figure 5.11b).

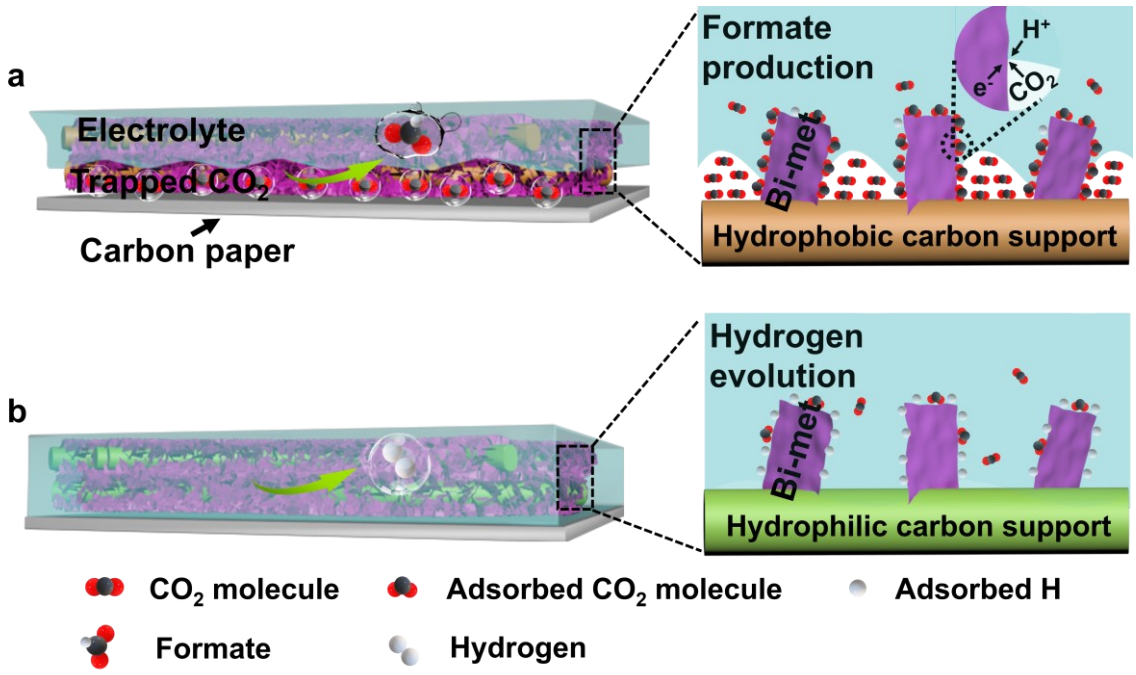

Figure 5.11 Illustration of microenvironment for ECR over (a) Bi_2O_3@C/HB and (b) Bi_2O_3@C/HL. The catalyst here is denoted as Bi-met because the Bi_2O_3 is quickly reduced to Bi^0 during ECR as confirmed by *in situ* Raman.

Based on the findings and results from this study, we then consider the applicability of the hydrophobic engineering presented herein for other types of electrochemical reactions involving gas phase. It is worth mentioning that our work differs from some previous studies in which a hydrophobic microenvironment was created by coating hydrophobic organics on the catalyst surface[22] or by adding PTFE suspensions in catalyst layer.[45] These approaches will have to sacrifice the activity to some extent. Another potential issue related to these polymer modifiers is the desorption and flushing-away of some small organic pieces, as mentioned in the Introduction.[23] It should also be mentioned that these polymers usually contain amine group which benefits CO_2 adsorption and binding of key reaction intermediates.[46-48] Thus, it is not easy to attribute the improved ECR performance solely to the hydrophobicity over the effects from amine group. Moreover, most prior studies mainly focused on enhancing the production of C_{2+} products over

Cu-based materials by surface hydrophobic engineering. Although most C_1-producing catalysts (such as Pd, Ag, Bi, In and Sn) have achieved high selectivity for C_1 products (formate or CO),[49-52] their formation rates still fall below the commercial requirement because it is difficult to attain high *j* in the presence of competing HER and the CO_2 mass transport limitation in aqueous medium. Benefiting from the hydrophobic microenvironment, the developed Bi_2O_3@C/HB catalyst in this study exhibits high selectivity at a high *j* for ECR toward formate production, thereby achieving high formate formation rate. Since carbon materials are extensively employed as the co-materials in catalyst design, the method of tuning surface chemistry of carbon support to create a hydrophobic microenvironment near catalyst surface could serve as a general approach to improving the electrolysis involving gas phase.

5.3 Conclusion

In summary, a hydrophobic microenvironment is realized by simply growing Bi_2O_3 NSs on hydrophobic carbon support. The Bi_2O_3@C/HB electrode exhibits a significant improved ECR activity towards formate production with high *j* of 102.1 mA cm^{-2} and $FE_{formate} > 90\%$ over a broad potential window (1000 mV). The hydrophobic microenvironment significantly inhibits HER by repelling water away from the catalyst surface and improves CO_2 mass transport by increasing the local CO_2 concentration. A higher surface pH is also achieved, which further enhances ECR activity while suppressing hydrogen evolution. This desirable microenvironment for ECR is constructed through tailoring the surface chemistry of carbon support. Since carbon materials have been widely employed as a catalyst support or improver, these findings provide a promising pathway to greatly boosting the performance of gas-involving electrolysis in aqueous medium.

5.4 References

1. Ma, Y.; Wang, J.; Yu, J.; Zhou, J.; Zhou, X.; Li, H.; He, Z.; Long, H.; Wang, Y.; Lu, P., Surface modification of metal materials for high-performance electrocatalytic carbon dioxide reduction. *Matter* 2021, *4* (3), 888-926.

2. De Luna, P.; Hahn, C.; Higgins, D.; Jaffer, S. A.; Jaramillo, T. F.; Sargent, E. H., What would it take for renewably powered electrosynthesis to displace petrochemical processes? *Science* 2019, *364* (6438).

3. Sordakis, K.; Tang, C.; Vogt, L. K.; Junge, H.; Dyson, P. J.; Beller, M.; Laurenczy, G., Homogeneous catalysis for sustainable hydrogen storage in formic acid and alcohols. *Chem. Rev.* 2018, *118* (2), 372-433.

4. Grasemann, M.; Laurenczy, G., Formic acid as a hydrogen source–recent developments and future trends. *Energy Environ. Sci.* 2012, *5* (8), 8171-8181.

5. Rahaman, M.; Dutta, A.; Broekmann, P., Size-Dependent Activity of Palladium Nanoparticles: Efficient Conversion of CO_2 into Formate at Low Overpotentials. *Chemsuschem* 2017, *10* (8), 1733-1741.

6. Wei, F.; Wang, T.; Jiang, X.; Ai, Y.; Cui, A.; Cui, J.; Fu, J.; Cheng, J.; Lei, L.; Hou, Y., Controllably engineering mesoporous surface and dimensionality of SnO_2 toward high-performance CO_2 electroreduction. *Adv. Funct. Mater.* 2020, *30* (39), 2002092.

7. Li, Z.; Cao, A.; Zheng, Q.; Fu, Y.; Wang, T.; Arul, K. T.; Chen, J. L.; Yang, B.; Adli, N. M.; Lei, L., Elucidation of the synergistic effect of dopants and vacancies on promoted selectivity for CO_2 electroreduction to formate. *Adv. Mater.* 2021, *33* (2), 2005113.

8. Liu, S.; Xiao, J.; Lu, X. F.; Wang, J.; Wang, X.; Lou, X. W., Efficient electrochemical reduction of CO_2 to HCOOH over sub-2 nm SnO_2 quantum wires with exposed grain boundaries. *Angew. Chem., Int. Ed.* 2019, *58* (25), 8499-8503.

9. Liu, S.-Q.; Gao, M.-R.; Feng, R.-F.; Gong, L.; Zeng, H.; Luo, J.-L., Electronic Delocalization of Bismuth Oxide Induced by Sulfur Doping for Efficient CO_2 Electroreduction to Formate. *ACS Catal.* 2021, *11*, 7604-7612.

10. Liu, S.; Lu, X. F.; Xiao, J.; Wang, X.; Lou, X. W., Bi_2O_3 nanosheets grown on multi-channel carbon matrix to catalyze efficient CO_2 electroreduction to HCOOH. *Angew. Chem.* 2019, *131* (39), 13966-13971.

11. Wen, G.; Lee, D. U.; Ren, B.; Hassan, F. M.; Jiang, G.; Cano, Z. P.; Gostick, J.; Croiset, E.; Bai, Z.; Yang, L., Orbital interactions in Bi-Sn bimetallic electrocatalysts for highly selective electrochemical CO_2 reduction toward formate production. *Adv. Energy Mater.* 2018, *8* (31), 1802427.

12. Ma, W.; Xie, S.; Zhang, X.-G.; Sun, F.; Kang, J.; Jiang, Z.; Zhang, Q.; Wu, D.-Y.; Wang, Y., Promoting electrocatalytic CO_2 reduction to formate *via* sulfur-boosting water activation on indium surfaces. *Nat. Commun.* 2019, *10* (1), 1-10.

13. Wu, D.; Wang, X.; Fu, X.-Z.; Luo, J.-L., Ultrasmall Bi nanoparticles confined in carbon nanosheets as highly active and durable catalysts for CO_2 electroreduction. *Appl. Catal. B* 2021, *284*, 119723.

14. Wuttig, A.; Yaguchi, M.; Motobayashi, K.; Osawa, M.; Surendranath, Y., Inhibited proton transfer enhances Au-catalyzed CO_2-to-fuels selectivity. *Proc. Natl. Acad. Sci. U.S.A.* 2016, *113* (32), 4585-4593.

15. Zhang, B. A.; Ozel, T.; Elias, J. S.; Costentin, C.; NoECRa, D. G., Interplay of homogeneous reactions, mass transport, and kinetics in determining selectivity of the reduction of CO_2 on Gold electrodes. *ACS Cent. Sci.* 2019, *5* (6), 1097-1105.

16. Li, J.; Chen, G.; Zhu, Y.; Liang, Z.; Pei, A.; Wu, C.-L.; Wang, H.; Lee, H. R.; Liu, K.; Chu, S., Efficient electrocatalytic CO_2 reduction on a three-phase interface. *Nat. Catal.* 2018, *1* (8), 592-600.

17. Pan, F.; Yang, Y., Designing CO_2 reduction electrode materials by morphology and interface engineering. *Energy Environ. Sci.* 2020, *13* (8), 2275-2309.

18. Raciti, D.; Mao, M.; Park, J. H.; Wang, C., Mass transfer effects in CO_2 reduction on Cu nanowire electrocatalysts. *Catal. Sci. Technol.* 2018, *8* (9), 2364-2369.

19. Wang, J.; Cheng, T.; Fenwick, A. Q.; Baroud, T. N.; Rosas-Hernández, A.; Ko, J. H.; Gan, Q.; Goddard Iii, W. A.; Grubbs, R. H., Selective CO_2 Electrochemical Reduction Enabled by a Tricomponent Copolymer Modifier on a Copper Surface. *J. Am. Chem. Soc.* 2021, *143* (7), 2857-2865.

20. Chen, X.; Chen, J.; Alghoraibi, N. M.; Henckel, D. A.; Zhang, R.; Nwabara, U. O.; Madsen, K. E.; Kenis, P. J.; Zimmerman, S. C.; Gewirth, A. A., Electrochemical CO_2-to-ethylene conversion on polyamine-incorporated Cu electrodes. *Nat. Catal.* 2021, *4* (1), 20-27.

21. Shi, R.; Guo, J.; Zhang, X.; Waterhouse, G. I.; Han, Z.; Zhao, Y.; Shang, L.; Zhou, C.; Jiang, L.; Zhang, T., Efficient wettability-controlled electroreduction of CO_2 to CO at Au/C interfaces. *Nat. Commun.* 2020, *11* (1), 1-10.

22. Wakerley, D.; Lamaison, S.; Ozanam, F.; Menguy, N.; Mercier, D.; Marcus, P.; Fontecave, M.; Mougel, V., Bio-inspired hydrophobicity promotes CO_2 reduction on a Cu surface. *Nat. Mater.* 2019, *18* (11), 1222-1227.

23. Schmitt, K. G.; Gewirth, A. A., *In situ* surface-enhanced Raman spectroscopy of the electrochemical reduction of carbon dioxide on silver with 3, 5-diamino-1, 2, 4-triazole. *J. Phys. Chem. C* 2014, *118* (31), 17567-17576.

24. Chen, R.; Su, H. Y.; Liu, D.; Huang, R.; Meng, X.; Cui, X.; Tian, Z. Q.; Zhang, D. H.; Deng, D., Highly selective production of ethylene by the electroreduction of carbon monoxide. *Angew. Chem.* 2020, *132* (1), 160-166.

25. Verma, S.; Hamasaki, Y.; Kim, C.; Huang, W.; Lu, S.; Jhong, H.-R. M.; Gewirth, A. A.; Fujigaya, T.; Nakashima, N.; Kenis, P. J., Insights into the low overpotential electroreduction of CO_2 to CO on a supported gold catalyst in an alkaline flow electrolyzer. *ACS Energy Lett.* 2017, *3* (1), 193-198.

26. Li, F.; Chen, L.; Knowles, G. P.; MacFarlane, D. R.; Zhang, J., Hierarchical mesoporous SnO2 nanosheets on carbon cloth: a robust and flexible electrocatalyst for CO_2 reduction with high efficiency and selectivity. *Angew. Chem.* 2017, *129* (2), 520-524.

27. Zhao, Z.; Hossain, M. D.; Xu, C.; Lu, Z.; Liu, Y.-S.; Hsieh, S.-H.; Lee, I.; Gao, W.; Yang, J.; Merinov, B. V., Tailoring a Three-Phase Microenvironment for High-Performance Oxygen Reduction Reaction in Proton Exchange Membrane Fuel Cells. *Matter* 2020, *3* (5), 1774-1790.

28. Zhang, X.; Sun, X.; Guo, S.-X.; Bond, A. M.; Zhang, J., Formation of lattice-dislocated bismuth nanowires on copper foam for enhanced electrocatalytic CO_2 reduction at low overpotential. *Energy Environ. Sci.* 2019, *12* (4), 1334-1340.

29. Yan, Y.; Cui, J.; Chan-Park, M.; Wang, X.; Wu, Q., Systematic studies of covalent functionalization of carbon nanotubes *via* argon plasma-assisted UV grafting. *Nanotechnology* 2007, *18* (11), 115712.

30. Lu, Z.; Xu, W.; Ma, J.; Li, Y.; Sun, X.; Jiang, L., Superaerophilic carbon-nanotube-array electrode for high-performance oxygen reduction reaction. *Adv. Mater.* 2016, *28* (33), 7155-7161.

31. Bligaard, T.; Nørskov, J. K.; Dahl, S.; Matthiesen, J.; Christensen, C. H.; Sehested, J., The Brønsted–Evans–Polanyi relation and the volcano curve in heterogeneous catalysis. *J. Catal.* 2004, *224* (1), 206-217.

32. Xing, Z.; Hu, L.; Ripatti, D. S.; Hu, X.; Feng, X., Enhancing carbon dioxide gas-diffusion electrolysis by creating a hydrophobic catalyst microenvironment. *Nat. Commun.* 2021, *12* (1), 1-11.

33. Gong, Q.; Ding, P.; Xu, M.; Zhu, X.; Wang, M.; Deng, J.; Ma, Q.; Han, N.; Zhu, Y.; Lu, J., Structural defects on converted bismuth oxide nanotubes enable highly active electrocatalysis of carbon dioxide reduction. *Nat. Commun.* 2019, *10* (1), 1-10.

34. Lee, C. W.; Hong, J. S.; Yang, K. D.; Jin, K.; Lee, J. H.; Ahn, H.-Y.; Seo, H.; Sung, N.-E.; Nam, K. T., Selective electrochemical production of formate from carbon dioxide with bismuth-based catalysts in an aqueous electrolyte. *ACS Catal.* 2018, *8* (2), 931-937.

35. Tran-Phu, T.; Daiyan, R.; Fusco, Z.; Ma, Z.; Amal, R.; Tricoli, A., Nanostructured β-Bi_2O_3 fractals on carbon fibers for highly selective CO_2 electroreduction to formate. *Adv. Funct. Mater.* 2020, *30* (3), 1906478.

36. Dutta, A.; Zelocualtecatl Montiel, I. n.; Kiran, K.; Rieder, A.; Grozovski, V.; Gut, L.; Broekmann, P., A Tandem (Bi_2O_3→ Bimet) Catalyst for Highly Efficient ec-CO_2 Conversion into Formate: Operando Raman Spectroscopic Evidence for a Reaction Pathway Change. *ACS Catal.* 2021, *11*, 4988-5003.

37. Deng, P.; Yang, F.; Wang, Z.; Chen, S.; Zhou, Y.; Zaman, S.; Xia, B. Y., Metal–Organic Framework-Derived Carbon Nanorods Encapsulating Bismuth Oxides for Rapid and Selective CO_2 Electroreduction to Formate. *Angew. Chem., Int. Ed.* 2020, *59* (27), 10807-10813.

38. Dinh, C.-T.; Burdyny, T.; Kibria, M. G.; Seifitokaldani, A.; Gabardo, C. M.; De Arquer, F. P. G.; Kiani, A.; Edwards, J. P.; De Luna, P.; Bushuyev, O. S., CO_2 electroreduction to ethylene *via* hydroxide-mediated copper catalysis at an abrupt interface. *Science* 2018, *360* (6390), 783-787.

39. Yang, J.; Wang, X.; Qu, Y.; Wang, X.; Huo, H.; Fan, Q.; Wang, J.; Yang, L. M.; Wu, Y., Bi-based metal-organic framework derived leafy bismuth nanosheets for carbon dioxide electroreduction. *Adv. Energy Mater.* 2020, *10* (36), 2001709.

40. O'Brien, T. F.; Bommaraju, T. V.; Hine, F., History of the chlor-alkali industry. In *Handbook of chlor-alkali technology*, Springer: 2005; pp 17-36.

41. Bai, C.; Herzfeld, J., Surface propensities of the self-ions of water. *ACS Cent. Sci.* 2016, *2* (4), 225-231.

42. Liang, H.-Q.; Zhao, S.; Hu, X.-M.; Ceccato, M.; Skrydstrup, T.; Daasbjerg, K., Hydrophobic copper interfaces boost electroreduction of carbon dioxide to ethylene in water. *ACS Catal.* 2021, *11* (2), 958-966.

43. Gupta, N.; Gattrell, M.; MacDougall, B., Calculation for the cathode surface concentrations in the electrochemical reduction of CO_2 in $KHCO_3$ solutions. *J. Appl. Electrochem.* 2006, *36* (2), 161-172.

44. Xiao, H.; Cheng, T.; Goddard III, W. A.; Sundararaman, R., Mechanistic explanation of the pH dependence and onset potentials for hydrocarbon products from electrochemical reduction of CO on Cu (111). *J. Am. Chem. Soc.* 2016, *138* (2), 483-486.

45. Cai, Z.; Zhang, Y.; Zhao, Y.; Wu, Y.; Xu, W.; Wen, X.; Zhong, Y.; Zhang, Y.; Liu, W.; Wang, H., Selectivity regulation of CO_2 electroreduction through contact interface engineering on superwetting Cu nanoarray electrodes. *Nano Res.* 2019, *12* (2), 345-349.

46. Zhao, Y.; Wang, C.; Liu, Y.; MacFarlane, D. R.; Wallace, G. G., Engineering surface amine modifiers of ultrasmall gold nanoparticles supported on reduced graphene oxide for improved electrochemical CO_2 reduction. *Adv. Energy Mater.* 2018, *8* (25), 1801400.

47. Chen, Z.; Zhang, X.; Jiao, M.; Mou, K.; Zhang, X.; Liu, L., Engineering Electronic Structure of Stannous Sulfide by Amino-Functionalized Carbon: Toward Efficient Electrocatalytic Reduction of CO_2 to Formate. *Adv. Energy Mater.* 2020, *10* (8), 1903664.

48. Kim, C.; Eom, T.; Jee, M. S.; Jung, H.; Kim, H.; Min, B. K.; Hwang, Y. J., Insight into electrochemical CO_2 reduction on surface-molecule-mediated Ag nanoparticles. *ACS Catal.* 2017, *7* (1), 779-785.

49. Lu, P.; Tan, X.; Zhao, H.; Xiang, Q.; Liu, K.; Zhao, X.; Yin, X.; Li, X.; Hai, X.; Xi, S., Atomically Dispersed Indium Sites for Selective CO_2 Electroreduction to Formic Acid. *ACS Nano* 2021, *15* (3), 5671-5678.

50. Liu, S.; Tao, H.; Zeng, L.; Liu, Q.; Xu, Z.; Liu, Q.; Luo, J.-L., Shape-dependent electrocatalytic reduction of CO_2 to CO on triangular silver nanoplates. *J. Am. Chem. Soc.* 2017, *139* (6), 2160-2163.

51. Han, N.; Ding, P.; He, L.; Li, Y.; Li, Y. J. A. E. M., Promises of main group metal–based nanostructured materials for electrochemical CO_2 reduction to formate. *Adv. Energy Mater.* 2020, *10* (11), 1902338.
52. Qi, K.; Zhang, Y.; Li, J.; Charmette, C.; Ramonda, M.; Cui, X.; Wang, Y.; Zhang, Y.; Wu, H.; Wang, W., Enhancing the CO_2-to-CO Conversion from 2D Silver Nanoprisms *via* Superstructure Assembly. *ACS Nano* 2021, *15* (4), 7682-7693.

5.5 Supporting information

5.5.1 Experimental section

Preparation of C/HL and C/HB: C/HB was the original PR-25-XT-HHTcarbon nanofiber. C/HL was prepared by acid treatment of C/HB as follows: 300 mg C/HB was refluxed at 120 ℃ in a mixed acid solution of H_2SO_4 and HNO_3 (3:1, *V*/*V*) for 12 h. The black powder was collected by centrifugation and washed with distilled water up to pH=7 and dried in vacuum.

Preparation of Bi_2O_3@C/HB and Bi_2O_3@C/HL: In a typical procedure of Bi_2O_3@C/HB preparation, $Bi(NO_3)_3{\cdot}5H_2O$ (0.97 g) was firstly dissolved in a mixture solution containing 26 mL ethanol and 13 ml ethylene glycol. After stirring for 30 min, C/HB (100 mg) was added and magnetically stirred for another 1 h. Then, the mixture was put into a Teflon-lined autoclave (100 mL) and the autoclave was sealed and heated at 160 ℃ for 5 h. The blackish precipitation was collected and washed with water and ethanol for three times, and freeze-dried under vacuum overnight. Bi_2O_3@C/HL was prepared by the same procedure as that of Bi_2O_3@C/HB except that C/HL was used in the hydrothermal reaction.

Preparation of SnO_2@C/HB and SnO_2@C/HL: In a typical procedure of SnO_2@C/HB preparation, $SnCl_4$ (40 uL) was added into DMF (24 mL) and stirred for 30 min. Then, 50 mg C/HB was added and stirred for another 1 h. The mixture was then poured into the Teflon-lined autoclave (100 mL) and reacted at 180 ℃ for 24 h. After cooling to room temperature, the products were collected and

washed repeatedly with water and ethanol for three times, and freeze-dried under vacuum overnight. SnO_2@C/HL was prepared by the same procedure as that of SnO_2@C/HB except that C/HL was used in the hydrothermal reaction.

Preparation of In_2O_3@C/HB and In_2O_3@C/HL: In a typical procedure of In_2O_3@C/HB preparation, $In(NO_3)_3{\cdot}9H_2O$ (0.924 g) was firstly dissolved in 20 mL ethanol completely, and then 20 ml distilled water was added. After stirring for 30 min, 100 mg C/HB was added and stirred for another 1 h. The mixture was then transferred into a Teflon-lined autoclave and reacted under 180 ℃ for 24 h. After colling, the precipitation was collected and washed with water and ethanol for three times and freeze-dried under vacuum overnight. In_2O_3@C/HL was prepared by the same procedure as that of In_2O_3@C/HB except that C/HL was used in the hydrothermal reaction.

5.5.2 Molecular Dynamics (MD) Simulations

OPLS-AA force field implemented GROMACS (version 2020.4) was used to perform MD.[S1-2] Two models of 2×2 nm^2 carbon surfaces were generated with different surface oxygen to carbon ratios (0.27 and 10.57 %). The force field parameters for the carbon surfaces were generated from the LigParGen server.[S3-4] Charge Model 5 (CM5) with a scale factor of 1.20 was used for the partial atomic charges.[S5] Each carbon surface was solvated with TIP4P water model[S6] in a box with dimensions of 4nm×4nm×5 nm. The system was firstly stabilized by energy minimization with a force tolerance of 1000 kJ mol^{-1} nm^{-1}, followed by a 200 ps equilibration. The production run was then carried out in NPT ensemble (isothermal-isobaric) for 10 ns. To determine hydrogen bonding, the following two criteria were used: 1) donor and acceptor distance lower than 3.5 Å; 2) angle of the hydrogen-donor-acceptor lower than 30°.

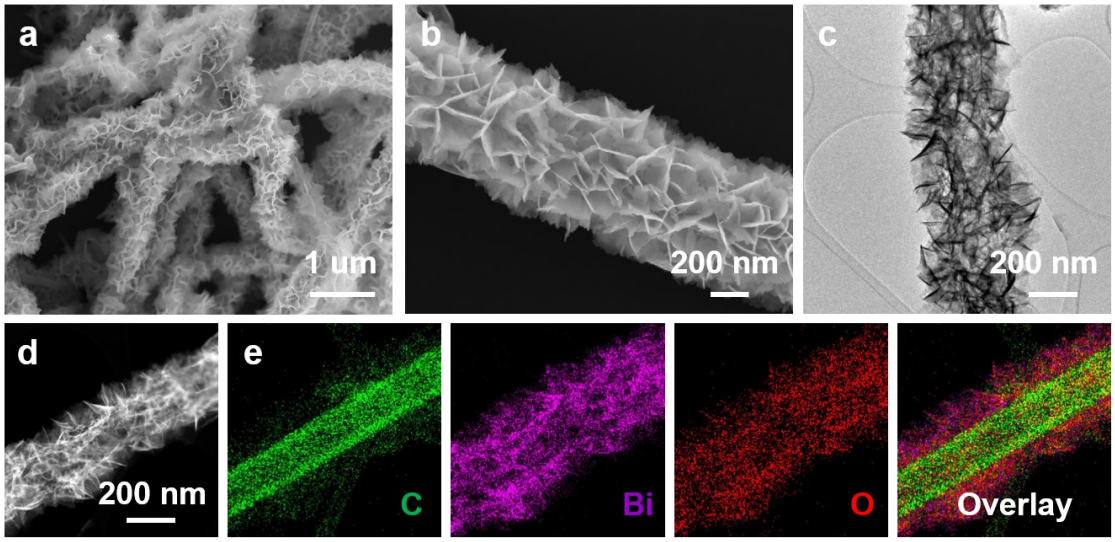

Figure S5.1 (a)-(c) SEM and TEM images of Bi_2O_3@C/HL. (d), (e) The HAADF-STEM image of Bi_2O_3@C/HL and corresponding elemental maps of C, Bi, and O.

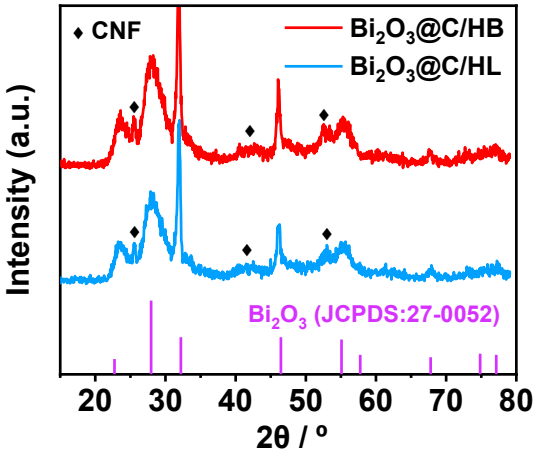

Figure S5.2 XRD patterns for Bi_2O_3@C/HB and Bi_2O_3@C/HL.

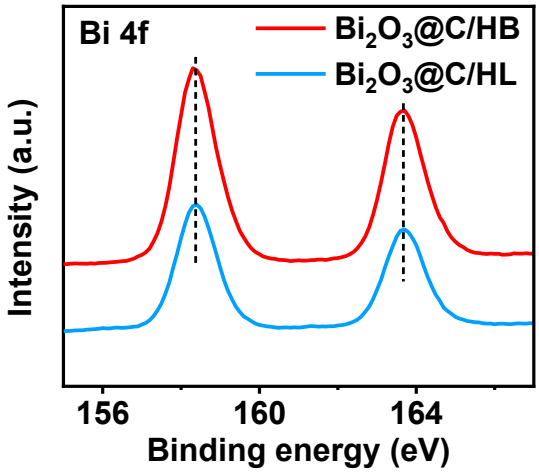

Figure S5.3 XPS spectra of Bi 4f for Bi_2O_3@C/HB and Bi_2O_3@C/HL.

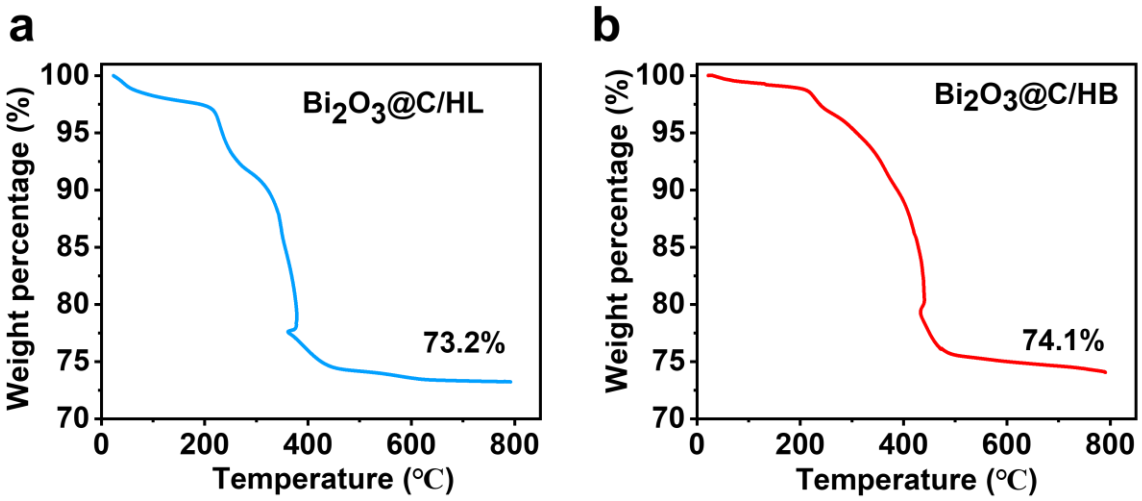

Figure S5.4 Weight losses for (a) Bi_2O_3@C/HL and (b) Bi_2O_3@C/HB.

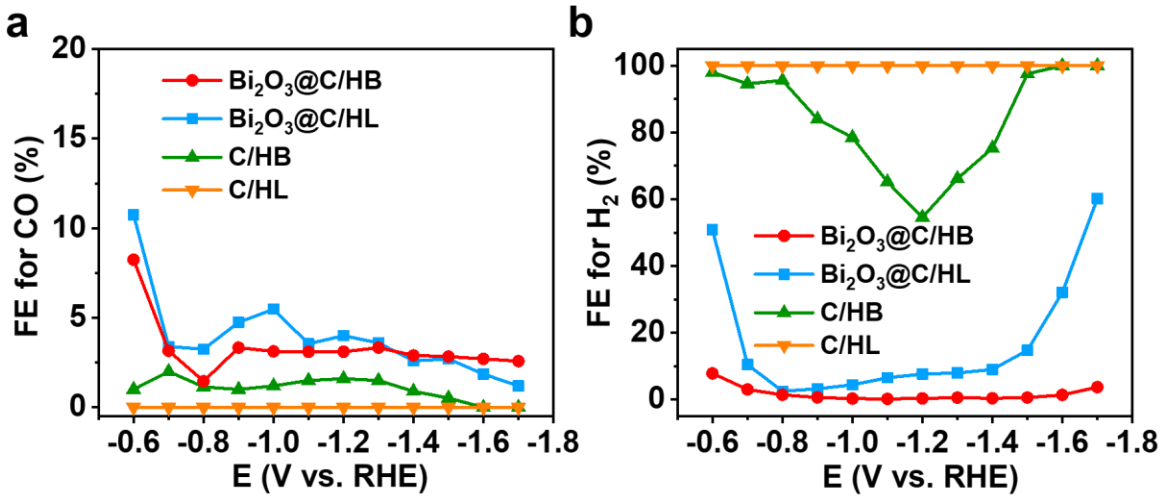

Figure S5.5 FEs of (a) CO and (b) H_2 for Bi_2O_3@C/HB, Bi_2O_3@C/HL, C/HB, and C/HL.

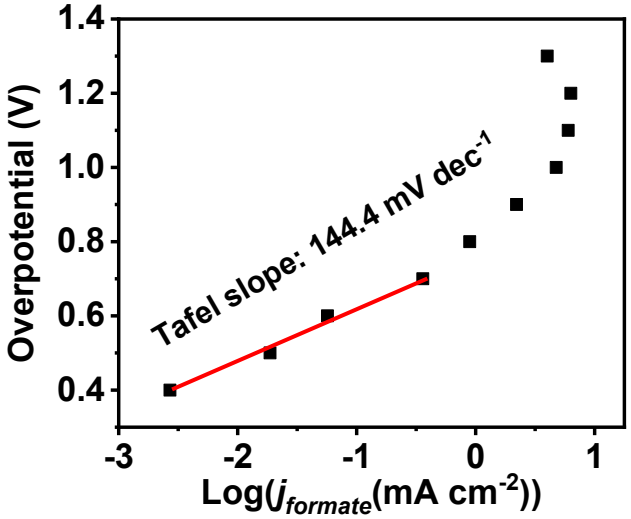

Figure S5.6 Tafel plot of C/HB for formate production.

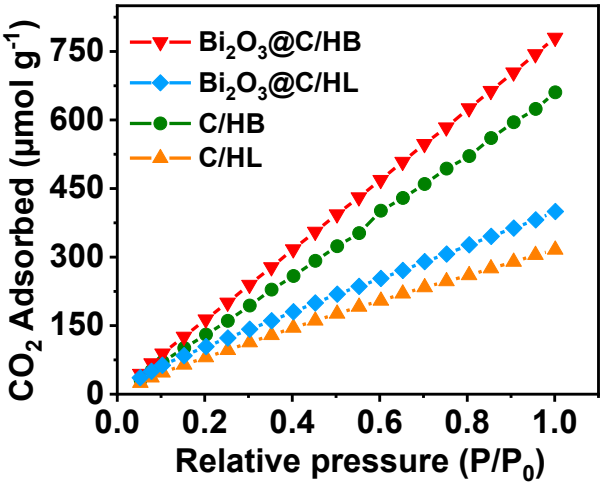

Figure S5.7 CO_2 adsorption isotherms of Bi_2O_3@C/HB, Bi_2O_3@C/HL, C/HB, and C/HL.

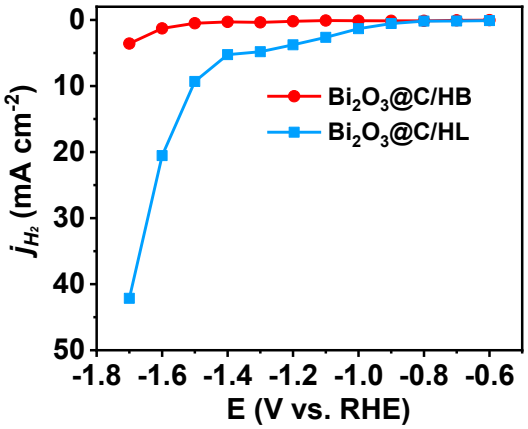

Figure S5.8 Partial current densities of H_2 on Bi_2O_3@C/HB and Bi_2O_3@C/HL.

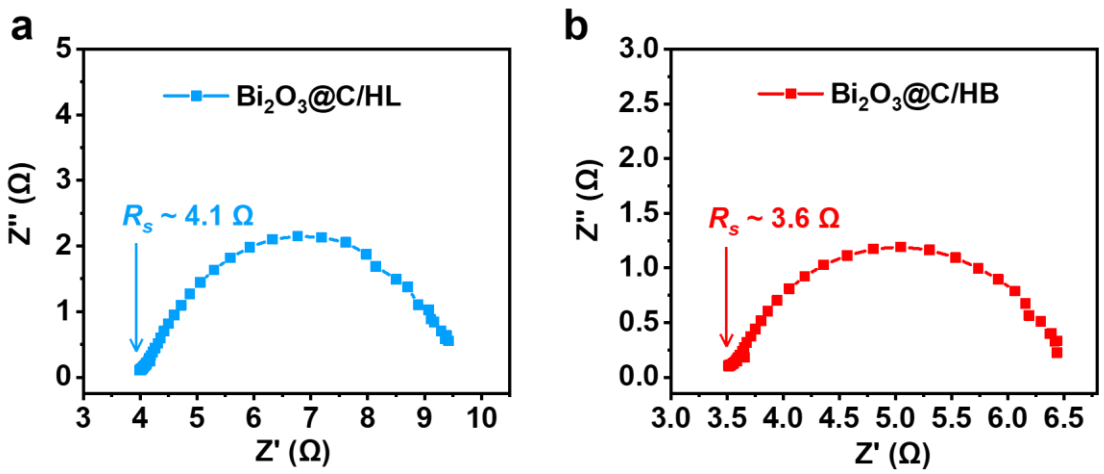

Figure S5.9 Electrochemical impedance spectra (EIS) of (a) Bi_2O_3@C/HL and (b) Bi_2O_3@C/HB.

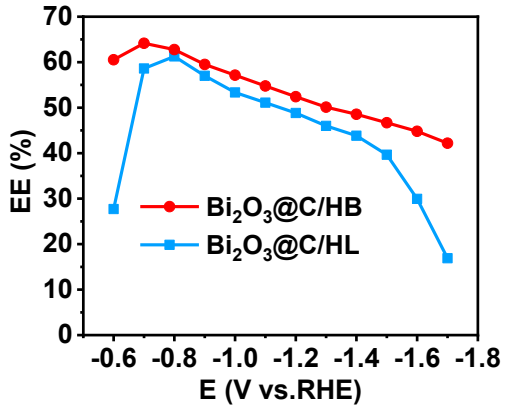

Figure S5.10 EEs of Bi_2O_3@C/HB and Bi_2O_3@C/HL.

Table S5.1 Electrocatalytic performances for CO_2 to formate in H-type cell over state-of-the-art catalysts reported recently.

Catalysts	Electrolyte	Potential (V *vs.* RHE)	$FE_{formate}$ (%)	$j_{formate}$ (mA cm^{-2})	Formation rate (μmol h^{-1} cm^{-2})	Potential window (mV; $FE_{formate}$ > 90 %)
Bimuthene@BP[S7]	0.5 M $KHCO_3$	−0.58	99	17	317	200
Bi nanotubes[S8]	0.5 M $KHCO_3$	−1.22	90	48	896	450
Bi_2O_3 nanotubes[S9]	0.5 M $KHCO_3$	−1.05	90	60	1120	300
Bi_2O_3NSs@MCCM[S10]	0.1 M $KHCO_3$	−1.355	90	17.7	330	300
Bi-ene[S11]	0.5 M $KHCO_3$	−1.18	99	72	1343	450
$Sn_{0.8}Bi_{0.2}$@Bi-SnO_x[S12]	0.5 M $KHCO_3$	−1.38	72	74.6	1392	250
Bismuth nanosheets[S13]	0.5 M $KHCO_3$	−0.7	100	8	149	130
Bi-Sn/CF[S14]	0.5 M $KHCO_3$	−1.14	96	45	740	160
Mesoporous Bi[S15]	0.5 M $NaHCO_3$	−1.05	82	17	317	240
POD-Bi[S16]	0.5 M $KHCO_3$	−1.16	95	52.8	985	300
BiO_x/C[S17]	0.1 M $KHCO_3$	−0.856	96	12.5	233	350
Bi NWs/copper foam[S18]	0.5 M $NaHCO_3$	−1.0	92	45	840	300
Bi_2O_3-NGQDs[S19]	0.5 M $KHCO_3$	−0.9	100	18	336	350
BiOBr[S20]	0.1 M $KHCO_3$	−0.9	95	60	1120	50
Bi-Sn aerogel[S21]	0.1 M $KHCO_3$	−1.0	93.9	9.3	173	200
Bi(btb)[S22]	0.5 M $KHCO_3$	−0.97	95	5	93	200
Bi_2O_3@C[S23]	0.5 M $KHCO_3$	−0.9	92	7.5	140	100
S-In_2O_3 derived In[S24]	0.5 M $KHCO_3$	−1.23	85	80.8	1501	100
S modified Sn[S25]	0.1 M $KHCO_3$	−0.75	93	55	1026	150
Bi_2O_3@C/HB (This study)	0.5 M $KHCO_3$	−1.4	96.7	77.3	1442	1000
		−1.5	96.5	86.1	1607	
		−1.6	96	94.1	1754	
		−1.7	93.7	102.1	1905	

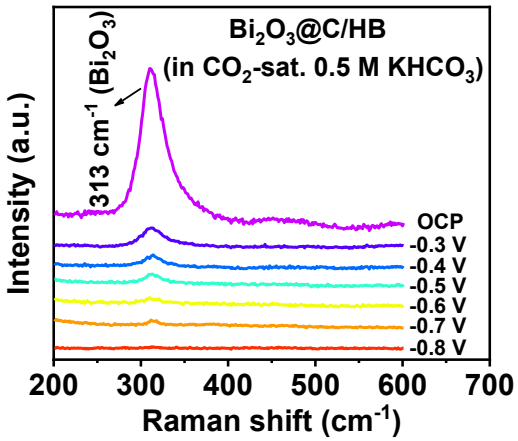

Figure S5.11 Series of potential-dependent Raman spectra showing the transition of Bi_2O_3 in CO_2-sat. 0.5 M $KHCO_3$ solution.

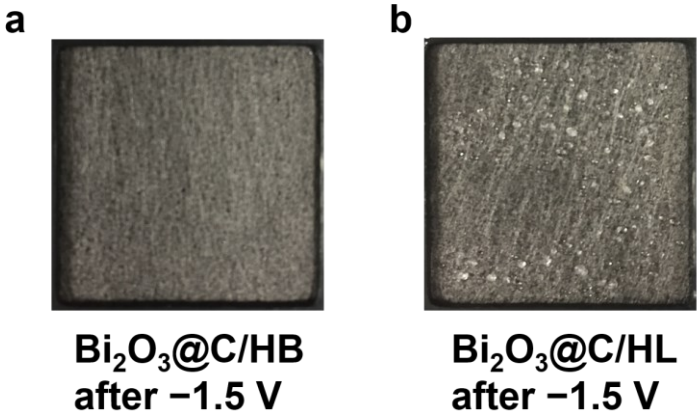

Figure S5.12 The backside of (a) Bi_2O_3@C/HB and (b) Bi_2O_3@C/HL electrodes after −1.5 V in flow cell.

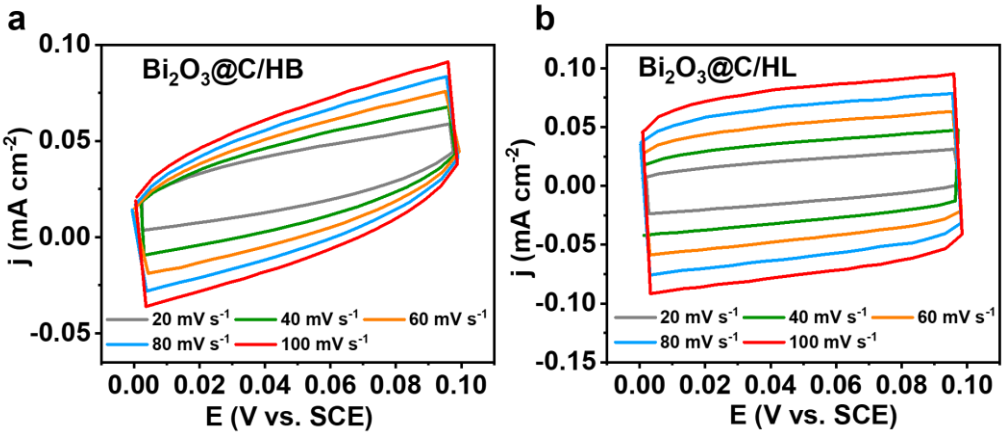

Figure S5.13 CV curves of (a) Bi_2O_3@C/HB and (b) Bi_2O_3@C/HL at various scan rates.

5.5.3 References

S1. Kaminski, G. A.; Friesner, R. A.; Tirado-Rives, J.; Jorgensen, W. L., Evaluation and reparametrization of the OPLS-AA force field for proteins *via* comparison with accurate quantum chemical calculations on peptides. *J. Phys. Chem. B* 2001, *105* (28), 6474-6487.

S2. Berendsen, H.; Hess, B.; Lindahl, E.; Van Der Spoel, D.; Mark, A.; Groenhof, G., GROMACS: fast, flexible, and free. *J. Comput. Chem.* 2005, *26* (16), 1701-1718.

S3. Jorgensen, W. L.; Tirado-Rives, J., Potential energy functions for atomic-level simulations of water and organic and biomolecular systems. *Proc. Natl. Acad. Sci. U.S.A.* 2005, *102* (19), 6665-6670.

S4. Dodda, L. S.; Cabeza de Vaca, I.; Tirado-Rives, J.; Jorgensen, W. L., LigParGen web server: an automatic OPLS-AA parameter generator for organic ligands. *Nucleic Acids Res.* 2017, *45* (W1), W331-W336.

S5. Dodda, L. S.; Vilseck, J. Z.; Cutrona, K. J.; Jorgensen, W. L., Evaluation of CM5 charges for nonaqueous condensed-phase modeling. *J. Chem. Theory Comput.* 2015, *11* (9), 4273-4282.

S6. Abascal, J. L.; Vega, C., A general purpose model for the condensed phases of water: TIP4P/2005. *J. Chem. Phys.* 2005, *123* (23), 234505.

S7. Yang, F.; Elnabawy, A. O.; Schimmenti, R.; Song, P.; Wang, J.; Peng, Z.; Yao, S.; Deng, R.; Song, S.; Lin, Y., Bismuthene for highly efficient carbon dioxide electroreduction reaction. *Nat. Commun.* 2020, *11* (1), 1-8.

S8. Fan, K.; Jia, Y.; Ji, Y.; Kuang, P.; Zhu, B.; Liu, X.; Yu, J., Curved surface boosts electrochemical CO_2 reduction to formate *via* bismuth nanotubes in a wide potential window. *ACS Catal.* 2019, *10* (1), 358-364.

S9. Gong, Q.; Ding, P.; Xu, M.; Zhu, X.; Wang, M.; Deng, J.; Ma, Q.; Han, N.; Zhu, Y.; Lu, J., Structural defects on converted bismuth oxide nanotubes enable highly active electrocatalysis of carbon dioxide reduction. *Nat. Commun.* 2019, *10* (1), 1-10.

S10. Liu, S.; Lu, X. F.; Xiao, J.; Wang, X.; Lou, X. W., Bi_2O_3 nanosheets grown on multi-channel carbon matrix to catalyze efficient CO_2 electroreduction to HCOOH. *Angew. Chem., Int. Ed.* 2019, *58* (39), 13828-13833.

S11. Cao, C.; Ma, D. D.; Gu, J. F.; Xie, X.; Zeng, G.; Li, X.; Han, S. G.; Zhu, Q. L.; Wu, X. T.; Xu, Q., Metal–organic layers leading to atomically thin bismuthene for efficient carbon dioxide electroreduction to liquid fuel. *Angew. Chem.* 2020, *132* (35), 15124-15130.

S12. Yang, Q.; Wu, Q.; Liu, Y.; Luo, S.; Wu, X.; Zhao, X.; Zou, H.; Long, B.; Chen, W.; Liao, Y., Novel Bi-Doped Amorphous SnO_x Nanoshells for Efficient Electrochemical CO_2 Reduction into Formate at Low Overpotentials. *Adv. Mater.* 2020, *32* (36), 2002822.

S13. Yi, L.; Chen, J.; Shao, P.; Huang, J.; Peng, X.; Li, J.; Wang, G.; Zhang, C.; Wen, Z., Molten-Salt-Assisted Synthesis of Bismuth Nanosheets for Long-term Continuous Electrocatalytic Conversion of CO_2 to Formate. *Angew. Chem.* 2020, *132* (45), 20287-20294.

S14. Wen, G.; Lee, D. U.; Ren, B.; Hassan, F. M.; Jiang, G.; Cano, Z. P.; Gostick, J.; Croiset, E.; Bai, Z.; Yang, L., Orbital interactions in Bi-Sn bimetallic electrocatalysts for highly selective electrochemical CO_2 reduction toward formate production. *Adv. Energy Mater.* 2018, *8* (31), 1802427.

S15. Yang, H.; Han, N.; Deng, J.; Wu, J.; Wang, Y.; Hu, Y.; Ding, P.; Li, Y.; Li, Y.; Lu, J., Selective CO_2 reduction on 2D mesoporous Bi nanosheets. *Adv. Energy Mater.* 2018, *8* (35), 1801536.

S16. He, S.; Ni, F.; Ji, Y.; Wang, L.; Wen, Y.; Bai, H.; Liu, G.; Zhang, Y.; Li, Y.; Zhang, B., The p-orbital delocalization of main-group metals to boost CO_2 electroreduction. *Angew. Chem., Int. Ed.* 2018, *57* (49), 16114-16119.

S17. Lee, C. W.; Hong, J. S.; Yang, K. D.; Jin, K.; Lee, J. H.; Ahn, H.-Y.; Seo, H.; Sung, N.-E.; Nam, K. T., Selective electrochemical production of formate from carbon dioxide with bismuth-based catalysts in an aqueous electrolyte. *ACS Catal.* 2018, *8* (2), 931-937.

S18. Zhang, X.; Sun, X.; Guo, S.-X.; Bond, A. M.; Zhang, J., Formation of lattice-dislocated bismuth nanowires on copper foam for enhanced electrocatalytic CO_2 reduction at low overpotential. *Energy Environ. Sci.* 2019, *12* (4), 1334-1340.

S19. Chen, Z.; Mou, K.; Wang, X.; Liu, L., Nitrogen-doped graphene quantum dots enhance the activity of Bi_2O_3 nanosheets for electrochemical reduction of CO_2 in a wide negative potential region. *Angew. Chem., Int. Ed.* 2018, *57* (39), 12790-12794.

S20. García de Arquer, F. P.; Bushuyev, O. S.; De Luna, P.; Dinh, C. T.; Seifitokaldani, A.; Saidaminov, M. I.; Tan, C. S.; Quan, L. N.; Proppe, A.; Kibria, M. G., 2D metal oxyhalide-derived catalysts for efficient CO_2 electroreduction. *Adv. Mater.* 2018, *30* (38), 1802858.

S21. Ma, T.; Wu, Z.; Wu, H.; Cai, W.; Wen, Z.; Wang, L.; Jin, W.; Jia, B., Engineering Bi-Sn Interface in Bimetallic Aerogel with 3D Porous Structure for Highly Selective Electrocatalytic CO_2 Reduction to HCOOH. *Angew. Chem., Int. Ed.* 2021, *60* (22), 12554-12599.

S22. Lamagni, P.; Miola, M.; Catalano, J.; Hvid, M. S.; Mamakhel, M. A. H.; Christensen, M.; Madsen, M. R.; Jeppesen, H. S.; Hu, X. M.; Daasbjerg, K., Restructuring metal–organic frameworks to nanoscale bismuth electrocatalysts for highly active and selective CO_2 reduction to formate. *Adv. Funct. Mater.* 2020, *30* (16), 1910408.

S23. Deng, P.; Yang, F.; Wang, Z.; Chen, S.; Zhou, Y.; Zaman, S.; Xia, B. Y., Metal–Organic Framework-Derived Carbon Nanorods Encapsulating Bismuth Oxides for Rapid and Selective CO_2 Electroreduction to Formate. *Angew. Chem., Int. Ed.* 2020, *59* (27), 10807-10813.

S24. Ma, W.; Xie, S.; Zhang, X.-G.; Sun, F.; Kang, J.; Jiang, Z.; Zhang, Q.; Wu, D.-Y.; Wang, Y., Promoting electrocatalytic CO_2 reduction to formate *via* sulfur-boosting water activation on indium surfaces. *Nat. Commun.* 2019, *10* (1), 1-10.

S25. Zheng, X.; De Luna, P.; de Arquer, F. P. G.; Zhang, B.; Becknell, N.; Ross, M. B.; Li, Y.; Banis, M. N.; Li, Y.; Liu, M., Sulfur-modulated tin sites enable highly selective electrochemical reduction of CO_2 to formate. *Joule* 2017, *1* (4), 794-805.

Chapter 6 A pair-electrolysis tactic for low energy generation of formate

So far in this thesis, the counter anodic half-reaction of CO_2 electrolyzers is the oxygen evolution reaction (OER). However, ~ 90% of the energy input is consumed by OER in a conventional CO_2 electrolyzer according to thermodynamic analysis. Also, its product, O_2, is not of significant value. Lowering the full-cell energy input in CO_2 electrolyzer by replacing OER with more energy favorable organic oxidation reactions is of importance. In this chapter, I introduced a pair-electrolysis, cathodic ECR and anodic ethylene glycol oxidation (EGO), to co-produce formate at both cathode and anode with much lower energy input.

Herein, I prepared single Cu atom doped Bi (BiCu) as the cathodic ECR catalyst *via* an *in situ* electrochemical reduction method. X-ray absorption spectroscopy was used to identify the single atom form of Cu within the BiCu catalyst. The incorporation of single Cu atom almost doubled the production rate of formate as compared to pure Bi catalyst. The BiCu exhibited a record-high formate partial current density of ~1.1 A cm^{-2} at −0.9 V *vs*. RHE with excellent stability. For the anodic EGO catalyst, I synthesized a nickel-modified cobalt phosphide nanosheet on nickel foam (NiCoP/NF). The NiCoP/NF could selectively electrooxidize ethylene glycol to formate with FE > 90%. The ECR-EGO coupling system showed ~ 760 mV decrease of cell voltage for reaching the same current density compared with ECR-OER system.

The work in this chapter has been submitted to a Journal for review. As first author, I prepared the catalysts, performed all characterizations and electrocatalysis experiments, and wrote the manuscript. Min-Rui Gao conducted the DFT calculations.

Abstract: Electrochemical CO_2 reduction provides a promising route to storing renewable energy and simultaneously mitigating global reliance on fossil fuels. However, the counter anodic OER reduces the energy efficiency of the process without providing a valuable product. Substituting OER with thermodynamically favorable oxidation reactions is an emerging strategy to reduce the full-cell energy input and generate valuable products on both sides of the cell. In this work, we report a pair-electrolysis strategy for efficient formate generation by a concurrent cathodic ECR and anodic EGO using single Cu atom doped Bi (BiCu) and nickel-modified cobalt phosphide nanosheet grown on nickel foam (NiCoP/NF) as cathodic and anodic catalysts, respectively. Anodic NiCoP/NF enables an extremely lowered potential of 1.5 V *vs*. RHE (200 mA cm^{-2}), featuring a significantly enhanced electro-activity in comparison to the OER. The cathodic BiCu shows a record-high formate partial current density of 1.1 A cm^{-2} at −0.9 V *vs*. RHE. Compared with ECR-OER system, the coupled ECR-EGO system requires a cell voltage of ~ 760 mV lower to achieve 40 mA cm^{-2}.

6.1 Introduction

As revealed by a recent Gibbs free energy analysis, the counter anodic OER consumes about 90 % of the total energy input in a typical ECR to formate.[1-2] In addition, the economic value of the produced O_2 is negligible and may result in reactive oxygen species, which will shorten the life of cell membrane.[3] Replacing OER with thermodynamically more favorable anode reactions is highly desirable because it not only can lower the overall energy input but also generate value-added products from inexpensive industrial feedstocks or renewable biomass sources. Recently, various organic oxidation reactions such as methanol oxidation,[4] glycerol oxidation,[5] glucose oxidation,[6] ethylene glycol oxidation,[7] ethanol oxidation,[8] and furfural oxidation[9] have been utilized to replace OER in water splitting for hydrogen production.

Polyethylene terephthalate (PET), the most abundant polyester plastic, is produced from textiles and packaging up ~ 70 million per year.[10] However, only < 20% of them are recycled through thermomechanical means. Recent studies show that PET can be depolymerized into monomers, such as ethylene glycol (EG) or terephthalic acid (TPA), *via* alkaline hydrolysis under mild conditions.[11-12] Recently, Zhou and co-workers reported an electrocatalytic strategy for PET waste upcycling to commodity chemicals of potassium diformate (KDF) and TPA paired with H_2 production.[7] The EG monomer of PET is selectively (> 90%) electro-oxidized to formate over anodic $CoNi_{0.25}P$ catalyst which improves H_2 production rate at cathode. Considering that ~ 90% of the overall energy requirements is coming from the OER, this pair-electrolysis strategy can also be applicable for overall ECR system. Therefore, coupling ECR with EGO could provide a sustainable way to implement waste PET upcycling to value-added products if the EG monomer directly comes from PET decomposition *via* alkaline hydrolysis.

A Gibbs free energy analysis is then conducted to evaluate the feasibility of ECR-EGO system. The half-reactions on the anode and the cathode as well as overall reaction for ECR-OER and ECR-EGO are proposed to be as Equations (6.1), (6.2), (6.3), (6.4), and (6.5), respectively.

$$\text{Cathode reaction (ECR): } CO_2 + 2H^+ + 2e^- \rightarrow HCOOH \quad (6.1)$$

$$\text{Anode reaction (OER): } H_2O \rightarrow 2H^+ + 2e^- + 0.5O_2 \quad (6.2)$$

$$\text{Anode reaction (EGO): } C_2H_6O_2 + 2H_2O \rightarrow 2HCOOH + 6H^+ + 6e^- \quad (6.3)$$

$$\text{Overall reaction (ECR-OER): } CO_2 + H_2O \rightarrow HCOOH + 0.5O_2 \quad (6.4)$$

$$(\Delta_f G^0 = 270.1 \text{ kJ mol}^{-1}, E^0_{cell} = 1.4 \text{ V})$$

$$\text{Overall reaction (ECR-EGO): } 0.6CO_2 + 0.2C_2H_6O_2 + 0.4H_2O \rightarrow HCOOH \quad (6.5)$$

$$(\Delta_f G^0 = 34.7 \text{ kJ mol}^{-1}, E^0_{cell} = 0.3 \text{ V})$$

The standard Gibbs free energies of the reaction ($\Delta_f G^0$) for Equations (6.4) and (6.5) are calculated using Hess's law, and the analysis indicates that the ECR-EGO system is more energy favorable than ECR-OER system. Naturally, a much lower equilibrium potential of 0.3 V is required to derive the ECR-EGO system compared to ECR-OER (1.4V). From the thermodynamic perspective, ~ 80% of the overall energy consumption can be reduced by replacing OER with EGO.

To this end, I herein introduce a pair-electrolysis tactic for concurrent ECR at the cathode and EGO at the anode to an identical value-added product of formate with rather low energy input and non-precious metal catalysts. Transition metal-based phosphides (especially for earth-abundant Co and Ni) are promising electrocatalyst for EGO. Ni and Co phosphides *in situ* grown on three-dimensional substrate enable fast electron and mass transfer due to the seamless contact. The Ni modified Co phosphides nanosheets grown on nickel foam (NiCoP/NF), prepared *via* tandem electrodeposition and phosphidation according to a previous work[7], were utilized as the anodic catalyst for EGO. Not surprisingly, the as-obtained NiCoP/NF catalyst exhibits high activity and selectivity for oxidizing ethylene glycol to formate.

Although Bi-based catalysts have been reported to convert CO_2 into formate with high selectivity, they unfortunately have all suffered from either low activity (< 500 mA cm^{-2}) or poor stability (< 20 h), which hinders their practical application for ECR.[13-15] Recent studies have revealed that the water dissociation process also plays a significant role in the overall ECR because the intermediate protonation steps ($*CO_2 \rightarrow *OCHO \rightarrow *HCOOH$) are closely related to the water dissociation process.[16-19] Bi itself is kinetic sluggish for water dissociation because of its weak hydrogen adsorption energy.[20-21] This could be a reason for Bi-based catalyst to fail in limited partial formate current density. Single-atom alloy catalysts are fabricated in a way that the foreign atoms are atomically dispersed into the matrix of a host metal. These catalysts have been widely utilized to

promote water dissociation for HER by optimizing the adsorption energy of *H.[22-27] According to a volcano plot of exchange current density as a function of hydrogen adsorption free energy over various metals, Cu possesses a moderate hydrogen binding strength that is stronger than that of Bi but weaker than those of Pt and Ni.[21] Introducing atomic Cu into Bi matrix may enable a favorable water dissociation to produce *H and easy subsequent desorption to neighbor Bi site for intermediate protonation. Therefore, single Cu atom doped Bi (BiCu) was developed and employed as an efficient cathodic catalyst for ECR to formate. Benefiting from the promoted water dissociation ability from single Cu atom incorporation, the as-obtained BiCu shows a record-high ECR-to-formate performance, including a high $j_{formate}$ of ~1.1 A cm^{-2} and good long-term stability (200 mA cm^{-2} for 45 h).

Finally, when equipped with NiCoP/NF at the anode and BiCu at the cathode, the established electrolyzer only needs a cell voltage as low as 1.78 V to achieve 40 mA cm^{-2}, which is 760 mV lower than that of conventional overall ECR under the same catalysis condition with NiCoP/NF at anode and BiCu at cathode without the addition of EG. The present pair-electrolysis strategy provides an innovative and highly promising way for the efficient production of formate with high efficiency.

6.2 Results and discussion

6.2.1 Synthesis and characterization of anodic NiCoP/NF catalyst

The NiCoP/NF catalyst was synthesized *via* a tandem electrodeposition and phosphidation process.[7] Firstly, the metal hydroxides ($NiCo(OH)_2$) were electrodeposited on NF within a three-electrode system in an aqueous solution. As shown in Figure 6.1a, the $NiCo(OH)_2$ exhibits a typical nanosheet morphology with smooth surface. After phosphidation treatment at 300 ^oC for 2h with NaH_2PO_2 as phosphorus source, the dense and uniform nanosheets morphology can be well

retained (Figure 6.1b-d), while the surface of nanosheets becomes rough and porous. From the XRD pattern of $NiCo(OH)_2$/NF (Figure 6.2), two characteristic peaks at 10.9° and 60.1° can be assigned to (001) and (110) planes of α-$Co(OH)_2$ (JCPDS:74-1057). These two peaks disappeared after phosphidation, while two new peaks at 41° and 54.5° coincided well with (111) and (300) planes of NiCoP (JCPDS: 71-2336). The EDX mapping results display the homogeneous distribution of Ni, Co, and P elements throughout the nanosheet, suggesting the successful fabrication of metal phosphides.

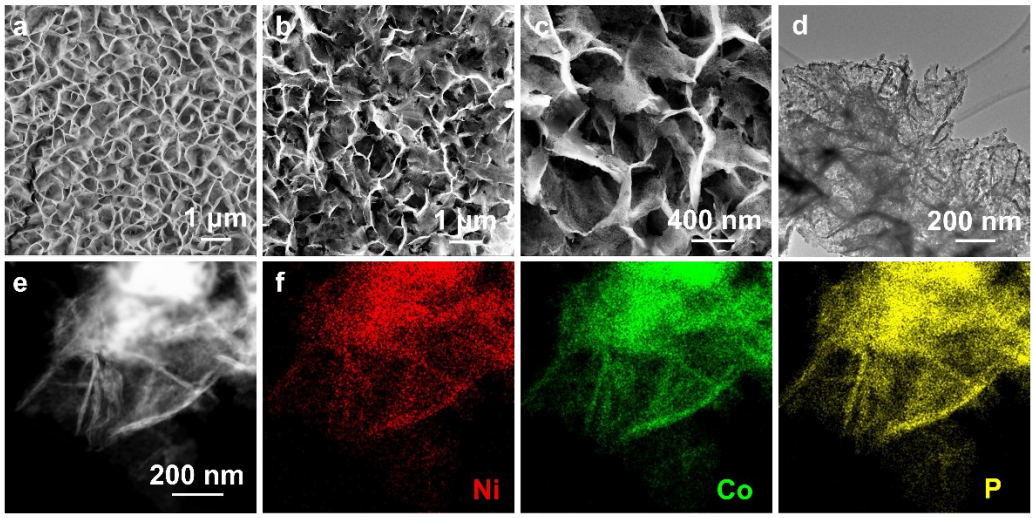

Figure 6.1 (a) SEM image of $NiCo(OH)_2$/NF and (b, c) NiCoP/NF. (d) TEM image of NiCoP. HAADF-STEM image and corresponding EDX mapping of NiCoP.

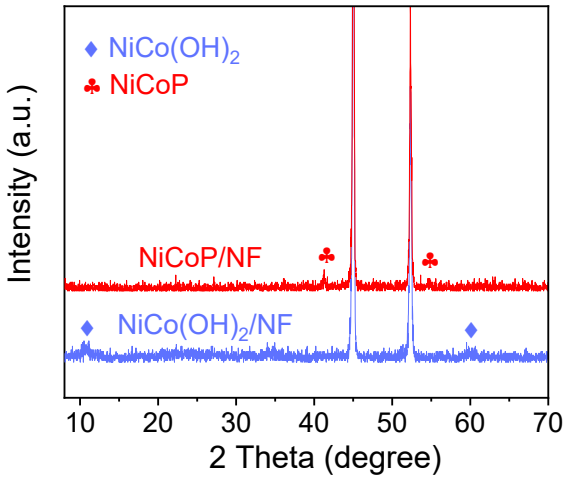

Figure 6.2 XRD patterns for $NiCo(OH)_2$/NF and NiCoP/NF.

6.2.2 Synthesis and characterization of cathodic BiCu catalyst

I first synthesized the Cu doped layered bismuth nitrate-$Bi_6O_6(OH)_3(NO_3)_3 \cdot 1.5H_2O$ (BiOON-Cu) precursor by hydrolyzing commercial bismuth nitrate with the addition of Copper (II) acetylacetonate. The XRD pattern of BiOON-Cu confirmed its crystalline nature (Figure 6.3a). SEM and TEM images of the BiOON-Cu showed that it was composed of hierarchical microflowers that were assembled from few-layer-thick nanosheets (Figure 6.3b, c). The lattice spacing in the HRTEM image was measured to be 0.37 nm, corresponding to the (101) plane of tetragonal BiOON (Figure 6.3d, e). EDX element mapping exhibits a uniform spatial distribution of Bi, Cu, Br, O, and N in the BiOON-Cu nanosheet, suggesting the successful incorporation of Cu (Figure 6.3f, g). To prepare the single Cu atom doped Bi catalyst, the BiOON-Cu precursor was electrochemically reduced at −1.6 V *vs*. SCE in 1.0 M KOH electrolyte for 10 min. XRD peaks of the reduced material can be well matched to the metallic Bi (Figure 6.4a), coinciding with the XPS analysis (Figure 6.4b, c). I further utilized operando X-ray absorption spectroscopy (XAS) to catch this reduction process. As indicated by the Bi L3-edge XAS spectra under different applied

potentials (Figure 6.4d), the absorption edge of Bi shifted negatively from open circuit voltage and overlapped with metallic Bi reference. This suggests that the active phase during ECR is metallic. It is worth noting that the *in situ* formed BiCu catalyst still retains the original nanosheet morphology of BiOON-Cu (Figure 6.5a-c). HRTEM analysis revealed obvious lattice spacing of 0.33 nm, which agrees well with the (012) interplanar spacing in rhombohedral Bi (Figure 6.5d, e).

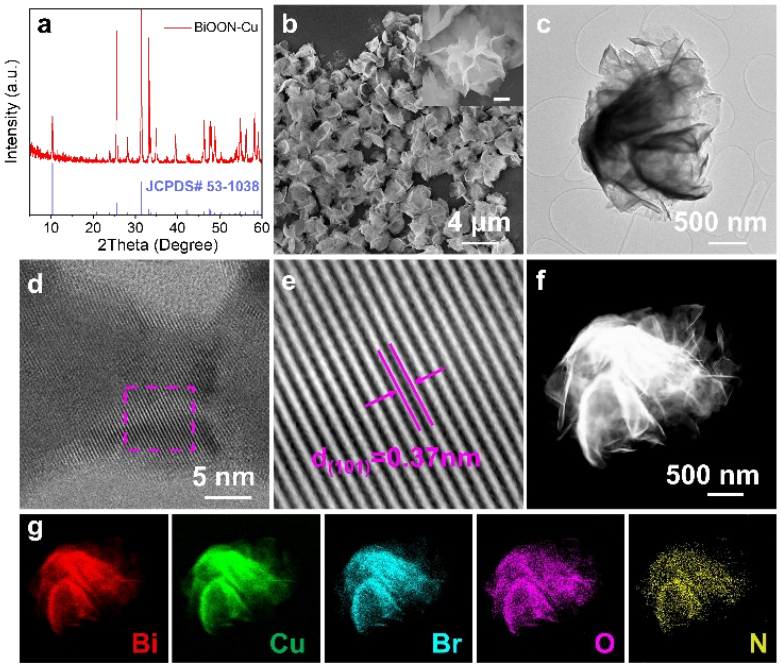

Figure 6.3 (a) XRD pattern of BiOON-Cu. (b) SEM images of BiOON-Cu (scale bar in the top-right corner: 500 nm). (c) TEM image of BiOON-Cu. (d, e) HRTEM images of BiOON-Cu. (f, g) HAADF-STEM image and corresponding EDX mapping of BiOON-Cu.

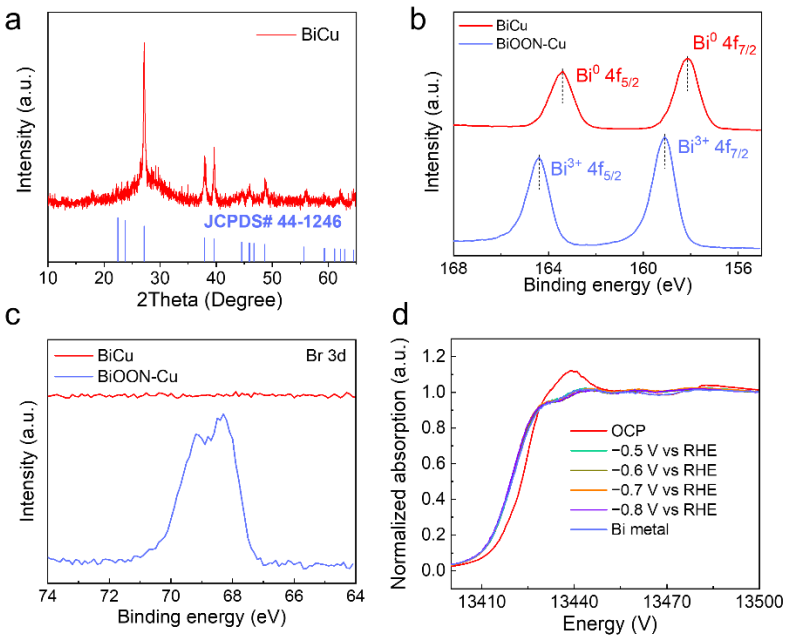

Figure 6.4 (a) XRD pattern of BiCu. (b) High-resolution Bi 4f and (c) Br XPS spectra for BiOON-Cu and BiCu. (d) *In situ* Bi L-edge XAS spectra of BiOON-Cu at different potentials during electrocatalytic ECR.

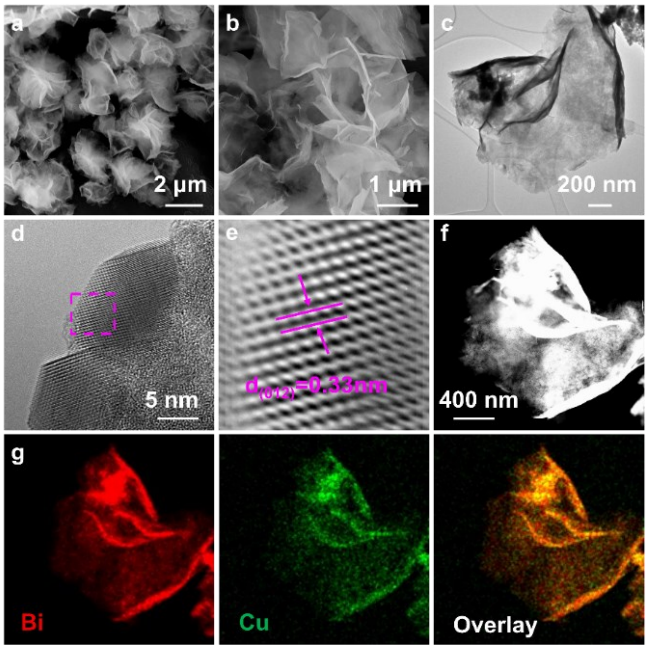

Figure 6.5 (a, b) SEM images of BiCu. (c) TEM image of BiCu. (d, e) HRTEM images of BiCu. (f, g) HAADF-STEM image and corresponding EDX mapping of BiCu.

High-angle annular dark-field scanning transmission electron microscopy (HAADF-STEM) was conducted to investigate the atomic structure (Figure 6.6a, b). The darker dots marked by white circle can be assigned to Cu atom according to the disparity in Z-contrast between Cu and Bi atoms.[28] The line intensity profile in Figure 6.6c also validates the isolated Cu atom in Bi lattice. This was also confirmed by scanning transmission electron microscopy energy-dispersive X-ray spectroscopy (STEM-EDS) analysis (Figure 6.6d). To further investigate the local structure of the Cu atoms in the BiCu catalyst, I performed X-ray absorption spectroscopy (XAS) measurements with standard Cu foil, CuO, and Cu_2O as the references. As shown in Figure 6.7a, the Cu K-edge X-ray absorption near-edge energies of BiCu are lower than that of CuO but higher than that of Cu foil, indicating a positive Cu valence between Cu^0 and Cu^{2+}. The Fourier-transformed extended X-ray absorption fine structure (EXAFS) spectra are shown in Figure 6.7b. The EXAFS curve of BiCu shows a peak at around 1.5 Å attributed to Cu-O bond, while no Cu-Cu bond at 2.2 Å was detected. The wavelet transform (WT) plot (Figure 6.7c) of BiCu shows the WT maximum at 4.7 $Å^{-1}$, corresponding to the Cu-O bond by comparing with Cu foil, Cu_2O, and CuO. The Cu-O bond might be due to the oxidation of the BiCu catalyst during *ex situ* tests. These verify that the Cu atoms are atomically dispersed in Bi lattice.

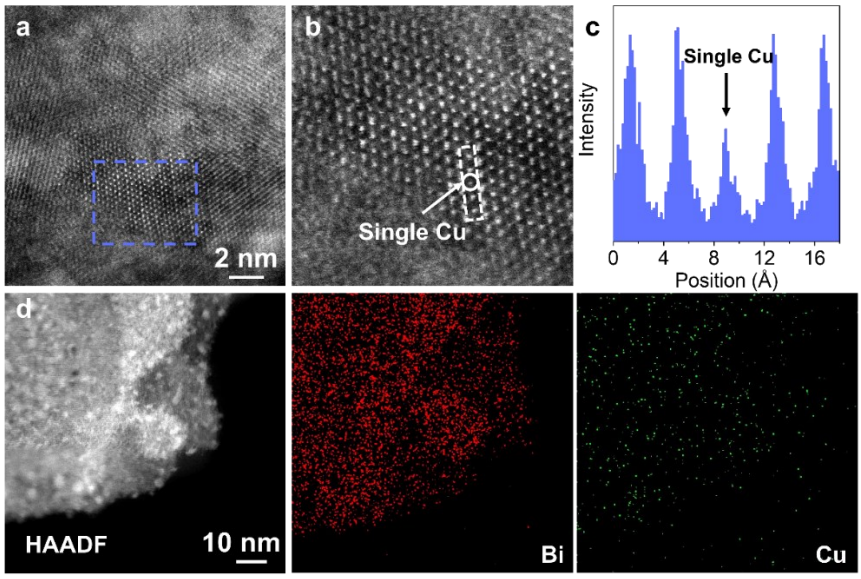

Figure 6.6 (a, b) Atomic-resolution aberration-corrected HAADF-STEM images and (c) corresponding intensity line profile of BiCu. (d) STEM-EDS mapping of BiCu catalyst.

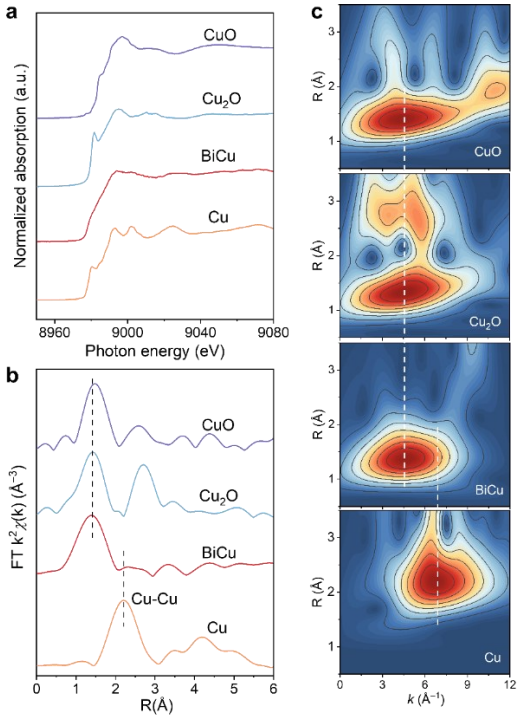

Figure 6.7 (a) XAS spectra at the Cu K-edge of BiCu catalyst with the spectra of CuO, Cu_2O and Cu as references. (b) EXAFS spectra at Cu-K edge of BiCu catalyst. (c) WT plots of BiCu, Cu, CuO, and Cu_2O.

6.2.3 Electrocatalytic performance of NiCoP/NF for EGO

The anodic EGO performance of the as-prepared NiCoP/NF catalysts was accessed in Ar-saturated 1.0 M KOH with 0.5 M EG added. The LSV curves clearly show that the onset potential for EGO is about 1.3 V, which is 100 mV lower than OER (Figure 6.8a). With the applied potential becoming more positive after the onset potential, the oxidation current densities increased rapidly and reached 100 mA cm^{-2} at a much lower potential of 1.34 V as compared to OER (1.55 V). As shown in Figure 6.8b, the potentials for EGO are lowered by at least 150 mV at the current densities of 200, 300, 400, and 500 mA cm^{-2}, compared with those of OER. Furthermore, the oxidation products during EGO were analyzed by IC. As shown in Figure 6.8c, formate is the dominating product with FE of ~ 90% across a broad potential window (1.3−1.7 V *vs*. RHE).

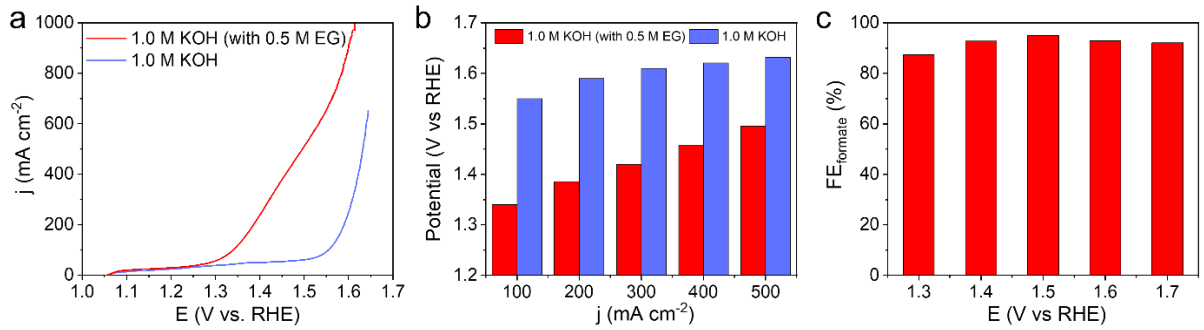

Figure 6.8 (a) LSV curves of NiCoP/NF in 1.0 M KOH with or without 0.5 M EG. (b) Anodic potentials to achieve varied current densities (100, 200, 300, 400, and 500 mA cm^{-2}) by NiCoP/NF in 1.0 M KOH with and without addition of 0.5 M EG. (c) Faraday efficiencies of partial EG oxidation to formate at varied potentials.

6.2.4 Electrocatalytic performance of BiCu for ECR

I next examined the ECR catalytic activity of BiCu catalyst in a flow cell using recirculated 1 M KOH as electrolyte. LSV curve of BiCu showed a much higher current density in CO_2-saturated electrolyte than in Ar atmosphere, indicating the participation of CO_2 gas in the reaction (Figure

6.9a). It was found that formate was the only liquid product for both BiCu and Bi during ECR, together with a small amount of H_2 and CO (Figure 6.9b, c). The formate FE of BiCu catalyst was always higher than that of pure Bi at all the potentials examined. The maximal formate FE on BiCu reached about 95.6% at −0.6 V *vs*. RHE. A high plateau of formate FEs over 90% was retained in a wide potential range from −0.5 to −0.8 V vs RHE, and the competitive HER was suppressed to below 6%. Notably, the BiCu achieved a formate partial current density of ~ −536 mA cm^{-2} at −0.8 V *vs*. RHE while still maintaining a FE of 91% (Figure 6.9d). At −0.9 V *vs*. RHE, BiCu delivered a record-high partial current density of −1143 mA cm^{-2}, corresponding to the formate production rate of 21.3 mmol h^{-1} cm^{-2} (Figure 6.9e), these are the highest values reported so far in KOH environments (Table S6.1).[29-34] Moreover, the BiCu catalyst exhibits a formate cathodic energy efficiency of 78.7% (Figure 6.9f), which rivals most of the reported Bi-based electrocatalysts for formate production. The long-term electrochemical stability of the BiCu catalyst was examined in flow cell reactor with 1.0 M KOH electrolyte. As shown in Figure 6.9g, the BiCu catalyst can continuously run for 45h at −0.6 V with negligible performance decay ($FE_{formate}$ > 93.8%, $j \approx -200$ mA cm^{-2}). By comparing the performance metrics presented herein with recent literature benchmarks (Figure 6.9h), I can conclude that the single Cu doping offers an effective strategy to achieve selective, high-rate CO_2-to-formate conversion in KOH environments.[33, 35-37]

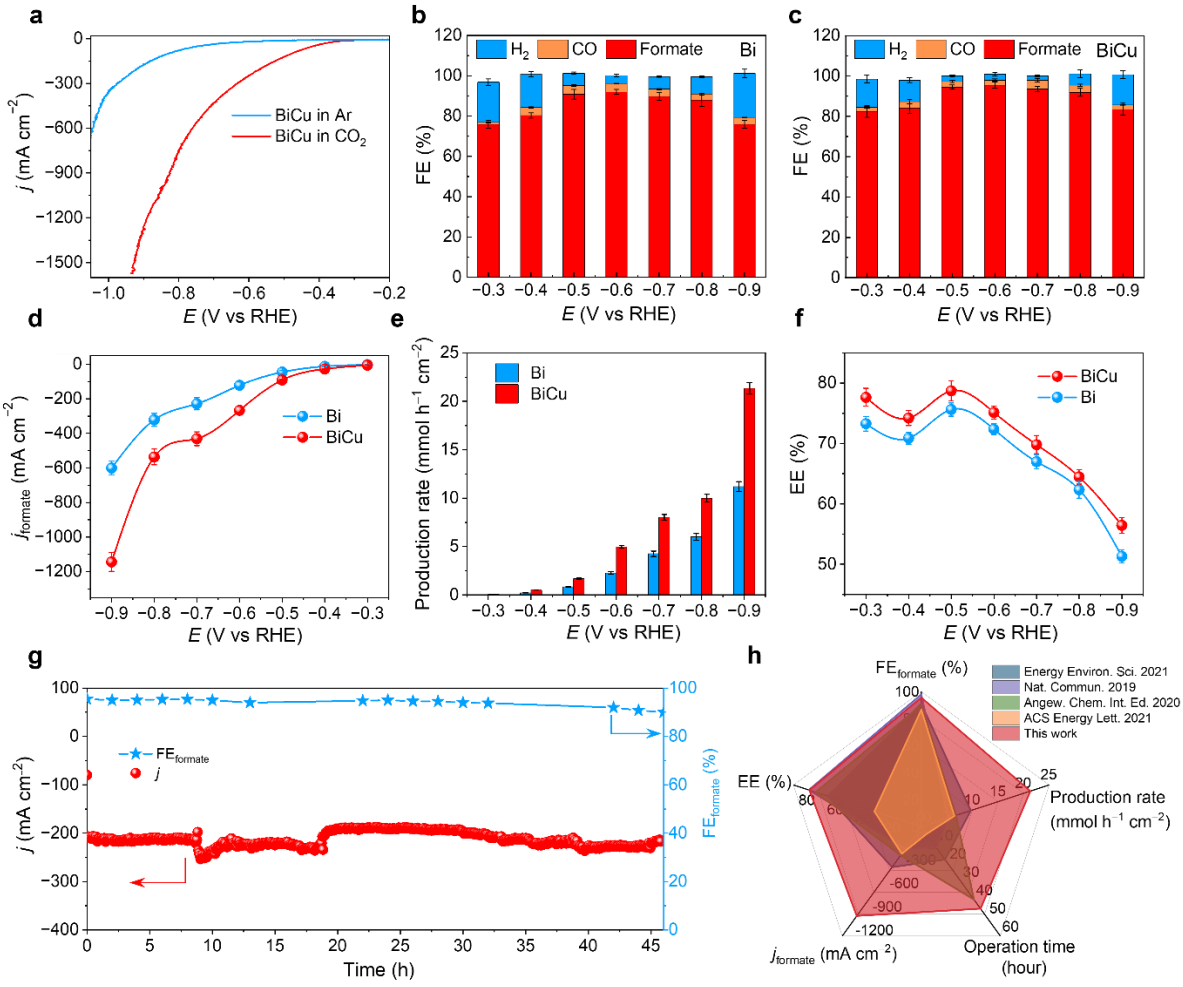

Figure 6.9 (a) LSV curves for BiCu catalyst at CO_2 and Ar atmosphere. (b, c) Potential-dependent Faradic efficiencies for products on BiCu and Cu. Comparison of formate partial current densities (d), formate production rate (e), and energy efficiencies (f) for BiCu and Cu. (g) Stability test of BiCu at −0.6 V for 45h. (h) Comparison of performance metrics of BiCu catalyst with reported benchmarks.

6.2.5 Mechanics insights for the enhanced formate production

DFT was used to gain insights into the promoting effects of single Cu atom. I compared the Gibbs free energies (ΔG) for the formation of formate on the surfaces of BiCu and Bi models. The computation results indicate that the *HCOOH formation is the limiting step for both catalysts (Figure 6.10a). The energy barrier of *HCOOH formation is 0.456 eV for BiCu and lower than

that of 0.516 eV for Bi. This suggests that the single Cu atom incorporation indeed promotes the CO_2-to-formate conversion. By contrast, *COOH (intermediate of CO product) formation is highly endergonic on these two Bi-based catalysts (Figure 6.10b), causing the production of CO to be virtually prohibited. The free energy diagrams for the competitive HER were also given in Figure 6.10c. It is noteworthy that as compared to Bi, the BiCu catalyst enables lower formation energy of *H species, suggesting that the incorporation of single Cu facilitates the water dissociation. Recent studies show that the synergistic adsorption of H_2O and CO_2 molecules plays an important role in ECR because the adsorbed H_2O is believed to be the proton donor for ECR intermediates. The enhanced water dissociation to form *H can speed up the overall ECR process by boosting the intermediate protonation. I thus reasonably surmise that single Cu atom doping permits easier H_2O dissociation to adsorbed *H species, which then boosts the intermediate protonation step of ECR and consequently, the whole ECR process. Note that the difference between the limiting potentials for ECR and HER (i.e., $\Delta P_{limit} = P_{limit}(CO_2) - P_{limit}(H_2)$, where $P_{limit} = -\Delta G_0/e$) had been a useful descriptor for the selectivity of ECR and a more positive ΔP_{limit} value represented a higher selectivity.[38-41] As shown in Figure 6.10d, the BiCu showed a more positive ΔP_{limit} value than Bi, clearly indicating its good performance for ECR to formate.

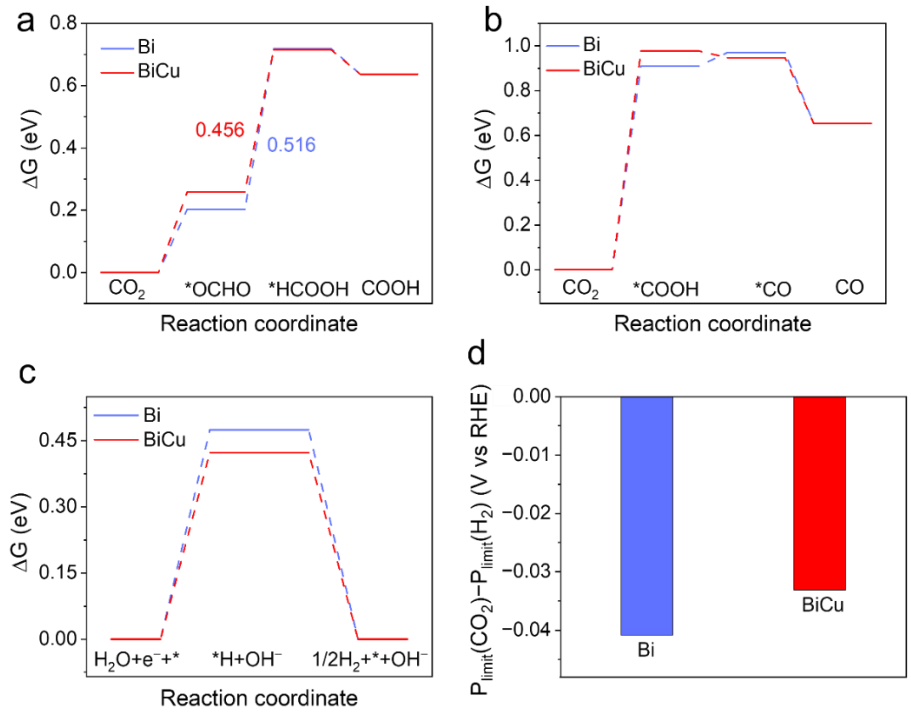

Figure 6.10 (a) Gibbs free energy diagrams for ECR to formate on BiCu and Bi surfaces. (b) Gibbs free energy diagrams for ECR to CO on BiCu and Bi surfaces. (c) Gibbs free energies for the formation of *H on BiCu and Bi surfaces. (d) The limiting potential difference for ECR and HER on BiCu and Cu.

6.2.6 Electrocatalytic performance of ECR-EGO system

Based on the excellent electrocatalytic performance of NiCoP/NF for anodic EGO and BiCu for cathodic ECR, a coupled two-electrode electrolyzer using NiCoP/CF as the anode in 1M KOH electrolyte containing 0.5 M EG, and BiCu as the cathode in 1M $KHCO_3$ electrolyte (denoted NiCoP/NF||BiCu) has been set up and operated at room temperature for the concurrent electrochemical formate productions at both anode and cathode (Figure 6.11a). The ECR-EGO electrolyzer requires a cell voltage of 1.78 V to deliver 40 mA cm^{-2}. This voltage is 760 mV lower than that of conventional ECR-OER system under the same catalysis condition with NiCoP/NF at anode and BiCu at cathode without the anodic addition of EG (Figure 6.11b). In addition, the

generated products in both electrodes were quantitatively analyzed and formate was the main product (Figure 6.11c).

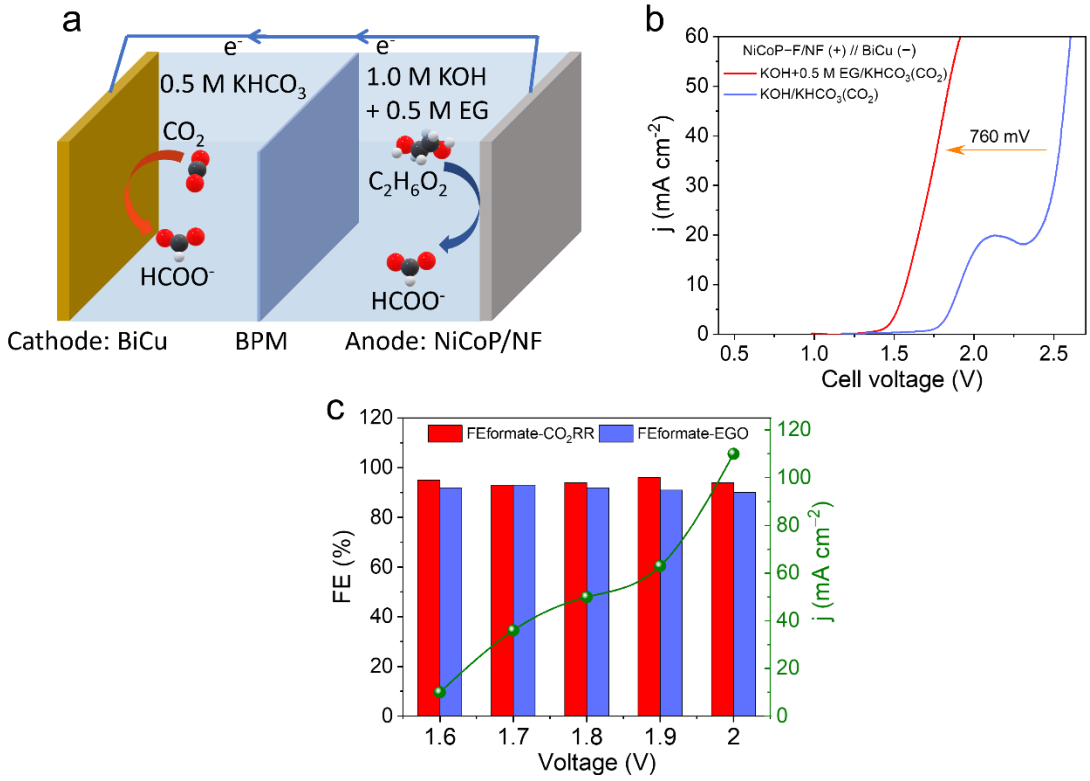

Figure 6.11 (a) Schematic illustration of the constructed EGO assisted CO_2 electrolysis system. (b) Polarization curves of ECR-OER and ECR-EGO over the NiCoP/NF||BiCu pair. (c) Voltage-dependent current densities and FEs of anodic EGO and cathodic ECR over NiCoP/NF||BiCu pair.

6.3 Conclusions

In summary, a pair-electrolysis tactic has been demonstrated for concurrent and energy-saving formate productions at both anode and cathode by EGO and ECR, respectively. A single Cu atom doped Bi was developed as cathodic ECR catalyst. The computational simulations reveal that the introduction of single Cu atom into Bi matrix promotes H_2O dissociation to form adsorbed *H species. The adsorbed *H species can benefit the intermediate protonation step of ECR, thus speeding up the whole ECR process. The BiCu catalyst exhibited prominent ECR performances

with the maximum $FE_{formate}$ of 96% and an extraordinary $j_{formate}$ of −1143 mA cm^{-2} at −0.9 V in the flow cell, ranking above all the other previously reported formate-producing catalysts. For the anodic catalyst for EGO, a NiCoP/NF catalyst was prepared. It showed a high selectivity for EG-to-formate with high current density. When coupling the BiCu and NiCoP/NF in a full cell configuration, the assembled electrolyzer requires a quite low cell voltage of 1.78 V at 40 mA cm^{-2} for overall reaction, which is more than 760 mV lower than that of conventional overall ECR-OER under the same condition. The distinct advantages of this strategy (e.g., low cost, reduced energy input, high value-added chemicals obtained at both sides) endow the strategy with an appealing future for producing formate from both electrochemical CO_2 reduction and partial ethylene glycol oxidation.

6.4 References

1. Verma, S.; Lu, S.; Kenis, P. J., Co-electrolysis of CO_2 and glycerol as a pathway to carbon chemicals with improved technoeconomics due to low electricity consumption. *Nat. Energy* 2019, *4* (6), 466-474.
2. Wei, X.; Li, Y.; Chen, L.; Shi, J., Formic Acid Electro-Synthesis by Concurrent Cathodic CO_2 Reduction and Anodic CH_3OH Oxidation. *Angew. Chem., Int. Ed.* 2021, *60* (6), 3148-3155.
3. Rausch, B.; Symes, M. D.; Chisholm, G.; Cronin, L., Decoupled catalytic hydrogen evolution from a molecular metal oxide redox mediator in water splitting. *Science* 2014, *345* (6202), 1326-1330.
4. Xiang, K.; Wu, D.; Deng, X.; Li, M.; Chen, S.; Hao, P.; Guo, X.; Luo, J. L.; Fu, X. Z., Boosting H_2 generation coupled with selective oxidation of methanol into value-added chemical over cobalt hydroxide@hydroxysulfide nanosheets electrocatalysts. *Adv. Funct. Mater.* 2020, *30* (10), 1909610.
5. Si, D.; Xiong, B.; Chen, L.; Shi, J., Highly selective and efficient electrocatalytic synthesis of glycolic acid in coupling with hydrogen evolution. *Chem Catal.* 2021, *1* (4), 941-955.

6. Liu, W.-J.; Xu, Z.; Zhao, D.; Pan, X.-Q.; Li, H.-C.; Hu, X.; Fan, Z.-Y.; Wang, W.-K.; Zhao, G.-H.; Jin, S., Efficient electrochemical production of glucaric acid and H_2 *via* glucose electrolysis. *Nat. Commun.* 2020, *11* (1), 1-11.

7. Zhou, H.; Ren, Y.; Li, Z.; Xu, M.; Wang, Y.; Ge, R.; Kong, X.; Zheng, L.; Duan, H., Electrocatalytic upcycling of polyethylene terephthalate to commodity chemicals and H_2 fuel. *Nat. Commun.* 2021, *12* (1), 1-9.

8. Yin, K.; Chao, Y.; Lv, F.; Tao, L.; Zhang, W.; Lu, S.; Li, M.; Zhang, Q.; Gu, L.; Li, H., One nanometer PtIr nanowires as high-efficiency bifunctional catalysts for electrosynthesis of ethanol into high value-added multicarbon compound coupled with hydrogen production. *J. Am. Chem. Soc.* 2021, *143* (29), 10822-10827.

9. Wang, T.; Tao, L.; Zhu, X.; Chen, C.; Chen, W.; Du, S.; Zhou, Y.; Zhou, B.; Wang, D.; Xie, C., Combined anodic and cathodic hydrogen production from aldehyde oxidation and hydrogen evolution reaction. *Nat. Catal.* 2022, *5* (1), 66-73.

10. Tournier, V.; Topham, C.; Gilles, A.; David, B.; Folgoas, C.; Moya-Leclair, E.; Kamionka, E.; Desrousseaux, M.-L.; Texier, H.; Gavalda, S., An engineered PET depolymerase to break down and recycle plastic bottles. *Nature* 2020, *580* (7802), 216-219.

11. Ügdüler, S.; Van Geem, K. M.; Denolf, R.; Roosen, M.; Mys, N.; Ragaert, K.; De Meester, S., Towards closed-loop recycling of multilayer and coloured PET plastic waste by alkaline hydrolysis. *Green Chem.* 2020, *22* (16), 5376-5394.

12. Uekert, T.; Kasap, H.; Reisner, E., Photoreforming of nonrecyclable plastic waste over a carbon nitride/nickel phosphide catalyst. *J. Am. Chem. Soc.* 2019, *141* (38), 15201-15210.

13. Zheng, X.; De Luna, P.; de Arquer, F. P. G.; Zhang, B.; Becknell, N.; Ross, M. B.; Li, Y.; Banis, M. N.; Li, Y.; Liu, M., Sulfur-modulated tin sites enable highly selective electrochemical reduction of CO_2 to formate. *Joule* 2017, *1* (4), 794-805.

14. Yang, F.; Elnabawy, A. O.; Schimmenti, R.; Song, P.; Wang, J.; Peng, Z.; Yao, S.; Deng, R.; Song, S.; Lin, Y., Bismuthene for highly efficient carbon dioxide electroreduction reaction. *Nat. Commun.* 2020, *11* (1), 1-8.

15. Shi, Y.; Ji, Y.; Long, J.; Liang, Y.; Liu, Y.; Yu, Y.; Xiao, J.; Zhang, B., Unveiling hydrocerussite as an electrochemically stable active phase for efficient carbon dioxide electroreduction to formate. *Nat. Commun.* 2020, *11* (1), 1-10.

16. Wang, X.; Sang, X.; Dong, C. L.; Yao, S.; Shuai, L.; Lu, J.; Yang, B.; Li, Z.; Lei, L.; Qiu, M., Proton capture strategy for enhancing electrochemical CO_2 reduction on atomically dispersed metal–nitrogen active sites. *Angew. Chem., Int. Ed.* 2021, *60* (21), 11959-11965.

17. Ma, W.; Xie, S.; Zhang, X.-G.; Sun, F.; Kang, J.; Jiang, Z.; Zhang, Q.; Wu, D.-Y.; Wang, Y., Promoting electrocatalytic CO_2 reduction to formate *via* sulfur-boosting water activation on indium surfaces. *Nat. Commun.* 2019, *10* (1), 1-10.

18. Chen, D.; Zhang, L. H.; Du, J.; Wang, H.; Guo, J.; Zhan, J.; Li, F.; Yu, F., A Tandem Strategy for Enhancing Electrochemical CO_2 Reduction Activity of Single-Atom Cu-S_1N_3 Catalysts *via* Integration with Cu Nanoclusters. *Angew. Chem., Int. Ed.* 2021, *60* (45), 24022-24027.

19. Liu, C.; Wu, Y.; Sun, K.; Fang, J.; Huang, A.; Pan, Y.; Cheong, W.-C.; Zhuang, Z.; Zhuang, Z.; Yuan, Q., Constructing FeN_4/graphitic nitrogen atomic interface for high-efficiency electrochemical CO_2 reduction over a broad potential window. *Chem* 2021, *7* (5), 1297-1307.

20. Trasatti, S., Work function, electronegativity, and electrochemical behaviour of metals: III. Electrolytic hydrogen evolution in acid solutions. *J. Electroanal. Chem. Interf. Electrochem.* 1972, *39* (1), 163-184.

21. Nørskov, J. K.; Bligaard, T.; Rossmeisl, J.; Christensen, C. H., Towards the computational design of solid catalysts. *Nat. Chem.* 2009, *1* (1), 37-46.

22. Mao, J.; He, C.-T.; Pei, J.; Chen, W.; He, D.; He, Y.; Zhuang, Z.; Chen, C.; Peng, Q.; Wang, D., Accelerating water dissociation kinetics by isolating cobalt atoms into ruthenium lattice. *Nat. Commun.* 2018, *9* (1), 1-8.

23. Chen, C. H.; Wu, D.; Li, Z.; Zhang, R.; Kuai, C. G.; Zhao, X. R.; Dong, C. K.; Qiao, S. Z.; Liu, H.; Du, X. W., Ruthenium-based single-atom alloy with high electrocatalytic activity for hydrogen evolution. *Adv. Energy Mater.* 2019, *9* (20), 1803913.

24. Wan, R.; Luo, M.; Wen, J.; Liu, S.; Kang, X.; Tian, Y., Pt-Co single atom alloy catalysts: accelerated water dissociation and hydrogen evolution by strain regulation. *J. Energy Chem.* 2022, *69*, 44-53.

25. Shang, L.; Wang, J.-Q.; Cheng, C.-Q.; Zhang, Y.; Zhang, F.-F.; Xie, Y.-M.; Lu, J.-D.; Mao, J.; Guo, Q.-J.; Dong, C.-K., Oxidized single nickel atoms embedded in Ru matrix for highly efficient hydrogen evolution reaction. *J. Alloys Compd.* 2021, *874*, 159909.

26. Chao, T.; Luo, X.; Chen, W.; Jiang, B.; Ge, J.; Lin, Y.; Wu, G.; Wang, X.; Hu, Y.; Zhuang, Z., Atomically dispersed copper–platinum dual sites alloyed with palladium nanorings catalyze the hydrogen evolution reaction. *Angew. Chem.* 2017, *129* (50), 16263-16267.

27. Li, M.; Duanmu, K.; Wan, C.; Cheng, T.; Zhang, L.; Dai, S.; Chen, W.; Zhao, Z.; Li, P.; Fei, H., Single-atom tailoring of platinum nanocatalysts for high-performance multifunctional electrocatalysis. *Nat. Catal.* 2019, *2* (6), 495-503.

28. Zhou, J.; Lin, J.; Huang, X.; Zhou, Y.; Chen, Y.; Xia, J.; Wang, H.; Xie, Y.; Yu, H.; Lei, J., A library of atomically thin metal chalcogenides. *Nature* 2018, *556* (7701), 355-359.

29. Gong, Q.; Ding, P.; Xu, M.; Zhu, X.; Wang, M.; Deng, J.; Ma, Q.; Han, N.; Zhu, Y.; Lu, J., Structural defects on converted bismuth oxide nanotubes enable highly active electrocatalysis of carbon dioxide reduction. *Nat. Commun.* 2019, *10* (1), 1-10.

30. García de Arquer, F. P.; Bushuyev, O. S.; De Luna, P.; Dinh, C. T.; Seifitokaldani, A.; Saidaminov, M. I.; Tan, C. S.; Quan, L. N.; Proppe, A.; Kibria, M. G., 2D metal oxyhalide-derived catalysts for efficient CO_2 electroreduction. *Adv. Mater.* 2018, *30* (38), 1802858.

31. Xia, C.; Zhu, P.; Jiang, Q.; Pan, Y.; Liang, W.; Stavitski, E.; Alshareef, H. N.; Wang, H., Continuous production of pure liquid fuel solutions *via* electrocatalytic CO_2 reduction using solid-electrolyte devices. *Nat. Energy* 2019, *4* (9), 776-785.

32. Ye, K.; Zhou, Z.; Shao, J.; Lin, L.; Gao, D.; Ta, N.; Si, R.; Wang, G.; Bao, X., *In Situ* Reconstruction of a Hierarchical Sn-Cu/SnO_x Core/Shell Catalyst for High-Performance CO_2 Electroreduction. *Angew. Chem., Int. Ed.* 2020, *59* (12), 4814-4821.

33. Grigioni, I.; Sagar, L. K.; Li, Y. C.; Lee, G.; Yan, Y.; Bertens, K.; Miao, R. K.; Wang, X.; Abed, J.; Won, D. H., CO_2 electroreduction to formate at a partial current density of 930 mA cm^{-2} with InP colloidal quantum dot derived catalysts. *ACS Energy Lett.* 2020, *6* (1), 79-84.

34. Li, Y.; Chen, J.; Chen, S.; Liao, X.; Zhao, T.; Cheng, F.; Wang, H., *In Situ* Confined Growth of Bismuth Nanoribbons with Active and Robust Edge Sites for Boosted CO_2 Electroreduction. *ACS Energy Lett.* 2022, *7*, 1454-1461.

35. Zhang, M.; Wei, W.; Zhou, S.; Ma, D.-D.; Cao, A.; Wu, X.-T.; Zhu, Q.-L., Engineering a conductive network of atomically thin bismuthene with rich defects enables CO_2 reduction to formate with industry-compatible current densities and stability. *Energy Environ. Sci.* 2021, *14* (9), 4998-5008.

36. Han, N.; Wang, Y.; Yang, H.; Deng, J.; Wu, J.; Li, Y.; Li, Y., Ultrathin bismuth nanosheets from *in situ* topotactic transformation for selective electrocatalytic CO_2 reduction to formate. *Nat. Commun.* 2018, *9* (1), 1-8.
37. Wang, Y.; Li, Y.; Liu, J.; Dong, C.; Xiao, C.; Cheng, L.; Jiang, H.; Jiang, H.; Li, C., $BiPO_4$-Derived 2D Nanosheets for Efficient Electrocatalytic Reduction of CO_2 to Liquid Fuel. *Angew. Chem.* 2021, *133* (14), 7759-7763.
38. Li, X.; Bi, W.; Chen, M.; Sun, Y.; Ju, H.; Yan, W.; Zhu, J.; Wu, X.; Chu, W.; Wu, C., Exclusive Ni–N_4 sites realize near-unity CO selectivity for electrochemical CO_2 reduction. *J. Am. Chem. Soc.* 2017, *139* (42), 14889-14892.
39. Ren, W.; Tan, X.; Yang, W.; Jia, C.; Xu, S.; Wang, K.; Smith, S. C.; Zhao, C., Isolated diatomic Ni-Fe metal–nitrogen sites for synergistic electroreduction of CO_2. *Angew. Chem., Int. Ed.* 2019, *58* (21), 6972-6976.
40. Kim, D.; Xie, C.; Becknell, N.; Yu, Y.; Karamad, M.; Chan, K.; Crumlin, E. J.; Nørskov, J. K.; Yang, P., Electrochemical activation of CO_2 through atomic ordering transformations of AuCu nanoparticles. *J. Am. Chem. Soc.* 2017, *139* (24), 8329-8336.
41. Zhang, E.; Wang, T.; Yu, K.; Liu, J.; Chen, W.; Li, A.; Rong, H.; Lin, R.; Ji, S.; Zheng, X., Bismuth single atoms resulting from transformation of metal–organic frameworks and their use as electrocatalysts for CO_2 reduction. *J. Am. Chem. Soc.* 2019, *141* (42), 16569-16573.

6.5 Supporting information

6.5.1 Experimental section

Preparation of NiCoP/NF anode catalyst: The commercial NF (2×3 cm) pieces were sequentially washed with 0.5 M HCl, ethanol and DI water (each for 10 min) to remove surficial oxides and contaminants. The electrodeposition of $NiCo(OH)_2$ nanosheet array was carried out in a three-electrode system, using saturated calomel electrode (SCE) and Pt foil as reference and counter electrodes, respectively. The $NiCo(OH)_2$ nanosheets were prepared by applying a constant potential of −1.0 V *vs*. SCE in an aqueous solution with 100 mM $Co(NO_3)_2$ and 25 mM $Ni(NO_3)_2$ electrolyte for 10 min. The resulting $NiCo(OH)_2$ nanosheets array was withdrawn and rinsed

thoroughly with ethanol and DI water. To prepare NiCoP/NF, NaH_2PO_2 and $NiCo(OH)_2$/NF were put at two separate positions in a porcelain boat with NaH_2PO_2 (1.0 g) at the upstream side of the furnace. Subsequently, the samples were heated at 300 °C in argon atmosphere for 2 h, and then naturally cooled down to ambient temperature.

Preparation of BiOON-Cu precursor: In a typical procedure of BiCu preparation, 2 mmol $Bi(NO_3)_3 \cdot 5H_2O$, 0.2 mmol Cupric(II) acetylacetonate, and 1.4 mmol Cetyltrimethylammonium bromide (CTAB) were firstly dissolved in 60 ml DI water. Then, 50 mmol urea was added to 40 ml ethanol to form a homogeneous solution using sonication. The urea-ethanol mixture solution was quickly added into the above $Bi(NO_3)_3$ solution, and the mixture was stirred for 30 min to form a white homogeneous solution. This homogeneous solution was then kept at 90 °C in water bath for 4 h and naturally cooled down to room temperature. The obtained green products were collected by centrifugation, washed with DI water and ethanol, and vacuum dried at 60 °C.

Preparation of BiCu catalyst: Typically, 10 mg of as-prepared BiOON-Cu powder was mixed with 1550 µl of IPA, 400 µl of water, and 50 µl of Nafion resin solution (5%), and sonicated for 1 h to obtain a homogeneous ink. 200 µl of the ink was pipetted onto GDL (1 mg cm^{-2} mass loading) and air dried before usage. Then, the BiOON-Cu loaded GDL was *in situ* reduced at −1.6 V *vs*. SCE in CO_2-saturated 1.0 M KOH solution for 10 min to obtain black BiCu catalyst.

6.5.2 Computational Details

Density functional theory (DFT) calculations were carried out by Vienna Ab initio Simulation Package (VASP).[S1-3] Projector-augmented plane-wave (PAW)[S4] method and Perdew-Burke-Ernzer (PBE)[S5] function were utilized in order to treat the electron-ion interaction and exchange-interaction, respectively. The cut-off energy has been set at 520 eV and the spin polarization of all the elements were taken into consideration. A (2×2) surface model with six atomic layers were

built based an optimized unit cell of Bi. In order to avoid the interaction between the neighboring slabs, a vacuum layer with at least 15 Angstrom was added. Monkhorst-Pack (5×3×1) was set for k points sampling of Brillouin zone. A Gaussian smearing of 0.2eV was employed for optimization of surface geometries while it was set at 0.01eV for gas-phase species. The degree of ions relaxation was not terminated until a maximum force component of 0.05eV/Angstrom was achieved. Different geometries of surface with and without the adsorption of intermediates were considered and the one with the lowest electronic energy was chosen. During the surface optimization, the first three atomic layers were fully relaxed while the other layers were fully fixed. Based on equation S6.1 shown below, a Gibbs free energy diagram for ECR was built.[S6]

$$G=E_{DFT}+ZPE+\int C_p dT-TS \quad \text{(S6.1)}$$

Here, the DFT calculated electronic energy, zero point energy, enthalpy correction and entropy correction are represented by E_{DFT}, ZPE, $\int C_p dT$ and –TS individually. The contribution from PV was neglected. 3N freedom degrees were treated as frustrated harmonic vibrations to calculate ZPE and enthalpy correction while a proposed standard method was used to calculate entropy contribution and transfer it to thermodynamic data at room temperature.[S7-8] The computational hydrogen electrode (CHE)[S9] model describing each electrochemical reaction step as a simultaneous transfer of proton and electron was employed. ECR is divided into three steps as shown in equations S6.2 to S6.4 where * represents the corresponding surface where intermediates were adsorbed.

$$*+CO_2+2(H^++e^-) = *OCHO+(H^++e^-) \quad \text{(S6.2)}$$

$$*OCHO +(H^++e^-) = *HCOOH \quad \text{(S6.3)}$$

$$*HCOOH=*+HCOOH \quad \text{(S6.4)}$$

The initial state in which H_2O molecular is freely above clean surface is taken as the reference. Therefore, the Gibbs free energy change of each step is expressed in equations S6.5-S6.7.

$$\Delta G[*OCHO] = G[*OCHO]–G[H^+ + e^–]–G[*]–G[CO_2] \quad (S6.5)$$

$$\Delta G[*HCOOH] = G[*HCOOH]–2G[H^+ + e^–]–G[*]–G[CO_2] \quad (S6.6)$$

$$\Delta G[HCOOH] = G[HCOOH]–2G[H^+ + e^–]–G[*]–G[CO_2] \quad (S6.7)$$

The hydrogen evolution reaction (HER) is written as $H^+ + e^– = 0.5H_2$. Based on CHE model, the Gibbs free energy of $(H^+ + e^–)$ is expressed in equation S6.8.

$$G[H^+ + e^–] = 0.5G[H_2]–G[*] \quad (S6.8)$$

Table S6.1 Comparison of the partial ECR current densities for formate production by BiCu electrocatalyst and the literature.

Electrocatalyst	Electrolyte	Electrolyzer	Potential (V vs. RHE)	$j_{formate}$ (mA cm^{-2})	Production rate (mmol h^{-1} cm^{-2})	Ref.
BiCu	1 M KOH	Flow cell	−0.9	−1143	21.3	This work
Bi-ene-NW	1 M KOH	Flow cell	−0.97	−518	9.67	S10
Bi_2O_3 nanotubes	1 M KOH	Flow cell	−0.61	−282	5.26	S11
PD-Bi1	1 M KOH	Flow cell	−0.56	−181	3.37	S12
Leafy Bi-NS	1 M KOH	Flow cell	−0.67	−356	6.63	S13
Bi_2O_3@C-800	1 M KOH	Flow cell	−1.1	−193	3.6	S14
s-SnLi	1 M KOH	Flow cell	−1.2	−1012	18.9	S15
$Sn_{2.7}Cu$	1 M KOH	Flow cell	−0.7	−365	6.81	S16

6.5.3 References

S1. Kresse, G.; Hafner, J., Ab initio molecular dynamics for liquid metals. *Phys. Rev. B* 1993, *47* (1), 558.

S2. Kresse, G.; Furthmüller, J.; Hafner, J., Theory of the crystal structures of selenium and tellurium: the effect of generalized-gradient corrections to the local-density approximation. *Phys. Rev. B* 1994, *50* (18), 13181.

S3. Kresse, G.; Furthmüller, J., Efficient iterative schemes for ab initio total-energy calculations using a plane-wave basis set. *Phys. Rev. B* 1996, *54* (16), 11169.

S4. Hammer, B.; Hansen, L. B.; Nørskov, J. K., Improved adsorption energetics within density-functional theory using revised Perdew-Burke-Ernzerhof functionals. *Phys. Rev. B* 1999, *59* (11), 7413.

S5. Monkhorst, H. J.; Pack, J. D., Special points for Brillouin-zone integrations. *Phys. Rev. B* 1976, *13* (12), 5188.

S6. Xu, Y.; Shelton, W. A., O_2 reduction by lithium on Au (111) and Pt (111). *J. Chem. Phys.* 2010, *133* (2), 024703.

S7. Cramer, C. J., *Essentials of computational chemistry: theories and models*. John Wiley & Sons: 2013.

S8. Tripković, V.; Skúlason, E.; Siahrostami, S.; Nørskov, J. K.; Rossmeisl, J., The oxygen reduction reaction mechanism on Pt (111) from density functional theory calculations. *Electrochim. Acta* 2010, *55* (27), 7975-7981.

S9. Durand, W. J.; Peterson, A. A.; Studt, F.; Abild-Pedersen, F.; Nørskov, J. K., Structure effects on the energetics of the electrochemical reduction of CO_2 by copper surfaces. *Surf. Sci.* 2011, *605* (15-16), 1354-1359.

S10. Zhang, M.; Wei, W.; Zhou, S.; Ma, D.-D.; Cao, A.; Wu, X.-T.; Zhu, Q.-L., Engineering a conductive network of atomically thin bismuthene with rich defects enables CO_2 reduction to formate with industry-compatible current densities and stability. *Energy Environ. Sci.* 2021, *14* (9), 4998-5008.

S11. Gong, Q.; Ding, P.; Xu, M.; Zhu, X.; Wang, M.; Deng, J.; Ma, Q.; Han, N.; Zhu, Y.; Lu, J., Structural defects on converted bismuth oxide nanotubes enable highly active electrocatalysis of carbon dioxide reduction. *Nat. Commun.* 2019, *10* (1), 1-10.

S12. Wang, Y.; Li, Y.; Liu, J.; Dong, C.; Xiao, C.; Cheng, L.; Jiang, H.; Jiang, H.; Li, C., $BiPO_4$-Derived 2D Nanosheets for Efficient Electrocatalytic Reduction of CO_2 to Liquid Fuel. *Angew. Chem.* 2021, *133* (14), 7759-7763.

S13. Yang, J.; Wang, X.; Qu, Y.; Wang, X.; Huo, H.; Fan, Q.; Wang, J.; Yang, L. M.; Wu, Y., Bi-based metal-organic framework derived leafy bismuth nanosheets for carbon dioxide electroreduction. *Adv. Energy Mater.* 2020, *10* (36), 2001709.

S14. Deng, P.; Yang, F.; Wang, Z.; Chen, S.; Zhou, Y.; Zaman, S.; Xia, B. Y., Metal–Organic Framework-Derived Carbon Nanorods Encapsulating Bismuth Oxides for Rapid and Selective CO_2 Electroreduction to Formate. *Angew. Chem.* 2020, *132* (27), 10899-10905.

S15. Yan, S.; Peng, C.; Yang, C.; Chen, Y.; Zhang, J.; Guan, A.; Lv, X.; Wang, H.; Wang, Z.; Sham, T. K., Electron Localization and Lattice Strain Induced by Surface Lithium Doping Enable Ampere-Level Electrosynthesis of Formate from CO_2. *Angew. Chem.* 2021, *133* (49), 25945-25949.

S16. Ye, K.; Zhou, Z.; Shao, J.; Lin, L.; Gao, D.; Ta, N.; Si, R.; Wang, G.; Bao, X., *In Situ* Reconstruction of a Hierarchical Sn-Cu/SnO_x Core/Shell Catalyst for High-Performance CO_2 Electroreduction. *Angew. Chem., Int, Ed,* 2020, *59* (12), 4814-4821.

Chapter 7 Summary and prospects

7.1 Summary

Throughout this thesis, I have presented three distinct strategies (element doping engineering, hydrophobic engineering, and pair-electrocatalysis strategies) to promote formate production from ECR. The advances and ideas presented herein are described as below:

- Incorporating S element fine tunes the electronic structure of catalyst which in turn stabilizes reaction intermediates and speeds up the reaction.

  In chapter 4, I presented a S doped Bi_2O_3 catalysts for efficient ECR to formate. The as-synthesized catalysts not only exhibit an outstanding catalytic activity for CO_2 to formate conversion through ECR, but also can maintain high faradaic efficiency (FE > 90 %) of formate at high current density (48.6 mA cm^{-2}), which outperforms most of the previously reported catalysts. This study reveals that S doping can advance the ECR to formate process by offering the following advantages: 1) more undercoordinated Bi active sites; 2) faster electron transfer; 3) enhanced CO_2 adsorption; and 4) electronic delocalization of Bi. All of these synergistically benefit ECR to formate while effectively inhibiting HER, thus achieving the high current density and high FE. Besides the considerably enhanced catalytic activity, the two key achievements of this work are the development of a feasible strategy to fine tune the electronic structure and simultaneously increase the amount of active sites (thus overcoming the obstacle of formate FE losing to H_2 production at high current density), and the understanding of the roles of sulfur in the highly active sulfur modified ECR catalysts. The S doping approach reported herein could pave the path to more creative designs for metal-based electrocatalysts for ECR.

- Creating a hydrophobic microenvironment *via* tuning the surface chemistry of carbon support can be used as a general approach to accelerating reaction rate.

In Chapter 5, I illustrated that the surface wettability of the catalyst plays an important role in controlling the performance of ECR. Bi_2O_3 nanosheets (NSs) grown on carbon nanofiber (CNF) with inherent hydrophobicity exhibit high formate Faradaic efficiency ($FE_{formate}$) of >93 % over an extremely wide potential window of 1000 mV and a peak formate current density of 102.1 mA cm^{-2}, which, to the best of my knowledge, outperforms all of the reported results so far. The experimental results and molecular dynamics simulation reveal that the boosted ECR performance can be attributed to the following reasons: 1) the hydrophobic CNF repels water molecules by avoiding the formation of hydrogen bond, thus creating a hydrophobic microenvironment; 2) a concentrated CO_2 gaseous layer is formed near the catalyst surface, thus increasing the mass transport of CO_2; 3) a large amount of triple-phase boundaries are formed due to the water repulsion property; 4) a high local pH is achieved near the catalyst surface, which restricts the availability of protons on the surface. All of these synergistically benefit ECR to formate while effectively inhibiting HER, thus achieving the high production rate of formate (1905 μmol h^{-1} cm^{-2}). Besides the considerably enhanced catalytic activity, the two key achievements of this work are (1) having developed a feasible strategy to create a desirable hydrophobic microenvironment for ECR by tuning the surface chemistry of carbon support to overcome the obstacle of the limited CO_2 mass transport in aqueous medium, and (2) having demonstrated a general approach to improving the activity of ECR catalysts.

- Replacing the anodic OER with more thermodynamically favorable EGO can greatly reduce the energy input of the full system.

In Chapter 6, I presented a pair-electrosynthesis tactic for concurrent formate generation by coupling ECR and EGO to achieve value-added synthesis in both electrodes with lower energy consumption. In such exotic electrolytic system, the self-supported NiCoP/NF and single Cu atom doped Bi were applied as the high-performance EGO and ECR catalysts, respectively. Benefiting from the high activity of both catalysts, the integrated ECR-EGO full cell requires much lower energy input compared to conventional ECR-OER system to concurrently produce formate at both sides. The distinct advantages of this coupling strategy (e.g., low cost, reduced energy input, high value-added chemicals obtained at both sides) endow the strategy with a promising future for formate production from both ECR and EGO.

7.2 Future prospects

While the work presented in this thesis is robust, it is far from comprehensive. As stated below, future research opportunities remain so as to build upon the outputs of this thesis that may serve as a guide for continuing the exploration in the realm of ECR.

The first task is to find out the reason for the dynamic reconstruction of catalyst under applied potential and when immersed in electrolytes. It can be seen that all of the Bi catalysts presented in this thesis undergo dynamic transformations in terms of valence and morphology. Similar phenomena are also reported on other catalysts (Cu, Sn, and In). Understanding how these dynamic changes happen, how these changes influence the activity and selectivity, and how to control and stabilize the active sites is essential to developing stable and selective catalysts. This asks for *in situ* characterization techniques to interrogate the electrochemical interface. Particularly, infrared spectroscopy and Raman spectroscopy can provide the structural fingerprints of the surface-adsorbed species, X-ray adsorption spectroscopy can provide the precise local structural

information of the target atoms such as coordination number and chemical bond length. These *in situ* techniques will help to gain deep insights into how the catalyst and reaction progress under bias, which should be center of focus for this research direction.

Secondly, research efforts should be focused on tuning the selectivity and activity by molecular additives. Chapter 5 has shown how the surface hydrophobic engineering creates a favorable triple-phase boundary and enhances the reaction rate. It is noteworthy that the CO_2 gas source used in this work is pure CO_2 (99.99%). However, the majority of the human induced CO_2 mainly comes from flue gas composed of CO_2 (15 %), O_2 (8 %), and N_2 (77 %). The low CO_2 concentration would result in the low efficiency of direct electroreduction of CO_2 from flue gas. Meanwhile, the competitive oxygen reduction reaction (ORR) is another key factor that will compromise the CO_2 reduction efficiency. Surface modification of electrodes with organic compounds which have a strong affinity of CO_2 over O_2 would be an effective strategy to enrich local CO_2 and inhibit ORR for direct flue gas CO_2 reduction. One may integrate the surface hydrophobic engineering illustrated in Chapter 5 with surface modification of organic compounds to further boost the direct electroreduction of flue gas CO_2.

The third direction will be to seek and/or design the high-performance and low-cost electrocatalysts that can withstand strong oxidation conditions. Chapter 6 has shown the pair-electrocatalytic strategy that can significantly reduce the energy input for overall ECR system. Despite the improved energy efficiency, the cell current density is still far from satisfactory for practical application ($j > 300$ mA cm^{-2}). The utilization of membrane-electrode assembly can be a good choice to enhance the current density. However, the key is to develop effective catalyst that can maintain high activity and selectivity for anode organic oxidation reactions under high potentials. This is because applying high positive potential would unavoidably result in

uncontrolled OER, therefore hampering the overall efficiency and profitability required for industrial production of the value-added products *via* CO_2 reduction that requires high current density.

Bibliography

1. Gao, D.; Arán-Ais, R. M.; Jeon, H. S.; Cuenya, B. R. J. N. C., Rational catalyst and electrolyte design for CO_2 electroreduction towards multicarbon products. *Nat. Catal.* 2019, *2* (3), 198-210.
2. Gao, W.; Liang, S.; Wang, R.; Jiang, Q.; Zhang, Y.; Zheng, Q.; Xie, B.; Toe, C. Y.; Zhu, X.; Wang, J.; Huang, L.; Gao, Y.; Wang, Z.; Jo, C.; Wang, Q.; Wang, L.; Liu, Y.; Louis, B.; Scott, J.; Roger, A. C.; Amal, R.; He, H.; Park, S. E., Industrial carbon dioxide capture and utilization: state of the art and future challenges. *Chem. Soc. Rev.* 2020, *49* (23), 8584-8686.
3. National Ocean and Atmospheric Administration (NOAA), Climate Change: Atmospheric Carbon Dioxide. https://www.climate.gov/news-features/understanding-climate/climate-change-atmospheric-carbon-dioxide.
4. Tzimas, E.; Peteves, S., *Controlling Carbon Emissions: The Option of Carbon Seqestration*. Office for Official Publications of the European Communities Luxembourg: 2003.
5. Davis, S. J.; Caldeira, K.; Matthews, H. D., Future CO_2 emissions and climate change from existing energy infrastructure. *Science* 2010, *329* (5997), 1330-1333.
6. Li, H.; Zhao, J.; Luo, L.; Du, J.; Zeng, J., Symmetry-Breaking Sites for Activating Linear Carbon Dioxide Molecules. *Acc. Chem. Res.* 2021, *54* (6), 1454-1464.
7. Chang, X.; Wang, T.; Gong, J., CO_2 photo-reduction: insights into CO_2 activation and reaction on surfaces of photocatalysts. *Energy Environ. Sci.* 2016, *9* (7), 2177-2196.
8. Chen, C.; Kotyk, J. F. K.; Sheehan, S. W., Progress toward commercial application of electrochemical carbon dioxide reduction. *Chem* 2018, *4* (11), 2571-2586.
9. Wang, Y.; Han, P.; Lv, X.; Zhang, L.; Zheng, G., Defect and interface engineering for aqueous electrocatalytic CO_2 reduction. *Joule* 2018, *2* (12), 2551-2582.
10. Liu, Q.; Wu, L.; Jackstell, R.; Beller, M., Using carbon dioxide as a building block in organic synthesis. *Nat. Commun.* 2015, *6* (1), 1-15.
11. Shi, J.; Jiang, Y.; Jiang, Z.; Wang, X.; Wang, X.; Zhang, S.; Han, P.; Yang, C., Enzymatic conversion of carbon dioxide. *Chem. Soc. Rev.* 2015, *44* (17), 5981-6000.

12. Han, N.; Ding, P.; He, L.; Li, Y.; Li, Y. J. A. E. M., Promises of main group metal–based nanostructured materials for electrochemical CO_2 reduction to formate. *Adv. Energy Mater.* 2020, *10* (11), 1902338.
13. Sun, Z.; Ma, T.; Tao, H.; Fan, Q.; Han, B., Fundamentals and challenges of electrochemical CO_2 reduction using two-dimensional materials. *Chem* 2017, *3* (4), 560-587.
14. Zhang, L.; Zhao, Z. J.; Gong, J., Nanostructured materials for heterogeneous electrocatalytic CO_2 reduction and their related reaction mechanisms. *Angew. Chem., Int. Ed.* 2017, *56* (38), 11326-11353.
15. Zhu, D. D.; Liu, J. L.; Qiao, S. Z., Recent advances in inorganic heterogeneous electrocatalysts for reduction of carbon dioxide. *Adv. Mater.* 2016, *28* (18), 3423-3452.
16. Peterson, A. A.; Abild-Pedersen, F.; Studt, F.; Rossmeisl, J.; Nørskov, J. K., How copper catalyzes the electroreduction of carbon dioxide into hydrocarbon fuels. *Energy Environ. Sci.* 2010, *3* (9), 1311-1315.
17. Feaster, J. T.; Shi, C.; Cave, E. R.; Hatsukade, T.; Abram, D. N.; Kuhl, K. P.; Hahn, C.; Nørskov, J. K.; Jaramillo, T. F., Understanding selectivity for the electrochemical reduction of carbon dioxide to formic acid and carbon monoxide on metal electrodes. *ACS Catal.* 2017, *7* (7), 4822-4827.
18. Kortlever, R.; Shen, J.; Schouten, K. J. P.; Calle-Vallejo, F.; Koper, M. T., Catalysts and reaction pathways for the electrochemical reduction of carbon dioxide. *J. Phys. Chem. Lett.* 2015, *6* (20), 4073-4082.
19. Kuhl, K. P.; Cave, E. R.; Abram, D. N.; Jaramillo, T. F., New insights into the electrochemical reduction of carbon dioxide on metallic copper surfaces. *Energy Environ. Sci.* 2012, *5* (5), 7050-7059.
20. Gattrell, M.; Gupta, N.; Co, A., A review of the aqueous electrochemical reduction of CO_2 to hydrocarbons at copper. *J. Electroanal. Chem.* 2006, *594* (1), 1-19.
21. Yoo, J. S.; Christensen, R.; Vegge, T.; Nørskov, J. K.; Studt, F., Theoretical insight into the trends that guide the electrochemical reduction of carbon dioxide to formic acid. *ChemSusChem* 2016, *9* (4), 358-363.
22. Hori, Y.; Wakebe, H.; Tsukamoto, T.; Koga, O., Electrocatalytic process of CO selectivity in electrochemical reduction of CO_2 at metal electrodes in aqueous media. *Electrochim. Acta* 1994, *39* (11-12), 1833-1839.

23. Montoya, J. H.; Shi, C.; Chan, K.; Nørskov, J. K., Theoretical insights into a CO dimerization mechanism in CO_2 electroreduction. *J. Phys. Chem. Lett.* 2015, *6* (11), 2032-2037.
24. Li, J.; Chen, G.; Zhu, Y.; Liang, Z.; Pei, A.; Wu, C.-L.; Wang, H.; Lee, H. R.; Liu, K.; Chu, S., Efficient electrocatalytic CO_2 reduction on a three-phase interface. *Nat. Catal.* 2018, *1* (8), 592-600.
25. Ren, W.; Zhao, C., Paths towards enhanced electrochemical CO_2 reduction. *Natl. Sci. Rev.* 2020, *7* (1), 7-9.
26. Asadi, M.; Kim, K.; Liu, C.; Addepalli, A. V.; Abbasi, P.; Yasaei, P.; Phillips, P.; Behranginia, A.; Cerrato, J. M.; Haasch, R., Nanostructured transition metal dichalcogenide electrocatalysts for CO_2 reduction in ionic liquid. *Science* 2016, *353* (6298), 467-470.
27. Zhao, C.; Wang, J., Electrochemical reduction of CO_2 to formate in aqueous solution using electro-deposited Sn catalysts. *Chem. Eng. J.* 2016, *293*, 161-170.
28. Higgins, D.; Hahn, C.; Xiang, C.; Jaramillo, T. F.; Weber, A. Z., Gas-diffusion electrodes for carbon dioxide reduction: a new paradigm. *ACS Energy Lett.* 2018, *4* (1), 317-324.
29. Dinh, C.-T.; Burdyny, T.; Kibria, M. G.; Seifitokaldani, A.; Gabardo, C. M.; García de Arquer, F. P.; Kiani, A.; Edwards, J. P.; De Luna, P.; Bushuyev, O. S., CO_2 electroreduction to ethylene via hydroxide-mediated copper catalysis at an abrupt interface. *Science* 2018, *360* (6390), 783-787.
30. Gong, Q.; Ding, P.; Xu, M.; Zhu, X.; Wang, M.; Deng, J.; Ma, Q.; Han, N.; Zhu, Y.; Lu, J., Structural defects on converted bismuth oxide nanotubes enable highly active electrocatalysis of carbon dioxide reduction. *Nat. Commun.* 2019, *10* (1), 1-10.
31. García de Arquer, F. P.; Dinh, C.-T.; Ozden, A.; Wicks, J.; McCallum, C.; Kirmani, A. R.; Nam, D.-H.; Gabardo, C.; Seifitokaldani, A.; Wang, X., CO_2 electrolysis to multicarbon products at activities greater than 1 A cm^{-2}. *Science* 2020, *367* (6478), 661-666.
32. Endrodi, B.; Kecsenovity, E.; Samu, A.; Darvas, F.; Jones, R.; Török, V.; Danyi, A.; Janáky, C., Multilayer electrolyzer stack converts carbon dioxide to gas products at high pressure with high efficiency. *ACS Energy Lett.* 2019, *4* (7), 1770-1777.
33. Verma, S.; Hamasaki, Y.; Kim, C.; Huang, W.; Lu, S.; Jhong, H.-R. M.; Gewirth, A. A.; Fujigaya, T.; Nakashima, N.; Kenis, P. J., Insights into the low overpotential

electroreduction of CO_2 to CO on a supported gold catalyst in an alkaline flow electrolyzer. *ACS Energy Lett.* 2017, *3* (1), 193-198.

34. Kutana, A.; Giapis, K., Atomistic simulations of electrowetting in carbon nanotubes. *Nano Lett.* 2006, *6* (4), 656-661.
35. Larrazábal, G. O.; Strøm-Hansen, P.; Heli, J. P.; Zeiter, K.; Therkildsen, K. T.; Chorkendorff, I.; Seger, B., Analysis of mass flows and membrane cross-over in CO_2 reduction at high current densities in an MEA-type electrolyzer. *ACS Appl. Mater. Interfaces* 2019, *11* (44), 41281-41288.
36. Yang, K.; Kas, R.; Smith, W. A., In situ infrared spectroscopy reveals persistent alkalinity near electrode surfaces during CO_2 electroreduction. *J. Am. Chem. Soc.* 2019, *141* (40), 15891-15900.
37. Liu, K.; Smith, W. A.; Burdyny, T., Introductory guide to assembling and operating gas diffusion electrodes for electrochemical CO_2 reduction. *ACS Energy Lett.* 2019, *4* (3), 639-643.
38. Ge, L.; Rabiee, H.; Li, M.; Subramanian, S.; Zheng, Y.; Lee, J. H.; Burdyny, T.; Wang, H., Electrochemical CO_2 reduction in membrane-electrode assemblies. *Chem* 2022, 8 (3) 663-692.
39. Kim, D.; Choi, W.; Lee, H. W.; Lee, S. Y.; Choi, Y.; Lee, D. K.; Kim, W.; Na, J.; Lee, U.; Hwang, Y. J., Electrocatalytic Reduction of Low Concentrations of CO_2 Gas in a Membrane Electrode Assembly Electrolyzer. *ACS Energy Lett.* 2021, *6* (10), 3488-3495.
40. Li, F.; Thevenon, A.; Rosas-Hernández, A.; Wang, Z.; Li, Y.; Gabardo, C. M.; Ozden, A.; Dinh, C. T.; Li, J.; Wang, Y., Molecular tuning of CO_2-to-ethylene conversion. *Nature* 2020, *577* (7791), 509-513.
41. Zheng, T.; Jiang, K.; Ta, N.; Hu, Y.; Zeng, J.; Liu, J.; Wang, H., Large-scale and highly selective CO_2 electrocatalytic reduction on nickel single-atom catalyst. *Joule* 2019, *3* (1), 265-278.
42. Kibria, M. G.; Edwards, J. P.; Gabardo, C. M.; Dinh, C. T.; Seifitokaldani, A.; Sinton, D.; Sargent, E. H., Electrochemical CO_2 reduction into chemical feedstocks: from mechanistic electrocatalysis models to system design. *Adv. Mater.* 2019, *31* (31), 1807166.
43. Jouny, M.; Luc, W.; Jiao, F., General techno-economic analysis of CO_2 electrolysis systems. *Ind. Eng. Chem. Res.* 2018, *57* (6), 2165-2177.

44. Bushuyev, O. S.; De Luna, P.; Dinh, C. T.; Tao, L.; Saur, G.; van de Lagemaat, J.; Kelley, S. O.; Sargent, E. H., What should we make with CO_2 and how can we make it? *Joule* 2018, *2* (5), 825-832.

45. Garza, A. J.; Bell, A. T.; Head-Gordon, M., Mechanism of CO_2 reduction at copper surfaces: pathways to C_2 products. *ACS Catal.* 2018, *8* (2), 1490-1499.

46. Reller, C.; Krause, R.; Volkova, E.; Schmid, B.; Neubauer, S.; Rucki, A.; Schuster, M.; Schmid, G., Selective electroreduction of CO_2 toward ethylene on nano dendritic copper catalysts at high current density. *Adv. Energy Mater.* 2017, *7* (12), 1602114.

47. Delacourt, C.; Ridgway, P. L.; Kerr, J. B.; Newman, J., Design of an electrochemical cell making syngas ($CO+H_2$) from CO_2 and H_2O reduction at room temperature. *J. Electrochem. Soc.* 2007, *155* (1), B42.

48. Liu, S.; Tao, H.; Zeng, L.; Liu, Q.; Xu, Z.; Liu, Q.; Luo, J.-L., Shape-dependent electrocatalytic reduction of CO_2 to CO on triangular silver nanoplates. *J. Am. Chem. Soc.* 2017, *139* (6), 2160-2163.

49. Gileadi, E., *Electrode kinetics for chemists, chemical engineers, and materials scientists*. Capstone: 1993.

50. Lee, C. W.; Cho, N. H.; Im, S. W.; Jee, M. S.; Hwang, Y. J.; Min, B. K.; Nam, K. T., New challenges of electrokinetic studies in investigating the reaction mechanism of electrochemical CO_2 reduction. *J. Mater. Chem. A* 2018, *6* (29), 14043-14057.

51. Pumera, M.; Sofer, Z., 2D monoelemental arsenene, antimonene, and bismuthene: beyond black phosphorus. *Adv. Mater.* 2017, *29* (21), 1605299.

52. Yang, F.; Elnabawy, A. O.; Schimmenti, R.; Song, P.; Wang, J.; Peng, Z.; Yao, S.; Deng, R.; Song, S.; Lin, Y., Bismuthene for highly efficient carbon dioxide electroreduction reaction. *Nat. Commun.* 2020, *11* (1), 1-8.

53. Wang, Y.; Li, Y.; Liu, J.; Dong, C.; Xiao, C.; Cheng, L.; Jiang, H.; Jiang, H.; Li, C., $BiPO_4$-Derived 2D Nanosheets for Efficient Electrocatalytic Reduction of CO_2 to Liquid Fuel. *Angew. Chem., Int. Ed.* 2021, *60* (14), 7687-7685.

54. Li, F.; Xue, M.; Li, J.; Ma, X.; Chen, L.; Zhang, X.; MacFarlane, D. R.; Zhang, J., Unlocking the electrocatalytic activity of antimony for CO_2 reduction by two-dimensional engineering of the bulk material. *Angew. Chem., Int. Ed.* 2017, *56* (46), 14718-14722.

55. Han, N.; Wang, Y.; Yang, H.; Deng, J.; Wu, J.; Li, Y.; Li, Y., Ultrathin bismuth nanosheets from in situ topotactic transformation for selective electrocatalytic CO_2 reduction to formate. *Nat. Commun.* 2018, *9* (1), 1-8.

56. Lamagni, P.; Miola, M.; Catalano, J.; Hvid, M. S.; Mamakhel, M. A. H.; Christensen, M.; Madsen, M. R.; Jeppesen, H. S.; Hu, X. M.; Daasbjerg, K., Restructuring metal–organic frameworks to nanoscale bismuth electrocatalysts for highly active and selective CO_2 reduction to formate. *Adv. Funct. Mater.* 2020, *30* (16), 1910408.

57. Deng, P.; Yang, F.; Wang, Z.; Chen, S.; Zhou, Y.; Zaman, S.; Xia, B. Y., Metal–Organic Framework-Derived Carbon Nanorods Encapsulating Bismuth Oxides for Rapid and Selective CO_2 Electroreduction to Formate. *Angew. Chem., Int. Ed.* 2020, *59* (27), 10807-10813.

58. Yao, D.; Tang, C.; Vasileff, A.; Zhi, X.; Jiao, Y.; Qiao, S. Z., The Controllable Reconstruction of Bi-MOFs for Electrochemical CO_2 Reduction through Electrolyte and Potential Mediation. *Angew. Chem., Int. Ed.* 2021, *60* (33), 18178-18184.

59. Zhang, E.; Wang, T.; Yu, K.; Liu, J.; Chen, W.; Li, A.; Rong, H.; Lin, R.; Ji, S.; Zheng, X., Bismuth single atoms resulting from transformation of metal–organic frameworks and their use as electrocatalysts for CO_2 reduction. *J. Am. Chem. Soc.* 2019, *141* (42), 16569-16573.

60. Cao, C.; Ma, D. D.; Gu, J. F.; Xie, X.; Zeng, G.; Li, X.; Han, S. G.; Zhu, Q. L.; Wu, X. T.; Xu, Q., Metal–organic layers leading to atomically thin bismuthene for efficient carbon dioxide electroreduction to liquid fuel. *Angew. Chem., Int. Ed.* 2020, *59* (35), 15014-15020.

61. Yang, J.; Wang, X.; Qu, Y.; Wang, X.; Huo, H.; Fan, Q.; Wang, J.; Yang, L. M.; Wu, Y., Bi-based metal-organic framework derived leafy bismuth nanosheets for carbon dioxide electroreduction. *Adv. Energy Mater.* 2020, *10* (36), 2001709.

62. Zhang, Y.; Zhang, X.; Ling, Y.; Li, F.; Bond, A. M.; Zhang, J., Controllable synthesis of few-layer bismuth subcarbonate by electrochemical exfoliation for enhanced CO_2 reduction performance. *Angew. Chem.* 2018, *130* (40), 13467-13471.

63. Zhang, M.; Wei, W.; Zhou, S.; Ma, D.-D.; Cao, A.; Wu, X.-T.; Zhu, Q.-L., Engineering a conductive network of atomically thin bismuthene with rich defects enables CO_2 reduction to formate with industry-compatible current densities and stability. *Energy Environ. Sci.* 2021, *14* (9), 4998-5008.

64. Lim, H.-K.; Shin, H.; Goddard III, W. A.; Hwang, Y. J.; Min, B. K.; Kim, H., Embedding covalency into metal catalysts for efficient electrochemical conversion of CO_2. *J. Am. Chem. Soc.* 2014, *136* (32), 11355-11361.

65. Wu, Y.; Cao, S.; Hou, J.; Li, Z.; Zhang, B.; Zhai, P.; Zhang, Y.; Sun, L., Rational design of nanocatalysts with nonmetal species modification for electrochemical CO_2 reduction. *Adv. Energy Mater.* 2020, *10* (29), 2000588.

66. Chen, X.; Chen, H.; Zhou, W.; Zhang, Q.; Yang, Z.; Li, Z.; Yang, F.; Wang, D.; Ye, J.; Liu, L., Boron Dopant Induced Electron-Rich Bismuth for Electrochemical CO_2 Reduction with High Solar Energy Conversion Efficiency. *Small* 2021, *17* (29), 2101128.

67. Zhao, Y.; Liu, X.; Liu, Z.; Lin, X.; Lan, J.; Zhang, Y.; Lu, Y.-R.; Peng, M.; Chan, T.-S.; Tan, Y., Spontaneously Sn-Doped Bi/BiO_x Core–Shell Nanowires Toward High-Performance CO_2 Electroreduction to Liquid Fuel. *Nano Lett.* 2021, *21* (16), 6907-6913.

68. Wen, G.; Lee, D. U.; Ren, B.; Hassan, F. M.; Jiang, G.; Cano, Z. P.; Gostick, J.; Croiset, E.; Bai, Z.; Yang, L., Orbital interactions in Bi-Sn bimetallic electrocatalysts for highly selective electrochemical CO_2 reduction toward formate production. *Adv. Energy Mater.* 2018, *8* (31), 1802427.

69. Li, L.; Ozden, A.; Guo, S.; García de Arquer, F. P.; Wang, C.; Zhang, M.; Zhang, J.; Jiang, H.; Wang, W.; Dong, H., Stable, active CO_2 reduction to formate via redox-modulated stabilization of active sites. *Nat. Commun.* 2021, *12* (1), 1-9.

70. Chen, Z.; Mou, K.; Wang, X.; Liu, L., Nitrogen-doped graphene quantum dots enhance the activity of Bi_2O_3 nanosheets for electrochemical reduction of CO_2 in a wide negative potential region. *Angew. Chem.* 2018, *130* (39), 12972-12976.

71. Chen, Z.; Zhang, X.; Jiao, M.; Mou, K.; Zhang, X.; Liu, L., Engineering Electronic Structure of Stannous Sulfide by Amino-Functionalized Carbon: Toward Efficient Electrocatalytic Reduction of CO_2 to Formate. *Adv. Energy Mater.* 2020, *10* (8), 1903664.

72. Liu, S.; Lu, X. F.; Xiao, J.; Wang, X.; Lou, X. W., Bi_2O_3 nanosheets grown on multi-channel carbon matrix to catalyze efficient CO_2 electroreduction to HCOOH. *Angew. Chem.* 2019, *131* (39), 13966-13971.

73. Zhang, W.; Yang, S.; Jiang, M.; Hu, Y.; Hu, C.; Zhang, X.; Jin, Z., Nanocapillarity and nanoconfinement effects of pipet-like bismuth@carbon nanotubes for highly efficient electrocatalytic CO_2 reduction. *Nano Lett.* 2021, *21* (6), 2650-2657.

74. Duan, Y. X.; Liu, K. H.; Zhang, Q.; Yan, J. M.; Jiang, Q., Efficient CO_2 reduction to HCOOH with high selectivity and energy efficiency over Bi/rGO catalyst. *Small Methods* 2020, *4* (5), 1900846.

75. Huang, J.; Guo, X.; Yang, J.; Wang, L., Electrodeposited Bi dendrites/2D black phosphorus nanosheets composite used for boosting formic acid production from CO_2 electroreduction. *J. CO_2 Util.* 2020, *38*, 32-38.

76. Wu, D.; Wang, X.; Fu, X.-Z.; Luo, J.-L., Ultrasmall Bi nanoparticles confined in carbon nanosheets as highly active and durable catalysts for CO_2 electroreduction. *Appl. Catal. B* 2021, *284*, 119723.

77. Su, P.; Xu, W.; Qiu, Y.; Zhang, T.; Li, X.; Zhang, H., Ultrathin bismuth nanosheets as a highly efficient CO_2 reduction electrocatalyst. *ChemSusChem* 2018, *11* (5), 848-853.

78. Tran-Phu, T.; Daiyan, R.; Fusco, Z.; Ma, Z.; Amal, R.; Tricoli, A., Nanostructured β-Bi_2O_3 fractals on carbon fibers for highly selective CO_2 electroreduction to formate. *Adv. Funct. Mater.* 2020, *30* (3), 1906478.

79. Lee, C. W.; Hong, J. S.; Yang, K. D.; Jin, K.; Lee, J. H.; Ahn, H.-Y.; Seo, H.; Sung, N.-E.; Nam, K. T., Selective electrochemical production of formate from carbon dioxide with bismuth-based catalysts in an aqueous electrolyte. *ACS Catal.* 2018, *8* (2), 931-937.

80. Meng, F. L.; Zhang, Q.; Liu, K. H.; Zhang, X. B., Integrated Bismuth Oxide Ultrathin Nanosheets/Carbon Foam Electrode for Highly Selective and Energy-Efficient Electrocatalytic Conversion of CO_2 to HCOOH. *Chem. Eur. J.* 2020, *26* (18), 4013-4018.

81. Zhang, X.; Sun, X.; Guo, S.-X.; Bond, A. M.; Zhang, J., Formation of lattice-dislocated bismuth nanowires on copper foam for enhanced electrocatalytic CO_2 reduction at low overpotential. *Energy Environ. Sci.* 2019, *12* (4), 1334-1340.

82. Fan, J.; Zhao, X.; Mao, X.; Xu, J.; Han, N.; Yang, H.; Pan, B.; Li, Y.; Wang, L.; Li, Y., Large-Area Vertically Aligned Bismuthene Nanosheet Arrays from Galvanic Replacement Reaction for Efficient Electrochemical CO_2 Conversion. *Adv. Mater.* 2021, *33* (35), 2100910.

83. Park, G.; Hong, S.; Choi, M.; Lee, S.; Lee, J., Au on highly hydrophobic carbon substrate for improved selective CO production from CO_2 in gas-phase electrolytic cell. *Catal. Today* 2020, *355*, 340-346.

84. Hall, A. S.; Yoon, Y.; Wuttig, A.; Surendranath, Y., Mesostructure-induced selectivity in CO_2 reduction catalysis. *J. Am. Chem. Soc.* 2015, *137* (47), 14834-14837.

85. Weekes, D. M.; Salvatore, D. A.; Reyes, A.; Huang, A.; Berlinguette, C. P., Electrolytic CO_2 reduction in a flow cell. *Acc. Chem. Res.* 2018, *51* (4), 910-918.

86. Wakerley, D.; Lamaison, S.; Ozanam, F.; Menguy, N.; Mercier, D.; Marcus, P.; Fontecave, M.; Mougel, V., Bio-inspired hydrophobicity promotes CO_2 reduction on a Cu surface. *Nat. Mater.* 2019, *18* (11), 1222-1227.

87. Niu, Z.-Z.; Gao, F.-Y.; Zhang, X.-L.; Yang, P.-P.; Liu, R.; Chi, L.-P.; Wu, Z.-Z.; Qin, S.; Yu, X.; Gao, M.-R., Hierarchical copper with inherent hydrophobicity mitigates electrode flooding for high-rate CO_2 electroreduction to multicarbon products. *J. Am. Chem. Soc.* 2021, *143* (21), 8011-8021.

88. Pan, F.; Yang, Y., Designing CO_2 reduction electrode materials by morphology and interface engineering. *Energy Environ. Sci.* 2020, *13* (8), 2275-2309.

89. Jiang, Y.; Zhang, X.; Xu, D.; Li, W.; Liu, M.; Qiu, X., Efficient three-phase electrocatalytic CO_2 reduction to formate on superhydrophobic Bi–C interfaces. *Chem. Commun.* 2021, *57* (49), 6011-6014.

90. Zhang, X. Y.; Li, W. J.; Wu, X. F.; Liu, Y. W.; Chen, J.; Zhu, M.; Yuan, H. Y.; Dai, S.; Wang, H. F.; Jiang, Z., Selective methane electrosynthesis enabled by a hydrophobic carbon coated copper core–shell architecture. *Energy Environ. Sci.* 2022, *15* (1) 234-243.

91. Xue, L.; Wu, X.; Liu, Y.; Xu, B.; Wang, X.; Dai, S.; Liu, P.; Yang, H., Hydrophobic 1-octadecanethiol functionalized copper catalyst promotes robust high-current CO_2 gas-diffusion electrolysis. *Nano Res.* 2022, *15* (2), 1393-1398.

92. Wang, J.; Yang, H.; Liu, Q.; Liu, Q.; Li, X.; Lv, X.; Cheng, T.; Wu, H. B., Fastening Br–Ions at Copper–Molecule Interface Enables Highly Efficient Electroreduction of CO_2 to Ethanol. *ACS Energy Lett.* 2021, *6* (2), 437-444.

93. Liang, H.-Q.; Zhao, S.; Hu, X.-M.; Ceccato, M.; Skrydstrup, T.; Daasbjerg, K., Hydrophobic copper interfaces boost electroreduction of carbon dioxide to ethylene in water. *ACS Catal.* 2021, *11* (2), 958-966.

94. Chang, S.; Xuan, Y.; Duan, J.; Zhang, K., High-Performance Electroreduction CO_2 to Formate at Bi/Nafion Interface. *Appl. Catal. B* 2022, 306, 121135.

95. Machan, C. W.; Yin, J.; Chabolla, S. A.; Gilson, M. K.; Kubiak, C. P., Improving the efficiency and activity of electrocatalysts for the reduction of CO_2 through supramolecular assembly with amino acid-modified ligands. *J. Am. Chem. Soc.* 2016, *138* (26), 8184-8193.

96. Ahn, S.; Klyukin, K.; Wakeham, R. J.; Rudd, J. A.; Lewis, A. R.; Alexander, S.; Carla, F.; Alexandrov, V.; Andreoli, E., Poly-amide modified copper foam electrodes for enhanced electrochemical reduction of carbon dioxide. *ACS Catal.* 2018, *8* (5), 4132-4142.

97. Xing, Z.; Hu, L.; Ripatti, D. S.; Hu, X.; Feng, X., Enhancing carbon dioxide gas-diffusion electrolysis by creating a hydrophobic catalyst microenvironment. *Nat. Commun.* 2021, *12* (1), 1-11.

98. Xing, Z.; Hu, X.; Feng, X., Tuning the microenvironment in gas-diffusion electrodes enables high-rate CO_2 electrolysis to formate. *ACS Energy Lett.* 2021, *6* (5), 1694-1702.

99. Baruch, M. F.; Pander III, J. E.; White, J. L.; Bocarsly, A. B., Mechanistic insights into the reduction of CO_2 on tin electrodes using in situ ATR-IR spectroscopy. *ACS Catal.* 2015, *5* (5), 3148-3156.

100. Deng, W.; Zhang, L.; Li, L.; Chen, S.; Hu, C.; Zhao, Z.-J.; Wang, T.; Gong, J., Crucial role of surface hydroxyls on the activity and stability in electrochemical CO_2 reduction. *J. Am. Chem. Soc.* 2019, *141* (7), 2911-2915.

101. An, X.; Li, S.; Yoshida, A.; Wang, Z.; Hao, X.; Abudula, A.; Guan, G., Electrodeposition of tin-based electrocatalysts with different surface tin species distributions for electrochemical reduction of CO_2 to HCOOH. *ACS Sustain. Chem. Eng.* 2019, *7* (10), 9360-9368.

102. Wu, J.; Bai, X.; Ren, Z.; Du, S.; Song, Z.; Zhao, L.; Liu, B.; Wang, G.; Fu, H., Multivalent Sn species synergistically favours the CO_2-into-HCOOH conversion. *Nano Res.* 2021, *14* (4), 1053-1060.

103. Chen, Z.; Gao, M.-R.; Duan, N.; Zhang, J.; Zhang, Y.-Q.; Fan, T.; Zhang, J.; Dong, Y.; Li, J.; Liu, Q., Tuning adsorption strength of CO_2 and its intermediates on tin oxide-based electrocatalyst for efficient CO_2 reduction towards carbonaceous products. *Appl. Catal. B* 2020, *277*, 119252.

104. Li, F.; Chen, L.; Knowles, G. P.; MacFarlane, D. R.; Zhang, J., Hierarchical mesoporous SnO_2 nanosheets on carbon cloth: a robust and flexible electrocatalyst for CO_2 reduction with high efficiency and selectivity. *Angew. Chem.* 2017, *129* (2), 520-524.

105. Wei, F.; Wang, T.; Jiang, X.; Ai, Y.; Cui, A.; Cui, J.; Fu, J.; Cheng, J.; Lei, L.; Hou, Y., Controllably engineering mesoporous surface and dimensionality of SnO_2 toward high-performance CO_2 electroreduction. *Adv. Funct. Mater.* 2020, *30* (39), 2002092.

106. Kim, K.-S.; Kim, W. J.; Lim, H.-K.; Lee, E. K.; Kim, H., Tuned chemical bonding ability of Au at grain boundaries for enhanced electrochemical CO_2 reduction. *ACS Catal.* 2016, *6* (7), 4443-4448.

107. Kumar, B.; Atla, V.; Brian, J. P.; Kumari, S.; Nguyen, T. Q.; Sunkara, M.; Spurgeon, J. M., Reduced SnO_2 porous nanowires with a high density of grain boundaries as catalysts for efficient electrochemical CO_2-into-HCOOH conversion. *Angew. Chem., Int. Ed.* 2017, *56* (13), 3645-3649.

108. Liu, S.; Xiao, J.; Lu, X. F.; Wang, J.; Wang, X.; Lou, X. W., Efficient electrochemical reduction of CO_2 to HCOOH over sub-2 nm SnO_2 quantum wires with exposed grain boundaries. *Angew. Chem., Int. Ed.* 2019, *58* (25), 8499-8503.

109. Zhang, S.; Kang, P.; Meyer, T. J., Nanostructured tin catalysts for selective electrochemical reduction of carbon dioxide to formate. *J. Am. Chem. Soc.* 2014, *136* (5), 1734-1737.

110. Tsujiguchi, T.; Kawabe, Y.; Jeong, S.; Ohto, T.; Kukunuri, S.; Kuramochi, H.; Takahashi, Y.; Nishiuchi, T.; Masuda, H.; Wakisaka, M., Acceleration of electrochemical CO_2 reduction to formate at the Sn/reduced graphene oxide interface. *ACS Catal.* 2021, *11* (6), 3310-3318.

111. Yuan, L.-P.; Jiang, W.-J.; Liu, X.-L.; He, Y.-H.; He, C.; Tang, T.; Zhang, J.; Hu, J.-S., Molecularly engineered strong metal oxide–support interaction enables highly efficient and stable CO_2 electroreduction. *ACS Catal.* 2020, *10* (22), 13227-13235.

112. Pan, Y.; Lin, R.; Chen, Y.; Liu, S.; Zhu, W.; Cao, X.; Chen, W.; Wu, K.; Cheong, W.-C.; Wang, Y., Design of single-atom Co–N_5 catalytic site: a robust electrocatalyst for CO_2 reduction with nearly 100% CO selectivity and remarkable stability. *J. Am. Chem. Soc.* 2018, *140* (12), 4218-4221.

113. Zhang, H.; Li, J.; Xi, S.; Du, Y.; Hai, X.; Wang, J.; Xu, H.; Wu, G.; Zhang, J.; Lu, J., A graphene-supported single-atom FeN_5 catalytic site for efficient electrochemical CO_2 reduction. *Angew. Chem.* 2019, *131* (42), 15013-15018.

114. Su, X.; Yang, X.-F.; Huang, Y.; Liu, B.; Zhang, T., Single-atom catalysis toward efficient CO_2 conversion to CO and formate products. *Acc. Chem. Res.* 2018, *52* (3), 656-664.

115. Zheng, T.; Liu, C.; Guo, C.; Zhang, M.; Li, X.; Jiang, Q.; Xue, W.; Li, H.; Li, A.; Pao, C.-W., Copper-catalysed exclusive CO_2 to pure formic acid conversion via single-atom alloying. *Nat. Nanotechnol.* 2021, *16* (12), 1386-1393.

116. Zu, X.; Li, X.; Liu, W.; Sun, Y.; Xu, J.; Yao, T.; Yan, W.; Gao, S.; Wang, C.; Wei, S., Efficient and robust carbon dioxide electroreduction enabled by atomically dispersed $Sn^{\delta+}$ sites. *Adv. Mater.* 2019, *31* (15), 1808135.

117. Ni, W.; Gao, Y.; Lin, Y.; Ma, C.; Guo, X.; Wang, S.; Zhang, S., Nonnitrogen coordination environment steering electrochemical CO_2-to-CO conversion over single-atom tin catalysts in a wide potential window. *ACS Catal.* 2021, *11* (9), 5212-5221.

118. Zeng, Z.; Gan, L. Y.; Bin Yang, H.; Su, X.; Gao, J.; Liu, W.; Matsumoto, H.; Gong, J.; Zhang, J.; Cai, W., Orbital coupling of hetero-diatomic nickel-iron site for bifunctional electrocatalysis of CO_2 reduction and oxygen evolution. *Nat. Commun.* 2021, *12* (1), 1-11.

119. Ren, W.; Tan, X.; Yang, W.; Jia, C.; Xu, S.; Wang, K.; Smith, S. C.; Zhao, C., Isolated diatomic Ni-Fe metal–nitrogen sites for synergistic electroreduction of CO_2. *Angew. Chem., Int. Ed.* 2019, *58* (21), 6972-6976.

120. Xie, W.; Li, H.; Cui, G.; Li, J.; Song, Y.; Li, S.; Zhang, X.; Lee, J. Y.; Shao, M.; Wei, M., NiSn atomic pair on an integrated electrode for synergistic electrocatalytic CO_2 reduction. *Angew. Chem.* 2021, *133* (13), 7458-7464.

121. Li, H.; Xiao, N.; Wang, Y.; Liu, C.; Zhang, S.; Zhang, H.; Bai, J.; Xiao, J.; Li, C.; Guo, Z., Promoting the electroreduction of CO_2 with oxygen vacancies on a plasma-activated SnO_x/carbon foam monolithic electrode. *J. Mater. Chem. A* 2020, *8* (4), 1779-1786.

122. Li, L.; Zhao, Z.-J.; Hu, C.; Yang, P.; Yuan, X.; Wang, Y.; Zhang, L.; Moskaleva, L.; Gong, J., Tuning oxygen vacancies of oxides to promote electrocatalytic reduction of carbon dioxide. *ACS Energy Lett.* 2020, *5* (2), 552-558.

123. Liu, G.; Li, Z.; Shi, J.; Sun, K.; Ji, Y.; Wang, Z.; Qiu, Y.; Liu, Y.; Wang, Z.; Hu, P., Black reduced porous SnO_2 nanosheets for CO_2 electroreduction with high formate selectivity and low overpotential. *Appl. Catal. B* 2020, *260*, 118134.

124. He, J.; Liu, X.; Liu, H.; Zhao, Z.; Ding, Y.; Luo, J., Highly selective electrocatalytic reduction of CO_2 to formate over Tin (IV) sulfide monolayers. *J. Catal.* 2018, *364*, 125-130.

125. Zhang, A.; He, R.; Li, H.; Chen, Y.; Kong, T.; Li, K.; Ju, H.; Zhu, J.; Zhu, W.; Zeng, J., Nickel doping in atomically thin tin disulfide nanosheets enables highly efficient CO_2 reduction. *Angew. Chem.* 2018, *130* (34), 11120-11124.

126. Chen, M.; Wan, S.; Zhong, L.; Liu, D.; Yang, H.; Li, C.; Huang, Z.; Liu, C.; Chen, J.; Pan, H., Dynamic Restructuring of Cu-Doped SnS_2 Nanoflowers for Highly Selective Electrochemical CO_2 Reduction to Formate. *Angew. Chem., Int. Ed.* 2021, *60* (50), 26233-26237.

127. Zheng, X.; De Luna, P.; de Arquer, F. P. G.; Zhang, B.; Becknell, N.; Ross, M. B.; Li, Y.; Banis, M. N.; Li, Y.; Liu, M., Sulfur-modulated tin sites enable highly selective electrochemical reduction of CO_2 to formate. *Joule* 2017, *1* (4), 794-805.

128. Pan, B.; Yuan, G.; Zhao, X.; Han, N.; Huang, Y.; Feng, K.; Cheng, C.; Zhong, J.; Zhang, L.; Wang, Y., Highly Dispersed Indium Oxide Nanoparticles Supported on Carbon Nanorods Enabling Efficient Electrochemical CO_2 Reduction. *Small Science* 2021, *1* (10), 2100029.

129. Jang, Y. J.; Lee, J.; Kim, J. H.; Lee, B. J.; Lee, J. S., One-dimensional CuIn alloy nanowires as a robust and efficient electrocatalyst for selective CO_2-to-CO conversion. *J. Power Sources* 2018, *378*, 412-417.

130. Zhang, A.; Liang, Y.; Li, H.; Zhao, X.; Chen, Y.; Zhang, B.; Zhu, W.; Zeng, J., Harmonizing the electronic structures of the adsorbate and catalysts for efficient CO_2 reduction. *Nano Lett.* 2019, *19* (9), 6547-6553.

131. Hoffman, Z. B.; Gray, T. S.; Moraveck, K. B.; Gunnoe, T. B.; Zangari, G., Electrochemical reduction of carbon dioxide to syngas and formate at dendritic copper–indium electrocatalysts. *ACS Catal.* 2017, *7* (8), 5381-5390.

132. Luo, W.; Xie, W.; Li, M.; Zhang, J.; Züttel, A., 3D hierarchical porous indium catalyst for highly efficient electroreduction of CO_2. *J. Mater. Chem. A* 2019, *7* (9), 4505-4515.

133. Zhang, Z.; Ahmad, F.; Zhao, W.; Yan, W.; Zhang, W.; Huang, H.; Ma, C.; Zeng, J., Enhanced electrocatalytic reduction of CO_2 via chemical coupling between indium oxide and reduced graphene oxide. *Nano Lett.* 2019, *19* (6), 4029-4034.

134. Shang, H.; Wang, T.; Pei, J.; Jiang, Z.; Zhou, D.; Wang, Y.; Li, H.; Dong, J.; Zhuang, Z.; Chen, W., Design of a Single-Atom Indium$^{\delta+}$–N_4 Interface for Efficient Electroreduction of CO_2 to Formate. *Angew. Chem., Int. Ed.* 2020, *59* (50), 22465-22469.

135. Zhang, J.; Yin, R.; Shao, Q.; Zhu, T.; Huang, X., Oxygen vacancies in amorphous InO_x nanoribbons enhance CO_2 adsorption and activation for CO_2 electroreduction. *Angew. Chem., Int. Ed.* 2019, *58* (17), 5609-5613.

136. Ma, W.; Xie, S.; Zhang, X.-G.; Sun, F.; Kang, J.; Jiang, Z.; Zhang, Q.; Wu, D.-Y.; Wang, Y., Promoting electrocatalytic CO_2 reduction to formate via sulfur-boosting water activation on indium surfaces. *Nat. Commun.* 2019, *10* (1), 1-10.

137. Zhang, A.; Liang, Y.; Li, H.; Zhang, B.; Liu, Z.; Chang, Q.; Zhang, H.; Zhu, C.-F.; Geng, Z.; Zhu, W., In-situ surface reconstruction of InN nanosheets for efficient CO_2 electroreduction into formate. *Nano Lett.* 2020, *20* (11), 8229-8235.

138. Chi, L.-P.; Niu, Z.-Z.; Zhang, X.-L.; Yang, P.-P.; Liao, J.; Gao, F.-Y.; Wu, Z.-Z.; Tang, K.-B.; Gao, M.-R., Stabilizing indium sulfide for CO_2 electroreduction to formate at high rate by zinc incorporation. *Nat. Commun.* 2021, *12* (1), 1-9.

139. Lee, C. H.; Kanan, M. W., Controlling H^+ vs CO_2 reduction selectivity on Pb electrodes. *ACS Catal.* 2015, *5* (1), 465-469.

140. Shi, Y.; Ji, Y.; Long, J.; Liang, Y.; Liu, Y.; Yu, Y.; Xiao, J.; Zhang, B., Unveiling hydrocerussite as an electrochemically stable active phase for efficient carbon dioxide electroreduction to formate. *Nat. Commun.* 2020, *11* (1), 1-10.

141. Medina-Ramos, J.; Pupillo, R. C.; Keane, T. P.; DiMeglio, J. L.; Rosenthal, J., Efficient conversion of CO_2 to CO using tin and other inexpensive and easily prepared post-transition metal catalysts. *J. Am. Chem. Soc.* 2015, *137* (15), 5021-5027.

142. Jiang, Z.; Wang, T.; Pei, J.; Shang, H.; Zhou, D.; Li, H.; Dong, J.; Wang, Y.; Cao, R.; Zhuang, Z., Discovery of main group single $Sb–N_4$ active sites for CO_2 electroreduction to formate with high efficiency. *Energy Environ. Sci.* 2020, *13* (9), 2856-2863.

143. Nielsen, D. U.; Hu, X.-M.; Daasbjerg, K.; Skrydstrup, T., Chemically and electrochemically catalysed conversion of CO_2 to CO with follow-up utilization to value-added chemicals. *Nat. Catal.* 2018, *1* (4), 244-254.

144. Ross, M. B.; De Luna, P.; Li, Y.; Dinh, C.-T.; Kim, D.; Yang, P.; Sargent, E. H., Designing materials for electrochemical carbon dioxide recycling. *Nat. Catal.* 2019, *2* (8), 648-658.

145. Scofield, M. E.; Koenigsmann, C.; Wang, L.; Liu, H.; Wong, S. S., Tailoring the composition of ultrathin, ternary alloy PtRuFe nanowires for the methanol oxidation reaction and formic acid oxidation reaction. *Energy Environ. Sci.* 2015, *8* (1), 350-363.

146. Qiao, J.; Liu, Y.; Hong, F.; Zhang, J., A review of catalysts for the electroreduction of carbon dioxide to produce low-carbon fuels. *Chem. Soc. Rev.* 2014, *43* (2), 631-675.

147. Chen, Y.; Kanan, M. W., Tin oxide dependence of the CO_2 reduction efficiency on tin electrodes and enhanced activity for tin/tin oxide thin-film catalysts. *J. Am. Chem. Soc.* 2012, *134* (4), 1986-1989.

148. Centi, G.; Quadrelli, E. A.; Perathoner, S., Catalysis for CO_2 conversion: a key technology for rapid introduction of renewable energy in the value chain of chemical industries. *Energy Environ. Sci.* 2013, *6* (6), 1711-1731.

149. Ji, X.; Lee, K. T.; Holden, R.; Zhang, L.; Zhang, J.; Botton, G. A.; Couillard, M.; Nazar, L. F., Nanocrystalline intermetallics on mesoporous carbon for direct formic acid fuel cell anodes. *Nat. Chem.* 2010, *2* (4), 286-293.

150. Ding, J.; Liu, Z.; Liu, X.; Liu, J.; Deng, Y.; Han, X.; Zhong, C.; Hu, W., Mesoporous decoration of freestanding palladium nanotube arrays boosts the electrocatalysis capabilities toward formic acid and formate oxidation. *Adv. Energy Mater.* 2019, *9* (25), 1900955.

151. Fan, L.; Xia, C.; Zhu, P.; Lu, Y.; Wang, H., Electrochemical CO_2 reduction to high-concentration pure formic acid solutions in an all-solid-state reactor. *Nat. Commun.* 2020, *11* (1), 1-9.

152. Zhou, Y.; Zhou, R.; Zhu, X.; Han, N.; Song, B.; Liu, T.; Hu, G.; Li, Y.; Lu, J.; Li, Y., Mesoporous PdAg nanospheres for stable electrochemical CO_2 reduction to formate. *Adv. Mater.* 2020, *32* (30), 2000992.

153. Jiang, B.; Zhang, X.-G.; Jiang, K.; Wu, D.-Y.; Cai, W.-B., Boosting formate production in electrocatalytic CO_2 reduction over wide potential window on Pd surfaces. *J. Am. Chem. Soc.* 2018, *140* (8), 2880-2889.

154. Zhang, A.; Liang, Y.; Li, H.; Zhang, B.; Liu, Z.; Chang, Q.; Zhang, H.; Zhu, C.-F.; Geng, Z.; Zhu, W., In-Situ Surface Reconstruction of InN Nanosheets for Efficient CO_2 Electroreduction into Formate. *Nano Lett.* 2020, 20 (11) 8229-8235.

155. Zhang, W.; Hu, Y.; Ma, L.; Zhu, G.; Zhao, P.; Xue, X.; Chen, R.; Yang, S.; Ma, J.; Liu, J., Liquid-phase exfoliated ultrathin Bi nanosheets: uncovering the origins of enhanced electrocatalytic CO_2 reduction on two-dimensional metal nanostructure. *Nano Energy* 2018, *53*, 808-816.

156. Liu, S.; Lu, X. F.; Xiao, J.; Wang, X.; Lou, X. W., Bi_2O_3 Nanosheets Grown on Multi-Channel Carbon Matrix to Catalyze Efficient CO_2 Electroreduction to HCOOH. *Angew. Chem., Int. Ed.* 2019, *58* (39), 13828-13833.

157. Koh, J. H.; Won, D. H.; Eom, T.; Kim, N.-K.; Jung, K. D.; Kim, H.; Hwang, Y. J.; Min, B. K., Facile CO_2 electro-reduction to formate via oxygen bidentate intermediate stabilized by high-index planes of Bi dendrite catalyst. *ACS Catal.* 2017, *7* (8), 5071-5077.

158. Zhang, Z.; Chi, M.; Veith, G. M.; Zhang, P.; Lutterman, D. A.; Rosenthal, J.; Overbury, S. H.; Dai, S.; Zhu, H., Rational design of Bi nanoparticles for efficient electrochemical CO_2 reduction: the elucidation of size and surface condition effects. *ACS Catal.* 2016, *6* (9), 6255-6264.

159. Fan, K.; Jia, Y.; Ji, Y.; Kuang, P.; Zhu, B.; Liu, X.; Yu, J., Curved surface boosts electrochemical CO_2 reduction to formate via bismuth nanotubes in a wide potential window. *ACS Catal.* 2019, *10* (1), 358-364.

160. Li, Q.; Zhang, X.; Zhou, X.; Li, Q.; Wang, H.; Yi, J.; Liu, Y.; Zhang, J., Simply and effectively electrodepositing Bi-MWCNT-COOH composite on Cu electrode for efficient electrocatalytic CO_2 reduction to produce HCOOH. *J. CO_2 Util.* 2020, *37*, 106-112.

161. Pang, R.; Tian, P.; Jiang, H.; Zhu, M.; Su, X.; Wang, Y.; Yang, X.; Zhu, Y.; Song, L.; Li, C., Tracking structural evolution: operando regenerative CeO_x/Bi interface structure for high-performance CO_2 electroreduction. *Natl. Sci. Rev.* 2020, 8 (7) nwaa187.

162. Cheng, H.; Liu, S.; Zhang, J.; Zhou, T.; Zhang, N.; Zheng, X.-s.; Chu, W.; Hu, Z.; Wu, C.; Xie, Y., Surface Nitrogen-Injection Engineering for High Formation Rate of CO_2 Reduction to Formate. *Nano Lett.* 2020, *20* (8), 6097-6103.

163. Yu, J.; Guo, Y.; Miao, S.; Ni, M.; Zhou, W.; Shao, Z., Spherical ruthenium disulfide-sulfur-doped graphene composite as an efficient hydrogen evolution electrocatalyst. *ACS Appl. Mater. Interfaces* 2018, *10* (40), 34098-34107.

164. Yu, L.; Wu, L.; McElhenny, B.; Song, S.; Luo, D.; Zhang, F.; Yu, Y.; Chen, S.; Ren, Z., Ultrafast room-temperature synthesis of porous S-doped Ni/Fe (oxy) hydroxide electrodes for oxygen evolution catalysis in seawater splitting. *Energy Environ. Sci.* 2020, 13 (10) 3439-3446.

165. Wang, Y. C.; Lai, Y. J.; Song, L.; Zhou, Z. Y.; Liu, J. G.; Wang, Q.; Yang, X. D.; Chen, C.; Shi, W.; Zheng, Y. P., S-doping of an Fe/N/C ORR catalyst for polymer electrolyte membrane fuel cells with high power density. *Angew. Chem.* 2015, *127* (34), 10045-10048.

166. Tian, W.; Zhang, H.; Sun, H.; Suvorova, A.; Saunders, M.; Tade, M.; Wang, S., Heteroatom (N or N-S)-Doping Induced Layered and Honeycomb Microstructures of Porous Carbons for CO_2 Capture and Energy Applications. *Adv. Funct. Mater.* 2016, *26* (47), 8651-8661.

167. Yang, H.; Wu, Y.; Lin, Q.; Fan, L.; Chai, X.; Zhang, Q.; Liu, J.; He, C.; Lin, Z., Composition Tailoring via N and S Co-doping and Structure Tuning by Constructing Hierarchical Pores: Metal-Free Catalysts for High-Performance Electrochemical Reduction of CO_2. *Angew. Chem.* 2018, *130* (47), 15702-15706.

168. Zhang, X.; Fu, J.; Liu, Y.; Zhou, X.-D.; Qiao, J., Bismuth Anchored on MWCNTs with Controlled Ultrafine Nanosize Enables High-Efficient Electrochemical Reduction of Carbon Dioxide to Formate Fuel. *ACS Sustain. Chem. Eng.* 2020, *8* (12), 4871-4876.

169. Wu, D.; Huo, G.; Chen, W.; Fu, X.-Z.; Luo, J.-L., Boosting formate production at high current density from CO_2 electroreduction on defect-rich hierarchical mesoporous Bi/Bi_2O_3 junction nanosheets. *Appl. Catal. B* 2020, 118957.

170. Chen, W.; Li, X.; Duan, L.; Xie, X.; Cui, Y., Photoluminescence enhancement of $(NH_4)_2S_x$ passivated InP surface by rapid thermal annealing. *Appl. Surf. Sci.* 1996, *100*, 592-595.

171. Xu, L.; Jiang, Q.; Xiao, Z.; Li, X.; Huo, J.; Wang, S.; Dai, L., Plasma-engraved Co_3O_4 nanosheets with oxygen vacancies and high surface area for the oxygen evolution reaction. *Angew. Chem.* 2016, *128* (17), 5363-5367.

172. García de Arquer, F. P.; Bushuyev, O. S.; De Luna, P.; Dinh, C. T.; Seifitokaldani, A.; Saidaminov, M. I.; Tan, C. S.; Quan, L. N.; Proppe, A.; Kibria, M. G., 2D metal oxyhalide-derived catalysts for efficient CO_2 electroreduction. *Adv. Mater.* 2018, *30* (38), 1802858.

173. Reske, R.; Mistry, H.; Behafarid, F.; Roldan Cuenya, B.; Strasser, P., Particle size effects in the catalytic electroreduction of CO_2 on Cu nanoparticles. *J. Am. Chem. Soc.* 2014, *136* (19), 6978-6986.

174. Zheng, W.; Yang, J.; Chen, H.; Hou, Y.; Wang, Q.; Gu, M.; He, F.; Xia, Y.; Xia, Z.; Li, Z., Atomically defined undercoordinated active sites for highly efficient CO_2 electroreduction. *Adv. Funct. Mater.* 2020, *30* (4), 1907658.

175. Clark, E. L.; Ringe, S.; Tang, M.; Walton, A.; Hahn, C.; Jaramillo, T. F.; Chan, K.; Bell, A. T., Influence of Atomic Surface Structure on the Activity of Ag for the Electrochemical Reduction of CO_2 to CO. *ACS Catal.* 2019, *9* (5), 4006-4014.

176. Zhang, S.; Kang, P.; Ubnoske, S.; Brennaman, M. K.; Song, N.; House, R. L.; Glass, J. T.; Meyer, T. J., Polyethylenimine-enhanced electrocatalytic reduction of CO_2 to formate at nitrogen-doped carbon nanomaterials. *J. Am. Chem. Soc.* 2014, *136* (22), 7845-7848.

177. Zhao, K.; Quan, X., Carbon-Based Materials for Electrochemical Reduction of CO_2 to C_{2+} Oxygenates: Recent Progress and Remaining Challenges. *ACS Catal.* 2021, *11* (4), 2076-2097.

178. Qi, H.; Yu, P.; Wang, Y.; Han, G.; Liu, H.; Yi, Y.; Li, Y.; Mao, L., Graphdiyne oxides as excellent substrate for electroless deposition of Pd clusters with high catalytic activity. *J. Am. Chem. Soc.* 2015, *137* (16), 5260-5263.

179. Nørskov, J. K.; Abild-Pedersen, F.; Studt, F.; Bligaard, T., Density functional theory in surface chemistry and catalysis. *Proc. Natl. Acad. Sci. U.S.A.* 2011, *108* (3), 937-943.

180. Hammer, B.; Nørskov, J. K., Theoretical surface science and catalysis—calculations and concepts. In *Adv. Catal.* Elsevier: 2000; Vol. 45, pp 71-129.

181. Perdew, J. P.; Burke, K.; Ernzerhof, M., Generalized gradient approximation made simple. *Phys. Rev. Lett.* 1996, *77* (18), 3865.

182. Kresse, G.; Hafner, J., Ab initio molecular dynamics for liquid metals. *Phys. Rev. B* 1993, *47* (1), 558.

183. Kresse, G.; Furthmüller, J., Efficient iterative schemes for ab initio total-energy calculations using a plane-wave basis set. *Phys. Rev. B* 1996, *54* (16), 11169.

184. Blöchl, P. E., Projector augmented-wave method. *Phys. Rev. B* 1994, *50* (24), 17953.

185. Monkhorst, H. J.; Pack, J. D., Special points for Brillouin-zone integrations. *Phys. Rev. B* 1976, *13* (12), 5188.

186. Cramer, C. J., *Essentials of computational chemistry: theories and models*. John Wiley & Sons: 2013.

187. Tripković, V.; Skúlason, E.; Siahrostami, S.; Nørskov, J. K.; Rossmeisl, J., The oxygen reduction reaction mechanism on Pt (111) from density functional theory calculations. *Electrochim. Acta* 2010, *55* (27), 7975-7981.

188. Peterson, A. A.; Abild-Pedersen, F., F. studt, J. Rossmeisl and JK Nørskov. *Energy Environ. Sci.* 2010, *3*, 1311-1315.

189. Ma, W.; Xie, S.; Zhang, X.-G.; Sun, F.; Kang, J.; Jiang, Z.; Zhang, Q.; Wu, D.-Y.; Wang, Y., Promoting electrocatalytic CO_2 reduction to formate via sulfur-boosting water activation on indium surfaces. *Nat. Commun.* 2019, *10* (1), 1-10.

190. Xia, Z.; Freeman, M.; Zhang, D.; Yang, B.; Lei, L.; Li, Z.; Hou, Y., Highly selective electrochemical conversion of CO_2 to HCOOH on dendritic indium foams. *ChemElectroChem* 2018, *5* (2), 253-259.

191. He, W.; Liberman, I.; Rozenberg, I.; Ifraemov, R.; Hod, I., Electrochemically Driven Cation Exchange Enables the Rational Design of Active CO_2 Reduction Electrocatalysts. *Angew. Chem.* 2020, *132* (21), 8339-8346.

192. Shinagawa, T.; Larrazábal, G. n. O.; Martín, A. J.; Krumeich, F.; Pérez-Ramírez, J., Sulfur-modified copper catalysts for the electrochemical reduction of carbon dioxide to formate. *ACS Catal.* 2018, *8* (2), 837-844.

193. Yang, Q.; Wu, Q.; Liu, Y.; Luo, S.; Wu, X.; Zhao, X.; Zou, H.; Long, B.; Chen, W.; Liao, Y., Novel Bi-Doped Amorphous SnO_x Nanoshells for Efficient Electrochemical CO_2 Reduction into Formate at Low Overpotentials. *Adv. Mater.* 2020, 2002822.

194. Yuan, T.; Hu, Z.; Zhao, Y.; Fang, J.; Lv, J.; Zhang, Q.; Zhuang, Z.; Gu, L.; Hu, S., Two-Dimensional Amorphous SnO_x from Liquid Metal: Mass Production, Phase Transfer, and Electrocatalytic CO_2 Reduction toward Formic Acid. *Nano Lett.* 2020, *20* (4), 2916-2922.

195. Fan, L.; Xia, Z.; Xu, M.; Lu, Y.; Li, Z., 1D SnO_2 with Wire-in-Tube Architectures for Highly Selective Electrochemical Reduction of CO_2 to C_1 Products. *Adv. Funct. Mater.* 2018, *28* (17), 1706289.

196. Gu, J.; Héroguel, F.; Luterbacher, J.; Hu, X., Densely packed, ultra small SnO nanoparticles for enhanced activity and selectivity in electrochemical CO_2 reduction. *Angew. Chem.* 2018, *130* (11), 2993-2997.

197. Deng, P.; Yang, F.; Wang, Z.; Chen, S.; Zhou, Y.; Zaman, S.; Xia, B. Y., Metal–Organic Framework-Derived Carbon Nanorods Encapsulating Bismuth Oxides for Rapid and Selective CO_2 Electroreduction to Formate. *Angew. Chem., Int. Ed.* 2020, 59 (27) 10807-10813.

198. Wen, G.; Lee, D. U.; Ren, B.; Hassan, F. M.; Jiang, G.; Cano, Z. P.; Gostick, J.; Croiset, E.; Bai, Z.; Yang, L., Carbon Dioxide Electroreduction: Orbital Interactions in Bi-Sn Bimetallic Electrocatalysts for Highly Selective Electrochemical CO_2 Reduction toward Formate Production. *Adv. Energy Mater.* 2018, *8* (31), 1870138.

199. He, S.; Ni, F.; Ji, Y.; Wang, L.; Wen, Y.; Bai, H.; Liu, G.; Zhang, Y.; Li, Y.; Zhang, B., The p-orbital delocalization of main-group metals to boost CO_2 electroreduction. *Angew. Chem.* 2018, *130* (49), 16346-16351.

200. Yang, H.; Han, N.; Deng, J.; Wu, J.; Wang, Y.; Hu, Y.; Ding, P.; Li, Y.; Li, Y.; Lu, J., Selective CO_2 reduction on 2D mesoporous Bi nanosheets. *Adv. Energy Mater.* 2018, *8* (35), 1801536.

201. Zhang, X.; Lei, T.; Liu, Y.; Qiao, J., Enhancing CO_2 electrolysis to formate on facilely synthesized Bi catalysts at low overpotential. *Appl. Catal. B* 2017, *218*, 46-50.

202. Ma, Y.; Wang, J.; Yu, J.; Zhou, J.; Zhou, X.; Li, H.; He, Z.; Long, H.; Wang, Y.; Lu, P., Surface modification of metal materials for high-performance electrocatalytic carbon dioxide reduction. *Matter* 2021, *4* (3), 888-926.

203. De Luna, P.; Hahn, C.; Higgins, D.; Jaffer, S. A.; Jaramillo, T. F.; Sargent, E. H., What would it take for renewably powered electrosynthesis to displace petrochemical processes? *Science* 2019, *364* (6438).

204. Sordakis, K.; Tang, C.; Vogt, L. K.; Junge, H.; Dyson, P. J.; Beller, M.; Laurenczy, G., Homogeneous catalysis for sustainable hydrogen storage in formic acid and alcohols. *Chem. Rev.* 2018, *118* (2), 372-433.

205. Grasemann, M.; Laurenczy, G., Formic acid as a hydrogen source–recent developments and future trends. *Energy Environ. Sci.* 2012, *5* (8), 8171-8181.

206. Rahaman, M.; Dutta, A.; Broekmann, P., Size-Dependent Activity of Palladium Nanoparticles: Efficient Conversion of CO_2 into Formate at Low Overpotentials. *Chemsuschem* 2017, *10* (8), 1733-1741.

207. Li, Z.; Cao, A.; Zheng, Q.; Fu, Y.; Wang, T.; Arul, K. T.; Chen, J. L.; Yang, B.; Adli, N. M.; Lei, L., Elucidation of the synergistic effect of dopants and vacancies on promoted selectivity for CO_2 electroreduction to formate. *Adv. Mater.* 2021, *33* (2), 2005113.

208. Liu, S.-Q.; Gao, M.-R.; Feng, R.-F.; Gong, L.; Zeng, H.; Luo, J.-L., Electronic Delocalization of Bismuth Oxide Induced by Sulfur Doping for Efficient CO_2 Electroreduction to Formate. *ACS Catal.* 2021, *11*, 7604-7612.

209. Wuttig, A.; Yaguchi, M.; Motobayashi, K.; Osawa, M.; Surendranath, Y., Inhibited proton transfer enhances Au-catalyzed CO_2-to-fuels selectivity. *Proc. Natl. Acad. Sci. U.S.A.* 2016, *113* (32), E4585-E4593.

210. Zhang, B. A.; Ozel, T.; Elias, J. S.; Costentin, C.; Nocera, D. G., Interplay of homogeneous reactions, mass transport, and kinetics in determining selectivity of the reduction of CO_2 on Gold electrodes. *ACS Cent. Sci.* 2019, *5* (6), 1097-1105.

211. Li, J.; Chen, G.; Zhu, Y.; Liang, Z.; Pei, A.; Wu, C.-L.; Wang, H.; Lee, H. R.; Liu, K.; Chu, S., Efficient electrocatalytic CO_2 reduction on a three-phase interface. *Nat. Catal.* 2018, *1* (8), 592-600.

212. Raciti, D.; Mao, M.; Park, J. H.; Wang, C., Mass transfer effects in CO_2 reduction on Cu nanowire electrocatalysts. *Catal. Sci. Technol.* 2018, *8* (9), 2364-2369.

213. Wang, J.; Cheng, T.; Fenwick, A. Q.; Baroud, T. N.; Rosas-Hernández, A.; Ko, J. H.; Gan, Q.; Goddard Iii, W. A.; Grubbs, R. H., Selective CO_2 Electrochemical Reduction Enabled by a Tricomponent Copolymer Modifier on a Copper Surface. *J. Am. Chem. Soc.* 2021, *143* (7), 2857-2865.

214. Chen, X.; Chen, J.; Alghoraibi, N. M.; Henckel, D. A.; Zhang, R.; Nwabara, U. O.; Madsen, K. E.; Kenis, P. J.; Zimmerman, S. C.; Gewirth, A. A., Electrochemical CO_2-to-ethylene conversion on polyamine-incorporated Cu electrodes. *Nat. Catal.* 2021, *4* (1), 20-27.

215. Shi, R.; Guo, J.; Zhang, X.; Waterhouse, G. I.; Han, Z.; Zhao, Y.; Shang, L.; Zhou, C.; Jiang, L.; Zhang, T., Efficient wettability-controlled electroreduction of CO_2 to CO at Au/C interfaces. *Nat. Commun.* 2020, *11* (1), 1-10.

216. Wakerley, D.; Lamaison, S.; Ozanam, F.; Menguy, N.; Mercier, D.; Marcus, P.; Fontecave, M.; Mougel, V., Bio-inspired hydrophobicity promotes CO_2 reduction on a Cu surface. *Nat. Mater.* 2019, *18* (11), 1222-1227.

217. Schmitt, K. G.; Gewirth, A. A., In situ surface-enhanced Raman spectroscopy of the electrochemical reduction of carbon dioxide on silver with 3, 5-diamino-1, 2, 4-triazole. *J. Phys. Chem. C* 2014, *118* (31), 17567-17576.

218. Chen, R.; Su, H. Y.; Liu, D.; Huang, R.; Meng, X.; Cui, X.; Tian, Z. Q.; Zhang, D. H.; Deng, D., Highly selective production of ethylene by the electroreduction of carbon monoxide. *Angew. Chem.* 2020, *132* (1), 160-166.

219. Zhao, Z.; Hossain, M. D.; Xu, C.; Lu, Z.; Liu, Y.-S.; Hsieh, S.-H.; Lee, I.; Gao, W.; Yang, J.; Merinov, B. V., Tailoring a Three-Phase Microenvironment for High-Performance Oxygen Reduction Reaction in Proton Exchange Membrane Fuel Cells. *Matter* 2020, *3* (5), 1774-1790.

220. Yan, Y.; Cui, J.; Chan-Park, M.; Wang, X.; Wu, Q., Systematic studies of covalent functionalization of carbon nanotubes via argon plasma-assisted UV grafting. *Nanotechnology* 2007, *18* (11), 115712.

221. Lu, Z.; Xu, W.; Ma, J.; Li, Y.; Sun, X.; Jiang, L., Superaerophilic carbon-nanotube-array electrode for high-performance oxygen reduction reaction. *Adv. Mater.* 2016, *28* (33), 7155-7161.

222. Bligaard, T.; Nørskov, J. K.; Dahl, S.; Matthiesen, J.; Christensen, C. H.; Sehested, J., The Brønsted–Evans–Polanyi relation and the volcano curve in heterogeneous catalysis. *J. Catal.* 2004, *224* (1), 206-217.

223. Dutta, A.; Zelocualtecatl Montiel, I. n.; Kiran, K.; Rieder, A.; Grozovski, V.; Gut, L.; Broekmann, P., A Tandem (Bi_2O_3→ Bimet) Catalyst for Highly Efficient ec-CO_2 Conversion into Formate: Operando Raman Spectroscopic Evidence for a Reaction Pathway Change. *ACS Catal.* 2021, *11*, 4988-5003.

224. Deng, P.; Yang, F.; Wang, Z.; Chen, S.; Zhou, Y.; Zaman, S.; Xia, B. Y., Metal–Organic Framework-Derived Carbon Nanorods Encapsulating Bismuth Oxides for Rapid and Selective CO_2 Electroreduction to Formate. *Angew. Chem., Int. Ed.* 2020, *59* (27), 10807-10813.

225. Dinh, C.-T.; Burdyny, T.; Kibria, M. G.; Seifitokaldani, A.; Gabardo, C. M.; De Arquer, F. P. G.; Kiani, A.; Edwards, J. P.; De Luna, P.; Bushuyev, O. S., CO_2 electroreduction to ethylene via hydroxide-mediated copper catalysis at an abrupt interface. *Science* 2018, *360* (6390), 783-787.

226. O'Brien, T. F.; Bommaraju, T. V.; Hine, F., History of the chlor-alkali industry. In *Handbook of chlor-alkali technology*, Springer: 2005; pp 17-36.

227. Bai, C.; Herzfeld, J., Surface propensities of the self-ions of water. *ACS Cent. Sci.* 2016, *2* (4), 225-231.

228. Gupta, N.; Gattrell, M.; MacDougall, B., Calculation for the cathode surface concentrations in the electrochemical reduction of CO_2 in $KHCO_3$ solutions. *J. Appl. Electrochem.* 2006, *36* (2), 161-172.

229. Xiao, H.; Cheng, T.; Goddard III, W. A.; Sundararaman, R., Mechanistic explanation of the pH dependence and onset potentials for hydrocarbon products from electrochemical reduction of CO on Cu (111). *J. Am. Chem. Soc.* 2016, *138* (2), 483-486.

230. Cai, Z.; Zhang, Y.; Zhao, Y.; Wu, Y.; Xu, W.; Wen, X.; Zhong, Y.; Zhang, Y.; Liu, W.; Wang, H., Selectivity regulation of CO_2 electroreduction through contact interface engineering on superwetting Cu nanoarray electrodes. *Nano Res.* 2019, *12* (2), 345-349.

231. Zhao, Y.; Wang, C.; Liu, Y.; MacFarlane, D. R.; Wallace, G. G., Engineering surface amine modifiers of ultrasmall gold nanoparticles supported on reduced graphene oxide for improved electrochemical CO_2 reduction. *Adv. Energy Mater.* 2018, *8* (25), 1801400.

232. Kim, C.; Eom, T.; Jee, M. S.; Jung, H.; Kim, H.; Min, B. K.; Hwang, Y. J., Insight into electrochemical CO_2 reduction on surface-molecule-mediated Ag nanoparticles. *ACS Catal.* 2017, *7* (1), 779-785.

233. Lu, P.; Tan, X.; Zhao, H.; Xiang, Q.; Liu, K.; Zhao, X.; Yin, X.; Li, X.; Hai, X.; Xi, S., Atomically Dispersed Indium Sites for Selective CO_2 Electroreduction to Formic Acid. *ACS Nano* 2021, *15* (3), 5671-5678.

234. Qi, K.; Zhang, Y.; Li, J.; Charmette, C.; Ramonda, M.; Cui, X.; Wang, Y.; Zhang, Y.; Wu, H.; Wang, W., Enhancing the CO_2-to-CO Conversion from 2D Silver Nanoprisms via Superstructure Assembly. *ACS Nano* 2021, 15, (4) 7682-7693.

235. Kaminski, G. A.; Friesner, R. A.; Tirado-Rives, J.; Jorgensen, W. L., Evaluation and reparametrization of the OPLS-AA force field for proteins via comparison with accurate quantum chemical calculations on peptides. *J. Phys. Chem. B* 2001, *105* (28), 6474-6487.

236. Berendsen, H.; Hess, B.; Lindahl, E.; Van Der Spoel, D.; Mark, A.; Groenhof, G., GROMACS: fast, flexible, and free. *J. Comput. Chem.* 2005, *26* (16), 1701-1718.

237. Jorgensen, W. L.; Tirado-Rives, J., Potential energy functions for atomic-level simulations of water and organic and biomolecular systems. *Proc. Natl. Acad. Sci.* 2005, *102* (19), 6665-6670.

238. Dodda, L. S.; Cabeza de Vaca, I.; Tirado-Rives, J.; Jorgensen, W. L., LigParGen web server: an automatic OPLS-AA parameter generator for organic ligands. *Nucleic Acids Res.* 2017, *45* (W1), W331-W336.

239. Dodda, L. S.; Vilseck, J. Z.; Cutrona, K. J.; Jorgensen, W. L., Evaluation of CM5 charges for nonaqueous condensed-phase modeling. *J. Chem. Theory Comput.* 2015, *11* (9), 4273-4282.

240. Abascal, J. L.; Vega, C., A general purpose model for the condensed phases of water: TIP4P/2005. *J. Chem. Phys.* 2005, *123* (23), 234505.

241. Cao, C.; Ma, D. D.; Gu, J. F.; Xie, X.; Zeng, G.; Li, X.; Han, S. G.; Zhu, Q. L.; Wu, X. T.; Xu, Q., Metal–organic layers leading to atomically thin bismuthene for efficient carbon dioxide electroreduction to liquid fuel. *Angew. Chem.* 2020, *132* (35), 15124-15130.

242. Yang, Q.; Wu, Q.; Liu, Y.; Luo, S.; Wu, X.; Zhao, X.; Zou, H.; Long, B.; Chen, W.; Liao, Y., Novel Bi-Doped Amorphous SnO_x Nanoshells for Efficient Electrochemical CO_2 Reduction into Formate at Low Overpotentials. *Adv. Mater.* 2020, *32* (36), 2002822.

243. Yi, L.; Chen, J.; Shao, P.; Huang, J.; Peng, X.; Li, J.; Wang, G.; Zhang, C.; Wen, Z., Molten-Salt-Assisted Synthesis of Bismuth Nanosheets for Long-term Continuous Electrocatalytic Conversion of CO_2 to Formate. *Angew. Chem.* 2020, *132* (45), 20287-20294.

244. He, S.; Ni, F.; Ji, Y.; Wang, L.; Wen, Y.; Bai, H.; Liu, G.; Zhang, Y.; Li, Y.; Zhang, B., The p-orbital delocalization of main-group metals to boost CO_2 electroreduction. *Angew. Chem., Int. Ed.* 2018, *57* (49), 16114-16119.

245. Chen, Z.; Mou, K.; Wang, X.; Liu, L., Nitrogen-doped graphene quantum dots enhance the activity of Bi_2O_3 nanosheets for electrochemical reduction of CO_2 in a wide negative potential region. *Angew. Chem., Int. Ed.* 2018, *57* (39), 12790-12794.

246. Ma, T.; Wu, Z.; Wu, H.; Cai, W.; Wen, Z.; Wang, L.; Jin, W.; Jia, B., Engineering Bi-Sn Interface in Bimetallic Aerogel with 3D Porous Structure for Highly Selective Electrocatalytic CO_2 Reduction to HCOOH. *Angew. Chem., Int. Ed.* 2021, 60, (22) 12554-12599.

247. Verma, S.; Lu, S.; Kenis, P. J., Co-electrolysis of CO_2 and glycerol as a pathway to carbon chemicals with improved technoeconomics due to low electricity consumption. *Nat. Energy* 2019, *4* (6), 466-474.

248. Wei, X.; Li, Y.; Chen, L.; Shi, J., Formic Acid Electro-Synthesis by Concurrent Cathodic CO_2 Reduction and Anodic CH_3OH Oxidation. *Angew. Chem., Int. Ed.* 2021, *60* (6), 3148-3155.

249. Rausch, B.; Symes, M. D.; Chisholm, G.; Cronin, L., Decoupled catalytic hydrogen evolution from a molecular metal oxide redox mediator in water splitting. *Science* 2014, *345* (6202), 1326-1330.

250. Xiang, K.; Wu, D.; Deng, X.; Li, M.; Chen, S.; Hao, P.; Guo, X.; Luo, J. L.; Fu, X. Z., Boosting H_2 generation coupled with selective oxidation of methanol into value-added chemical over cobalt hydroxide@hydroxysulfide nanosheets electrocatalysts. *Adv. Funct. Mater.* 2020, *30* (10), 1909610.

251. Si, D.; Xiong, B.; Chen, L.; Shi, J., Highly selective and efficient electrocatalytic synthesis of glycolic acid in coupling with hydrogen evolution. *Chem. Catal.* 2021, *1* (4), 941-955.

252. Liu, W.-J.; Xu, Z.; Zhao, D.; Pan, X.-Q.; Li, H.-C.; Hu, X.; Fan, Z.-Y.; Wang, W.-K.; Zhao, G.-H.; Jin, S., Efficient electrochemical production of glucaric acid and H_2 via glucose electrolysis. *Nat. Commun.* 2020, *11* (1), 1-11.

253. Zhou, H.; Ren, Y.; Li, Z.; Xu, M.; Wang, Y.; Ge, R.; Kong, X.; Zheng, L.; Duan, H., Electrocatalytic upcycling of polyethylene terephthalate to commodity chemicals and H_2 fuel. *Nat. Commun.* 2021, *12* (1), 1-9.

254. Yin, K.; Chao, Y.; Lv, F.; Tao, L.; Zhang, W.; Lu, S.; Li, M.; Zhang, Q.; Gu, L.; Li, H., One nanometer PtIr nanowires as high-efficiency bifunctional catalysts for electrosynthesis of ethanol into high value-added multicarbon compound coupled with hydrogen production. *J. Am. Chem. Soc.* 2021, *143* (29), 10822-10827.

255. Wang, T.; Tao, L.; Zhu, X.; Chen, C.; Chen, W.; Du, S.; Zhou, Y.; Zhou, B.; Wang, D.; Xie, C., Combined anodic and cathodic hydrogen production from aldehyde oxidation and hydrogen evolution reaction. *Nat. Catal.* 2021, 1-8.

256. Tournier, V.; Topham, C.; Gilles, A.; David, B.; Folgoas, C.; Moya-Leclair, E.; Kamionka, E.; Desrousseaux, M.-L.; Texier, H.; Gavalda, S., An engineered PET depolymerase to break down and recycle plastic bottles. *Nature* 2020, *580* (7802), 216-219.

257. Ügdüler, S.; Van Geem, K. M.; Denolf, R.; Roosen, M.; Mys, N.; Ragaert, K.; De Meester, S., Towards closed-loop recycling of multilayer and coloured PET plastic waste by alkaline hydrolysis. *Green Chem.* 2020, *22* (16), 5376-5394.

258. Uekert, T.; Kasap, H.; Reisner, E., Photoreforming of nonrecyclable plastic waste over a carbon nitride/nickel phosphide catalyst. *J. Am. Chem. Soc.* 2019, *141* (38), 15201-15210.

259. Wang, X.; Sang, X.; Dong, C. L.; Yao, S.; Shuai, L.; Lu, J.; Yang, B.; Li, Z.; Lei, L.; Qiu, M., Proton capture strategy for enhancing electrochemical CO_2 reduction on atomically dispersed metal–nitrogen active sites. *Angew. Chem., Int. Ed.* 2021, *60* (21), 11959-11965.

260. Chen, D.; Zhang, L. H.; Du, J.; Wang, H.; Guo, J.; Zhan, J.; Li, F.; Yu, F., A Tandem Strategy for Enhancing Electrochemical CO_2 Reduction Activity of Single-Atom Cu-S_1N_3 Catalysts via Integration with Cu Nanoclusters. *Angew. Chem., Int. Ed.* 2021, *60* (45), 24022-24027.

261. Liu, C.; Wu, Y.; Sun, K.; Fang, J.; Huang, A.; Pan, Y.; Cheong, W.-C.; Zhuang, Z.; Zhuang, Z.; Yuan, Q., Constructing FeN_4/graphitic nitrogen atomic interface for high-efficiency electrochemical CO_2 reduction over a broad potential window. *Chem* 2021, *7* (5), 1297-1307.

262. Trasatti, S., Work function, electronegativity, and electrochemical behaviour of metals: III. Electrolytic hydrogen evolution in acid solutions. *J. Electroanal. Chem. Interf. Electrochem.* 1972, *39* (1), 163-184.

263. Nørskov, J. K.; Bligaard, T.; Rossmeisl, J.; Christensen, C. H., Towards the computational design of solid catalysts. *Nat. Chem.* 2009, *1* (1), 37-46.

264. Mao, J.; He, C.-T.; Pei, J.; Chen, W.; He, D.; He, Y.; Zhuang, Z.; Chen, C.; Peng, Q.; Wang, D., Accelerating water dissociation kinetics by isolating cobalt atoms into ruthenium lattice. *Nat. Commun.* 2018, *9* (1), 1-8.

265. Chen, C. H.; Wu, D.; Li, Z.; Zhang, R.; Kuai, C. G.; Zhao, X. R.; Dong, C. K.; Qiao, S. Z.; Liu, H.; Du, X. W., Ruthenium-based single-atom alloy with high electrocatalytic activity for hydrogen evolution. *Adv. Energy Mater.* 2019, *9* (20), 1803913.

266. Wan, R.; Luo, M.; Wen, J.; Liu, S.; Kang, X.; Tian, Y., Pt-Co single atom alloy catalysts: accelerated water dissociation and hydrogen evolution by strain regulation. *J. Energy Chem.* 2022, 69, 44-53.

267. Shang, L.; Wang, J.-Q.; Cheng, C.-Q.; Zhang, Y.; Zhang, F.-F.; Xie, Y.-M.; Lu, J.-D.; Mao, J.; Guo, Q.-J.; Dong, C.-K., Oxidized single nickel atoms embedded in Ru matrix for highly efficient hydrogen evolution reaction. *J. Alloys Compd.* 2021, *874*, 159909.

268. Chao, T.; Luo, X.; Chen, W.; Jiang, B.; Ge, J.; Lin, Y.; Wu, G.; Wang, X.; Hu, Y.; Zhuang, Z., Atomically dispersed copper–platinum dual sites alloyed with palladium nanorings catalyze the hydrogen evolution reaction. *Angew. Chem.* 2017, *129* (50), 16263-16267.

269. Li, M.; Duanmu, K.; Wan, C.; Cheng, T.; Zhang, L.; Dai, S.; Chen, W.; Zhao, Z.; Li, P.; Fei, H., Single-atom tailoring of platinum nanocatalysts for high-performance multifunctional electrocatalysis. *Nat. Catal.* 2019, *2* (6), 495-503.

270. Zhou, J.; Lin, J.; Huang, X.; Zhou, Y.; Chen, Y.; Xia, J.; Wang, H.; Xie, Y.; Yu, H.; Lei, J., A library of atomically thin metal chalcogenides. *Nature* 2018, *556* (7701), 355-359.

271. Xia, C.; Zhu, P.; Jiang, Q.; Pan, Y.; Liang, W.; Stavitski, E.; Alshareef, H. N.; Wang, H., Continuous production of pure liquid fuel solutions via electrocatalytic CO_2 reduction using solid-electrolyte devices. *Nat. Energy* 2019, *4* (9), 776-785.

272. Ye, K.; Zhou, Z.; Shao, J.; Lin, L.; Gao, D.; Ta, N.; Si, R.; Wang, G.; Bao, X., In Situ Reconstruction of a Hierarchical Sn-Cu/SnO_x Core/Shell Catalyst for High-Performance CO_2 Electroreduction. *Angew. Chem., Int. Ed.* 2020, *59* (12), 4814-4821.

273. Grigioni, I.; Sagar, L. K.; Li, Y. C.; Lee, G.; Yan, Y.; Bertens, K.; Miao, R. K.; Wang, X.; Abed, J.; Won, D. H., CO_2 electroreduction to formate at a partial current density of 930 mA cm^{-2} with InP colloidal quantum dot derived catalysts. *ACS Energy Lett.* 2020, *6* (1), 79-84.

274. Li, Y.; Chen, J.; Chen, S.; Liao, X.; Zhao, T.; Cheng, F.; Wang, H., In Situ Confined Growth of Bismuth Nanoribbons with Active and Robust Edge Sites for Boosted CO_2 Electroreduction. *ACS Energy Lett.* 2022, *7*, 1454-1461.

275. Li, X.; Bi, W.; Chen, M.; Sun, Y.; Ju, H.; Yan, W.; Zhu, J.; Wu, X.; Chu, W.; Wu, C., Exclusive Ni–N_4 sites realize near-unity CO selectivity for electrochemical CO_2 reduction. *J. Am. Chem. Soc.* 2017, *139* (42), 14889-14892.

276. Kim, D.; Xie, C.; Becknell, N.; Yu, Y.; Karamad, M.; Chan, K.; Crumlin, E. J.; Nørskov, J. K.; Yang, P., Electrochemical activation of CO_2 through atomic ordering transformations of AuCu nanoparticles. *J. Am. Chem. Soc.* 2017, *139* (24), 8329-8336.

277. Kresse, G.; Furthmüller, J.; Hafner, J., Theory of the crystal structures of selenium and tellurium: the effect of generalized-gradient corrections to the local-density approximation. *Phys. Rev. B* 1994, *50* (18), 13181.

278. Hammer, B.; Hansen, L. B.; Nørskov, J. K., Improved adsorption energetics within density-functional theory using revised Perdew-Burke-Ernzerhof functionals. *Phys. Rev. B* 1999, *59* (11), 7413.

279. Xu, Y.; Shelton, W. A., O_2 reduction by lithium on Au (111) and Pt (111). *J. Chem. Phys.* 2010, *133* (2), 024703.

280. Durand, W. J.; Peterson, A. A.; Studt, F.; Abild-Pedersen, F.; Nørskov, J. K., Structure effects on the energetics of the electrochemical reduction of CO_2 by copper surfaces. *Surf. Sci.* 2011, *605* (15-16), 1354-1359.

281. Yan, S.; Peng, C.; Yang, C.; Chen, Y.; Zhang, J.; Guan, A.; Lv, X.; Wang, H.; Wang, Z.; Sham, T. K., Electron Localization and Lattice Strain Induced by Surface Lithium Doping Enable Ampere-Level Electrosynthesis of Formate from CO_2. *Angew. Chem.* 2021, *133* (49), 25945-25949.